ISSN: 3082-849X (Online)
Volume 1 · Issue 3
September 2025

Engineering Science in ADDITIVE MANUFACTURING

Engineering Science in Additive Manufacturing (ESAM) aims to collate the cutting-edge research and review articles in additive manufacturing that highlight the engineering science

ACCSCIENCE PUBLISHING

Engineering Science in Additive Manufacturing

Online ISSN: 3082-849X

Engineering Science in Additive Manufacturing (ESAM) aims to collate the cutting-edge research and review articles in additive manufacturing that highlight the engineering science. The journal covers all fundamentals of additive manufacturing, including its principles and applications. The journal publishes articles that acknowledge the significant development in the field and its disruptive nature in the industry. ESAM provides a platform for publishing articles that advance the in-depth understanding of additive manufacturing. The journal also welcomes papers that employ theories, numerical methods and/or simulations that demonstrate relevance to the additive manufacturing community.

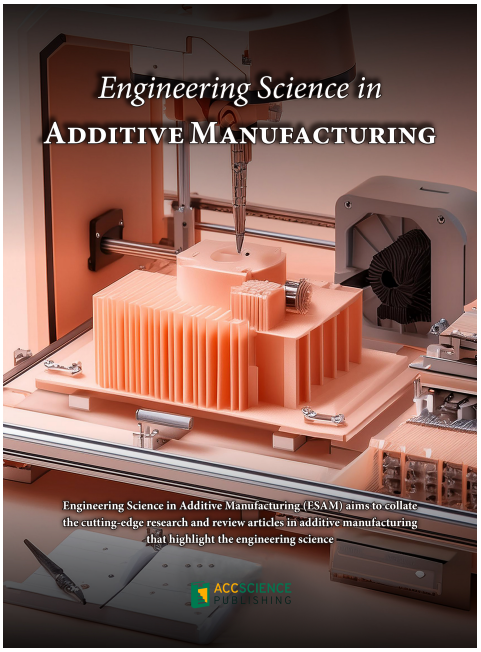

About the Publisher

AccScience Publishing is a publishing company based in Singapore. We publish a range of high-quality, open-access, peer-reviewed journals and books from a broad spectrum of disciplines.

Contact Us

Managing Editor
esam.office@accscience.sg

AccScience Publishing
9 Raffles Place, Republic Plaza 1 #06-00 Singapore 048619.

Volume 1 • Issue 3 • September 2025
ISSN 3082-849X (online)

ENGINEERING SCIENCE IN ADDITIVE MANUFACTURING

Editor-in-Chief
Swee Leong Sing
National University of Singapore, Singapore

ACCSCIENCE PUBLISHING
Access Science Without Barriers

ENGINEERING SCIENCE IN ADDITIVE MANUFACTURING

ISSN: 3082-849X (online)

Editorial and Production Credits

Publisher: AccScience Publishing
Managing Editor: Shirley Lu
Production Editor: Sharmila Velapasamy
Article Layout and Typeset: Sinjore Technologies (India)

For all advertising queries, contact esam.office@accscience.sg.

Supplementary file

Supplementary files of articles can be obtained at https://accscience.com/journal/ESAM/1/3.

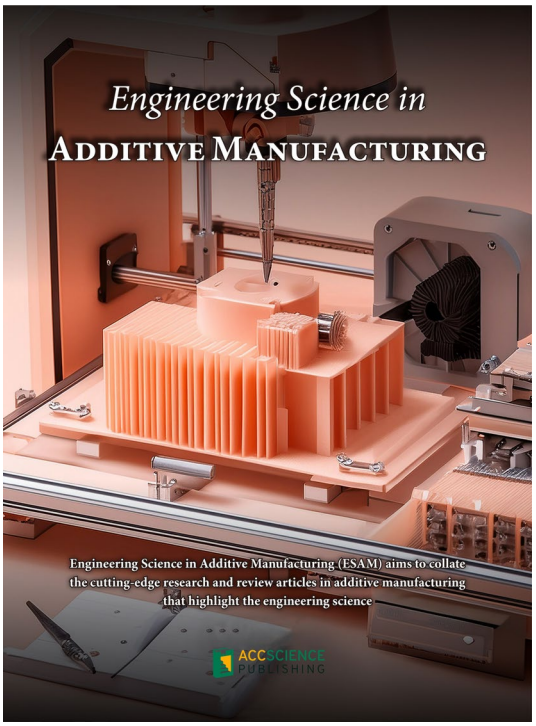

Disclaimer

AccScience Publishing is not liable to the statements, perspectives, and opinions contained in the publications. The appearance of advertisements in the journal shall not be construed as a warranty, endorsement, or approval of the products or services advertised and/or the safety thereof. AccScience Publishing disclaims responsibility for any injury to persons or property resulting from any ideas or products referred to in the publications or advertisements. AccScience Publishing remains neutral with regard to jurisdictional claims in published maps and institutional affiliations.

Engineering Science in Additive Manufacturing

Editorial Board

ACCSCIENCE PUBLISHING

Volume 1 | Issue 3 | September 2025

Engineering Science in Additive Manufacturing

https://accscience.com/journal/ESAM

CONTENTS

ACCSCIENCE PUBLISHING

Engineering Science in Additive Manufacturing

REVIEW ARTICLE

Recent advances in thermal management via additive manufacturing

Sooyeon Ji†, Junyeol Choi†, Myounggi Hong†, Jeongwoo Lee, Yong Choi, Jiheon Kim, Jaemin Lee*, and Wonjoon Choi*

School of Mechanical Engineering, Korea University, Seongbuk-Gu, Seoul, Republic of Korea

Abstract

Additive manufacturing (AM) has emerged as a transformative approach for advancing thermal management technologies, providing unprecedented freedom in design, material customization, and the implementation of novel thermal control strategies. This review presents a comprehensive overview of recent progress in AM-enabled thermal management, with an emphasis on enhancements in conductive, convective, boiling, and radiative heat transfer. AM facilitates the fabrication of complex architectures and composite materials with tailored thermal conductivities, substantially improving heat dissipation in diverse applications, including electronics, automotive systems, aerospace structures, and building technologies. Notably, recent developments in thermal metamaterials—such as structures capable of thermal cloaking and directional heat conduction—highlight the considerable potential of AM for manipulating complex thermal fields. Furthermore, the integration of phase change materials within AM-fabricated structures offers improved energy storage capacity and efficient thermal regulation. Future research should focus on the development of advanced composite materials, the integration of artificial intelligence for design optimization, the exploration of multifunctional metamaterials, and the advancement of sustainable and scalable AM processes. Hybrid and multimaterial AM techniques are particularly promising, enabling the fabrication of complex, functionally graded structures with precisely tailored thermal and mechanical properties. Addressing critical challenges—including structural integrity, microstructural control, material scalability, cost-effective production, and environmental sustainability—will further strengthen the role of AM in thermal management. In addition, the continued incorporation of high-fidelity computational simulations and real-time monitoring into AM workflows is expected to enhance process reliability and reproducibility. Expanding the range of AM applications to encompass lightweight and optically transparent polymer-based devices could unlock new avenues for thermal management in sensitive electronic and photonic systems.

Keywords: Thermal management; Conduction heat transfer; Convection heat transfer; Boiling heat transfer; Radiative cooling; Phase change material; Thermal metamaterial

†*These authors contributed equally to this work.*

***Corresponding authors:**
Jaemin Lee
(jmlee3025@korea.ac.kr)
Wonjoon Choi
(wojchoi@korea.ac.kr)

Citation: Ji S, Choi J, Hong M, *et al*. Recent advances in thermal management via additive manufacturing. *Eng Sci Add Manuf*. 2025;1(3):025260016. doi: 10.36922/ESAM025260016

Received: June 24, 2025

Revised: July 22, 2025

Accepted: July 28, 2025

Published online: August 18, 2025

1. Introduction

Thermal management is a critical aspect of modern engineering, impacting sectors from electronics cooling to building energy efficiency. The global building sector, for

example, consumes approximately 34% of energy and contributes 37% of global CO_2 emissions; improving insulation and thermal efficiency of building materials is a high priority.[1] At the same time, electronic and automotive systems are dissipating ever-higher heat fluxes due to device miniaturization and increased power density.[2,3] Conventional passive cooling solutions (e.g., air-cooled aluminum heat sinks) are approaching performance limits as heat fluxes can exceed 50–100 W/cm^2 in advanced devices.[4] These trends drive the need for new materials and designs that can spread and remove heat more effectively while minimizing weight and volume.

Additive manufacturing (AM) refers to layer-by-layer fabrication processes capable of producing complex and intricate geometries directly from digital models.[5] This innovative technology transforms digital designs into physical objects by successively depositing material layers, offering unparalleled flexibility and precision in manufacturing. Compared to traditional subtractive manufacturing methods, which involve removing material from a solid block, AM provides unprecedented geometric freedom. This freedom enables the creation of sophisticated internal structures such as lattices, fins, and porous architectures, which are challenging or even impossible to fabricate through conventional methods. In addition, AM allows precise control over the internal geometry, enabling designers to realize intricate and optimized structures tailored for specific applications.[6] Furthermore, AM facilitates the precise and customizable placement of materials, making it possible to produce advanced composite materials and functionally graded structures.[7-9] Such tailored material distributions allow engineers to finely adjust mechanical and thermal properties to satisfy stringent performance requirements and address complex design challenges.

In thermal management applications, these capabilities of AM offer substantial improvements in performance along with unprecedented design freedom compared to traditional fabrication techniques. For example, intricate and complex internal cooling channels can be directly integrated within heat exchangers, enabling efficient coolant circulation and significantly enhancing overall heat dissipation performance.[10] Furthermore, various lattice structures can be designed and fabricated to substantially increase the available surface area for heat transfer, effectively maximizing convective heat transfer efficiency.[11] In addition, AM technology allows precise control over the selection and placement of materials, enabling the production of customized composite structures optimized for specific thermal requirements. For instance, highly thermally conductive materials such as metallic or carbon-based fillers can be selectively incorporated in regions demanding high thermal conductivity.[12,13] Similarly, regions requiring enhanced radiative cooling performance can incorporate nanomaterials or nanoscale structures exhibiting high emissivity, thereby significantly boosting the overall thermal performance of the system.[14] Another notable advantage is the ability of AM processes to unify multiple individual thermal management components into a single integrated structure.[15] Such integrated designs drastically reduce thermal interface resistances arising from joints between separate components, thereby enhancing system reliability, durability, and thermal performance. Moreover, this approach simplifies manufacturing procedures and reduces production costs. Finally, AM technologies facilitate the creation of advanced thermal metamaterials specifically engineered to precisely manipulate heat flow characteristics, including directionality and magnitude.[16,17] These thermal metamaterials can achieve functionalities previously unattainable with conventional materials, such as thermal focusing, cloaking, and directional heat conduction. Consequently, AM-driven thermal metamaterials represent an innovative class of solutions, providing entirely new possibilities for controlling and managing thermal energy. Therefore, continuous development and adoption of AM technology are expected to play a critical role in advancing future thermal management solutions.

This review provides a comprehensive overview of how AM is advancing the field of thermal management. Section 2 introduces common AM methods and heat transfer mechanisms. Section 3 discusses conductive heat transfer: Enhancing thermal conductivity via AM-fabricated composites, achieving thermal insulation with lightweight structures and phase change materials (PCMs), and designing thermal metamaterials. Section 4.1 covers convection: passive and active heat sink innovations, micro/mini-channel and triply periodic minimal surface (TPMS)-based heat exchangers, and topology-optimized cooling structures. The latter part of section 4 addresses boiling heat transfer, both pool and flow boiling, including 3D-printed surfaces and two-phase devices. Section 5 discusses radiation heat transfer and passive daytime radiative cooling. The paper concludes with an outlook on future research directions, noting that while AM enables unprecedented thermal management designs, careful consideration of material behavior and fluid dynamics is required to fully capitalize on its potential.

2. AM for thermal management applications

2.1. AM techniques

AM, widely known as 3D printing, encompasses various layer-by-layer fabrication processes enabling intricate and

customized designs, which are impossible with traditional manufacturing methods. The primary AM techniques include material extrusion (MEX), vat photopolymerization (VPP), powder bed fusion (PBF), direct energy deposition, material jetting (MJ), and sheet lamination (SHL).[18]

MEX is a widely used AM technique, involving the selective deposition of materials through an extrusion nozzle to build 3D structures layer-by-layer. Prominent examples of MEX methods include fused filament fabrication (FFF) and direct ink writing (DIW). FFF is the most common MEX method, in which thermoplastic polymer filaments are melted in a heated nozzle and extruded layer-by-layer. DIW differs from FFF by extruding viscous inks, slurries, or pastes through a nozzle using pneumatic or mechanical pressure to form intricate structures directly. In thermal management using AM, materials employed in each MEX method are typically enhanced by mixing thermally conductive substances such as metals or ceramics to improve heat dissipation performance. In the specific case of DIW, materials are often structured into aerogels to significantly enhance thermal insulation performance. Beyond the conduction heat transfer mechanism, polymer composites used in MEX have also been primarily employed to regulate the radiation heat transfer mechanism by effectively interacting with infrared (IR).

VPP methods, such as stereolithography (SLA) and digital light processing (DLP), polymerize liquid resins via ultraviolet (UV) or visible light exposure. These methods produce high-resolution, smooth surfaces and complex geometries ideal for prototypes and intricate structures. For thermal management, fillers with high thermal conductivity (e.g., carbon-based materials and ceramics) are often incorporated into polymer resins. Therefore, this method is mainly used to control the conduction heat transfer mechanism.

Laser PBF (L-PBF) includes techniques such as direct metal laser sintering (DMLS), selective laser sintering, selective laser melting (SLM), and electron beam melting. These processes use thermal energy sources, such as lasers or electron beams, to fuse powdered materials, ranging from polymers and metals to ceramics. The strengths of PBF include superior mechanical properties, dimensional accuracy, and intricate structural capabilities. Due to these strengths, particularly the ability to fabricate complex structures with metals exhibiting high thermal conductivity, PBF has found practical applications across various thermal management fields. However, challenges involve high equipment costs, residual stress management, and porosity control.[19,20] In response to these challenges, particularly in metal-based L-PBF processes, there has been growing interest in simulation-based approaches to efficiently capture and manage the complex thermodynamic behavior.[21] Due to its capability to process metal powders, this technique is predominantly applied in controlling conduction and convection heat transfer mechanisms.

Directed energy deposition (DED) employs concentrated thermal energy, typically a laser, electron beam, or plasma arc, to melt and fuse material feedstock delivered as powders or wires. DED is effective for repairing high-value parts and fabricating large components with graded compositions. Yet, it faces challenges related to precision, surface finish, and thermal distortion. This fabrication technique is mainly employed to produce components designed for use in convection heat transfer mechanisms.

MJ involves jetting droplets of photopolymer or wax onto a build platform and subsequently curing them using UV light. MJ achieves high resolution and multimaterial capability, essential for functional prototypes and detailed models. However, it is limited by relatively slow build speeds and expensive materials. This method is primarily applied to the conduction mechanism.

SHL, exemplified by laminated object manufacturing and ultrasonic AM, bonds sheets of materials—typically metal foils, paper, or plastics—via adhesive or ultrasonic welding. It is suitable for large, layered components with embedded electronics but suffers from limited structural strength and design complexity compared to other AM techniques.

Each of these AM methods has unique advantages and inherent limitations, making method selection critical depending on targeted application needs, material requirements, structural complexity, and economic considerations.

2.2. Various heat transfer mechanisms for thermal management

Effective thermal management is critical in a broad spectrum of applications, from electronic cooling to energy systems. Achieving optimal thermal regulation involves utilizing various heat transfer mechanisms—conduction, convection, boiling, and radiation, each offering distinct advantages and characteristics.

Conduction heat transfer is fundamental and occurs through direct molecular or atomic interactions, typically occurring within solid materials, liquids, or gases at rest. It relies on temperature gradients, where heat spontaneously flows from regions of higher temperature to those of lower temperature due to particle vibrations and collisions. In

solids, particularly metals, conduction is highly efficient due to free electrons facilitating rapid energy transfer. The governing law for conduction is Fourier's law, expressed as Equation I:

$$q = -k\nabla T \quad (I)$$

Where q is the local heat flux density, W/m^2; k is the thermal conductivity, W/(m·K); and ∇T is the temperature gradient, K/m. Materials with high thermal conductivity, such as metals or ceramics, are excellent thermal conductors, whereas those with low thermal conductivity, such as polymers or aerogels, are effective insulators. Enhancing conduction involves incorporating highly conductive fillers (e.g., metal/metal oxide particles, carbon nanotubes [CNT], boron nitrides [BN]) into materials to improve heat dissipation.[22,23] Conversely, minimizing conduction for insulation purposes involves porous materials or aerogels to reduce the solid conduction pathways. Conduction heat transfer is critical in applications ranging from electronics cooling to building insulation design, significantly impacting energy efficiency and thermal management effectiveness.

Convection heat transfer refers to the transport of thermal energy due to the bulk movement of fluids, including liquids and gases. Unlike conduction, which relies on molecular vibration without bulk fluid movement, convection involves fluid motion that enhances heat transfer rates significantly. Convection can be categorized into natural (free) and forced convection. Natural convection occurs due to density variations within fluids, caused by temperature gradients; warmer fluids expand, becoming less dense and rising, while cooler fluids descend. In contrast, forced convection involves external forces—such as pumps, fans, or blowers—to actively drive fluid motion, thus increasing heat transfer efficiency. Newton's law of cooling mathematically describes convection as Equation II:

$$q = hA(Ts - T_\infty) \quad (II)$$

Where q is the heat transfer rate, W/m^2; h is the convective heat transfer coefficient, W/(m^2·K); A the surface area, m^2; T_s is the temperature of the surface, K; and T_∞ is the temperature of the fluid, K. Convection is pivotal in engineering applications such as heat exchangers, electronics cooling systems, HVAC design, and thermal management of engines. Optimizing convective heat transfer involves techniques such as employing fins, microchannels, or enhancing fluid turbulence, which significantly impact overall system efficiency and reliability.

Boiling heat transfer is a highly efficient thermal energy transport mechanism involving phase change from liquid to vapor. When a heated surface exceeds the liquid's saturation temperature, boiling initiates, forming vapor bubbles. Boiling is classified primarily into two types: Pool boiling and flow boiling. Pool boiling occurs in stagnant fluids, whereas flow boiling occurs in fluids forced over heated surfaces. The boiling curve identifies different boiling regimes—natural convection boiling, nucleate boiling, transition boiling, and film boiling—each with unique heat transfer characteristics (Figure 1A).[24] Nucleate boiling is especially effective, characterized by rapid bubble nucleation, growth, and departure, providing high heat-transfer coefficients (HTC) due to vigorous mixing near the heated surface. Critical heat flux (CHF) marks the transition to film boiling, where a vapor film insulates the surface, dramatically decreasing heat transfer efficiency. Enhancing boiling performance often involves surface modification techniques such as microstructures, porous coatings, or AM to increase nucleation sites, promoting efficient bubble dynamics.[25,26]

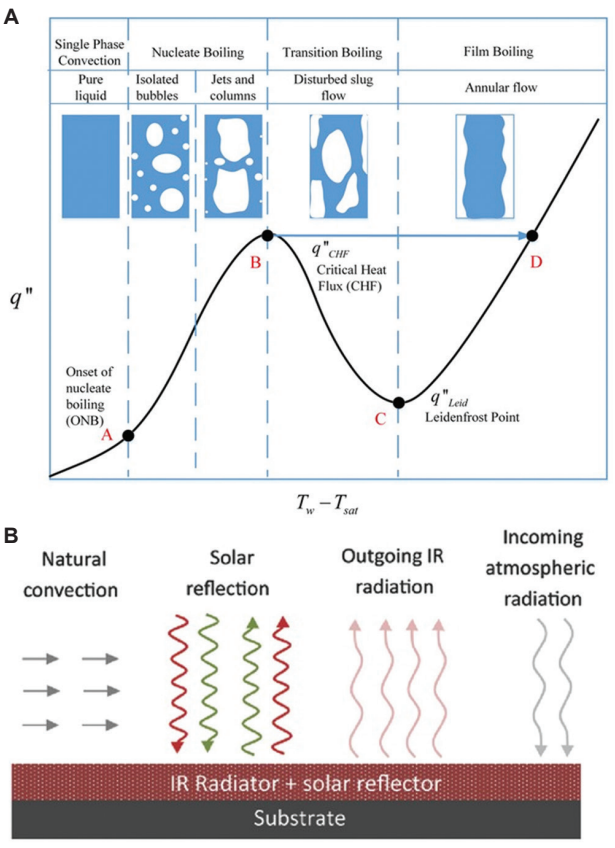

Figure 1. Examples of heat transfer mechanisms. (A) Boiling heat transfer.[24] Representative wall superheat and heat flux relation in the boiling phenomenon and bubble mechanism. (B) Radiative cooling.[27] Non-radiative heat transfer (e.g., natural convection), reflected or absorbed energy to the material from solar irradiation, the outgoing IR radiative energy emitted by the material, and incoming radiative heat to the material from the atmosphere.

Thermal transport devices leveraging liquid-to-vapor phase transitions include heat pipes and vapor chambers. Within a sealed, near-vacuum environment, the working fluid evaporates at the heated region (evaporator) and condenses at the cooler region (condenser). The condensed fluid then returns to the evaporator by capillary action, effectively transferring heat from the evaporator to the condenser. Applications of boiling heat transfer and phase-change devices span high-power electronics cooling, nuclear reactors, refrigeration systems, and chemical processing, highlighting their critical roles in advanced thermal management solutions.

Radiation heat transfer provides unique advantages, particularly in thermal management applications where conductive or convective pathways are limited. Radiative cooling technologies utilize engineered coatings and films designed with selective emissivity characteristics to exploit atmospheric transparency windows, effectively radiating heat into space without external energy input (Figure 1B).[27] Recent advancements include selective emitters and specialized radiative cooling coatings capable of achieving sub-ambient temperatures even under direct sunlight, highlighting their efficiency as passive cooling solutions. Due to these benefits, radiation cooling technologies are increasingly employed in sustainable thermal management applications such as building roofs, solar panels, electronics cooling, and space cooling systems. As a passive, energy-free method, radiation cooling represents an attractive and sustainable approach to energy conservation and thermal regulation.

In conclusion, understanding and exploiting these various heat transfer mechanisms through advanced material engineering and manufacturing processes like AM offer promising pathways to achieving superior thermal management solutions. Each mechanism, individually or in combination, can be optimized to meet specific thermal management challenges across diverse application domains.

3. Conduction heat transfer for thermal management using AM

3.1. Thermal conductivity enhancement through AM

Conductive heat transfer is mainly used to fabricate fundamental structures that can reinforce the performance of other heat transfer mechanisms. In this section, we focus on how AM technologies utilizing metallic, non-metallic, or hybrid materials can be strategically employed to tailor thermal conductivity. Specifically, we highlight approaches to increase thermal conductivity for efficient heat dissipation, decrease it for thermal insulation, and precisely control heat flow for the development of thermal metamaterials designed to direct or block heat as required.

In metal-based AM, desired geometries are fabricated by melting and solidifying metal particles using energy sources such as lasers or electron beams. In this process, both the particle size and composition of metal particles critically influence the resulting grain structure and thermal conductivity. A representative study used 316L stainless steel powder particles to control microstructure via electron beam PBF and laser-DED processes.[12] Unlike the columnar coarse crystals commonly found in traditional PBF processes, this work demonstrated that coarse particles in the powder bed undergo uneven melting, acting as seeds to induce fine spherical grains with high strength and ductility. Similarly, analysis of CoFeNi and CoCrFeNi high-entropy alloy systems revealed that lower thermal conductivity correlates with slower laser melting/cooling rates, influencing solidification patterns such as wider/longer remelted columnar grains.[28] As the grain size decreases, the density of grain boundaries increases, which enhances electron scattering at the interfaces and results in reduced thermal conductivity. Therefore, in metal-based AM processes, controlling grain size during fabrication is essential for improving thermal conductivity.

In addition, localized high-temperature melting and repeated powder reuse result in surface oxidation of metal powders and melt pools, forming oxide inclusions. These oxide layers and inclusions further decrease thermal conductivity within the metallic structure and increase interfacial thermal resistance, hindering heat transfer in the melt pool and deteriorating interlayer bonding quality. The presence of oxide films also decreases molten metal wettability, causing incomplete fusion between layers and interface defects such as micro-porosity, thus compromising structural reliability. Such oxidation effects and elevated interfacial thermal resistance adversely affect thermal and mechanical properties in practical applications, increasing residual stresses and complicating subsequent welding processes, ultimately diminishing component performance and reliability. Therefore, precise grain size control and careful oxidation management during fabrication are essential for optimizing thermal conductivity and structural integrity in metal-based AM processes.

To enhance thermal conductivity, the grain size can be increased by controlling the laser scan speed during the metal AM process. In the case of Cu-Al-Ni-Mn shape-memory alloys, the high thermal conductivity of the Cu and the shape-memory effect are advantageous. It was observed that increasing the scan speed leads to a reduction in martensite size, whereas lower scan speeds

result in less grain refinement and consequently higher thermal conductivity (Figure 2A and Table 1).[29] In another study, a CuNi2SiCr alloy fabricated via L-PBF exhibited a low thermal conductivity of approximately 70 W/(m·K) (at room temperature) due to increased free electron scattering from the supersaturated matrix containing Ni, Si, and Cr; however, after a heat treatment at 500°C for 3 h, nanoscale precipitates containing Ni, Si, and Cr formed with the matrix, reducing the concentration of alloying elements in solid solution. This microstructural change increased the electron mean free path from 5.6 nm to 13.4 nm—an elevation of about 2.4 times—resulting in a significant improvement in thermal conductivity reaching up to 180 W/(m·K) in the heat-treated samples (at room temperature).[30] In addition, incorporating graphene into aluminum using L-PBF achieved a 25.5 × 10-^{6}/°C lower coefficient of thermal expansion and approximately 10% higher thermal conductivity (140–180 W/m·K at 150–350°C) compared to conventional AlSi12 alloys.[13]

Polymer-based composites typically exhibit lower thermal conductivity compared to metals, but their excellent formability, low manufacturing costs, and low density make them particularly attractive for electric vehicles and aerospace mobility applications. Therefore, overcoming the limitation of low thermal conductivity in these polymer-based composites can enable broader substitution for metallic structures, potentially enhancing fuel efficiency of mobility platforms and reducing manufacturing costs associated with complex-shaped components. To address this, various studies have investigated enhancing thermal

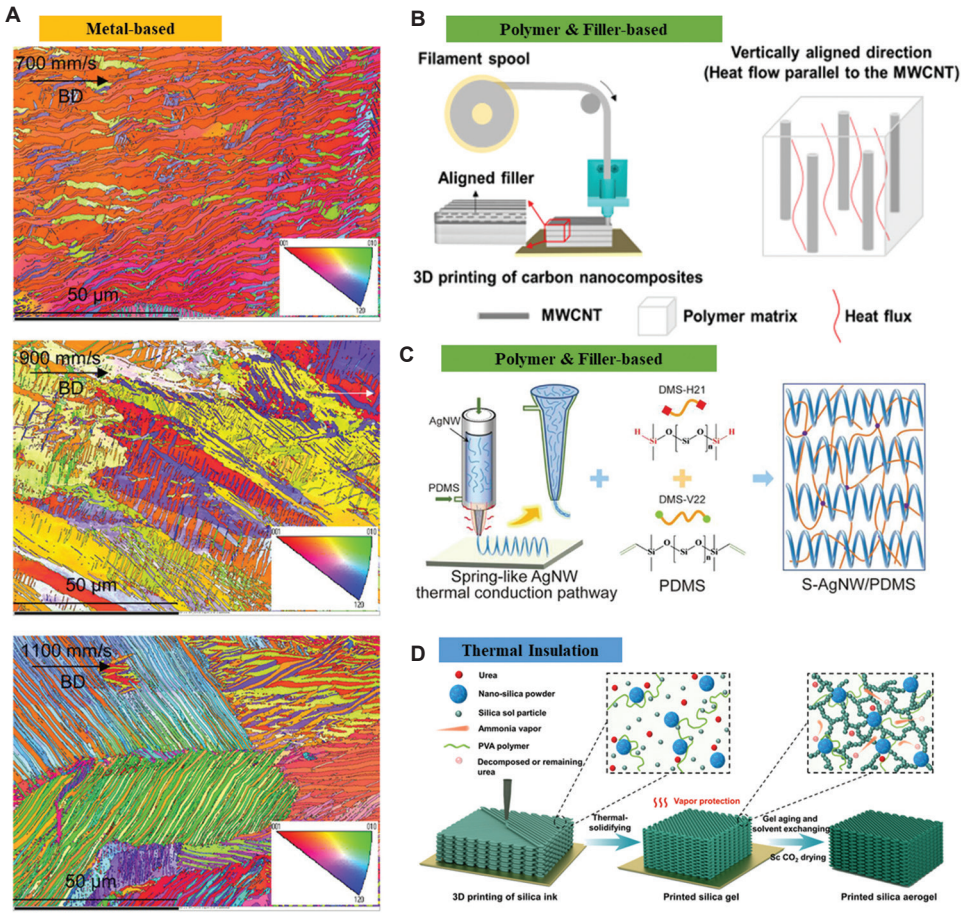

Figure 2. Thermal conductivity control using additive manufacturing. Metal-based thermal conductivity enhancement materials: (A) L-PBF of Cu–Al–Ni–Mn shape-memory alloy for the application of active heat sinks.[29] Copyright © 2023 Wiley. Reproduced with permission of Wiley. Polymer and filler-based materials: (B) MWCNT-filled PLA.[32] Copyright © 2023 American Chemical Society. Reproduced with permission of the American Chemical Society. (C) Spring-like thermal conduction pathways of silver nanowire compounded with PDMS (S-AgNW/PDMS) composites.[35] The average length and diameter of AgNW nanowires are 10.7 μm and 115 nm, respectively. The outer and inner diameters of S-AgNWs are ~1.8 mm and 1.0 mm, respectively. Copyright © 2024 Wiley. Reproduced with permission of Wiley. Thermal insulation materials: (D) 3D-printed silica aerogels by directly writing temperature-induced solidifiable inks.[43] Copyright © 2021 American Chemical Society. Reproduced with permission of the American Chemical Society.
Abbreviations: AgNW: Silver nanowire; MWCNT: Multi-walled carbon nanotubes; L-PBF: Laser powder bed fusion; PDMS: Polydimethylsiloxane; PLA: Polylactic acid; PVA: Polyvinyl alcohol; S-AgNW: Silver nanowire in spring-like structure.

Table 1. Summary of thermal conductivities measurement

Materials	AM method	Geometry	Thermal conductivity (W/[m·K])	Measured region (□)	References
Thermal conductivity enhancement					
Metal-based					
$CuNi_2SiCr$ alloy	L-PBF	Heat-treated	180–240	~25–620□	30
Graphene (25 wt%)-AlSi12 alloy	L-PBF	Carbon, Al_4C_3 cluster	140–170	~150–350□	13
Cu-Al-Ni-Mn alloys	L-PBF	Of course, low-scan rate	30–50	At 300□, 380□	29
Polymer-based			Max.		
LLDPE/BN@GNPs	FFF	Direction-dependent	3.11	Room temperature	38
BNNS (30 wt%)/TPU	FFF	Direction-dependent	1.80	Room temperature	31
MWCNT (20 wt%)/PLA	FFF	Direction-dependent	0.575	35–108□	32
Hexadecane/POE/AEO/GNPs	DIW	Direction-dependent	1.276	40□	36
Pitch carbon fiber PLA	FFF	Direction-dependent	37.1	N/A	33
3D-h-BN, graphene/PLA	FFF	Direction-dependent	3.82	N/A	37
Graphene (30 wt%)-TPU	FFF	Direction-dependent	4.54	−10–50□	39
20 vol% S-AgNW/PDMS	DIW	Direction-dependent	7.63	20–100□	35
Vertical-rGO/CNT/PDMS	DIW	Direction-dependent	6.04	Room temperature	40
h-BN/POE/Polypropylene	FA-FDM	Direction-dependent	1.43	N/A	34
Thermal insulation					
Silanized CNF aerogels	DIW	Porous aerogel	0.034	N/A	44
PLA VIP	FFF	8-interlayer panel	0.0155	15–35□	47
Silica aerogel particles/polyimide aerogel	DIW	Porous aerogel	0.076	N/A	46
PLA structures	FFF	Lamellar, cylindrical, gyroid	0.099, 0.094, 0.072	Room temperature	42

Abbreviations: AEO: Alkyl ether of ethylene oxide; AM: Additive manufacturing; BN: Boron nitride; BNNS: Boron nitride nanosheet; CNF: Cellulose nanofiber; CNT: Carbon nanotube; GNP: Graphene nanoplatelet; h-BN: Hexagonal boron nitride; MWCNT: Multi-walled carbon nanotube; LLDPE: Linear low-density polyethylene; L-PBF: Laser powder bed fusion; PDMS: Polydimethylsiloxane; PLA: Polylactic acid; POE: Polyolefin elastomer; rGO: Reduced graphene oxide; S-AgNW: Silver nanowire in spring-like structure; TPU: Thermoplastic polyurethane; VIP: Vacuum insulation panel; FFF: Fused filament fabrication; FDM: Fused deposition modeling.

conductivity by introducing fillers with high intrinsic thermal conductivity, such as nanomaterials (e.g., CNT, ceramics, and metal nanowires) and plate-like materials (e.g., graphene and BN), to establish effective pathways for rapid thermal energy transfer within the polymer matrix. Moreover, AM technologies have been actively explored to fabricate polymer composite parts or structures with significantly improved thermal performance.

A representative example of using fillers to enhance thermal conductivity involves incorporating hexagonal BN nanosheets (BNNS) into thermoplastic polyurethane (TPU) via FFF printing. Melt extrusion aligns BNNS within the TPU, achieving an in-plane thermal conductivity of 1.80 W/m·K (at room temperature) at 30 wt% BNNS, 650% higher than pure TPU.[31] Another study used multi-walled CNTs (MWCNTs) in polylactic acid (PLA) filaments, obtaining a thermal conductivity of ~0.575 W/m·K (at 35–108°C)at 20 wt% MWCNT, approximately 5.87 times higher than pure PLA due to alignment from shear forces[32] (Figure 2B). Continuous carbon fibers coated with PLA were printed using FFF, achieving a thermal conductivity of 37.1 W/m·K at 9.5 vol%, emphasizing fiber continuity's role.[33] In addition, anisotropic thermal conductivity was introduced by co-injecting thermally conductive BN fluids with polymer filaments, resulting in a composite with a conductivity of 1.43 W/m·K at 60 wt% BN.[34] This technology enables the precise design of thermally conductive pathways in heat-dissipating materials by adjusting the 3D printing model and parameters, and it has potential for use in thermal management and heat dissipation systems for electronic devices.

In MEX-based AM, not only FFF but also DIW techniques can be employed to fabricate various structures utilizing polymer composites with enhanced thermal

conductivity. For example, silver nanowire (AgNW) with high thermal conductivity filler, and polydimethylsiloxane (PDMS) composites achieved a conductivity of 7.63 W/m·K (at 20–100°C) at 20 vol% AgNW, maintaining stability under deformation[35] (Figure 2C). As described in Figure 2C, AgNWs with an average length and diameter of 10.7 μm and 115 nm, respectively, are first incorporated into PDMS (DMS-H21 + DMS-V22) and then 3D-printed into a spring-like (S-AgNW) structure. Afterwards, these S-AgNWs—with outer and inner diameters of approximately 1.8 mm and 1.0 mm, respectively—are again aligned and embedded within PDMS matrices. This 3D printing process enables the AgNWs to be arranged in a highly aligned, unidirectional structure, resulting in a remarkable enhancement of thermal conductivity along the printing direction due to the formation of an anisotropic network of conductive fillers. Another DIW composite (hexadecane/polyolefin elastomer [POE]/poly[alkyl ether of ethylene oxide] [AEO]/GNPs composites), combining hexadecane, POE, AEO, and graphene nanoplatelets (GNPs), exhibited 1.24 W/m·K (at 40°C) vertical conductivity and significantly reduced temperature differences on semiconductor surfaces compared to commercial products.[36] Although DIW differs from fused deposition modeling (FDM) in that it uses ink cured after deposition, it shares the common feature of combining polymers and fillers to boost thermal conductivity.

An important point is that research on polymer and filler composites can also be applied to develop multifunctional metamaterials and hybrid materials, such as a PLA skeleton filled with BN or graphene. These composites showed up to 3.82 W/m·K thermal conductivity with BN and enhanced mechanical strengths (20.3 MPa) and electrical insulation.[37] However, when graphene was used, the composite exhibited excellent thermal and electrical conductivity as well as a tensile strength (40.6 MPa). Compared to composites with only filler, these materials showed a 2.81-fold increase in thermal conductivity and 1.83-fold (BN filler) and 3.98-fold (graphene filler) increases in mechanical strength, respectively. Similarly, adding GNPs and BN to linear low-density polyethylene (LLDPE) created composites with thermal conductivity reaching 3.11 W/m·K (at room temperature), over 8 times higher than pure LLDPE.[38]

Research in polymer-filler composites also extends to energy applications. A bilayer structure using graphene-TPU films maximized anisotropic thermal conductivity, suitable for solar panels, with a sixfold through-plane conductivity difference.[39] Another example is a vertically printed reduced graphene oxide (rGO)/CNT-PDMS thermal interface material (TIM) device achieving 6.04 W/m·K (at room temperature) thermal conductivity, beneficial for thermal anomaly detection.[40] In this device, rGO/CNT was printed vertically by DIW, and the gaps were filled with PDMS to form the TIM. In addition, a topology-optimized aluminum structure infiltrated with PCM via SLM showed significant improvements in heat distribution and temperature uniformity.[41]

3.2. Thermal insulation using AM

In addition to heat dissipation, thermal insulation plays a crucial role in thermal management. Materials with superior insulation performance significantly reduce the energy consumption required to maintain optimal temperatures in buildings or refrigeration systems, thereby lowering greenhouse gas emissions and overall resource usage. Furthermore, enhancing insulation by achieving lower thermal conductivity allows comparable performance with reduced material thickness. This reduction substantially improves space efficiency in mobility applications and refrigeration equipment, facilitating more compact, lightweight, and energy-efficient designs.

To enhance thermal insulation performance, it is crucial to block or complicate the heat transfer pathways. Complex 3D structures based on unit cells are well-suited for this purpose, as they effectively disrupt heat flow and thereby improve insulation. In a study utilizing the FFF method, three structures—lamellar, gyroid, and cylindrical—were fabricated with the same volume fraction.[42] Among them, the lamellar structure exhibited the lowest thermal conductivity, demonstrating its superior insulating capability. However, despite their structural complexity, these architectures still exhibit higher thermal conductivity compared to conventional insulation materials. This limitation arises primarily because traditional insulators consist predominantly of air, known for its extremely low thermal conductivity. Consequently, there has been growing interest in methods capable of further reducing thermal conductivity by significantly increasing porosity. Recent studies have addressed this by combining DIW with freeze-drying to create aerogel structures characterized by ultra-low thermal conductivity, such as silica aerogels[43] (Figure 2D). For example, one study successfully fabricated an interpenetrating network structure of polymethylsilsesquioxane and cellulose nanofibers (CNFs) through DIW printing followed by freeze-drying, achieving an impressively low thermal conductivity of 0.034 W/m·K.[44] Similarly, another research group utilized lignocellulose nanofibrils to produce thermally insulating aerogels, highlighting the great potential of biopolymer-based aerogel structures fabricated by 3D printing techniques for advanced insulation applications.[45] In addition, a recent approach has explored the incorporation of silica aerogel particles into 3D-printed composite

aerogel structures to further enhance thermal insulation performance.[46]

Beyond aerogel-based methods, entirely different approaches combining 3D printing with thermal insulation technology have also emerged. One innovative example involves the use of FFF to fabricate polymer-based vacuum insulation panels (VIPs).[47] In this research, a 3D-printed VIP with eight solid interlayers was constructed under a vacuum pressure of approximately 10 Pa, achieving an exceptionally low thermal conductivity of 0.0155 W/m·K (at 15–35°C)—about 60% of the thermal conductivity of air (0.025 W/m·K). Likewise, thermal insulation aimed at preserving thermal energy is also an essential factor in thermal management, and many AM-based techniques have been utilized to address this aspect. For instance, methods such as lattice structure design, incorporation of low thermal conductivity aerogel particles, and fabrication of VIP panels with superior insulating performance have been employed to significantly enhance insulation performance.

3.3. Thermal metamaterial and PCM using AM

Advances in AM technologies have enabled the development of diverse thermal metamaterials that go beyond simply enhancing thermal conductivity or insulation performance. These advancements allow for precise control of heat flux and effective thermal energy storage across specific temperature ranges. Thermal metamaterials are materials engineered to exhibit unique thermal properties rarely found in nature and are used to manipulate or control heat transfer. 3D printing enables the free design and production of complex internal structures and diverse material combinations, greatly expanding the scope of research and applications for thermal metamaterials.

Active research is underway on thermal metamaterials that alter heat transfer pathways. For example, by integrating the theory of anisotropic thermal conductivity with custom MEX 3D printing technology, thermal cloaking functionality can be realized by embedding 0.3 mm copper wires into a PLA matrix.[17] This metal-polymer integration enhances the design freedom of thermal metamaterials and enables the fabrication of heat exchangers or temperature control devices with complex internal channels and structures. Furthermore, the required thermal conductivity distribution for desired thermal functions—such as heat concentration, rotation, and cloaking—can be calculated, divided into small grid units, and converted into a single STL file for 3D printing[48] (Figure 3A). For instance, after 3D-printing die steel (H13) and fixing it with PDMS, various thermal manipulation functions such as heat concentration (isotherms converging at the center), heat rotation (isotherms rotated by 45°C),and thermal cloaking (temperature distribution in the cloaked region matching the outside) can be experimentally confirmed. Through 3D printing, thermal metamaterials with complex shapes and functions can now be practically fabricated.

Meanwhile, research is also progressing to improve the mechanical properties and durability of thermal metamaterials. One example involves various additively manufactured lattice shapes, such as triangles, cubes, petals, and waves, using SLA, followed by chemical vapor infiltration to inject silicon carbide (SiC) whiskers inside the structures.[49] This process densely coats the lattice surfaces with SiC, effectively suppressing deformation and thermal expansion caused by temperature changes.

Efforts to maximize the performance of thermal metamaterials by combining various materials and structures continue, with recent attention on infiltrating liquid metals and PCMs into polymers to alter thermal conductivity, physical properties, specific heat, and electrical conductivity[50] (Figure 3B). For example, acrylonitrile butadiene styrene polymers fabricated by 3D printing can be placed in a vacuum chamber and infused with a Bi/In/Sn alloy liquid metal to create composites with high tensile strength (up to 35.41 MPa), thermal conductivity (up to 25.29 W/[m·K]), and electrical conductivity (up to 106 S/m)[51] (Figure 3C). These composites utilize solid-liquid phase change properties for high-power LED heat dissipation and temperature control, and also exhibit excellent electromagnetic shielding. This approach is also actively applied in energy storage research, combining PCMs. Over the past 5 years, various strategies have been developed to complement the intrinsic properties of PCMs.[52,53] A representative example is the DIW of inks mixing lignocellulose nanofibers, graphene oxide, and Pickering emulsion paraffin gel, followed by freeze-drying to create a structure with entangled paraffin microspheres.[54] This structure is used for solar-thermal-electric conversion and heat storage, with a 3D-printed concave solar collector heating up to 83.2°C,generating higher voltage and longer energy storage time than 2D planar collectors.

Research on PCM-based thermal energy storage via AM is progressing in various ways. For instance, lauric acid mixed with photocurable resin and printed by SLA effectively addresses PCM leakage issues, showing optimal thermal performance at 50% loading.[55] It exhibits 83.7 J/g latent heat enthalpy, 14.02 MPa tensile strength, and only about 1.31% loss after leakage testing (50°C, 60 min). Another study incorporated microencapsulated PCM (MEPCM), consisting of a paraffin mix as the core

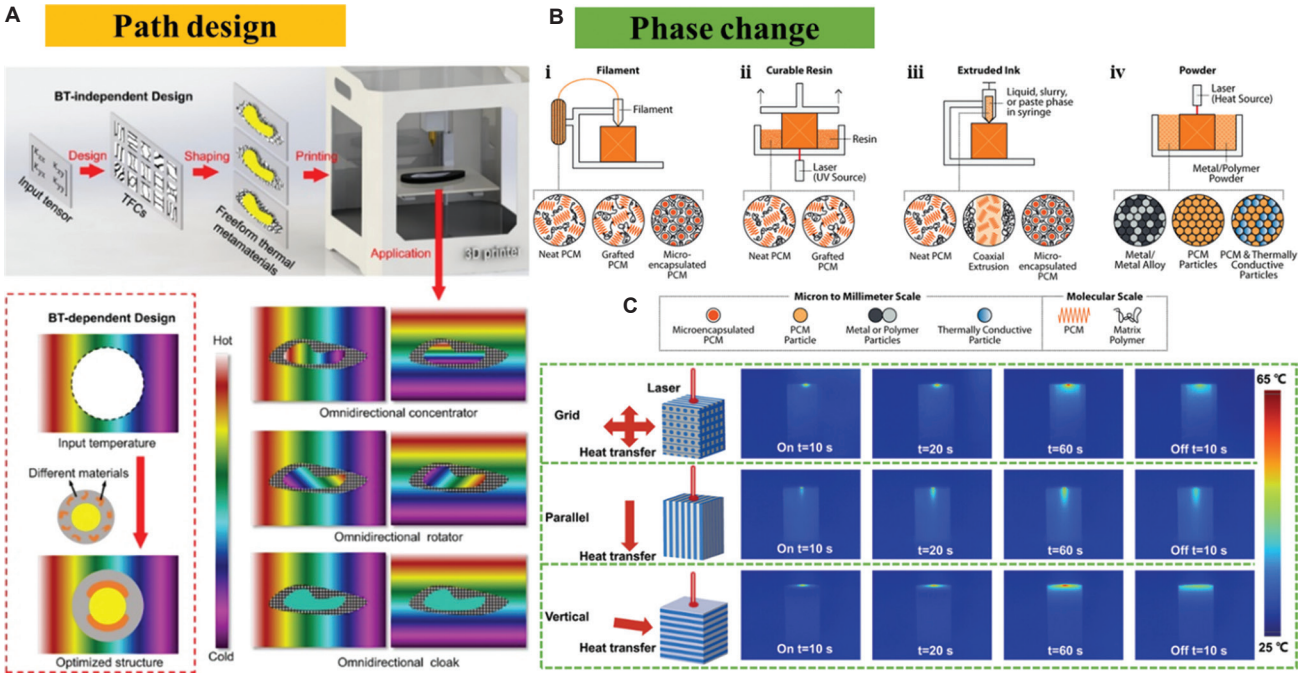

Figure 3. Thermal metamaterials using additive manufacturing. Thermal conduction path design: (A) Topological functional cells.[48] (B) Various approaches for incorporating phase change materials into material matrices: (i) fused filament fabrication or fused deposition modeling; (ii) stereolithography; (iii) direct ink writing; (iv) selective laser sintering or selective laser melting.[50] Metamaterials using phase change mechanism: (C) volume-metallization 3D-printed polymer composite.[51] Copyright © 2024 Wiley. Reproduced with permission of Wiley.

and melamine-formaldehyde as the shell in 15–30 μm spheres, into SLA resin, producing composites that absorb and release heat with temperature changes, significantly improving thermal stability and energy storage efficiency while maintaining mechanical performance.[56,57] The final samples with 40% MEPCM in resin exceeded 87 J/g of latent heat storage energy.

Furthermore, simply infusing PCM into 3D-printed lattice structures can significantly enhance energy storage efficiency. A representative example is a study in which 50 g of paraffin wax was injected into AlSi10Mg-0403 aluminum lattice structures (thermal conductivity: 96 W/[m·K]) of various sizes, confirming that the 10 mm-spaced structure exhibited the most uniform temperature distribution (below 8 K) and the fastest charging time (17% reduction).[58] Other studies have experimentally demonstrated that in aluminum body-centered cubic (BCC) lattice structures, the use of paraffin leads to shorter complete melting times of the PCM as the surface area of the structure increases.[59] In addition, research has reported the fabrication of structures using photosensitive resin and polyethylene glycol (PEG) mixed in various ratios and printed with a DLP 3D printer.[60] According to this study, higher PEG content (over 50%) results in more pronounced phase change characteristics. The composites exhibit excellent thermal energy storage properties. In this way, the combination of AM and PCM enables the realization of complex energy storage structures without PCM leakage issues. Meanwhile, when combining lattice structures with PCMs, it is important to consider not only conductive heat transfer but also natural convection during PCM melting. Research has shown that among various unit cell structures, the f2ccz structure demonstrates the best thermal performance per unit mass, attributed to its superior heat transfer characteristics in both conduction and natural convection during PCM melting.[61] The study emphasizes that the convective movement of PCM, considering gravity, is a crucial factor that cannot be ignored in the mechanism of thermal energy storage and heat transfer in PCM-3D structure composites.

In summary, AM technology has brought about transformative changes in the design and fabrication of thermal metamaterials. Although challenges remain—such as minimizing interfacial thermal resistance, optimizing the balance between natural convection and conduction, and developing application-specific materials—the integration of AM with thermal metamaterials is expected to provide innovative solutions in various fields, including thermal pathway design, thermal management for electronic devices, improved building energy efficiency, and renewable energy storage. This will make a significant contribution to the advancement of sustainable energy technologies.

4. Convective heat transfer for thermal management using AM

4.1. Various designs of passive and active cooling heat sinks

Since conductive heat transfer alone is often insufficient for effective thermal energy transport, most thermal management systems rely on convection heat transfer, which transfers heat via fluid motion. Two representative cooling devices that utilize convection are heat sinks and heat exchangers. A heat sink typically employs a pin-fin structure to maximize the contact area with the cooling fluid, thereby enhancing convective heat dissipation to working fluids such as air or coolant. Heat sinks are classified into natural convection (or passive thermal management) and forced convection (active thermal management) depending on whether external energy is used to circulate the fluid. Among them, natural convection is a cooling method where fluid motion is driven by the density variations within the fluid itself, made by temperature gradients. Passive thermal management is considered a free-source cooling mechanism as it operates naturally without requiring external power. Moreover, it offers the advantage of being silent due to the absence of externally powered systems. However, the convection heat transfer coefficient in passive systems is relatively low, which limits their broad usability.[62] For the extended applications, forced convection cooling (or active cooling) methods are often employed for applications requiring high cooling performance. It is driven by the external pressure or velocity sources, such as fans, pumps, or suction, which include air-cooling techniques as well as methods using liquid coolant.

Recently, AM has emerged as a promising approach for fabricating diverse heat sink structures. AM technologies provide unprecedented design freedom, enabling the diverse control of parameters such as truss shape, sizes, and lengths. It also allows the minimization of the material used, significantly reducing material waste. Thus, extensive structural and performance enhancements are being actively explored to improve convective heat transfer in AM-produced devices. To enhance cooling efficiency, recent research has focused on: (i) optimizing structural geometries such as cubic, truss, or BCC cells; (ii) refining pin-fin arrays; and (iii) exploring alternative heat sink materials.

In the early stages of heat sink research utilizing AM, most studies focused on structural modification using the L-PBF technique. In particular, many studies aimed to enhance cooling performance by increasing surface area through the manipulation of complex shapes and structures that were previously unmanufacturable before the advent of 3D printing, by adjusting cell structure, size, and geometry (Figure 4). Shamvedi *et al.*[63] fabricated a compact, lightweight, and efficient heat sink by increasing the surface area of lattice structures within a constant heat sink volume, simultaneously optimizing the lengths of the fins. Lorenzon *et al.*[64] developed BCC truss structures with various truss cross-sectional shapes, including circular, elliptical, droplet, and cam shapes, systematically controlling their sizes to achieve enhanced thermal performance (Figure 4A). Tseng *et al.*[65] created five distinct BCC porous truss configurations and experimentally validated their thermal performance under liquid flow cooling conditions.

In addition, significant research has been dedicated to optimizing pin-fin array configurations to enhance heat dissipation performance under natural convection conditions. Lazarov *et al.*[66] utilized L-PBF with aluminum to precisely control the size and arrangement of pin fins, achieving superior passive cooling performance in LED applications. Their optimized pin-fin designs outperformed traditional lattice structures by more than 21%, effectively doubling the life expectancy of the LED devices and reducing operational costs by approximately 50%. In addition to L-PBF, alternative AM techniques have also been explored for fabricating heat sinks. Notably, AM has been actively applied to ceramic-based heat sink designs. Ho *et al.*[67] employed a photopolymerization-based AM method to fabricate complex structures such as honeycomb, Kelvin cells, octet-truss lattices, and mini-gear configurations using ceramic fillers. Similarly, Sheng *et al.*[68] developed a heat sink composed of aluminum nitride powder, achieving structures characterized by robust mechanical properties, high thermal conductivity, and uniform microstructures.

Meanwhile, research has explored modifying the material composition of heat sinks. Traditionally, heat sinks rely on metals due to their inherently high thermal conductivity, which is essential for efficient heat conduction. However, metals typically introduce substantial weight, prompting increased demand for lighter or composite materials.[69] Consequently, polymer composites infused with thermally conductive fillers have garnered attention. Huttunen *et al.*[70] developed heat sinks using thermally conductive plastic filaments, achieving high thermal conductivity coupled with low electrical conductivity, which reduced thermal resistance by approximately 10–20% compared to conventional resin-based heat sinks (Figure 4B). Timbs *et al.*[71] produced heat sinks utilizing polymer filaments loaded with diverse fillers, such as carbon, copper, and bronze. Their study investigated heat sinks designed with straight and oblique fin geometries, comparing their thermal resistance, pressure drop, and heat dissipation

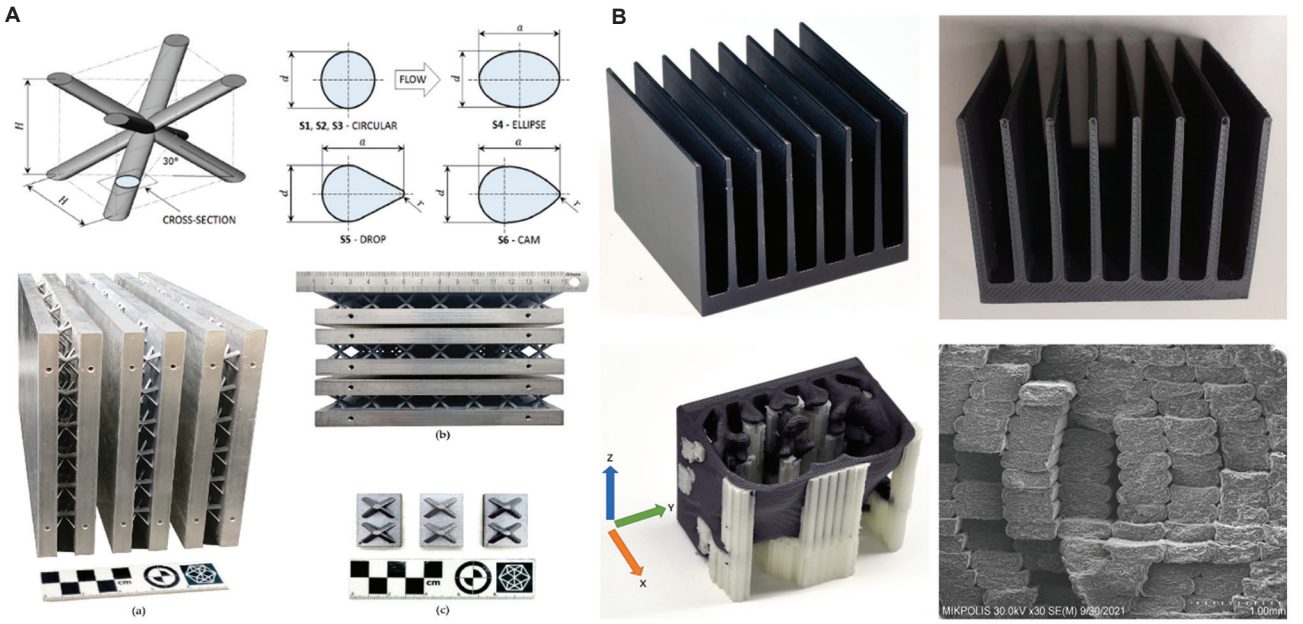

Figure 4. Additively, manufactured heat sinks improve convective heat transfer. (A) Four different cross-sectional fin shapes—circular, elliptical, drop-shape, and cam—were fabricated into real-scale heat sinks with various fin diameters.[64] Copyright © 2024 Luca Casarsa *et al*. Reproduced with permission from author(s). (B) Images of aluminum-based (upper left) and Ice9 Rigid Nylon-based (upper right) heat sinks fabricated via additive manufacturing, and SEM image of the internal layer structure of the Ice9 Rigid Nylon material (lower right).[70]

performance. Collectively, these studies highlight the promising potential of polymer-based heat sinks.

4.2. Micro/mini channel heat sink (MCHS) and TPMS heat sink

In addition to macro-scale thermal management, numerous studies have focused on micro-scale heat dissipation utilizing fluid channels. Particularly in microelectronics, there is significant interest in efficiently removing heat generated within confined spaces. Coolant-based liquid cooling methods are increasingly preferred over traditional air cooling due to their superior heat removal capabilities from the heat source to the surrounding environment. Consequently, extensive research has been conducted on increasing the surface area through micro- and mini-sized channels to enhance liquid cooling efficiency. In addition, the precision capabilities of AM have facilitated the fabrication of intricate micro-scale structures, previously unattainable through conventional manufacturing methods. Thus, current AM-based studies in this area primarily focus on two aspects: (i) the creation of microscale porous structures or channels to enhance convective heat transfer, and (ii) the development of TPMS structures that enable precise control over fluid flow paths, allowing fluids at different temperatures to flow simultaneously without mixing. This part will examine these studies in greater detail, highlighting their contributions and potential applications.

MCHS typically refer to channel structures with hydraulic diameters < 1 mm, enabling significantly higher heat transfer coefficients by minimizing boundary layers compared to larger, conventional heat sink channels. Due to their large surface area-to-volume ratios, these microchannels are extensively employed in compact micro devices, characterized by reduced heat exchanger sizes, minimized material usage during manufacturing, and decreased refrigerant requirements.

Ventola *et al.*[72] were among the first to introduce artificial surface roughness at the microscale, finding that rough-finned surfaces exhibited superior thermal performance (Figure 5A). Subsequently, Kirsch *et al.*[73] investigated microchannel pin-fin arrays with four distinct configurations, concluding that increased surface roughness notably amplified friction factors more than improved heat transfer when compared to smooth pin-fin arrays. Collins *et al.*[74] developed microchannel heat sinks with porous surfaces containing thermally conductive internal fins, which were benchmarked against manifold microchannel designs, achieving a thermal resistance reduction of approximately 17% and a pressure drop reduction of 28%.

Research has also expanded beyond basic pin-fin microchannels by integrating microjets to further enhance convection performance. Kempers *et al.*[75] fabricated hybrid microchannel-microjet heat sinks using a layer-by-

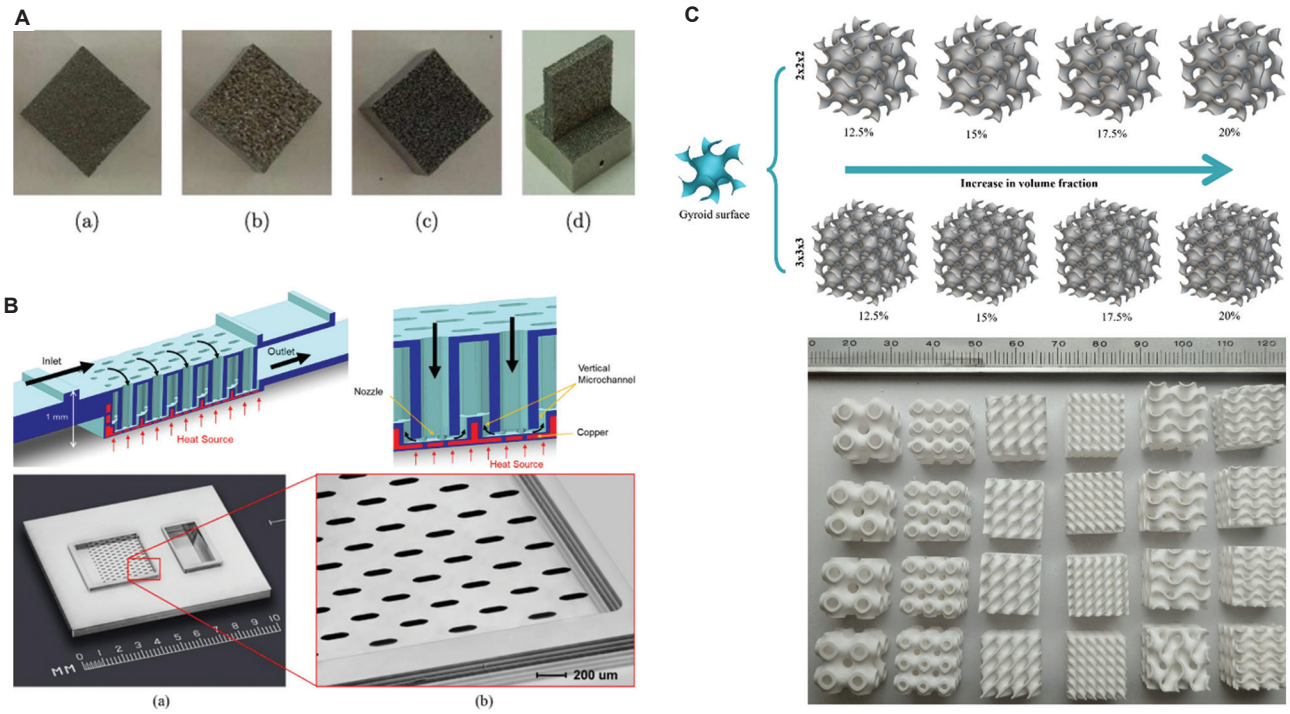

Figure 5. Micro-nanostructures and periodic cell design for enhancing convective heat transfer using additive manufacturing. (A) AlSiMg alloy heat sink manufactured by laser powder bed fusion (L-PBF) method with an artificial surface roughness.[72] (B) Microchannel pin-fin structure incorporating with microjet heat sink.[75] Copyright © 2020 Kempers *et al.* Reproduced with permission from authors(s). (C) Six different triply periodic minimal surface structures by controlling the volume fraction.[77]

layer electrodeposition approach, subsequently comparing performance with previous studies (Figure 5B). In addition, Xu *et al.*[76] explored pulsating flow conditions to enhance secondary flows and vortex formation within a three-layered microchannel heat sink, systematically analyzing the resulting flow characteristics and their impact on thermal performance.

Previous studies primarily focused on single-phase fluid flow within a single-channel configuration for heat transfer. In contrast, TPMS structures enable simultaneous, separate fluid flows at different temperatures within a single integrated design. TPMS structures comprise mathematically defined surfaces characterized by complex topologies, dividing a 3D space into two or more interconnected yet non-intersecting continuous domains. Such configurations have demonstrated substantial improvements in single-phase heat transfer efficiency. Moreover, due to their high surface density, high permeability, and optimal thermal conductivity, TPMS structures are not limited to heat sink applications but extend to fluid mixers, mold cooling modules, and other thermal management applications. Santos *et al.*[77] presented six different geometries and volume fractions of TPMS structures fabricated using aluminum-alumina composites, which show high compressive strengths with an energy absorption behavior (Figure 5C). Yan *et al.*[78] investigated gyroid TPMS structures, showing a significant reduction in pressure drop—up to 40%—through surface polishing. Similarly, Raafat *et al.*[79] developed a TPMS-based porous pin-fin heat sink structure, which exhibited enhanced Nusselt numbers with reduced channel blockage facilitated by the porous configuration. They verified that secondary cooling flows induced within the porous region effectively prevented disruption of the thermal boundary layer. Although TPMS structures are typically fabricated using metallic materials, such as AlSi10Mg alloys, recent studies have demonstrated their potential when produced using polymeric materials. For instance, Oh *et al.*[15] successfully fabricated polymer-based TPMS structures using the DLP printing method, conducting pressure-drop evaluations and detailed flow visualization studies to analyze their fluid flow characteristics. Especially, the transparent characteristic of polymer heat exchangers allows for easy visualization of temperature distribution at the inlet and outlet, either by direct observation or through IR imaging. This feature also offers the advantage of addressing the high-cost issues associated with conventional metal-based AM.

4.3. Structural optimization in AM

There is a growing demand for structures to be lightweight and material-efficient, minimizing material usage while

maintaining performance. However, optimizing the geometry of heat sinks to achieve the best thermal performance remains a critical challenge. Previous studies have predominantly relied on experimental approaches to fabricate and evaluate heat sinks and heat exchangers, systematically comparing performance to identify optimal structural configurations. Parameters such as cell type, porosity, and functional gradients are highly tunable through implicitly defined surfaces, including TPMS and MCHS geometries. Accordingly, numerical approaches and machine learning techniques are increasingly being used to optimize heat sink designs. Employing numerical simulations before actual manufacturing presents significant advantages, as it allows for parameter optimization of processing methods, printing techniques, and structural characteristics—such as thickness, size, and material selection—thus significantly reducing costs and minimizing material waste. Therefore, this part aims to comprehensively explore three prominent optimization methodologies used in AM-based heat sink and exchanger design: (i) geometry-based optimization, (ii) topology optimization, and (iii) machine learning-based optimization (Table 2).

Geometry-based optimization actively involves adjusting parameters such as pin-fin size, shape, and spacing to achieve optimal thermal performance and pressure drop characteristics. Ning *et al.*[80] numerically investigated fin structures, specifically twisted and rectangular fins, to evaluate their thermal performance and associated pressure drop, highlighting the potential of structural optimization through simulations by predicting inlet and outlet fluid-flow temperatures. Similarly, Ozguc *et al.*[81] employed computational fluid dynamics (CFD) simulations for optimizing pin-fin geometries, including size and shape, within water and ethylene glycol coolant mixtures, applying a gradient-based multi-objective optimization method. Kong *et al.*[82] conducted CFD-based thermal-fluid simulations on heat sinks combining pin fins and plate structures to determine configurations with optimal thermal resistance, pressure drop, and coefficient of performance, and successfully predicted overall thermal resistance and pressure drop. Bacellar *et al.*[83] proposed an optimum design by varying the channel and fin geometries of the microchannel heat exchangers into four types—round, elliptical, eye-shaped, and airfoil (leading and trailing shape). This approach resulted in more than a 50% reduction in size, material usage, and pressure drop.

Likewise, geometry-based optimization has also been extensively applied to TPMS structures using CFD methodologies. Raafat *et al.*[79] incorporated pin-fin arrays into TPMS-based structures, developing configurations capable of reducing pressure drop compared to conventional designs. Their optimized structures demonstrated high surface-to-area ratios, targeted enhanced Nusselt numbers, and maintained balanced hydrothermal performance through porous-like topologies that minimized channel blockage. Tang *et al.*[11] introduced a novel lattice-control method explicitly tailored for optimizing gyroid-type TPMS, accompanied by corresponding mathematical equations, and systematically compared simulated and experimental results to evaluate convective heat transfer performance and flow resistance. Further research efforts have focused on systematically analyzing the heat dissipation performance of various TPMS geometries to identify optimal configurations. Liu *et al.*[84] compared heat transfer and flow characteristics of four distinct TPMS structures (i.e., gyroid, primitive, diamond, and I-graph-wrapped package) through numerical simulations. Based on comparative performance results, the most effective TPMS structure was selected and validated experimentally under natural and forced-air convection conditions.

Meanwhile, topology optimization is a numerical approach employed to systematically optimize material distribution and structural configuration within a defined design domain. It aims to minimize material usage and strain energy while preserving mechanical integrity and enhancing overall performance. This method involves defining specific design variables, an objective or cost function, and appropriate constraints to achieve targeted design outcomes effectively. Tan *et al.*[85] applied topology optimization to compare four distinct microchannel heat sink designs—veiny, lateral veiny, snowflake-shaped, and spider-netted structures—numerically determining the optimal geometric parameters. Ozguc *et al.*[86] conducted topology optimization of microchannel heat sinks using a homogenization approach, specifically employing Pareto optimization to identify optimal configurations, including grid cell sizes, fin thickness, and pin-fin array layouts. Orakwe *et al.*[87] evaluated four different cold-plate designs: A conventional serpentine configuration, a geometrically similar replica of a reference design, and two hybrids, topologically optimized (TopOpt) lattice-based heat sinks. Their research utilized functionality-driven designs with AM frameworks, incorporating numerical methods based on field-driven implicit equations to optimize side-wall geometries within computer-aided design models. In addition, recent topology optimization approaches incorporate bio-inspired structures. For instance, Han *et al.*[88] developed a heat sink inspired by spider-web topology, targeting reduced temperature differences and pressure drops. To enhance heat-transfer performance and mitigate hot-spot temperatures, this study utilized staggered inlet and outlet configurations, ultimately selecting a three-inlet and three-outlet arrangement for

Table 2. Summary of AM-based structural optimization

Optimization methodology	Printing method	Material	Shape	Method	Working environment	Performance evaluation	Optimization target	References
Geometry optimization	L-PBF	Stainless steel	Twisted fin, rectangular fin	Numerical CFD, MOGA	DI water, oil, air	Thermal, pressure drop, COP	Optimal performance with fabrication capability	80
	L-PBF	AlSi10Mg	Rectangular pin fin	Numerical CFD	Water/ ethylene glycol mixture	Thermal, pressure drop	Minimizing thermal resistance with optimized pressure drop	81
	L-PBF	AlSi10Mg	Pin fin, plate	Numerical CFD	DI water	Thermal, pressure drop, COP	Optimal cooling performance in a high-temperature fluid environment	82
	L-PBF	AlSi10Mg	Gyroid TPMS	Numerical	Air	Thermal, flow resistance	Optimal thermal performance and pressure drop through lattice deformation	11
	L-PBF	AlSi7Mg	Gyroid, primitive, diamond, I-graph-wrapped package TPMS	Numerical CFD	Air static, flow	Thermal	Optimal thermal performance in various conditions	83
Topology optimization	-	6063 aluminum base	Ternate veiny, lateral veiny, snowflake shape, spider netted microchannel	Numerical	Water	Thermal	Optimal cooling performance in a high-temperature fluid environment	84
	L-PBF	AlSi10Mg	Square pin fin	Numerical CFD	Water	Thermal, pressure drop compared with the simulation result	Thermal performance enhancement and pressure drop optimization	85
	L-PBF	Copper	TPMS	Numerical CFD	Water	Thermal, pressure drop	Optimal thermal performance with fabrication capability	86
AI-driven optimization	L-PBF	AlSi10Mg	Straight, wavy fin	Deep reinforcement learning, MOGA, CFD	Air	Thermal, flow resistance, process availability	Optimal performance with fabrication capability	87
	L-PBF	AlSi10Mg	Rectangular, straight mini channel	Neural network, genetic algorithm	Water	Pressure drop	Optimal thermal performance in various conditions	88
	L-PBF	AlSi10Mg	Mini channel	Neural network, CFD	Water	Pressure drop	Optimal thermal performance in various conditions	89
	L-PBF	AlSi10Mg	Grid, rhombic	ANN, k-NN, SVR, ensemble ANN, ensemble k-NN, ensemble SVR	Air	Thermal performance prediction	Optimal thermal performance prediction of a complex structure	90

Abbreviations: AI: Artificial intelligence; AM: Additive manufacturing; ANN: Artificial neural network; CFD: Computational fluid dynamics; COP: Coefficient of performance; DI: Deionized; k-NN: k-nearest neighbors; L-PBF: Laser powder bed fusion; MOGA: Multi-objective genetic algorithm; SVR: Support vector regression; TPMS: Triply periodic minimal surface.

optimal performance. Helmholtz filtering combined with hyperbolic sine projection methods was integrated into the topology optimization process to further refine and achieve the desired outcomes.

However, predicting performance through numerical approaches to find an optimal point often does not precisely match real-world results. For instance, simulation environments typically apply highly constrained boundary conditions, which rarely occur in practical scenarios. Furthermore, purely simulation-based methods are limited in their capacity to generate novel, data-driven structures. To overcome these limitations, machine learning methods have been increasingly adopted. Artificial intelligence (AI)-driven optimization methods significantly enhance the efficiency and reliability of heat sinks, providing scalable solutions particularly suitable for high-power electronics. Specifically, the adoption of AI in AM supports various aspects, including design optimization, quality assurance, process optimization, and material development. Robertson *et al.*[89] employed an AI-driven optimization framework, combining deep reinforcement learning with a multi-objective genetic algorithm (MOGA), to determine optimal geometric parameters of heat sink fins, such as fin spacing, height, thickness, and base thickness, thus supporting both design and quality assurance goals. Wang *et al.*[90] utilized machine learning to facilitate design optimization, leveraging genetic algorithms to accumulate structural optimization data. They subsequently predicted performance evaluation criteria and heat-transfer efficiency using neural network-based predictions. In addition, Wang *et al.*[91] applied machine learning methods to estimate pressure-drop performance of heat sinks, validating their predictions against numerical simulations and experimental results for optimized performance. Commonly employed machine learning approaches involve neural networks and regression-based models, though various other predictive models have also been explored. Aksoy *et al.*[92] comparatively evaluated six different machine learning algorithms: Artificial neural network (ANN), k-nearest neighbors (k-NN), support vector regression (SVR), ensemble ANN, ensemble k-NN, and ensemble SVR. These methods utilized inputs such as time, current, gate voltage, and temperature to estimate heat sink temperatures, comparing predicted results with experimental data.

Moreover, machine learning methods have been extensively utilized in process optimization. Thakur *et al.*[93] studied optimal laser power, scanning speed, and hatching spacing parameters for 3D printing of heat sinks, subsequently validating residual stress and distortion predictions through simulations and real tests. They further developed data-driven mathematical relationships between residual stress and porosity using machine learning techniques, particularly multiple regression analysis and gray relational analysis. Through this model, the relationship between printing parameters and residual stress was systematically identified, facilitating comprehensive structural and manufacturing process optimization for heat sinks.

AM has enabled significant enhancement in the thermal performance of convection-based cooling systems. In particular, the fabrication of complex structures such as pin-fin arrays, MCHS, and TPMS geometries has become readily achievable. We summarize recent studies on active and passive cooling strategies employing AM heat sinks and heat exchangers. Furthermore, detailed attention is given to MCHS and TPMS structures that enhance convection performance through increased surface area. Moreover, the design and performance of these cooling systems can be further optimized using numerical simulations and machine learning techniques, which help to minimize time-consuming trial-and-error processes and material waste.

4.4. Boiling heat transfer for thermal management using AM

In previous examples involving MCHS and TPMS structures, cooling was achieved using oil, gas, or water, using only single-phase flow within the system. Such systems rely on natural or forced convection mechanisms, which exhibit heat transfer coefficients in the range of approximately 0.001–10 W/(cm^2·K).[94] However, high-performance systems such as radar modules, turbine blades, advanced electronics, and aerospace applications demand the removal of heat fluxes in the range of 25–1000 W/cm^2 or even higher, while maintaining material temperatures within prescribed safety limits. Under these extreme conditions, single-phase convection becomes insufficient for effective thermal management. As a result, two-phase boiling heat transfer has gained significant attention in recent research as a promising approach for dissipating high heat fluxes more efficiently. This method leverages the latent heat of vaporization and the dynamic interaction between liquid and vapor phases to achieve enhanced heat transfer performance. In phenomena such as pool boiling, staged mechanisms such as nucleation, bubble detachment, and rewetting further enhance heat transfer.

Single-phase and two-phase (liquid-vapor) heat transfer exhibit fundamental differences in their underlying mechanisms, and these differences are particularly apparent during boiling. In systems where the fluid exists in only one phase, either liquid or gas, heat is transferred primarily by conduction and convection. Heat is first conducted from the wall surface to the fluid, and it is then

transported within the fluid by natural or forced convection driven by temperature gradients. Energy transfer in this case relies mainly on sensible heat, the energy associated with a change in fluid temperature. By contrast, two-phase boiling heat transfer occurs when liquid and vapor coexist, and heat transfer is dominated by the formation and motion of bubbles generated as liquid evaporates from an overheated surface. This process involves latent heat associated with the phase change, making it far more efficient at transferring heat. In phenomena such as pool boiling, staged mechanisms such as nucleation, bubble detachment, and rewetting further enhance heat transfer.

4.5. Pool boiling

Pool boiling is a boiling phenomenon that occurs when a stationary liquid is heated and begins to evaporate. It is widely used in various thermal management systems that require high heat flow rates because it enables high heat transfer performance and stable operating temperature maintenance. Depending on the temperature of the wall, the process of pool boiling is categorized into four regimes: free convection, nucleate boiling, transition boiling, and film boiling (Figure 1A). In the free-convection stage, the surface temperature is only slightly above the liquid's saturation temperature, so the liquid is warming, but no bubbles have formed. In the process of nucleate boiling, the surface temperature increases to a sufficient degree to cause the formation of bubbles on the surface. This results in the occurrence of latent heat transfer, which is characterized by its high efficiency. Consequently, the maximum HTC is attained. Subsequently, transition boiling occurs when bubble coalescence and a vapor film form due to excessive bubble generation. In this phase, heat transfer is unstable and can decrease rapidly. Eventually, when the surface is covered with a continuous vapor film, known as film boiling, heat transfer efficiency is greatly reduced. This boiling process is divided into three points. The first point is known as the onset of nucleate boiling (ONB), which denotes the first point of bubble formation. The second is the point at which the maximum heat flux is reached in the nucleate boiling region. After this point, heat transfer decreases sharply due to coalescence and the vapor film. The third is the Leidenfrost point. Vapor film completely covers the wall surface, preventing contact with liquids and necessitating heat to transfer by means of radiation and vapor conduction. To improve pool boiling performance, it is important to precisely control bubble dynamics. By controlling bubble nucleation sites, detachment, and coalescence, both HTC and CHF can be improved simultaneously. Surface microstructure design can increase nucleation site density and wettability, thereby delaying CHF.

4.5.1. Bubble guide using AM

By enabling free design and single-process fabrication of micro-millimeter-scale structures, AM is changing the paradigm of pool boiling design.[95] L-PBF can be used to easily implement complex structures such as a vapor-guiding structure, a hollow conical structure, and a re-entrant microchannel structure. Structures similar to those mentioned increase bubble nucleation density, organize vapor-liquid separation pathways, and promote capillary pressure-based liquid replenishment, significantly enhancing HTC and CHF.[96] Taking advantage of L-PBF design flexibility, Shim *et al.*[97] showed the design and fabrication of a vapor-guiding structure. This structure effectively suppressed lateral coalescence by inducing vertical growth and stable detachment of bubbles and smoothly maintained liquid replenishment to prevent the formation of localized dry areas. Compared with a plain surface, this structure achieved a 90% increase in HTC and a 60% improvement in CHF. Another study attempted to control bubble growth using a bubble guide, as shown in Figures 6A and B.[98,99] Pi *et al.*[100] fabricated a re-entrant microchannel structure using L-PBF. This design incorporates an internal mechanism that captures the bubbles within the structure and directs them towards a narrow outlet at the upper point. This structure improved the heat transfer coefficient by at least 10% and up to 330% compared to flat surfaces. In addition, ONB temperature was significantly lowered, greatly improving the initial boiling transition conditions. Hayes *et al.*[101] fabricated a hollow conical structure for regulating flow via metal AM. The hollow conical body is equipped with vapor-exhaust outlets on the top and side walls. This structure allows the self-organization of vapor and liquid flow paths in accordance with the dimensions and relative positioning of these outlets. When this structure was applied, the heat transfer coefficient improved by up to 400% compared to a metal plane, and the CHF improved up to 200%. These L-PBF-based structures achieved higher performance than existing flat structures by effectively controlling the bubble dynamics, such as the location of bubble generation, growth direction, departure timing, fusion prevention, and liquid replenishment path.

4.5.2. Surface roughness modification

Another advantage of the L-PBF process is the high roughness of the surface formed during the fabrication process. A semi-molten metal powder forms on the surface of metals manufactured using L-PBF.[102] This creates a roughness ranging from micrometers to tens of micrometers.[96] This surface roughness increases the density of bubble nucleation sites, promoting initial bubble formation and contributing to improved heat

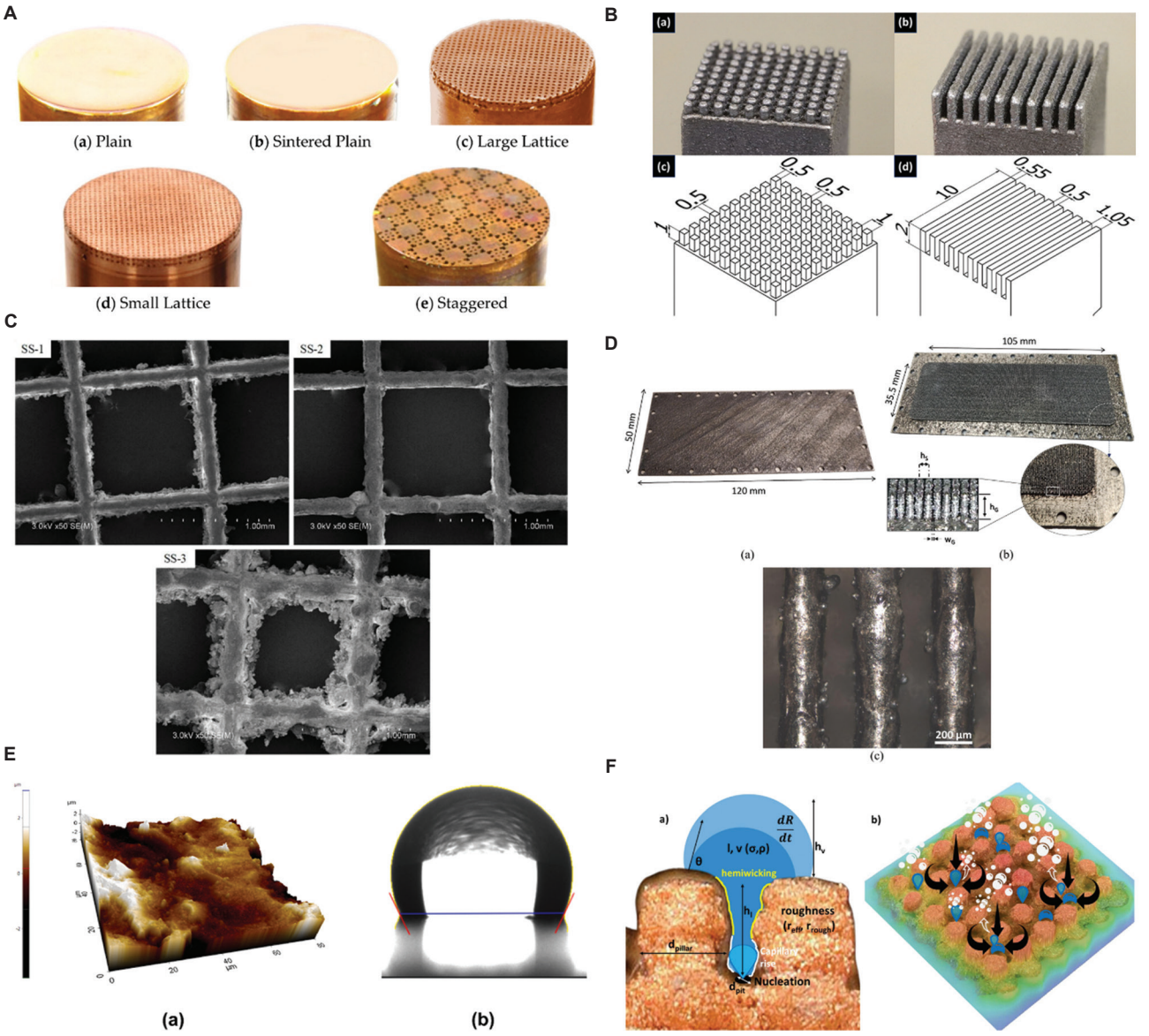

Figure 6. Pool boiling enhancement using additive manufacturing. (A) Vapor- guiding structure for bubble path.[98] (B) Images of different fin structures using L-PBF.[99] Copyright © 2025 American Chemical Society. Reproduced with permission of the American Chemical Society. (C) SEM image of a porous structure with different layer thickness fabricated by L-PBF.[105] (D) Bottom plate of heat sink using L-PBF.[104] Copyright © 2025 Kempers *et al*. Reproduced with permission from the author(s). (E) Surface roughness and contact angle of L-PBF surface.[103] Copyright © 2023 Kim *et al*. Reproduced with permission from the author(s). (F) Roughness and bubble guide using fused deposition modeling.[107] Copyright © 2025 Gupta *et al*. Reproduced with permission from the author(s).

transfer coefficients.[103] There are studies that have achieved improved HTC and CHF performance using only L-PBF-based roughness without a separate structural design.

Research has also shown that the L-PBF-based roughness across an entire macro-fin surface can enhance performance. As shown in Figure 6C and D, surface roughness can be increased using AM.[104,105] Lum *et al.*[106] showed various macro-fin geometries produced by L-PBF. The surface of the fin forms a micro-cavity with an average Ra of 10 µm due to the layer-by-layer method and partially sintered powder. The improved wettability promotes the formation of active nuclei on the sidewalls and top of the pins, causing bubbles to form on the whole structure. As a result, the emerging bubble coalesced with the growing bubble at an early stage, shortening the detachment cycle and increasing the heat transfer coefficient by up to 67%.

L-PBF-based roughness improves performance, but additional processing can further enhance pool boiling

performance. As illustrated in Figure 6E and F, surface roughness and contact angle can also be reduced using SLM.[103,107] Lum *et al.*[108] achieve a rough, porous layer with an average Ra ≈ 21 μm that boosts capillary pressure and secures liquid-spreading pathways using L-PBF. Chemical etching and boehmite oxidation lower the static contact angle from 44.7° to nearly 0°. This causes rapid re-wetting and increases the active nucleation density, allowing bubbles to form and escape quickly. Even without post-processing, the rough L-PBF surface improved HTC by 32.5% relative to Al 6061. Moreover, the maximum HTC increased by 103.8% with surface treatment.

Meanwhile, layer-by-layer processes such as FDM also enhance wettability. Elkholy *et al.*[109] proposed that PLA structures layered using the FDM naturally form a porosity of 11% because of inter-layer gaps. This gap creates a fine capillary network that improves surface wetting. This internal wicking ability reduced the contact angle to 34.5°, allowing the surface to wet easily and lowering the temperature required for the ONB. A significant improvement of up to 81% was achieved in terms of the HTC, attributed primarily to the integrated mechanism of capillary-driven liquid replenishment and low contact angle.

4.6. Flow boiling

Flow boiling is a complex heat transfer phenomenon in which a fluid flows along a heated surface and its phase changes from liquid to vapor. The mechanisms of heat transfer act in accordance with the flow behavior and phase change of the fluid. A key difference from pool boiling is that heat transfer by forced convection also occurs. Therefore, flow boiling regimes are classified by the liquid-vapor distribution (Figure 1A). When vapor quality is low, a continuous liquid phase containing small, scattered bubbles forms bubbly flow. As the temperature of the wall increases, the bubbles expand and merge, causing the slug flow to alternate between vapor slugs and liquid slugs. This provides strong turbulence and enhances heat transfer. As the steam quality increases, an annular flow is formed in which the steam dominates the center, and a thin liquid film forms on the wall. This maintains a high heat transfer coefficient, but when the heat flux increases rapidly and the liquid film disappears, it changes to a droplet flow in which the liquid droplets move with the steam. Finally, the wall dries out, and heat transfer decreases rapidly. In order to achieve efficient heat transfer in this flow boiling process, it is very important to precisely control bubble dynamics, such as bubble formation, growth, and separation, as well as forced convection flow. To improve these factors, structural designs that uniformize the flow distribution within the channel and surface modifications that improve wettability are being actively researched.

4.6.1. Flow control

As mentioned earlier, L-PBF offers a high degree of manufacturing flexibility, enabling complex and precise internal flow structures. These advantages are particularly beneficial in flow boiling. The coexistence of vapor and liquid due to fluid boiling creates a multiphase flow environment, which increases fluid heterogeneity and can cause problems such as localized dry-out and overheating.[110] To solve these problems, it is essential to design a flow path that ensures spatial uniformity of the inflowing fluid and effectively controls the vapor-liquid mixture state. L-PBF-based structural design is a suitable method for meeting these requirements, as it enables high-resolution implementation of lattice, TPMS, and gradient-based flow control structures, thereby enabling simultaneous improvement of flow uniformity and heat transfer coefficients (Figure 7A and B).[10,57]

Figures 7C-E show that various structures can be produced using L-PBF.[103,111,112] Wong *et al.*[113] fabricated a 3D porous metal structure. The gradient structure is designed to gradually reduce the cross-sectional area of the flow, thereby increasing the flow velocity as the flow progresses and implementing a mechanism that enhances fluid mixing. Inside the structure, nucleate boiling was dominant due to bubbly flow and churn flow. Among the different TPMS structure types surfaces, the gyroid is too complex to fabricate by conventional methods. However, as shown in Figure 7B, it was possible to fabricate a gyroid-based heat exchanger using L-PBF.[10] Because of the gyroid's continuous, periodic curved surfaces, the fluid is uniformly distributed throughout the exchanger. As flow rate increases, the heat transfer coefficient rises to 450 W/(m^2·K), and the device achieves more than a 50% mass reduction relative to a conventional shell-and-tube heat exchanger while actually improving thermal performance. Flow-boiling conditions involve rapid property changes accompanying vapor-liquid phase change, increasing design complexity. As shown in Figure 7F, structural optimization studies have therefore been undertaken.[114] Zhou *et al.*[115] obtained a root-like branching pin fin shape through 3D VOF (Volume of Fluid)-based numerical modeling. Simulations showed that, compared to a baseline configuration, the optimized structure delayed ONB through higher convective surface area and more uniform flow distribution, yielding up to an 87% increase in average HTC. A subsequent study fabricated the optimized design with DMLS.[116] The optimized heat sink reduced the ONB by up to 6.6 K compared to the baseline configuration, enabling rapid nucleate boiling. In addition, the flow visualization results showed that bubbly flow was highly stable and

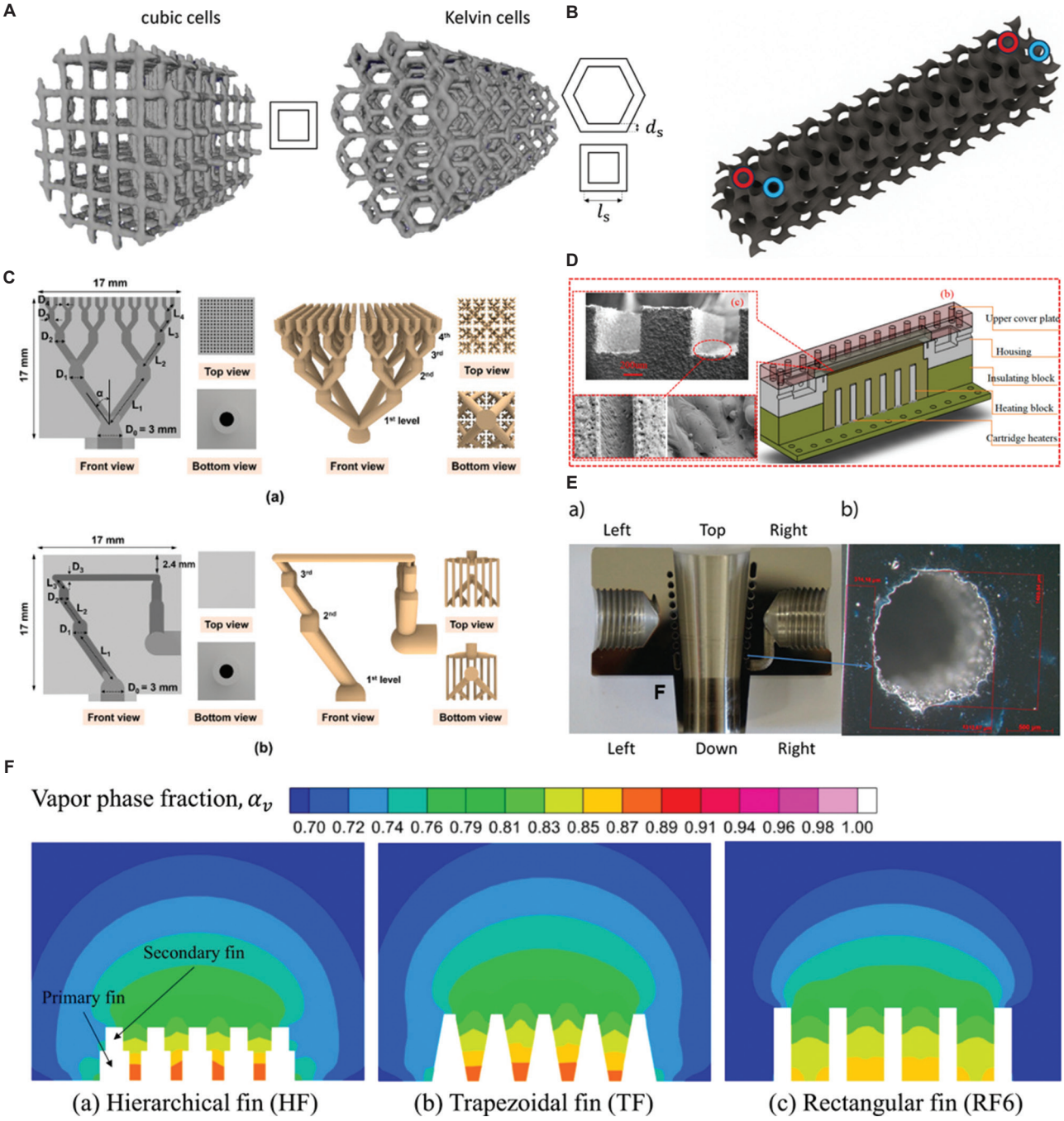

Figure 7. Flow boiling enhancement using additive manufacturing. (A) Flow boiling enhancement using additive manufacturing. (A) Computed tomography scan image of cubic cell and Kelvin cell fabricated using laser powder bed fusion (L-PBF).[57] (B) Illustration of Gyroid structure (L = 199.5 mm, H = 40.5 mm, and W = 41.51 mm).[10] (C) Design schematic image of a microchannel heat exchanger using L-PBF.[103] Copyright © 2023 Kim *et al*. Reproduced with permission from the author(s). (D) Schematic diagram of a mini-channel heat sink.[111] (E) Images of 3D-printed mini channel evaporator.[112] (F) Vapor phase fraction simulation for fin structure.[114] Copyright © 2025 Park *et al*. Reproduced with permission from author(s).

recorded the highest HTC in the slug flow section. L-PBF-based internal flow design effectively suppresses local overheating, dry out, and the resulting deterioration in thermal performance by equalizing fluid distribution in a flow boiling environment. L-PBF will be an effective manufacturing method for developing lightweight, high-efficiency heat exchangers by precisely implementing complex flow channels.

4.6.2. L-PBF roughness modification

Flow boiling is influenced by bubble dynamics such as bubble nucleation, growth, coalescence, and detachment from the channel wall. The microstructure of the surface has a decisive influence on bubble dynamics during this process.[117] Therefore, the unique roughness generated in the L-PBF can be utilized as a functional element directly related to the boiling heat transfer mechanism.[118] Ye *et al.*[119] conducted a study leveraging L-PBF advantages, in which the surface of mini channels forms a structure with particles of 3 μm in diameter and irregular grooves of 20 μm in size due to incomplete melting of the powder. As a result, the average Ra increases by about 40 times compared to Al. This size range coincides with the optimum bubble-nucleus radius for R134a (1–20 μm), increasing the density of nucleation sites and enhancing wettability. In addition, ONB was accelerated by lowering the initial superheat, and the heat transfer coefficient of the channel was approximately 60% higher than that of Al6061. Without separate post-processing, L-PBF roughness can simultaneously increase surface wettability and bubble nucleation density, achieving up to a 50% improvement in thermal performance. However, since the improvement is limited due to the uneven distribution of nucleation sites, additional design optimization is required to precisely control the roughness shape.

4.7. Two-phase thermal management devices

Two-phase thermal management devices can be classified into vapor chambers, flat heat pipes, loop heat pipes, and pulsating heat pipes according to the circulation mechanism of the internal fluid. The most common types are the flat heat pipe and vapor chamber. Both cases use capillary force through a wick structure installed inside to circulate the condensed liquid back to the evaporation section. A loop heat pipe, with a more complex layout, directs vapor and liquid through physically separated channels and uses wick-based capillary action to transport heat efficiently over long vertical distances. In a pulsating heat pipe, the working fluid oscillates in a plug-slug pattern, repeatedly evaporating and condensing to move heat.

4.7.1. Wick structure

Recent advances in AM have enabled the precise design and fabrication of wick structures inside heat pipes and vapor chambers.[120] As shown in Figure 8A, L-PBF makes it possible to form complex capillary pathways, tailor porosity, and produce integrated parts that can be bent.[121] Mezghani *et al.*[122] fabricated a micro-pillar wick that was implemented inside the vapor chamber using the L-PBF process. The wick structure is a cylindrical column with a diameter of several tens of micrometers. This ensures a high specific surface area and uniform capillary paths. Improvement of working-fluid replenishment and nucleation site enhances evaporation performance. This resulted in a reduction in thermal resistance of up to 58.9% compared to commercial vapor chambers. As shown in Figure 8B and C, AM also enables a high-porous wick structure to be fabricated using L-PBF.[123,124] Meng *et al.*[125] proposed a vapor chamber with a composite porous-wick architecture. This structure separates the evaporation, condensation, and liquid return functions, adopting TPMS structures with varying pore sizes for each. Specifically, a hybrid-pore wick was implemented through the differentiation of cell sizes, thereby resolving the trade-off between capillary pressure and permeability. This arrangement lowered thermal resistance by up to 49.6% relative to a conventional single-pore wick. As shown in Figure 8D, another advantage of this arrangement is the integrated design, unlike that achieved with conventional manufacturing methods.[126] Park *et al.*[127] fabricated a cylindrical heat pipe manufactured using the L-PBF method, which also incorporates an integral wick in the bent structure. A hybrid capillary system was realized by incorporating a screen-covered groove structure in the evaporator and a groove wick in the condenser and adiabatic sections. The screen mesh supplies not only a small pore radius to achieve high capillary pressure, but the groove wick provides high permeability for liquid circulation. This configuration reduced thermal resistance by up to 24.2% compared with a homogeneous groove-wick heat pipe and reached a maximum effective thermal conductivity of 25.7 W/(m·K). Thus, AM enables complex wick structures to be realized in a one-step process, achieving superior thermal performance and structural stability compared with assembled or conventional wicks. In particular, the freedom to design and fabricate wick geometry through L-PBF offers great flexibility for capillary-driven two-phase heat-transfer systems.

4.7.2. Wettability modification

L-PBF has been shown to yield surface roughness and wettability, which can contribute to maximizing the functionality of wick structures. The micro-nanoscale textures that inherently form during L-PBF enhance capillary forces and improve contact with the working liquid, enhancing heat-transfer performance.[128] One trade-off is that partially-sintered powder can remain trapped in internal features, making as-built L-PBF parts up to ~7% heavier than their nominal design mass.[129] Despite the slight loss of mass, numerous studies have shown that the improved wettability and capillary pumping effect provided by these micro-nano textures result in excellent heat transfer under conditions of high heat flux or gravitational influence. Such precise control is difficult to

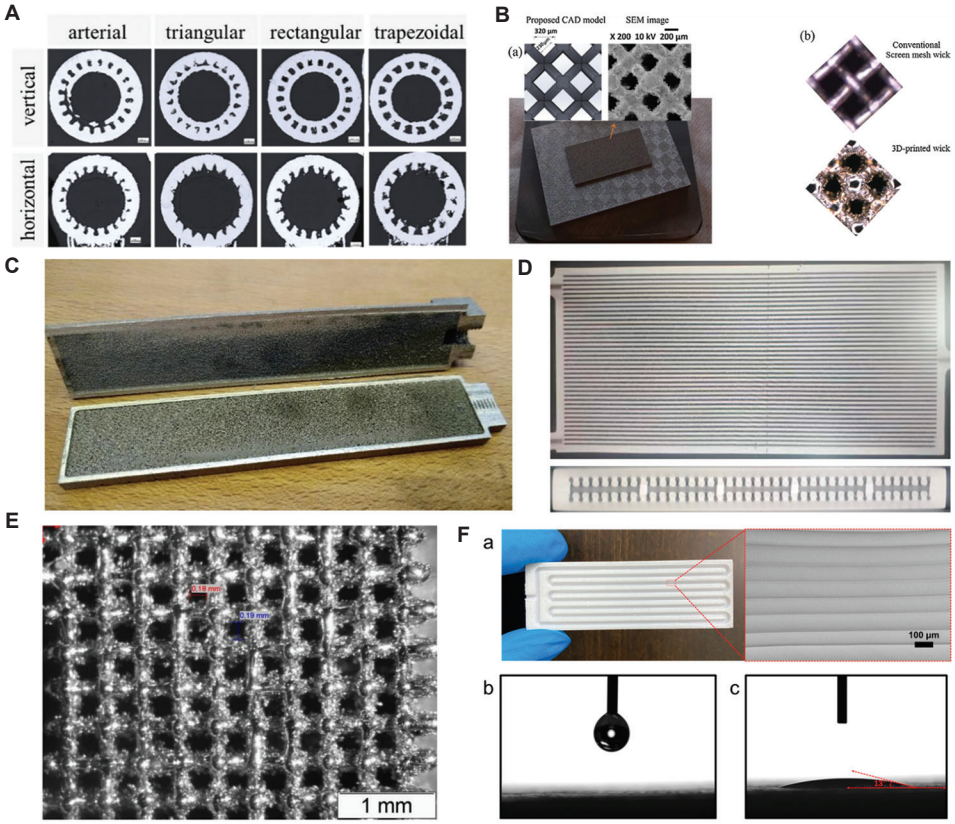

Figure 8. Two-phase heat spreader enhancement using additive manufacturing. (A) Different wick structure using L-PBF.[121] (B) SEM image of porous wick and comparison between conventional and 3D-printed wick.[124] Copyright © 2025 Geurts *et al.* Reproduced with permission from the author(s). (C) Porous wick heat pipe fabricated using L-PBF.[123] Copyright © 2021 R. Kempers *et al.* Reproduced with permission from author(s) (D) Heat pipe with wick structure using L-PBF.[126] (E) Scaffold internal structure for capillary.[130] (F) Photograph and contact angle of Pulsating heat pipe made with AM-based polymer.[133]

achieve with traditional machining or forming processes, which is particularly advantageous in high heat flux conditions or gravity-affected environments. As shown in Figure 8E, wettability is improved due to increased roughness caused by unmelted powders.[130] Yun *et al.*[131] fabricated a flat heat pipe with a groove-pattern wick by exploiting the inherent roughness of L-PBF. It exhibited a thermal resistance of 0.69°C/W and an effective thermal conductivity about 589% higher than that of the same volume of aluminum. These gains are attributed to the increased surface roughness created by L-PBF, which promotes liquid replenishment and increases boiling sites. Roughness can also be tuned by adjusting laser power. Cui *et al.*[132] suggested a porous wick composed of cylindrical-cubic unit cells in a loop heat pipe. Reducing the laser power from 170 W to 125 W left more partially melted particles on the surface, increasing micro-cavities. This increases the porosity to 52% and the capillary absorption to 3.53 g in 2 minutes. With this porous wick, thermal resistance fell by 26.5% compared with a conventional copper-powder wick, and the evaporator temperature dropped about 8.2% lower than that of the copper wick. Both studies confirm that the surface roughness and wettability of L-PBF-fabricated wick structures play a decisive role in enhancing the thermal performance of heat pipes and loop heat pipes. Despite an inherent L-PBF weight gain from trapped powder, the enhanced capillary pumping and liquid spreading still deliver superior heat transfer. These findings highlight that integrated optimization of geometry design, pore-size control, surface-roughness adjustment, and post-processing is crucial for further performance gains.

4.7.3. Polymer-based two-phase thermal management device

Application of AM with polymer materials, unlike L-PBF with metals, offers greater processability and design freedom, along with transparency and weight reduction. It is attracting attention for its potential applications in the precise observation of heat transfer mechanisms and passive thermal management devices for cooling electronic devices. Similar to Figure 8F,[133] Arai *et al.*[134] fabricated a pulsating heat pipe made of transparent

polycarbonate using an SLA-based AM process. With a channel diameter of 0.8 mm and a filling ratio of 30 vol%, it achieved a maximum effective thermal conductivity of 7.0×10^3 W/(m·K). In the small channel, a stable slug flow was seen, and this flow helped with heat transfer efficiency by activating the simultaneous transfer of latent heat and sensible heat between the evaporation and condensation sections. Pulsating heat pipe made with AM-based polymers has proven to be advantageous in internal flow visualization, various flow optimization, and hybrid design with composite materials, offering a practical alternative for high-power electronic devices and aerospace thermal-management systems.

5. Radiation heat transfer for thermal management using AM

This section introduces cases related to the regulation of visible light and IR radiation using AM. In the case of visible light, it is responsible for the largest portion of energy within the solar spectrum. Solar radiation spans from UV (~200 nm) to near-IR (~2500 nm), with visible light alone accounting for about 43% of solar radiation, indicating its high energy content. Meanwhile, IR covers a very broad range from near-IR at 750 nm—which is included in sunlight—to far-IR at 1 mm. Significant portions of the IR spectrum are absorbed by gases such as carbon dioxide and water vapor.[135] Particularly, the broad band of mid-IR (5–8 μm) is quickly absorbed by the atmosphere, making it impractical for atmospheric applications. Therefore, the IR regions most commonly utilized in research are the near-IR (750–2500 nm), corresponding to solar radiation, and certain portions of Earth's radiation, especially the atmospheric window in the long-wavelength IR region (8–13 μm). The atmospheric window is crucial because it allows radiative heat to pass from the Earth's surface (~300 K) directly to outer space (~3 K) with minimal atmospheric reabsorption.[136] By controlling the emissivity of materials in the visible and IR regions, various metamaterials with added functionalities can be developed.[137] For example, high solar reflectance and efficient thermal emission through the atmospheric window are two key factors for achieving passive daytime radiative cooling[27] (Figure 9A). In addition, modulating IR emissivity enables IR stealth.

As with previous sections, the use of particles via DIW is a prominent approach. For instance, a multifunctional material (methyltrimethoxysilane/SiO_2/CNFs ink) has been reported, utilizing CNFs and silica nanoparticles to achieve porous lattice radiative cooling with a thermal conductivity as low as 0.05 W/(m·K).[138] Through AM, a radiative cooling structure was developed that effectively cools electronic devices under sunlight during the day. The fabricated structure lowered device temperatures by 6.16°C thanks to high solar reflectance and high IR emissivity, while also ensuring mechanical stability. In a similar example, an ink composed of polyethylene and SiO_2 particles was prepared and printed by DIW to cool buildings through solar reflection and IR emission passively[139] (Figure 9B). Using commercial polymer processing technologies such as molding, extrusion, and 3D printing, a low-cost, mass-producible nanoporous polymer matrix composite was produced, achieving 96.2% solar reflectance, over 90% IR emissivity, 6.1°C cooling under direct sunlight, and a net cooling power of 85 W/m^2. Another study developed a polymer aerogel-based radiative cooling structure by DIW-based AM, featuring a cross-linked network of polymethylsilsesquioxane and CNFs, followed by freeze-drying. This structure exhibited almost no volume shrinkage during freeze-drying and greatly improved interlayer interfaces, resulting in excellent fatigue resistance and environmental durability. The aerogel also demonstrated 94.2% solar reflectance, 95.6% atmospheric window emissivity, a cooling performance of 72.2 W/m^2, a cooling effect of 5.8°C, excellent insulation (0.034 W/[m·K]), and both water repellency and flame retardancy. Examples of radiative cooling material development using additive methods such as DIW and SLA can be found in applications ranging from fully uniform films[140] to multifunctional wearable smart sportswear,[141,142] and robot shells[143] (Figure 9C-E). In addition, there are cases where inks with tunable visible light emissivity are developed and used to fabricate colored radiative cooling films via DIW-based 3D printing.[14] For example, colored radiative cooling films have been produced using PVC/DMF inks, demonstrating the vast research possibilities enabled by the versatility of inks and their particle components (Figure 9F).

Meanwhile, there are also reported cases of IR stealth research aimed at drastically lowering IR emissivity (Figure 9G). The use of 3D-printed molds to create 3D aerogel structures has been reported for some time; a representative example is the development of a honeycomb-based lightweight aerogel composite for IR stealth, integrating reduced emissivity, heat absorption, and insulation functions[144] (Figure 9H). Using MXene, PVA, and PCMs, these composites were fabricated via 3D-printed molds, freeze-drying, and vacuum impregnation, resulting in low emissivity (0.273), high latent heat (105.3 J/g), and excellent mechanical strength. Even when exposed to a heat source at 100–120°C,the radiative temperature remained around 30°C, demonstrating effective IR stealth performance. More recent research has even used 3D printers to directly print IR stealth metamaterials; for

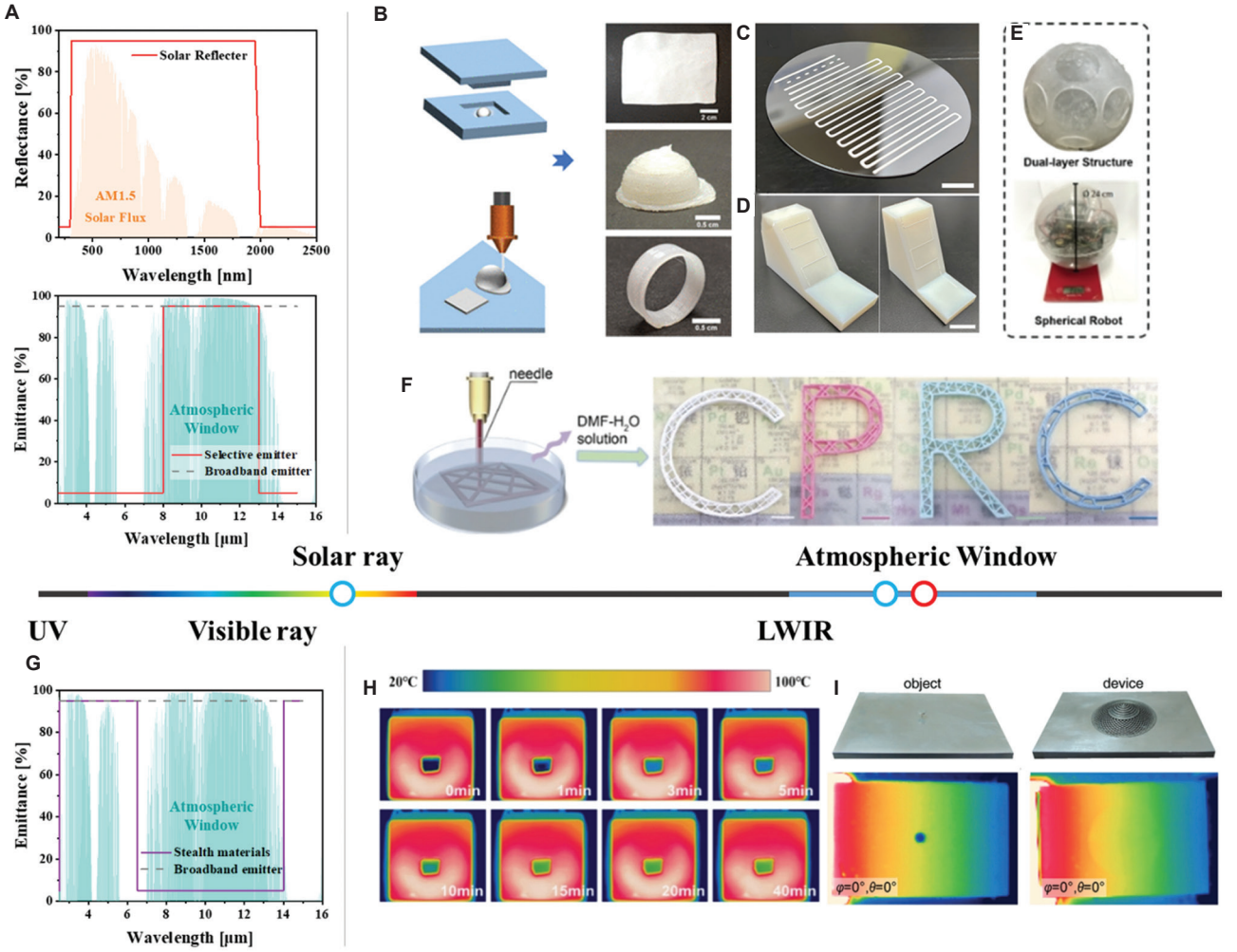

Figure 9. Working principles and representative examples of radiative thermal metamaterials based on additive manufacturing. (A) Conceptual graph illustrating selective emitters for solar reflection and IR emission to prevent radiative heat, such as radiative cooling. (B) 3D-printable nanoporous polymer matrix composites.[139] Copyright © 2021 American Chemical Society. Reproduced with permission of the American Chemical Society. (C and D) The 3D-printable polyvinylpyrrolidone-linked hollow silica nanoparticle.[140] (E) 3D-printed robot shell for daytime radiative cooling.[143] (F) PVC/DMF colored passive radiative coolers film.[14] Copyright © 2024 American Chemical Society. Reproduced with permission of the American Chemical Society. (G) Conceptual graph of IR emissivity for shielding against IR thermal radiation, such as IR stealth and thermal cloak. (H) Brick-like MXene@PVA/PCM composite aerogels with a honeycomb structure.[144] Copyright © 2024 American Chemical Society. Reproduced with permission of the American Chemical Society. (I) 3D meta-helmet for object camouflage.[16] Copyright © 2020 Wiley. Reproduced with permission of Wiley.
Abbreviations: DMF: *N*,*N*-Dimethylformamide; LWIR: Long-wave infrared; PCM: Phase change material; PVA: Polyvinyl alcohol; PVC: Polyvinyl chloride; UV: Ultraviolet.

example, an Al alloy helmet produced by L-PBF printing for IR camouflage has also been reported[16] (Figure 9I).

For this section, we have thoroughly reviewed the latest trends and application cases of AM technologies for controlling wavelength-selective radiative heat transfer in thermal metamaterials with structures ranging from the nanoscale to the macroscale. Depending on unit cell size and design requirements, a variety of AM processes, such as DIW and FFF, are selected. It has been confirmed that functional composites can be developed by precisely introducing metallic and ceramic particles into polymer matrices, enabling control over visible and IR light. For instance, porous structures fabricated from silica or cellulose nanofibers have demonstrated their effectiveness in a variety of applications, including radiative cooling achieved by high solar reflectance and IR emission. Recently, there have been consistent reports of advances such as aerogels with extremely low IR emissivity and 3D-printed helmets made from aluminum alloys, which simultaneously realize radiative heat concealment and IR stealth. In summary, AM

technologies drastically increase the freedom of shaping and structural design of thermal metamaterials and are a key solution for accurately implementing target properties in desired wavelength ranges by combining various functional particles. AM thus serves as a foundational technology that expands the boundaries of metamaterial applications, such as wavelength-selective radiation shielding, radiative cooling, and stealth, and is expected to play an increasingly important role in future thermal management and energy applications.

Furthermore, a recent study showed that a tubular ceramic lattice structure fabricated using SLA 3D printing can enhance radiative heat transfer by as much as 160–280% in high-temperature environments, while achieving low pressure drop and enabling efficient radiative heating of fluids within the structure.[145] This indicates that the convergence of radiative heat transfer and AM goes beyond the wavelength selectivity of the material itself, allowing for consideration of interactions with fluid flow. Such an integrated approach is expected to greatly contribute not only to broadening the potential for application in engineering devices such as heat exchangers but also to expanding the design freedom and application range of additive-manufactured radiative heat transfer materials.

6. Future perspectives

The continuous evolution of AM promises significant advancements in thermal management solutions across various sectors, including electronics, automotive, aerospace, and construction. Key future research directions can be categorized as follows:

(i) Advanced material development: Future research should focus on developing new composite materials with enhanced thermal properties. Combining high thermal conductivity materials, such as graphene and BN, with polymers through precise AM techniques will likely achieve unprecedented heat dissipation performance. In addition, integrating PCMs into complex AM structures may further revolutionize energy storage and temperature regulation systems.

(ii) Multifunctional metamaterials: Exploration into AM-enabled thermal metamaterials presents vast opportunities. The integration of thermal cloaking, thermal focusing, and directionally controlled heat transfer capabilities into single structures can open avenues for advanced thermal management applications in electronics cooling, building insulation, and stealth technologies. Further research into improving the mechanical robustness and scalability of these metamaterials is essential.

(iii) Optimization of computationally efficient thermal modeling tools using machine learning: There is great potential in combining AM with efficient computational thermal modeling tools such as topology optimization and machine learning algorithms. Enhanced predictive capabilities through AI will facilitate highly efficient and customized thermal management designs, significantly reducing design-to-product cycles. Developing standardized databases and predictive models for AM processes will streamline material selection and process parameter optimization.

(iv) Sustainability and scalability: Emphasis on environmentally friendly AM processes, recyclable materials, and waste reduction should be prioritized. Scaling AM technologies for mass production, particularly for large-scale thermal management solutions, is critical. Further development in high-throughput and cost-effective AM methods, such as VPP and MJ, will support broader adoption in industries.

(v) Hybrid and multimaterial printing: The future of AM thermal management will likely involve hybrid printing techniques combining multiple materials in a single process. This will enable functionally graded materials with tailored thermal, electrical, and mechanical properties, allowing for more integrated and complex thermal management solutions.

(vi) Reducing thermal interfacial resistance in multimaterial AM parts: Thermal interfacial resistance is essential for effective heat transfer. Interfaces between dissimilar materials often cause phonon scattering and weak bonding, increasing thermal resistance. Strategies such as functionally graded interfaces, optimized printing parameters, and surface treatments help improve interfacial thermal conductance. These approaches enhance both thermal performance and structural reliability in AM-based thermal management systems.

(vii) Designing lattice structures with validated thermo-mechanical performance cycling: Lattice structures are increasingly used in thermal management due to their lightweight and high surface area, which enhances heat dissipation and structural efficiency. However, repeated thermal and mechanical stresses can degrade their performance over time. To address this, researchers combine simulation and experimental methods to optimize geometry, material combinations, and structural density. This ensures stable thermal and mechanical performance even under long-term operational conditions.

7. Conclusion

Developments in the AM technology have significantly advanced thermal management, providing unparalleled

opportunities in design freedom, material customization, and performance optimization across conductive, convective, boiling, and radiative heat transfer applications. By enabling intricate internal geometries and precise material placement, AM facilitates the development of tailored thermal solutions such as advanced heat exchangers, sophisticated thermal metamaterials, and integrated two-phase cooling devices. Enhanced thermal conductivity through polymer composites and optimized microchannel and TPMS structures highlight AM's potential to meet escalating heat dissipation demands, particularly in electronics and high-power devices. Moreover, AM's ability to integrate PCMs and functionally graded materials allows for highly efficient thermal regulation, energy storage, and advanced thermal cloaking functionalities. Despite these promising advancements, significant challenges remain, including ensuring structural integrity, precise microstructural control, and scalable, cost-effective manufacturing processes. Addressing these issues through continued research and integration with computational methods like topology optimization and AI-driven design will be crucial.

Looking forward, hybrid and multimaterial AM techniques hold immense promise in overcoming current limitations, paving the way for multifunctional metamaterials and highly customizable thermal management solutions. As AM technologies continue to mature, their integration into broader engineering sectors will drive substantial improvements in energy efficiency, sustainability, and system reliability. Future advancements will likely focus on overcoming technical barriers associated with scaling production, ensuring repeatability, and developing standardized AM processes. Moreover, extensive exploration into recyclable and environmentally sustainable materials will be vital in aligning AM practices with global sustainability goals. Enhanced collaboration between academia, industry, and regulatory bodies will further accelerate AM innovations, ensuring rapid and effective implementation in practical scenarios. Ultimately, AM stands to significantly enhance future thermal management strategies, supporting innovative advancements in diverse industrial applications.

Acknowledgments

None.

Funding

This work was supported by an Agency for Defense Development of Korea (ADD) grant (915050201), National Research Foundation of Korea (NRF) funded by the Korean government (Ministry of Science and ICT) (2023R1A2C2006407, 2020R1A5A1018153), and Korea Evaluation Institute of Industrial Technology (KEIT) grant funded by the Korea government (MOTIE) (No. RS-2024-00433288).

Conflict of interest

Wonjoon Choi is an Editorial Board Member of this journal, but was not in any way involved in the editorial and peer-review process conducted for this paper, directly or indirectly. Separately, other authors declared that they have no known competing financial interests or personal relationships that could have influenced the work reported in this paper.

Author contributions

Conceptualization: Jaemin Lee, Wonjoon Choi
Writing–original draft: All authors
Writing–review & editing: Jaemin Lee, Wonjoon Choi

Ethics approval and consent to participate

Not applicable.

Consent for publication

Not applicable.

Availability of data

Not applicable.

References

1. Hamilton I, Kennard H, Rapf O, *et al. Global Status Report for Buildings and Construction-Beyond Foundations: Mainstreaming Sustainable Solutions to Cut Emissions from the Buildings Sector*; 2024.

2. Hwang FS, Confrey T, Reidy C, *et al*. Review of battery thermal management systems in electric vehicles. *Renew Sustain Energy Rev*. 2024;192:114171.

   doi: 10.1016/j.rser.2023.114171

3. Rakshith BL, Asirvatham LG, Angeline AA, *et al.* Cooling of high heat flux miniaturized electronic devices using thermal ground plane: An overview. *Renew Sustain Energy Rev*. 2022;170:112956.

   doi: 10.1016/j.rser.2022.112956

4. Nair V, Baby A, Anoop MB, Indrajith S, Murali M, Nair MB. A comprehensive review of air-cooled heat sinks for thermal management of electronic devices. *Int Commun Heat Mass Transfer*. 2024;159:108055.

   doi: 10.1016/j.icheatmasstransfer.2024.108055

5. Careri F, Khan RHU, Todd C, Attallah MM. Additive manufacturing of heat exchangers in aerospace applications: A review. *Appl Thermal Eng*. 2023;235:121387.

doi: 10.1016/j.applthermaleng.2023.121387

6. Khan N, Riccio A. A systematic review of design for additive manufacturing of aerospace lattice structures: Current trends and future directions. *Prog Aerospace Sci*. 2024;149:101021.

   doi: 10.1016/j.paerosci.2024.101021

7. Lim DD, Lee J, Park J, Choi W. High-resolution and electrically conductive three-dimensional printing of carbon nanotube-based polymer composites enabled by solution intercalation. *Carbon*. 2022;194:1-9.

8. Yadav S, Liu S, Singh RK, Sharma AK, Rawat P. A state-of-art review on functionally graded materials (FGMs) manufactured by 3D printing techniques: Advantages, existing challenges, and future scope. *J Manuf Processes*. 2024;131:2051-2072.

   doi: 10.1016/j.jmapro.2024.10.026

9. Lim DD, Park J, Lee J, *et al.* Broadband mechanical metamaterial absorber enabled by fused filament fabrication 3D printing. *Addit Manuf*. 2022;55:102856.

   doi: 10.1016/j.addma.2022.102856

10. Kruzel M, Dutkowski K, Bohdal T, Litwin A, Sawicki J, Kępa E. A new approach for heat transfer coefficient determination in triply periodic minimal surface-based heat exchangers. *Int Commun Heat Mass Transfer*. 2024;157:107778.

    doi: 10.1016/j.icheatmasstransfer.2024.107778

11. Tang W, Zou C, Zhou H, *et al*. A novel convective heat transfer enhancement method based on precise control of gyroid-type TPMS lattice structure. *Appl Thermal Eng*. 2023;230:120797.

    doi: 10.1016/j.applthermaleng.2023.120797

12. Chandra S, Wang C, Tor SB, Ramamurty U, Tan X. Powder-size driven facile microstructure control in powder-fusion metal additive manufacturing processes. *Nat Commun*. 2024;15(1):3094.

    doi: 10.1038/s41467-024-47257-w

13. Ghasemi A, Fereiduni E, Elbestawi M, *et al.* Influence of the graphene incorporation on nanostructure and thermal properties of the laser powder bed fusion processed AlSi12 matrix composites. *J Alloys Compds*. 2025;1010:177075.

    doi: 10.1016/j.jallcom.2024.177075

14. Lin Y, Qin C, Fang L, Wang J, Li D. Colored polymeric films with a bilayer porous design for efficient subambient radiative cooling. *ACS Appl Polym Mater*. 2024;6(1):722-731.

    doi: 10.1021/acsapm.3c02318

15. Oh SH, An CH, Seo B, Kim J, Park CY, Park K. Functional morphology change of TPMS structures for design and additive manufacturing of compact heat exchangers. *Addit Manuf*. 2023;76:103778.

    doi: 10.1016/j.addma.2023.103778

16. Peng YG, Li Y, Cao PC, Zhu XF, Qiu CW. 3D printed meta-helmet for wide-angle thermal camouflages. *Adv Funct Mater*. 2020;30(28):2002061.

    doi: 10.1002/adfm.202002061

17. Ahmad MJ, Tian X, Dai X, *et al.* Non-conformal thermal cloak metamaterial by continuous metal fiber embedded 3D printing. *Int J Heat Mass Transfer*. 2025;242:126796.

    doi: 10.1016/j.ijheatmasstransfer.2025.126796

18. ISO/ASTM 52900. *Additive Manufacturing-General Principles - Fundamentals and Vocabulary*. United States: ISO/ASTM; 2021.

19. Xiao Z, Chen C, Zhu H, *et al.* Study of residual stress in selective laser melting of Ti6Al4V. *Mater Design*. 2020;193:108846.

    doi: 10.1016/j.matdes.2020.108846

20. Panwisawas C, Gong Y, Tang YT, Reed RC, Shinjo J. Additive manufacturability of superalloys: Process-induced porosity, cooling rate and metal vapour. *Addit Manuf*. 2021;47:102339.

    doi: 10.1016/j.addma.2021.102339

21. Foteinopoulos P, Papacharalampopoulos A, Stavropoulos P. Additive manufacturing simulations: An approach based on space partitioning and dynamic 3D mesh adaptation. *Addit Manuf Lett*. 2024;11:100256.

    doi: 10.1016/j.addlet.2024.100256

22. Jiong S, Yun J, Lee J, *et al*. Nanosized boron nitride-incorporated polyvinyl alcohol composites with TEMPO-oxidized cellulose nanofibers as ultrathin thermal interface materials. *Chem Eng J*. 2024;500:157243.

23. Yun J, Lee J, Kim J, Lee J, Choi W. Hexagonal boron nitride nanosheets/graphene nanoplatelets/cellulose nanofibers-based multifunctional thermal interface materials enabling electromagnetic interference shielding and electrical insulation. *Carbon*. 2024;228:119397.

24. Hu H, Xu C, Zhao Y, Ziegler KJ, Chung JN. Boiling and quenching heat transfer advancement by nanoscale surface modification. *Sci Rep*. 2017;7(1):6117.

    doi: 10.1038/s41598-017-06050-0

25. Lee J, Kyeong D, Kim J, Choi W. Layer-by-layer self-assembled functional coatings of carbon nanotube-polyethylenimine for enhanced heat transfer of heat sinks. *Int J Heat Mass Transfer*. 2022;184:122344.

    doi: 10.1016/j.ijheatmasstransfer.2021.122344

26. Lee J, Kim J, Seo B, Shin D, Hwang S, Choi W. Layer-by-layer solution-processed two-dimensional graphene oxide-polyethylenimine thin-film coatings for enhanced pool boiling heat transfer. *Int J Heat Mass Transfer*. 2023;209:124067.

27. Hossain MM, Gu M. Radiative cooling: Principles, progress, and potentials. *Adv Sci*. 2016;3(7):1500360.

doi: 10.1002/advs.201500360

28. Radhakrishnan M, Sharma S, Palaniappan S, *et al*. Influence of thermal conductivity on evolution of grain morphology during laser-based directed energy deposition of CoCrxFeNi high entropy alloys. *Addit Manuf*. 2024;92:104387.

doi: 10.1016/j.addma.2024.104387

29. Lin K, Tian H, Gu D, Wang C, Yuan L, Sun J. Laser powder bed fusion of Cu–Al–Ni–Mn shape-memory alloy for the application of active heat sinks: Processability, microstructures, and shape-memory effect. *Adv Eng Mater*. 2024;26(4):2301224.

doi: 10.1002/adem.202301224

30. Fereiduni E, Ghasemi A, Sargent N, *et al*. Synergy of laser powder bed fusion (LPBF) and heat treatment for CuNi2SiCr alloy enhancement. *Mater Design*. 2025;255:114189.

doi: 10.1016/j.matdes.2025.114189

31. Gao J, Hao M, Wang Y, *et al*. 3D printing boron nitride nanosheets filled thermoplastic polyurethane composites with enhanced mechanical and thermal conductive properties. *Addit Manuf*. 2022;56:102897.

doi: 10.1016/j.addma.2022.102897

32. Zhang C, Deng K, Li X, Fu KK, Ni C. Thermally conductive 3D-printed carbon-nanotube-filled polymer nanocomposites for scalable thermal management. *ACS Appl Nano Mater*. 2023;6(14):13400-13408.

doi: 10.1021/acsanm.3c02067

33. Olcun S, Ibrahim Y, Isaacs C, Karam M, Elkholy A, Kempers R. Thermal conductivity of 3D-printed continuous pitch carbon fiber composites. *Addit Manuf Lett*. 2023;4:100106.

doi: 10.1016/j.addlet.2022.100106

34. Cai Z, Zhang J, Zhang L, *et al*. Fluid-assisted fused deposition modeling 3D printing of anisotropically thermally conductive polymer composites with precisely tunable heat transfer pathways. *Compos Commun*. 2024;46:101835.

doi: 10.1016/j.coco.2024.101835

35. Guo Y, Wang S, Zhang H, *et al*. Consistent thermal conductivities of spring-like structured polydimethylsiloxane composites under large deformation. *Adv Mater*. 2024;36(39):2404648.

doi: 10.1002/adma.202404648

36. Hou L, Ji JC, Cui GP, *et al*. 3D printable phase change based thermal interface material with lower total thermal resistance at operating temperature. *J Energy Storage*. 2024;99:113303.

doi: 10.1016/j.est.2024.113303

37. Fang B, Zhang G, Zou F, *et al*. 3D printing interconnected segregated composites to simultaneously enhance thermal conductivity and mechanical properties. *ACS Appl Polym Mater*. 2024;6(8):4904-4911.

doi: 10.1021/acsapm.4c00654

38. Peng Z, Lv Q, Jing J, Pei H, Chen Y, Ivanov E. FDM-3D printing LLDPE/BN@GNPs composites with double network structures for high-efficiency thermal conductivity and electromagnetic interference shielding. *Compos Part B Eng*. 2023;251:110491.

doi: 10.1016/j.compositesb.2022.110491

39. Kang Z, Xi M, Li N, Zhang S, Wang Z. Anisotropic thermal conductivity of 3D printed graphene enhanced thermoplastic polyurethanes structure toward photothermal conversion. *Carbon*. 2025;234:120023.

doi: 10.1016/j.carbon.2025.120023

40. Xia R, Zhu S, Zhen F, *et al*. Vertical 3D printing of rGO/CNTs arrays for thermal interface materials with *in-situ* local temperature monitoring function. *Chem Eng J*. 2024;496:153643.

doi: 10.1016/j.cej.2024.153643

41. Qiu L, Wang X, Feng G, Feng Y. Tailorable thermal conduction and thermal energy storage behaviors in 3D printed hierarchical cellular structure-based phase change materials. *Small Methods*. 2025;9:2402089.

doi: 10.1002/smtd.202402089

42. Taleb O, Jutkofsky M, Measel R, *et al*. Thermal conductivity of 3D-printed block-copolymer-inspired structures. *Int J Heat Mass Transfer*. 2024;235:126186.

doi: 10.1016/j.ijheatmasstransfer.2024.126186

43. Wang L, Feng J, Luo Y, *et al*. Three-dimensional-printed silica aerogels for thermal insulation by directly writing temperature-induced solidifiable inks. *ACS Appl Mater Interfaces*. 2021;13(34):40964-40975.

doi: 10.1021/acsami.1c12020

44. Zhu T, Ren Z, Wang D, *et al*. Reactive 3D printed silanized cellulose nanofiber aerogels for solar-thermal regulatory cooling. *Compos Part A Appl Sci Manuf*. 2025;192:108761.

doi: 10.1016/j.compositesa.2025.108761

45. Liu C, Li MC, Liu X, Zhou G, Liu C, Mei C. 3D printing of customized lignocellulose nanofibril aerogels for efficient thermal insulation. *Addit Manuf*. 2023;78:103841.

doi: 10.1016/j.addma.2023.103841

46. Fu Z, Yu D, Xue T, Zhang X, Fan W. 3D printed polyimide-based composite aerogels with shape memory and thermal insulation properties. *Compos Commun*. 2025;56:102335.

doi: 10.1016/j.coco.2025.102335

47. Pei Y, Shen Z, Zhou J, Yang B. Experimental and theoretical thermal performance analysis of additively manufactured polymer vacuum insulation panels. *Appl Thermal Eng*. 2024;256:123957.

doi: 10.1016/j.applthermaleng.2024.123957

48. Sha W, Xiao M, Zhang J, *et al*. Robustly printable freeform thermal metamaterials. *Nat Commun*. 2021;12(1):7228.

doi: 10.1038/s41467-021-27543-7

49. Rao Y, Yan Y, Mei H, *et al*. 3D-printed lattice structures with SiC whiskers to strengthen thermal metamaterials. *Ceramics Int*. 2022;48(21):32283-32289.

doi: 10.1016/j.ceramint.2022.07.170

50. Freeman TB, Foster KEO, Troxler CJ, *et al*. Advanced materials and additive manufacturing for phase change thermal energy storage and management: A review. *Adv Energy Mater*. 2023;13(24):2204208.

doi: 10.1002/aenm.202204208

51. Yu D, Chi G, Mao X, *et al*. Volume-metallization 3D-printed polymer composites. *Adv Mater*. 2024;36(35):2403088.

doi: 10.1002/adma.202403088

52. Lee J, Han H, Noh D, *et al*. Multiscale porous architecture consisting of graphene aerogels and metastructures enabling robust thermal and mechanical functionalities of phase change materials. *Adv Funct Mater*. 2024;34(42):2405625.

53. Song C, Lee J, Lim DD, Choi W. Rationally tunable phase change material thermal properties enabled by three-dimensionally printed structural materials and carbon-based functional additives. *Int J Energy Res*. 2023;2023(1):6658082.

54. Liu C, Liu X, Shi X, *et al*. 3D printing of phase change material-based Pickering emulsion gel for solar-thermal-electric conversion. *Chem Eng J*. 2024;499:155940.

doi: 10.1016/j.cej.2024.155940

55. Er Y, Güler O, Hekimoğlu G, *et al*. Thermophysical properties and solar thermal energy storage performance of phase change composites manufactured by vat photopolymerization 3D printing technique. *J Energy Storage*. 2023;73:109124.

doi: 10.1016/j.est.2023.109124

56. Er Y, Güler O, Ustaoğlu A, *et al*. Characterisation and energy storage performance of 3D printed-photocurable resin/microencapsulated phase change material composite. *Thermal Sci Eng Prog*. 2024;48:102381.

doi: 10.1016/j.tsep.2023.102381

57. Bender J, Dubil K, Korn F, Wetzel T, Dietrich B. Modelling of heat transfer and pressure drop during flow boiling of CO_2 in a horizontal tube with periodic open cellular inserts. *Chem Eng Process Process Intensification*. 2024;203:109891.

doi: 10.1016/j.cep.2024.109891

58. Righetti G, Savio G, Meneghello R, Doretti L, Mancin S. Experimental study of phase change material (PCM) embedded in 3D periodic structures realized via additive manufacturing. *Int J Thermal Sci*. 2020;153:106376.

doi: 10.1016/j.ijthermalsci.2020.106376

59. Diani A, Nonino C, Rossetto L. Melting of phase change materials inside periodic cellular structures fabricated by additive manufacturing: Experimental results and numerical simulations. *Appl Thermal Eng*. 2022;215:118969.

doi: 10.1016/j.applthermaleng.2022.118969

60. Wang C, Liu C, Li C. Additive manufacturing of shape-stabilized composite phase change materials via ultraviolet curing. *Addit Manuf*. 2023;61:103341.

doi: 10.1016/j.addma.2022.103341

61. Piacquadio S, Schirp-Schoenen M, Mameli M, Filippeschi S, Schröder KU. Experimental analysis of the thermal energy storage potential of a phase change material embedded in additively manufactured lattice structures. *Appl Thermal Eng*. 2022;216:119091.

doi: 10.1016/j.applthermaleng.2022.119091

62. Kim J, Lee J, Song C, Yun J, Choi W. Enhanced thermal performances of PCM heat sinks enabled by layer-by-layer-assembled carbon nanotube–polyethylenimine functional interfaces. *Energy Convers Manage*. 2022;266:115853.

63. Shamvedi D, Mccarthy OJ, Eoghan OD, Cyril D, Paul OL, Raghavendra R. 3D Metal printed heat sinks with longitudinally varying lattice structure sizes using direct metal laser sintering. *Virtual Phys Prototyp.* 2018;13(4):301-310.

doi: 10.1080/17452759.2018.1479528

64. Lorenzon A, Vaglio E, Casarsa L, Totis G. Effects of different cross-sections of body centered cubic cells on pressure drop and heat transfer of additively manufactured heat sinks. *Int J Heat Mass Transfer*. 2024;222:125170.

doi: 10.1016/j.ijheatmasstransfer.2024.125170

65. Tseng PH, Tsai KT, Chen AL, Wang CC. Performance of novel liquid-cooled porous heat sink via 3-D laser additive manufacturing. *Int J Heat Mass Transfer*. 2019;137:558-564.

doi: 10.1016/j.ijheatmasstransfer.2019.03.116

66. Lazarov BS, Sigmund O, Meyer KE, Alexandersen J. Experimental validation of additively manufactured optimized shapes for passive cooling. *Appl Energy*. 2018;226:330-339.

doi: 10.1016/j.apenergy.2018.05.106

67. Ho TYK, Ng AYR, Ye P, *et al*. Realization of vat photopolymerisation of dense SiC ceramics with SiO2/MgSO4 coated sub-micron powders for efficient heat dissipation. *Addit Manuf*. 2023;73:103664.

doi: 10.1016/j.addma.2023.103664

68. Sheng P, Nie G, Li Y, *et al*. Enhanced curing behavior, mechanical and thermal properties of 3D printed aluminum nitride ceramics using a powder coating strategy. *Addit Manuf*. 2023;74:103732.

doi: 10.1016/j.addma.2023.103732

69. Song C, Lee J, Seo B, Shim JH, Hu R, Choi W. Enhanced cooling performance of three-dimensional printed heat sink via solution-processed layer-by-layer CNT coatings. *Adv Eng Mater*. 2023;25(20):2300669.

70. Huttunen E, Nykänen MT, Alexandersen J. Material extrusion additive manufacturing and experimental testing of topology-optimised passive heat sinks using a thermally-conductive plastic filament. *Addit Manuf*. 2022;59:103123.

doi: 10.1016/j.addma.2022.103123

71. Timbs K, Khatamifar M, Antunes E, Lin W. Experimental study on the heat dissipation performance of straight and oblique fin heat sinks made of thermal conductive composite polymers. *Thermal Sci Eng Prog*. 2021;22:100848.

doi: 10.1016/j.tsep.2021.100848

72. Ventola L, Robotti F, Dialameh M, *et al*. Rough surfaces with enhanced heat transfer for electronics cooling by direct metal laser sintering. *Int J Heat Mass Transfer*. 2014;75:58-74.

doi: 10.1016/j.ijheatmasstransfer.2014.03.037

73. Kirsch KL, Thole KA. Pressure loss and heat transfer performance for additively and conventionally manufactured pin fin arrays. *Int J Heat Mass Transfer*. 2017;108:2502-2513.

doi: 10.1016/j.ijheatmasstransfer.2017.01.095

74. Collins IL, Weibel JA, Pan L, Garimella SV. A permeable-membrane microchannel heat sink made by additive manufacturing. *Int J Heat Mass Transfer*. 2019;131:1174-1183.

doi: 10.1016/j.ijheatmasstransfer.2018.11.126

75. Kempers R, Colenbrander J, Tan W, Chen R, Robinson AJ. Experimental characterization of a hybrid impinging microjet-microchannel heat sink fabricated using high-volume metal additive manufacturing. *Int J Thermofluids*. 2020;5-6:100029.

doi: 10.1016/j.ijft.2020.100029

76. Xu C, Xu S, Wang Z, Feng D. Experimental investigation of flow and heat transfer characteristics of pulsating flows driven by wave signals in a microchannel heat sink. *Int Commun Heat Mass Transfer*. 2021;125:105343.

doi: 10.1016/j.icheatmasstransfer.2021.105343

77. Santos S, Matos C, Duarte I, Olhero S, Miranda G. Effect of TPMS reinforcement on the mechanical properties of aluminium–alumina interpenetrating phase composites. *Prog Addit Manuf*. 2025;10(2):1187-1199.

78. Yan K, Deng H, Xiao Y, Wang J, Luo Y, Yan J. Influence of polishing process on surface morphology and thermo-hydraulic performance of additively manufactured Gyroid-structured heat exchanger. *Appl Thermal Eng*. 2024;253:123828.

doi: 10.1016/j.applthermaleng.2024.123828

79. Raafat A, Alteneiji M, Kamra M, Al Nuaimi S. Hydrothermal performance of microchannel heat sink integrating pin fins based on triply periodic minimal surfaces. *Case Stud Thermal Eng*. 2025;66:105773.

doi: 10.1016/j.csite.2025.105773

80. Ning J, Wang X, Sun Y, *et al*. Experimental and numerical investigation of additively manufactured novel compact plate-fin heat exchanger. *Int J Heat Mass Transfer*. 2022;190:122818.

doi: 10.1016/j.ijheatmasstransfer.2022.122818

81. Ozguc S, Pan L, Weibel JA. Optimization of permeable membrane microchannel heat sinks for additive manufacturing. *Appl Thermal Eng*. 2021;198:117490.

doi: 10.1016/j.applthermaleng.2021.117490

82. Kong D, Jung E, Kim Y, *et al*. An additively manufactured manifold-microchannel heat sink for high-heat flux cooling. *Int J Mechan Sci*. 2023;248:108228.

doi: 10.1016/j.ijmecsci.2023.108228

83. Bacellar D, Aute V, Huang Z, Radermacher R. Design optimization and validation of high-performance heat exchangers using approximation assisted optimization and additive manufacturing. *Sci Technol Built Environ*. 2017;23(6):896-911.

doi: 10.1080/23744731.2017.1333877

84. Liu C, Zhang M, Bi G, *et al*. Research on comprehensive heat dissipation characteristics of AlSi7Mg TPMS heat sinks manufactured by laser powder bed fusion. *Appl Thermal Eng*. 2025;261:124941.

doi: 10.1016/j.applthermaleng.2024.124941

85. Tan H, Wu L, Wang M, Yang Z, Du P. Heat transfer improvement in microchannel heat sink by topology design and optimization for high heat flux chip cooling. *Int J Heat Mass Transfer*. 2019;129:681-689.

doi: 10.1016/j.ijheatmasstransfer.2018.09.092

86. Ozguc S, Teague TFG, Pan L, Weibel JA. Experimental study of topology optimized, additively manufactured microchannel heat sinks designed using a homogenization approach. *Int J Heat Mass Transfer*. 2023;209:124108.

doi: 10.1016/j.ijheatmasstransfer.2023.124108

87. Orakwe JN, Shahabad SI, Ibhadode O, Bonakdar A, Toyserkani E. An integration of topology optimization and conformal minimal surfaces for additively manufactured liquid-cooled heat sinks. *Addit Manuf*. 2025;107:104814.

doi: 10.1016/j.addma.2025.104814

88. Han XH, Liu HL, Xie G, Sang L, Zhou J. Topology optimization for spider web heat sinks for electronic cooling. *Appl Thermal Eng*. 2021;195:117154.

doi: 10.1016/j.applthermaleng.2021.117154

89. Robertson J, Carter E, Thompson M, White S. Multi-objective design of heat sink fins for thermal efficiency and

manufacturability. *Int J Eng Adv*. 2025;2(1):32-39.

doi: 10.71222/1aqrg398

90. Wang W, Zhu H, Zhang W, Xiao Z. A high heat transfer performance of inclined rib mini-channel heat sink designed by machine learning and laser powder bed fusion. *Phys Fluids*. 2025;37(1):012009.

doi: 10.1063/5.0247582

91. Wang W, Zhang W, Yang X, Zhang B, Zhu H. Performance optimization of discrete sidewall features mini-channel heat sinks via laser powder bed fusion and machine learning. *Phys Fluids*. 2025;37(5):052002.

doi: 10.1063/5.0270757

92. Aksoy B, Salman OKM, Özsoy K. The estimation of the thermal performance of heat sinks manufactured by direct metal laser sintering based on machine learning. *Measurement*. 2024;225:113625.

doi: 10.1016/j.measurement.2023.113625

93. Thakur S, Talla G, Verma P. Residual stress, distortion, and porosity analysis of LED heat sink printed by SLM process using machine learning. *Eng Res Express*. 2021;3(4):045043.

doi: 10.1088/2631-8695/ac3dc6

94. Yeranee K, Rao Y. A review of recent investigations on flow and heat transfer enhancement in cooling channels embedded with triply periodic minimal surfaces (TPMS). *Energies*. 2022;15(23):8994.

95. Isenhart CR, Hayes AC, Whiting GL. Additive manufacturing of scalable jet impingement and radial taper enhancements for improved flow boiling performance. *Appl Therm Eng*. 2024;249:123355.

doi: 10.1016/j.applthermaleng.2024.123355

96. Liu H, Wang J, Gu Z, Fei X, Zhang L. Enhancement of pool boiling heat transfer using 3D-printed groove structure. *Int J Heat Mass Transfer*. 2022;183:122155.

doi: 10.1016/j.ijheatmasstransfer.2021.122155

97. Shim DI, Yun M, Kim YH, Lee D, Cho HH. 3D-Printed vapor guiding structures for enhanced pool boiling heat transfer. *Int J Mechan Sci*. 2025;286:109865.

doi: 10.1016/j.ijmecsci.2024.109865

98. Okwiri LA, Mochizuki T, Koito K, Fukui N, Enoki K. Enhanced pool boiling via binder-jetting 3D-printed porous copper structures: CHF and HTC investigation. *Appl Sci*. 2025;15(14):7892.

99. Lum LYX, Liu P, Ye H, Ho JY. Revealing microstructured surface critical heat flux degradation mechanisms and synergistic pool boiling enhancement in fluorinated fluids. *ACS Appl Mater Interfaces*. 2025;17(18):27331-27350.

doi: 10.1021/acsami.4c22543

100. Pi G, Deng D, Chen L, Xu X, Zhao C. Pool boiling performance of 3D-printed reentrant microchannels structures. *Int J Heat Mass Transfer*. 2020;156:119920.

doi: 10.1016/j.ijheatmasstransfer.2020.119920

101. Hayes A, Raghupathi PA, Emery TS, Kandlikar SG. Regulating flow of vapor to enhance pool boiling. *Appl Thermal Eng*. 2019;149:1044-1051.

doi: 10.1016/j.applthermaleng.2018.12.091

102. Shvetsov DA, Zhukov VI, Pavlenko AN. Heat transfer enhancement during boiling in horizontal layers of HFE-7100 on 2D modulated capillary-porous coatings. *Appl Thermal Eng*. 2025;263:125344.

doi: 10.1016/j.applthermaleng.2024.125344

103. Lee S, Yun S, Kwon J, Baek C, Lee D, Kim Y. Experimental investigation on boiling heat transfer performance of fractal microchannels for high heat dissipation applications. *Case Stud Thermal Eng*. 2023;52:103754.

doi: 10.1016/j.csite.2023.103754

104. Hasan M, Perna R, Elkholy A, Durfee J, Kempers R. A lightweight additively manufactured two-phase integrated natural convection heat sink. *Appl Thermal Eng*. 2025;266:125700.

doi: 10.1016/j.applthermaleng.2025.125700

105. Liu H, Gu Z, Liang J. Study on boiling heat transfer characteristics of composite porous structure fabricated by selective laser melting. *Materials*. 2023;16(19):6391.

106. Lum LYX, Leong KC, Ho JY. Optimizing additively manufactured macro-fin structure designs for enhanced pool boiling of dielectric fluids. *Int J Heat Mass Transfer*. 2024;219:124883.

doi: 10.1016/j.ijheatmasstransfer.2023.124883

107. Rozati SA, Gupta A. Enhanced phase change heat transfer with fused deposition modeling (FDM) printed pit and pillar (Pi2) arrays. *Exp Thermal Fluid Sci*. 2025;161:111337.

doi: 10.1016/j.expthermflusci.2024.111337

108. Lum LYX, Liu P, Ho JY. Micro/nanostructuring of metal additively manufactured aluminum alloy for enhanced pool boiling of dielectric fluids. *Int J Heat Mass Transfer*. 2024;221:125090.

doi: 10.1016/j.ijheatmasstransfer.2023.125090

109. Elkholy A, Kempers R. Enhancement of pool boiling heat transfer using 3D-printed polymer fixtures. *Exp Thermal Fluid Sci*. 2020;114:110056.

doi: 10.1016/j.expthermflusci.2020.110056

110. Ozguc S, Pan L, Weibel JA. An approach for topology optimization of heat sinks for two-phase flow boiling: Part 2 – Model calibration and experimental validation. *Appl Thermal Eng*. 2024;249:123338.

doi: 10.1016/j.applthermaleng.2024.123338

111. Zhou J, Yin Z. An experimental investigation on the flow boiling heat transfer performance of nanofluid in 3D printing minichannel heat sinks: A comparative study. *Nanomaterials* (*Basel*). 2025;15(14):1054.

doi: 10.3390/nano15141054

112. Kneer A, Wirtz M, Bozkurt MC, *et al.* One-piece stainless-steel 3D printed minichannel evaporators using flow boiling carbon dioxide. *Chem Eng Technol*. 2020;43(5):923-932.

doi: 10.1002/ceat.202000069

113. Wong KK, Leong KC. Nucleate flow boiling enhancement on engineered three-dimensional porous metallic structures in FC-72. *Appl Thermal Eng*. 2019;159:113846.

doi: 10.1016/j.applthermaleng.2019.113846

114. Silvi LD, Shanmugam AR, Park KS. Numerical study of pool boiling heat transfer on pin-fin surface submerged in dielectric fluid. *Thermal Sci Eng Prog*. 2025;61:103507.

doi: 10.1016/j.tsep.2025.103507

115. Zhou J, Li Q, Chen X. Micro pin fins with topologically optimized configurations enhance flow boiling heat transfer in manifold microchannel heat sinks. *Int J Heat Mass Transfer*. 2023;206:123956.

doi: 10.1016/j.ijheatmasstransfer.2023.123956

116. Zhou J, Zhou F, Zhao Q, Lu M, Li Q, Chen X. Flow boiling heat transfer in manifold microchannels with topologically optimized configurations. *Int Commun Heat Mass Transfer*. 2025;161:108555.

doi: 10.1016/j.icheatmasstransfer.2024.108555

117. Septet C, El Achkar G, Le Metayer O, Hugo JM. Experimental investigation of two-phase liquid-vapor flows in additive manufactured heat exchanger. *Appl Thermal Eng*. 2020;179:115638.

doi: 10.1016/j.applthermaleng.2020.115638

118. El Achkar G, Septet C, Le Metayer O, Hugo JM. Experimental thermohydraulic characterisation of flow boiling and condensation in additive manufactured plate-fin heat exchanger. *Int J Heat Mass Transfer*. 2022;199:123465.

doi: 10.1016/j.ijheatmasstransfer.2022.123465

119. Ye H, Lum LYX, Kandasamy R, Zhao H, Ho JY. Flow boiling heat transfer enhancement of R134a in additively manufactured minichannels with microengineered surfaces. *Appl Thermal Eng*. 2024;256:124150.

doi: 10.1016/j.applthermaleng.2024.124150

120. Akizuki Y, Odagiri K, Sawada K, Yoshizaki H, Sairaiji M, Ogawa H. Heat transport characterization on different orientations of a loop heat pipe with an additive manufactured evaporator. *Appl Thermal Eng*. 2025;264:125455.

doi: 10.1016/j.applthermaleng.2025.125455

121. Kappe K, Bihler M, Morawietz K, Hügenell PPC, Pfaff A, Hoschke K. Design concepts and performance characterization of heat pipe wick structures by LPBF additive manufacturing. *Materials*. 2022;15(24):8930.

122. Mezghani A, Dickman CJ, Reutzel EW, Nassar AR, Wolfe DE. Additively manufactured inconel 718 vapor chamber with conformal micro-pillar wicks: A low temperature concept demonstration. *Int J Heat Mass Transfer*. 2025;246:127056.

doi: 10.1016/j.ijheatmasstransfer.2025.127056

123. Robinson AJ, Colenbrander J, Deaville T, Durfee J, Kempers R. A wicked heat pipe fabricated using metal additive manufacturing. *Int J Thermofluids*. 2021;12:100117.

doi: 10.1016/j.ijft.2021.100117

124. Jafari D, Wits WW, Geurts BJ. Phase change heat transfer characteristics of an additively manufactured wick for heat pipe applications. *Appl Thermal Eng*. 2020;168:114890.

doi: 10.1016/j.applthermaleng.2019.114890

125. Meng X, Tan S, Yuan Z, Zhang Y, Chen L. Experimental study on the heat transfer performance of a vapour chamber with porous wick structures printed via metallic additive manufacturing. *Int Commun Heat Mass Transfer*. 2023;140:106496.

doi: 10.1016/j.icheatmasstransfer.2022.106496

126. Zhou J, Teng L, Shen Y, Jin Z. Simulation of, optimization of, and experimentation with small heat pipes produced using selective laser melting technology. *Materials*. 2023;16(21):6946.

127. Park YY, Bang IC. Experimental study on 3D printed heat pipes with hybrid screen–groove combined capillary wick structure. *Appl Thermal Eng*. 2023;232:121037.

doi: 10.1016/j.applthermaleng.2023.121037

128. Kamata M, Hayashi K, Watanabe N, *et al.* Thermal performance of ammonia-based thin flat loop heat pipe fabricated by additive manufacturing. *Int J Heat Mass Transfer*. 2025;236:126382.

doi: 10.1016/j.ijheatmasstransfer.2024.126382

129. Hunter LW, Brackett D, Brierley N, Yang J, Attallah MM. Assessment of trapped powder removal and inspection strategies for powder bed fusion techniques. *Int J Adv Manuf Technol*. 2020;106(9):4521-4532.

doi: 10.1007/s00170-020-04930-w

130. Esarte J, Blanco JM, Bernardini A, Sancibrián R. Performance assessment of a three-dimensional printed porous media produced by selective laser melting technology for the optimization of loop heat pipe wicks. *Appl Sci*. 2019;9(14):2905.

131. Yun M, Hsu WT, Shim DI, *et al.* Design and fabrication of heat pipes using additive manufacturing for thermal management. *Appl Thermal Eng*. 2024;236:121561.

doi: 10.1016/j.applthermaleng.2023.121561

132. Cui J, Hu Z, Xu W, Ma Y, Ling W, Zhou W. Selective laser melting manufacturing and heat transfer performance study of porous wick in loop heat pipe. *J Manuf Process*. 2024;124:1294-1305.

doi: 10.1016/j.jmapro.2024.07.017

133. Han Z, Chang C. Fabrication and thermal performance of a polymer-based flexible oscillating heat pipe via 3D printing technology. *Polymers*. 2023;15(2):414.

134. Arai T, Kawaji M. Thermal performance and flow characteristics in additive manufactured polycarbonate pulsating heat pipes with Novec 7000. *Appl Thermal Eng*. 2021;197:117273.

doi: 10.1016/j.applthermaleng.2021.117273

135. Jacob DJ. *Introduction to Atmospheric Chemistry*. New Jersey: Princeton University Press; 1999.

136. Zhao B, Hu M, Ao X, Chen N, Pei G. Radiative cooling: A review of fundamentals, materials, applications, and prospects. *Appl Energy*. 2019;236:489-513.

doi: 10.1016/j.apenergy.2018.12.018

137. Park S, Choi J, Lee J, *et al*. Gradient porous and carbon black-integrated cellulose acetate aerogel for scalable radiative cooling. *Small*. 2025;21(7):2409873.

doi: 10.1002/smll.202409873

138. Shi X, Liu C, Lin B, *et al*. 3D printed cellulose nanofiber/silica nanoparticle scaffolds for daytime radiative cooling. *Addit Manuf*. 2024;92:104392.

doi: 10.1016/j.addma.2024.104392

139. Zhou K, Li W, Patel BB, *et al*. Three-dimensional printable nanoporous polymer matrix composites for daytime radiative cooling. *Nano Lett*. 2021;21(3):1493-1499.

doi: 10.1021/acs.nanolett.0c04810

140. Park SJ, Seo SB, Shim J, *et al*. Three-dimensionally printable hollow silica nanoparticles for subambient passive cooling. *Nanophotonics*. 2024;13(5):611-620.

doi: 10.1515/nanoph-2023-0603

141. Hazarika A, Deka BK, Park H, *et al*. Hierarchically designed 3-D printed porous nylon fabric-based personal thermoregulatory for radiative and directional wick-evaporative cooling. *Chem Eng J*. 2023;471:144536.

doi: 10.1016/j.cej.2023.144536

142. Hazarika A, Lee S, Park H, *et al*. 3D printed gradient porous fabric-based thermal and moisture regulating composite integrated triboelectric nanogenerator for human motion cognizance. *Nano Energy*. 2024;132:110350.

doi: 10.1016/j.nanoen.2024.110350

143. Wu WL, Tsai SY, Lo YC, *et al*. Design of a multifunctional resin-based outdoor spherical robot shell for ultrahigh visible to near-infrared transmittance and mid-infrared radiative cooling. *ACS Omega*. 2025;10(3):3080-3089.

doi: 10.1021/acsomega.4c09954

144. Zhang T, Zhang X, Zhang S, Wang L, Yu D, Wang W. 3D printing-assisted honeycomb-structured bricklike aerogels applied for infrared stealth with good thermal management. *ACS Appl Polym Mater*. 2024;6(22):13828-13840.

doi: 10.1021/acsapm.4c02747

145. Pelanconi M, Barbato M, Zavattoni S, Vignoles GL, Ortona A. Thermal design, optimization and additive manufacturing of ceramic regular structures to maximize the radiative heat transfer. *Mater Design*. 2019;163:107539.

doi: 10.1016/j.matdes.2018.107539

ACCSCIENCE PUBLISHING

Engineering Science in Additive Manufacturing

ORIGINAL RESEARCH ARTICLE

A machine learning approach for enhancing process screening and qualification in metal additive manufacturing

Ze Chen[1,2], Jingwen Gao[2], Chengcheng Wang[1], Zhuohong Zeng[1,2], Chenyang Zhu[2], and Wei Fan[1,3]*

[1]Singapore Centre for 3D Printing, Nanyang Technological University, Singapore

[2]School of Mechanical and Aerospace Engineering, Nanyang Technological University, Singapore

[3]State Key Laboratory of Solidification Processing, Northwestern Polytechnical University, Xi'an, Shaanxi, China

Abstract

The prevailing screening and qualification methodologies heavily depend on conventional manufacturing processes, which incur significant costs and prolonged lead times due to extensive physical testing. These challenges are also present in the growing field of additive manufacturing (AM), where numerous process parameters must be considered. However, the net-shape forming advantage of AM renders conventional screening and qualification methods inadequate. In the context of ongoing industrial digital transformation, a promising approach to enhancing process screening and qualification for metal AM is the adoption of a digital methodology tailored to the unique characteristics of this manufacturing technique. In this study, a convolutional neural network model is employed to extract features from images to predict material properties in laser-directed energy deposition (L-DED) processes. The model achieved a mean absolute percentage error of 2.3% and a root mean square error of 15.0 MPa for predicting ultimate tensile strength, with a prediction residual within ±1% for density. Unlike conventional approaches that rely on bulk or multilayer builds, this study uniquely demonstrates the feasibility of using early-stage single-track print features to predict final part properties with limited view and material involvement. This established model and workflow pave the way for highly efficient and low-cost property prediction in L-DED processes.

Keywords: Additive manufacturing; Directed energy deposition; Machine learning; Process screening; Qualification

***Corresponding author:**
Wei Fan
(fanw92@nwpu.edu.cn)

Citation: Chen Z, Gao J, Wang C, Zeng Z, Zhu C, Fan W. A machine learning approach for enhancing process screening and qualification in metal additive manufacturing. *Eng Sci Add Manuf*. 2025;1(3):025280018. doi: 10.36922/ESAM025280018

Received: July 9, 2025

1st revised: August 4, 2025

2nd revised: August 14, 2025

Accepted: August 14, 2025

Published online: August 30, 2025

1. Introduction

Laser-directed energy deposition (L-DED) is a promising method for metal additive manufacturing (AM) and is widely used to fabricate net-shaped and near-net-shaped parts.[1,2] This technique enables the direct manufacture of highly complex parts from high-performance materials using computer-aided design data. Metal powder is fed either coaxially or through a set of radially symmetric nozzles into a molten pool created by laser energy during the L-DED process.[3] This material is deposited layer

by layer to fabricate a three-dimensional (3D) structure. The key to producing intricate structures using L-DED lies in identifying suitable process parameters.[4] Process parameters, such as power feed, scan speed, mass flow rate, and gas flow rate, play a crucial role in determining the final properties of additively manufactured parts.[5,6] Over the past decade, significant research efforts have focused on identifying optimal processing regimes for various materials to achieve defect-free manufacturing. These efforts have primarily relied on costly trial-and-error experiments and computationally expensive mechanistic simulations.[7]

The use of machine learning (ML) in materials engineering and smart manufacturing has been gaining popularity.[8,9] Researchers are increasingly adopting ML methods in metal AM to accelerate the development of process parameters and to reduce costs.[10] Utilizing ML enables the creation of process maps that provide a detailed view of the process windows, which aids in the efficient optimization of parameters.[11,12] This strategy helps researchers streamline the development of parameters, resulting in shorter development times and reduced costs from trial-and-error experiments. In addition, ML leverages extensive datasets to predict mechanical properties, expediting qualification and optimizing material selection and processing parameters.[13,14] This predictive capability integrates seamlessly with both in-process and post-process productive metrology, offering a comprehensive evaluation of manufactured components.[15,16]

The prevailing screening and qualification methodologies heavily rely on conventional manufacturing processes, such as casting, forging, and powder metallurgy. Consequently, these methodologies are associated with significant costs and prolonged lead times, primarily attributable to the extensive physical testing required. Moreover, it is imperative to acknowledge that these traditional approaches may not be well-suited for metal AM processes.[17] For L-DED, the flowchart of the prevailing traditional methods is shown in Figure 1A. The process begins with printing numerous single-bead samples based on experimental designs. These samples undergo several preparatory steps, including wire cutting, mounting, and polishing, to create metallurgical samples. These prepared samples are then examined under an optical microscope to capture the geometry index of the cross-sectional bead. Preliminary process window screening is carried out based on the bead geometry index, and the "good" parameters are selected for printing block samples. The final evaluation primarily focuses on the porosity and tensile properties of these block samples. Parameters that meet user-defined requirements are identified as the optimal process window. If the requirements are not met, the unsatisfactory parameters need to be revised. Depending on the complexity of the case, this may involve minor revisions for block printing or major redesigns for single-bead sample printing. The traditional methods can impose substantial costs and long lead times on commercial organizations due to insufficient qualification protocols.

Several prior studies in metal AM have applied convolutional neural networks (CNNs) to high-speed imaging data—particularly in powder bed fusion—to detect defects and predict properties. For example, Zhang *et al.*[18] achieved ~92.7 % classification accuracy recognizing quality levels from melt-pool, plume, and spatter images in stainlesssteel 316L single-track laser powder bed fusion. In addition, Herzog *et al.*[19] leveraged multi-axis infrared monitoring of completed builds, combined with ML, to detect defects in L-DED. Unfortunately, whether using *in situ* measurement data or full-build surface data, the acquisition workflow remains resource-intensive. AM inherently builds from lines (tracks) to volumes (parts); therefore, the quality of a single track could, to some extent, serve as fundamental feedback on final part quality. This is an intriguing yet underexplored proposition.

To address the constraints associated with the traditional method, this study introduces the ML-Qvision model, designed to achieve two primary functions: Function 1—rapid process window screening by scanning the surface profile of printed single-bead samples to predict the quality of the printed blocks using the CNN model—and Function 2—qualification of L-DED printed parts by scanning the surface profile of printed blocks to predict their porosity and tensile properties, as illustrated in Figure 1B. This study explores the use of ML techniques for screening process parameters and establishing surface-to-property relationships in L-DED fabricated Monel K-500 alloy. The novelty of this study lies in its use of surface profile images from single-bead tracks to predict final properties of L-DED builds. Traditional process screening and property qualification in AM typically require extensive multilayer printing and post-processing. In contrast, our approach enables early prediction of key quality metrics, potentially reducing the trial-and-error cycle in new material development, saving time, material, and cost.

2. Materials and methods

2.1. Directed energy deposition

The manufacturing process for all samples was conducted using the BeAM Magic 800 system (AddUp Group, France). Monel K-500 powder (Sandvik Osprey Ltd, United Kingdom), characterized by a size distribution ranging from 53 to 150 μm, was utilized for sample

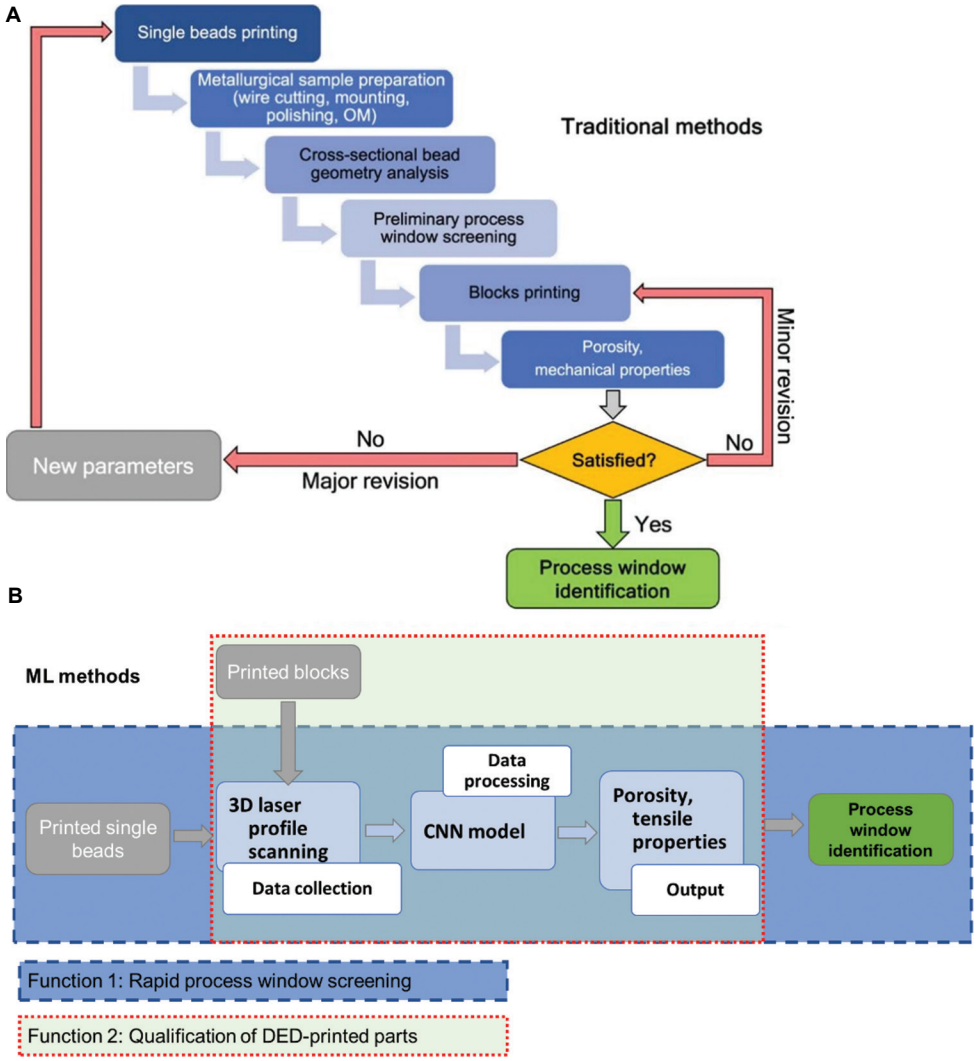

Figure 1. Schematic of proposed workflow and comparison with conventional methods
Abbreviations: 3D: Three-dimensional; CNN: Convolutional neural network; DED: Directed energy deposition; OM: Optical microscopy.

fabrication. The chemical composition of the powder is detailed in Table 1. Powder that is compatible with the L-DED process can achieve fully densified samples with optimal parameters.[4] Throughout the fabrication process, meticulous attention was devoted to capturing the surface morphology of the printed samples. In addition, the density of each block was carefully measured, with subsequent tensile testing exclusively administered to samples demonstrating the capability to yield valid results.

A full factorial design was employed to investigate the effect of three factors on the L-DED process, as detailed in Table 2. A total of $6 \times 7 \times 3 = 126$ combinations of process parameters were used for the L-DED process, encompassing both single-bead and block samples, to train the ML model. Notably, all single-bead samples were printed onto a single substrate and had a uniform length of 80 mm. The block samples generated possessed dimensions of 20 mm × 30 mm × 20 mm.

2.2. Materials characterization

The surface profiles of both printed blocks (Figure 2A) and single beads (Figure 2B) were captured by a laser profile sensor (LLT3010-25/BL, Micro-Epsilon, Germany), as shown in Figure 2C. The measured profiles were processed using the scanCONTROL 3D-View 3.7 software for illustration and image export. Before ML processing, all exported images were resized and set to a resolution of 650 × 650 pixels, which illustrates the surface roughness and continuity of the printed surface as a function of scan speed and laser power under the same feed rate. A complete dataset of the surface morphologies of both blocks and single beads is illustrated in Figure A1.

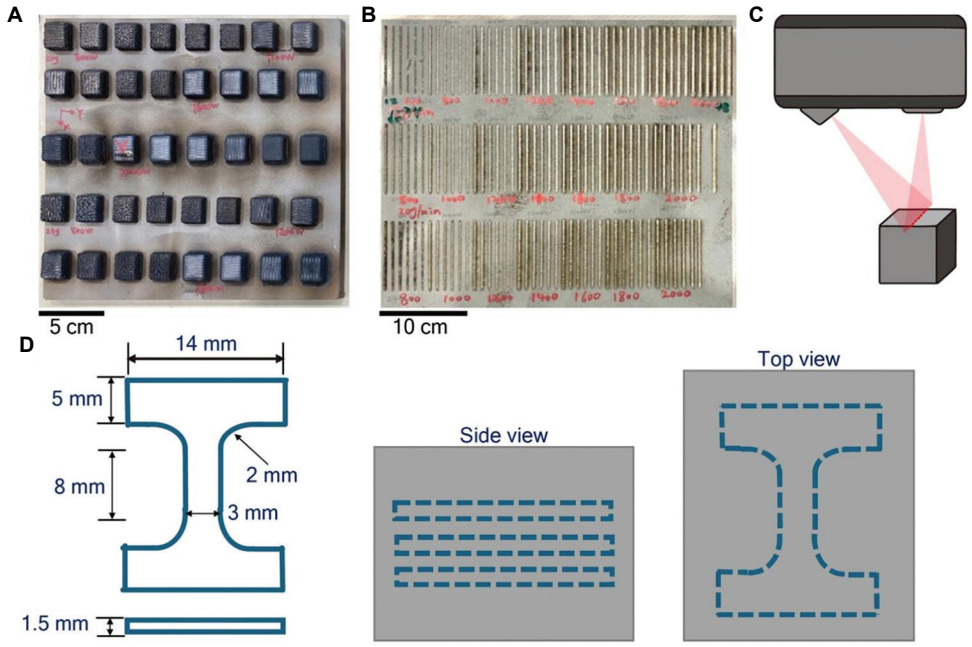

Figure 2. Experimental setups. (A) Printed blocks on the substrate. Scale bar: 5 cm. (B) Single beads on the substrate. Scale bar: 10 cm. (C) Schematic of a three-dimensional laser surface profile scanner. (D) Design of the tensile sample and the positions in the block sample.

Table 1. Chemical composition of the Monel K-500 powder

Element	Copper	Aluminum	Iron	Manganese	Titanium	Oxygen	Nickel
Percentage (wt%)	30	2.35	1.2	1.1	0.82	0.01	Bal.

Table 2. Parameters used for laser-directed energy deposition

Parameters	Value
Laser power (W)	800, 1,000, 1,200, 1,400, 1,600, 1,800, 2,000
Scanning speed (mm/min)	1,000, 1,400, 1,800, 2,200, 2,600, 3,000
Powder feed rate (g/min)	16, 20, 24
Secondary gas flow rate (L/min)	10
Central gas flow rate (L/min)	6
Laser spot size (mm)	2.25
Z step (mm)	0.3, 0.45
XY step (mm)	1.5
Powder carrier gas level	60%

Density measurement was only conducted on block samples. Block samples were wire cut from the substrate, and densities were determined via Archimedes' method using a densitometer (XS204; Mettler Toledo, United States). After acquiring the densities of the blocks, the samples were shaped into dog-bone specimens using electrical discharge machining for tensile testing. The design of the tensile coupons is shown in Figure 2D. Three specimens were cut from the printed block samples from the middle part. Several samples were excluded due to printing defects, such as pores and lack of fusion, as illustrated in Figure A2. Only 61 samples qualified for tensile testing to acquire the ultimate tensile strength (UTS) and elongation at failure. The tensile tests were conducted on a uniaxial tester (AGX 50 KN, Shimadzu, Japan) with a non-contact digital video extensometer, with a strain rate of 0.5 mm/min at room temperature. Testing was conducted on each block sample using three identical tensile coupons.

2.3. ML framework

A CNN is a robust neural network architecture for image-related tasks, including classification and regression.[20] It can automatically detect the critical features from raw images without manual supervision. As surface morphology images are the inputs for the predictive model training in this research work, CNN handles the image dataset and establishes the surface-to-property relationships.

2.3.1. Model implementation

The ML-Qvision framework was implemented in the Python Tensorflow library (version 2.1.0) using the Keras

functional application programming interface.[21] This model, as schematically illustrated in Figure 3, has three pairs of convolutional and pooling layers followed by three fully connected layers. The number of filters for the three convolutional layers was set as 16, 32, and 64, respectively, to capture different pattern combinations from the images. The size of each filter was 3 × 3, followed by a "same" padding. The output generated by each convolutional layer was fed into a max pooling layer to obtain a down-sampled feature map. The max pooling layers have a pool size of 2 × 2, halving the dimensions in horizontal and vertical directions. The feature map generated by the last max pooling layer was flattened into a vector and then fed to the first fully connected layer. The number of nodes in the three fully connected layers was 16, 4, and *N*, where *N* depends on the required number of outputs. For the case of only one output, a total of 89,721 trainable parameters were leveraged in the model. Batch normalization and dropout with a rate of 0.4 were applied only after the first fully connected layer to prevent overfitting. The output layer used the linear activation function for the regression task. The model was trained with 1000 epochs and a batch size of eight. The train-test split ratio was 80/20, as a general practice.

The input images are represented with dimensions n × n × m, where *n* is the width and height of the surface morphology image, and *m* is the number of channels (for a color image, *m* = 3 for red, green, and blue channels, whereas *m* = 1 for grayscale images). All input images were normalized from the original range of 0–255 to a standardized range of 0–1 before being input into the CNN. This normalization reduces computational complexity and accelerates model convergence.

2.3.2. Objective functions

Error metrics designed for numeric values were used to evaluate predictions made by regression models. These metrics provide an indicative score that summarizes the predictive performance of the trained model, allowing users to compare accuracy across different model settings and datasets. The two most commonly used error metrics for regression predictions are mean absolute percentage error (MAPE) and root mean square error (RMSE).[22] MAPE is the mean of all absolute percentage errors between the predicted and actual values, whereas RMSE is the square root of the mean squared error between the predicted and actual values. MAPE expresses the error as a percentage, facilitating easier model comparisons, whereas RMSE is on the same scale as the target variable. However, MAPE is more sensitive to outliers, as it can produce significant percentage errors when the target value is very small. Consequently, both MAPE and RMSE were monitored to predict density and tensile properties.

2.3.3. k-fold cross-validation

Model performance validation is essential for ensuring the accuracy of any predictions of an ML model. Typically, the unseen data (test set) is separated from the overall dataset using a user-defined ratio; for instance, an 80/20 ratio is set for this model training and testing. However, this splitting can introduce bias if the data distribution in the test set significantly differs from the training set, a problem that is more pronounced with limited data. Cross-validation is a technique used to evaluate ML models on limited datasets.[23,24] It provides a more robust estimate of the trained model's generalization error.

In *k*-fold cross-validation, the dataset was first shuffled to ensure that the order of the inputs and outputs was utterly random. This step helps to ensure that the data are less biased. Then, the dataset was split into *k* non-overlapping subsets of equal size. Each *k*-subset was treated as a test set, whereas all other subsets were collectively used as a training set. The overall model performance was calculated as the mean of the *k* hold-out test performances. *k*=5 was chosen for this analysis on the small dataset.[23]

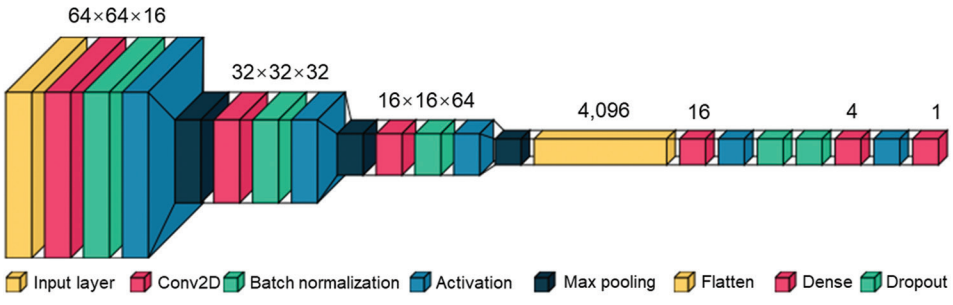

Figure 3. Convolutional neural network architecture used for feature extraction from surface profile images
Abbreviation: conv2D: Two-dimensional convoluted layer.

3. Results

3.1. Dataset collection and data processing

Input data for the ML model is separated into two parts: (i) The input surface profile images, and (ii) the targeted properties for the regression work, including density and tensile properties (UTS and elongation at failure). For every processing parameter combination of scan speed, power, and feed rate, two profiles from the printed block surface and the single-bead surface were collected. A top view of this 3D profile, color-coded by the height of the sample surface, was used as raw images for the input. Each raw color image was first resized to the pre-determined input size of 64 × 64. The RGB images were then normalized to a range of (0, 1) by dividing the raw values by 255. In this sense, a total of 126 images of block top surface and 126 images of single-bead surface were generated from the measured surface profile as the input for the model training process. Figure 4A shows the input images matrix printed at a fixed feed rate of 16 g/min, while varying the other two processing parameters. The inputs for the other two feed rate conditions are shown in Figure A1. The block surface morphology changed significantly with varying power and scan speed, as shown in Figure 4A. Lower scan speeds combined with higher power resulted in rougher and more textured surfaces, whereas higher scan speeds and lower power produced smoother surfaces with fewer pronounced features. When the same parameters were applied to print single-bead samples, higher power enhanced the intensity of the red lines, indicating higher regions, while lower power resulted in less pronounced features. In addition, processing parameters that produce a rough block surface also resulted in a thinner, less smooth surface. This correlation in surface features suggests that the bulk sample surface can be inferred from the single-bead surface, enabling predictions for the larger sample based on observations of the bead surface.

The metrics for the properties on the output side of the Qvision model are density and tensile properties. The densities of all 126 block samples are plotted in Figure 4B. For all types of feed rate, the defect samples—typically with lower densities—were consistently observed at lower power levels and higher scan speeds. Notably, the printed material, Monel 400 nickel-based super alloy, has a nominal density of around 8.5 g/cm^3. When laser power is above 1200 W, the printed blocks are close to the nominal density and are considered nearly dense. Tensile coupons were cut from these printed blocks. However, only 61 of them were free of defects—such as large poles and a lack of interior fusion defects—at the designed positions. The existence and the distribution of defects could significantly detriment the tensile properties of the blocks. Blocks that could not produce tensile coupons with minimal macroscopic defects were excluded as potential outliers. Measured tensile properties for the 61 qualified parameter combinations are plotted in Figure 4C and categorized by powder feed rate. The 16 g/min and 24 g/min feed rates showed more variability in both metrics of tensile properties, with noticeable clusters indicating optimal ranges. In contrast, the 20 g/min feed rate exhibited a more consistent performance, with less variability in both UTS and elongation. It achieved higher UTS values while maintaining moderate elongation.

3.2. Process window screening

Process window screening is a critical method for evaluating and optimizing printing process parameters within a defined range to achieve the desired printing outcomes. This approach involves systematically varying and analyzing factors such as laser power, scan speed, and powder feed rate to identify the optimal combination that yields the best print quality and mechanical properties. By adjusting these parameters, manufacturers can fine-tune the printing process to produce parts that meet stringent specifications and performance standards.

For the L-DED fabricated Monel K-500 alloy, density and UTS values predicted from surface profiles of printed single-bead samples were used as screening references. A scatter plot relating these two properties is shown in Figure 5A. According to the specific application requirements, users can define acceptable thresholds for both UTS and density to differentiate satisfactory printed samples from unsatisfactory ones. In this study, the threshold values selected were a UTS of at least 500 MPa and a density greater than 8.4 g/cm^3. These criteria were used to establish a qualified region within the scatter plot, which was shaded green for visual clarity in Figure 5A. Within this qualified region, a total of 21 samples met the defined criteria, although three of these were excluded from further tensile testing. The samples that did not meet the criteria and fell outside the green shaded region were disqualified. It was observed as the inset of Figure 5A that the qualified samples within the green region exhibited relatively smoother surfaces and fewer discontinuities in the single-bead surface profile. This was consistent with the expectations, as stronger (higher UTS) and denser (higher density) samples typically correlate with better overall sample quality and fewer defects in printed materials. A comprehensive visual representation is shown in Figure 5B, in which red circles represent the process parameters that produced a disqualified sample due to either poor tensile properties or low density, and green surfaces enclose all the qualified processing parameter combinations, which indicate the optimized process window.

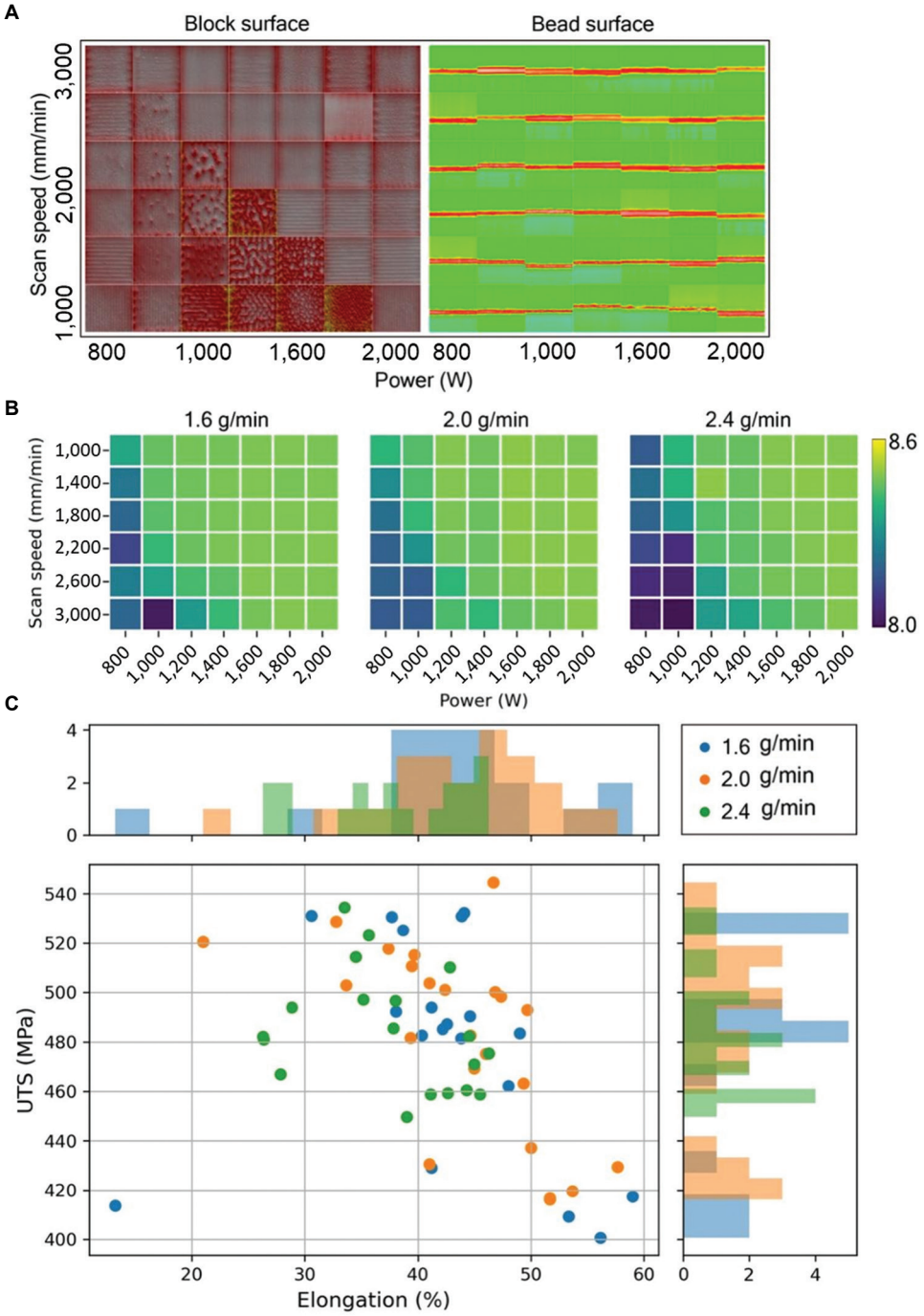

Figure 4. Measured data for Qvision model training. (A) Surface profile for both block and single-bead samples for powder feed rate of 16 g/min. (B) Measured density for all 126 block samples as a function of three variables. (C) Tensile properties (ultimate tensile strength and elongation at failure) for 61 qualified block samples that could produce a valid tensile coupon for uniaxial tensile testing.

3.3. Input image size tuning

CNNs can process input of arbitrary size by applying a combination of downsampling and pooling. However, it has been found that CNN models are not agnostic to the input size;[25] they exhibit significant differences in performance based on the input size. Presenting the same image at different scales can result in varying outcomes.[26] There is no straightforward relationship between input

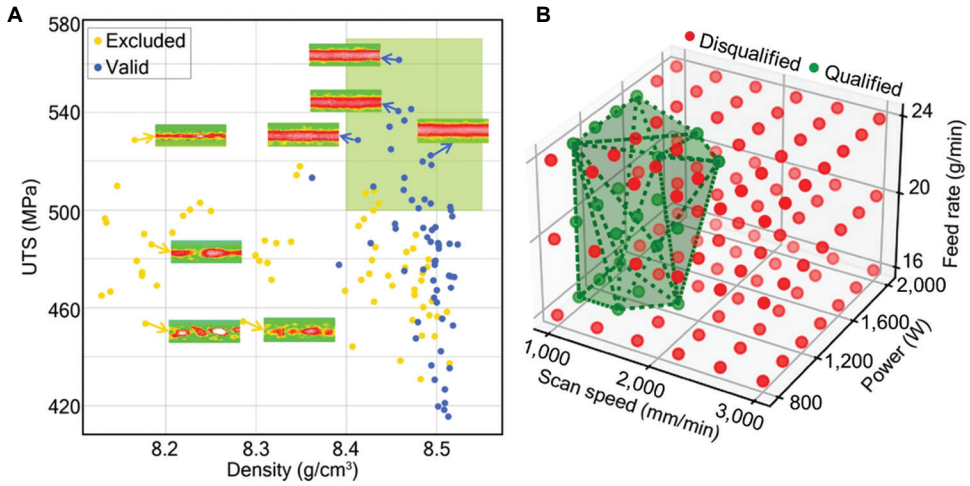

Figure 5. Print parameter screening. (A) Scatter plot of ultimate tensile strength versus density for printed single-bead samples and its role in identifying the qualification region. (B) Three-dimensional plot unveils process window with parameters and qualification status.

size and model performance; instead, each network has an optimal input size at which it performs best. Therefore, three different input image sizes (32 × 32, 64 × 64, 128 × 128) were investigated before training the final model to determine an optimal value that can yield more accurate prediction results.

Figure 6 reveals that the performance of the CNN model varies significantly with different input image sizes. For both density and UTS predictions, the error metrics (MAPE and RMSE) showed a similar trend. The optimal performance for both properties was observed at an image size of 64 × 64, where the MAPE and RMSE values were the lowest. This indicated that the model could achieve the highest accuracy and lowest prediction error at this image size. In contrast, smaller (32 × 32) or larger (128 × 128) image input would increase error metrics, suggesting a decrease in model performance. Interestingly, although higher resolution (128 × 128) retained more spatial information, its use led to degraded performance compared to the 64 × 64 size. The reduced accuracy with a smaller input size is expected, as the limited resolution provides insufficient spatial information for reliable predictions. In contrast, although a larger input size of 128 × 128 retained finer details and higher resolution, the model performance did not improve as anticipated. The enlarged input size introduced a greater number of redundant features, increasing the risk of overfitting and complicating the feature–target relationships beyond the capacity of the current network architecture. In small-data settings, richer input can exacerbate overfitting due to the curse of dimensionality, where the required number of training samples grows exponentially with input feature dimensionality.[27] Furthermore, higher resolution increases the number of learned parameters, potentially exceeding the model capacity for this dataset and reducing generalization ability. These observations confirmed that each model exhibits an optimal input size, and in this case, the size of 64 × 64 yielded the best results for predicting both density and UTS.

3.4. Performance evaluation

After validating the proposed CNN model using the five-fold cross-validation, a new model was trained with a single output on a newly split training set for predicting sample density and tensile properties. Notably, for one process parameter, printing was conducted for both the block and a single bead. The output metrics, the properties of the printed sample, were measured and selected from block samples only. Two models were trained on different input surface profiles from single beads and blocks, respectively. All test cases were close to the blue regression line, on which the predicted and actual densities were the same, as shown in Figure 7A, except for an obvious outlier for single beads. The block samples exhibited higher prediction accuracy compared to single bead samples, as indicated by the higher R^2 value. The residual analysis shown in Figure 7B also indicates that the predicted outcome varies within a ±1% range of the ground truth values. In addition, the calculated residuals did not exhibit a visible pattern, i.e., the error is independent of predicted density value, indicating that the model is a good fit for the density prediction. A higher indexing accuracy was achieved for samples with a density over 8.4 g/cm³, which is close to the completely dense state. The model performed better as the number of dense samples for the training input was greater than that of defective ones with lower density, as shown in Figure 4B. A more evenly distributed dataset could be used for model training to achieve a more reliable prediction.

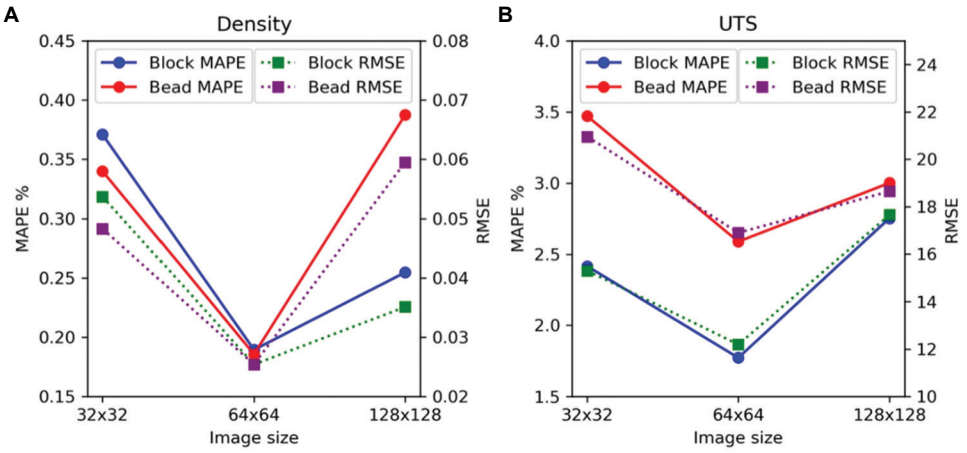

Figure 6. Model performance to compare results for block and bead samples across different image sizes. (A) Density. (B) UTS. Abbreviations: MAPE: Mean absolute percentage error; RMSE: Root mean square error; UTS: Ultimate tensile strength.

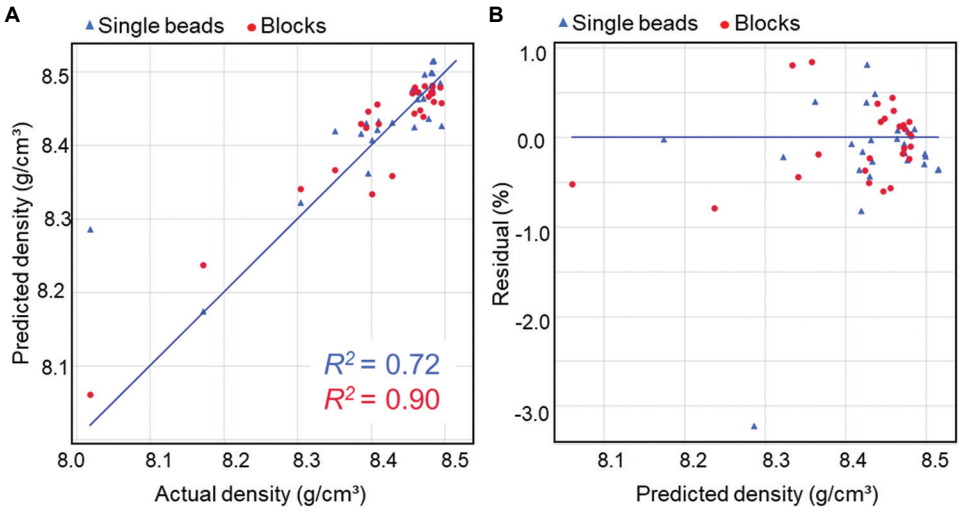

Figure 7. Surface to density prediction result. (A) Plot of predicted versus measured densities for single-bead and block samples, and (B) the corresponding residual plot.

Figure 8A shows the predicted versus measured UTS for single-bead and bulk samples based on the testing surface profiles (the input images). Both the R^2 values of single-bead and block samples are lower than 0.5. The predicted values are more scattered from the ground truth line, and higher residuals (±5%) were found for the model predicting UTS compared to the density prediction (±1%), as illustrated in Figure 8B. This reduced accuracy can be partly attributed to the limited dataset size, as only 61 samples were available for training and testing the UTS prediction model. The model had fewer examples from the full UTS range, which likely contributed to the increased complexity in learning the relationship. Furthermore, UTS prediction is inherently more challenging than density prediction, as tensile strength depends on multiple factors beyond porosity, including grain structure, phase composition, and defect morphology, many of which are not fully captured in surface profile images. In contrast, density is more directly related to surface-visible features, such as lack-of-fusion defects or irregular melt tracks, making it easier for the model to establish a consistent mapping. Nevertheless, the performance of UTS prediction from single-bead samples was comparable with that from block surfaces. The model's ability to exploit the additional geometric and textural information present in block surface profiles was constrained by the limited data size. As a result, both input types provided a similar level of predictive capability for UTS within the current data conditions. A larger and more diverse dataset could potentially reveal clearer performance differences between the two input types.

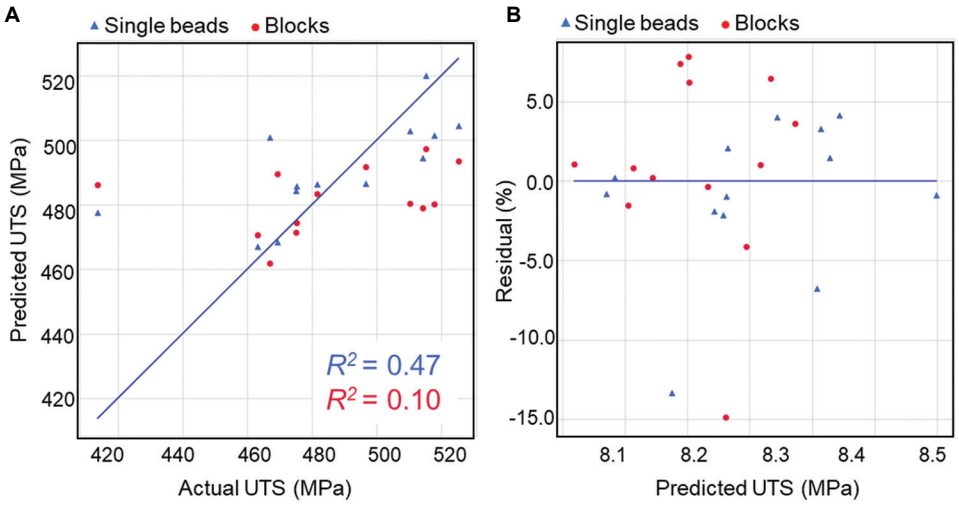

Figure 8. Surface to UTS prediction result. (A) Plot of predicted UTS versus measured UTS for single-bead and block samples, and (B) the corresponding residual plot.
Abbreviation: UTS: Ultimate tensile strength.

Apart from UTS, elongation at failure was also predicted. Numerous studies have reported a systematic strength-ductility trade-off across metallic systems, where UTS tends to increase as elongation decreases, reflecting shared but competing structural influences. This relationship motivated the development of a multi-output regression model, featuring a shared convolutional backbone and separate fully connected output heads for UTS and elongation. The expectation was that shared layers could capture common predictive features from surface profiles, enabling knowledge transfer[28] and improving both outputs. However, as shown in Table 3, the multi-output model produced higher MAPE and RMSE values than the corresponding single-output models. The differences in error between the single-output model and multi-output model for UTS and elongation are 1.3% and 2.3%, respectively. This result indicates that while UTS and elongation share some dependencies, they are not perfectly correlated in terms of predictive features extracted from surface images. In the context of the current small dataset, this partial overlap may have limited the benefit of shared feature learning, leading instead to negative knowledge transfer. Another contributing factor could be the curse of dimensionality.[29] Increasing the dimensionality of the output space without a corresponding increase in sample size raises the computational complexity of the learning problem and the risk of overfitting, ultimately reducing prediction accuracy.

Table 3. Performance comparison for single and multi-output convolutional neural network models

Model type	MAPE %		RMSE	
	UTS	Elongation	UTS	Elongation
Single-output	2.3	6.9	15.0	3.1
Multi-output	3.6	9.2	21.6	4.5

Abbreviations: MAPE: Mean absolute percentage error; RMSE: Root mean square error; UTS: Ultimate tensile strength.

4. Discussion

The proposed ML-Qvision model uses image input that offers distinct advantages over traditional process parameters. Images inherently contain a wealth of information with intricate spatial relationships, which provides a more comprehensive representation of the subject matter compared to numerical or categorical data alone.[30] In this study, the smoothness of the surface profile, discontinuous sites (originating from the surface roughness), and relative intensity variation (resulting from the height difference of the surface) on the corresponding input images provided valuable insights to the model. The top surface is an essential indicator of the part's overall quality, i.e., the final properties of built samples.[31] It also reflects the quality of the laser-material interaction during the building process and can be used to reveal potential issues such as overheating, insufficient melting, or improper layer bonding. Qualitatively, insufficient energy input during the printing process can induce lack of fusion defects and leave behind unmelted powders, resulting in a porous surface post-melting.[32] Conversely, excessive energy input may cause spherical pores and bubbles due to the Marangoni flow in the melt pool.[33,34] An uneven or wavy surface may correlate with internal defects, whereas an ideal surface would exhibit minimal surface roughness,

indicating a defect-free internal structure. Thus, a well-processed surface often correlates with a sound internal microstructure, while surface imperfections can indicate underlying issues within the material.

The trained ML-Qvision eliminates the need for manual feature extraction and analysis, often required when using process parameters, thereby streamlining the data preparation phase and reducing potential human error. In this work, the accuracy of density prediction significantly surpasses that of tensile properties. The key distinction lies in the quantity of valid input data available for model training. Out of all 126 fabricated samples, only 61 samples successfully generated images paired with corresponding measured data for predicting tensile properties from the surface profile. CNN models generally necessitate substantial datasets to accurately capture intricate patterns and relationships within the data. In scenarios where the available data is limited, the model may struggle to effectively learn complex features, resulting in suboptimal performance.[35] Increasing the number of inputs could improve the performance of the model. However, L-DED samples produced under certain processing parameters are prone to defects, which hinder the production of valid tensile coupons. Despite defective samples being inevitable within these process parameters—due to issues such as lack of fusion or extensive porosity commonly found in unsuitable metal AM parameters.[36,37]—including more input data for the tensile property prediction model would enhance its accuracy and versatility. In the meantime, the defects mentioned above could be predicted by the proposed model, enriching the information that is deduced from the simple surface profile measurement. Obtaining this information for printed samples typically requires X-ray tomography scans or destructive screening by microscopes.[38,39] In the context of CNN models with multiple outputs, leveraging the correlation between outputs can be highly informative and productive.[27] Future research could be directed toward developing an image data-driven model capable of simultaneously predicting defects and tensile properties, in which the eliminated data due to defects can be utilized.

The current workflow aimed to correlate surface profile data with the properties of the samples. The trained model achieved comparable prediction performance when a full image of a block surface and a single line from a single-bead sample were used. This indicates that properties can be effectively predicted based on the surface profile image of a single bead during the L-DED process. Consequently, property inspection does not require a fully built sample for testing, which typically involves tedious and destructive sample preparation procedures. Instead, the quality inspection of required properties, such as density and tensile strength, can be predicted by capturing the surface profile of a single track. This approach streamlines the inspection process, reducing the time and material costs associated with traditional testing methods. In addition, the L-DED process is conducted in a line-by-line and layer-by-layer manner. Capturing the surface profile during the printing process has been successful using various vision systems, such as laser and structured light-based techniques.[40,41] By implementing the trained model into monitoring techniques for the printed surface profile, it is possible to perform *in situ* monitoring of the surface and accurately deduce the related properties of the sample. This integration allows for real-time quality assessment during the printing process, enhancing efficiency and reducing the need for post-production testing.

5. Conclusion

An ML approach enables rapid property prediction and process screening for additively manufactured alloys. This study introduced ML-Qvision, a CNN-based model designed to predict the density and tensile properties of laser-DED Monel K-500 alloy from surface morphology profiles. The predicted densities showed a strong correlation with the tested data. In addition to predicting densities and tensile properties from the whole block surface morphology, the model achieved comparable prediction performance by training on single-bead surfaces printed using the same processing parameters. The study provides evidence that printed surfaces with clear melt lines and smooth features correlate with higher density (lower porosity) and higher UTS, consistent with experimental findings. This suggests that the ML model accurately identified important predictive features. The proposed approach paves the way for using ML-Qvision for quick and robust process parameter screening from a single-bead print surface and quality assessment from bulk surfaces. In addition, this approach demonstrates versatility, making it applicable to other metal AM techniques and various material systems.

Acknowledgments

None.

Funding

This work was supported by the Fundamental Research Funds for the Central Universities (Grant No. D5000250077).

Conflict of interest

Wei Fan is an Editorial Board Member of this journal, but was not in any way involved in the editorial and peer-review

process conducted for this paper, directly or indirectly. Separately, other authors declared that they have no known competing financial interests or personal relationships that could have influenced the work reported in this paper.

Author contributions

Conceptualization: Ze Chen, Wei Fan
Formal analysis: Wei Fan
Investigation: Chengcheng Wang, Zhuohong Zeng, Chenyang Zhu
Methodology: Jingwen Gao
Writing–original draft: Ze Chen
Writing–review & editing: Wei Fan

Ethics approval and consent to participate

Not applicable.

Consent for publication

Not applicable.

Availability of data

The data presented in this study are available upon request from the corresponding author.

References

1. Svetlizky D Das M Zheng B *et al.* Directed energy deposition (DED) additive manufacturing: Physical characteristics defects challenges and applications. *Mater Today*. 2021;49:271-295.

   doi: 10.1016/j.mattod.2021.03.020.

2. Ahn DG. Directed energy deposition (DED) process: State of the art. *Int J Precis Eng Manuf Green Tech*. 2021;8:703-742.

   doi: 10.1007/s40684-020-00302-7

3. Guner A, Bidare P, Jiménez A, Dimov S, Essa K. Nozzle designs in powder-based direct laser deposition: A review. *Int J Precis Eng Manuf*. 2022;23:1077-1094.

   doi: 10.1007/s12541-022-00688-1

4. Chen Z, Wang C, Tang C, *et al.* Microstructure and mechanical properties of a Monel K-500 alloy fabricated by directed energy deposition. *Mater Sci Eng A*. 2022;857:144113.

   doi: 10.1016/j.msea.2022.144113

5. Ostolaza M, Arrizubieta JI, Queguineur A, Valtonen K, Lamikiz A, Flores II. Influence of process parameters on the particle-matrix interaction of WC-Co metal matrix composites produced by laser-directed energy deposition. *Mater Des*. 2022;223:111172.

   doi: 10.1016/j.matdes.2022.111172

6. Eisenbarth D, Stoll P, Klahn C, Heinis TB, Meboldt M, Wegener K. Unique coding for authentication and anti-counterfeiting by controlled and random process variation in L-PBF and L-DED. *Addit Manuf*. 2020;35:101298.

   doi: 10.1016/j.addma.2020.101298

7. Stavropoulos P, Foteinopoulos P. Modelling of additive manufacturing processes: A review and classification. *Manuf Rev*. 2018;5:2.

   doi: 10.1051/mfreview/2017014

8. Stavropoulos P, Sabatakakis K, Papacharalampopoulos A, Mourtzis D. Infrared (IR) quality assessment of robotized resistance spot welding based on machine learning. *Int J Adv Manuf Technol*. 2022;119:1785-1806.

   doi: 10.1007/s00170-021-08320-8

9. Wang J, Zhang X, Lu Y. Machine learning in image-based metal additive manufacturing process monitoring and control: A review. *Eng Sci Addit Manuf*. 2025;1(1):8548.

   doi: 10.36922/esam.8548

10. Johnson NS, Vulimiri PS, To AC, *et al.* Invited review: Machine learning for materials developments in metals additive manufacturing. *Addit Manuf*. 2020;36:101641.

    doi: 10.1016/j.addma.2020.101641

11. Zhang M, Sun CN, Zhang X, *et al.* High cycle fatigue life prediction of laser additive manufactured stainless steel: A machine learning approach. *Int J Fatigue*. 2019;128:105194.

    doi: 10.1016/j.ijfatigue.2019.105194

12. Tapia G, Khairallah S, Matthews M, King WE, Elwany A. Gaussian process-based surrogate modeling framework for process planning in laser powder-bed fusion additive manufacturing of 316L stainless steel. *Int J Adv Manuf Technol*. 2018;94:35913603.

    doi: 10.1007/s00170-017-1045-z

13. Zhu K, Fuh JYH, Lin X. Metal-based additive manufacturing condition monitoring: A review on machine learning based approaches. *IEEE/ASME Trans Mechatron*. 2021;27:2495-2510.

    doi: 10.1109/tmech.2021.3110818

14. Qi X, Chen G, Li Y, Cheng X, Li C. Applying neural-network-based machine learning to additive manufacturing: Current applications, challenges and future perspectives. *Engineering*. 2019;5:721-729.

    doi: 10.1016/j.eng.2019.04.012

15. Zhang Y, Yan W. Applications of machine learning in metal powder-bed fusion in-process monitoring and control: Status and challenges. *J Intell Manuf*. 2023;34:2557-2580.

    doi: 10.1007/s10845-022-01972-7

16. Zhang X, Saniie J, Heifetz A. Detection of defects in additively manufactured stainless steel 316L with compact infrared camera and machine learning algorithms. *JOM*. 2020;72:4244-4253.

    doi: 10.1007/s11837-020-04428-6

17. Achillas C, Tzetzis D, Raimondo MO. Alternative production strategies based on the comparison of additive and traditional manufacturing technologies. *Int J Prod Res*. 2017;55:3497-3509.

doi: 10.1080/00207543.2017.1282645

18. Zhang Y, Hong GS, Dongsen Y, *et al.* Extraction and evaluation of melt pool plume and spatter information for powder-bed fusion AM process monitoring. *Mater Des*. 2018;156:458-469.

doi: 10.1016/j.matdes.2018.07.002

19. Herzog T, Brandt M, Trinchi A, *et al.* Process monitoring and machine learning for defect detection in laser-based metal additive manufacturing. *J Intell Manuf*. 2024;35:1407-1437.

doi: 10.1007/s10845-023-02119-y

20. Seddiki K, Saudemont P, Precioso F, *et al.* Cumulative learning enables convolutional neural network representations for small mass spectrometry data classification. *Nat Commun*. 2020;11:1-11.

doi: 10.1038/s41467-020-19354-z

21. Abadi M, Barham P, Chen J, *et al.* TensorFlow: A System for Large-Scale Machine Learning. In: *Proceedings of the 12th USENIX Conference on Operating Systems Design and Implementation*. USENIX Association; 2016. p. 265-283.

22. Lv R, Yuan Z, Lei B. A high-fidelity digital twin predictive modeling of air-source heat pump using FCPM-SBLS algorithm. *J Build Eng*. 2024;87:109082.

doi: 10.1016/j.jobe.2024.109082

23. Xiong Z, Cui Y, Liu Z, Zhao Y, Hu M, Hu J. Evaluating explorative prediction power of machine learning algorithms for materials discovery using k-fold forward cross-validation. *Comput Mater Sci*. 2020;171:109203.

doi: 10.1016/j.commatsci.2019.109203

24. Zhang Y, Ling C. A strategy to apply machine learning to small datasets in materials science. *NPJ Comput Mater*. 2018;4:25.

doi: 10.1038/s41524-018-0081-z

25. Rukundo O. Effects of image size on deep learning. *Electronics*. 2023;12:985.

doi: 10.3390/electronics12040985

26. Richter ML, Byttner W, Krumnack U, Wiedenroth A, Schallner L, Shenk J. (Input) size matters for CNN classifiers. In: Farkaš I, Masulli P, Otte S, Wermter S, editors. *Artificial Neural Networks and Machine Learning - ICANN 2021*. Berlin: Springer International Publishing; 2021. p. 133-144.

doi: 10.1007/978-3-030-86340-1_11

27. Thambawita V, Strumke I, Hicks SA, Halvorsen P, Parasa S, Riegler MA. Impact of image resolution on deep learning performance in endoscopy image classification: An experimental study using a large dataset of endoscopic images. *Diagnostics (Basel)*. 2021;11:2183.

doi: 10.3390/diagnostics11122183

28. Yu H, Yang K, Zhang L, *et al.* Multi-output ensemble deep learning: A framework for simultaneous prediction of multiple electrode material properties. *Chem Eng J*. 2023;475:146280.

doi: 10.1016/j.cej.2023.14628

29. Bessa MA, Bostanabad R, Liu Z, *et al.* A framework for data-driven analysis of materials under uncertainty: Countering the curse of dimensionality. *Comput Methods Appl Mech Eng*. 2017;320:633-667.

doi: 10.1016/j.cma.2017.03.037

30. Ling J, Hutchinson M, Antono E, DeCost B, Holm EA, Meredig B. Building data-driven models with microstructural images: Generalization and interpretability. *Mater Discov*. 2017;10:19-28.

doi: 10.1016/j.md.2018.03.002

31. Gui Y, Aoyagi K, Bian H, Chiba A. Detection classification and prediction of internal defects from surface morphology data of metal parts fabricated by powder bed fusion type additive manufacturing using an electron beam. *Addit Manuf*. 2022;54:102736.

doi: 10.1016/j.addma.2022.102736

32. Thompson SM, Bian L, Shamsaei N, Yadollahi A. An overview of direct laser deposition for additive manufacturing; Part I: Transport phenomena modeling and diagnostics. *Addit Manuf*. 2015;8:36-62.

doi: 10.1016/j.addma.2015.07.001

33. Zhang K, Chen Y, Marussi S, *et al.* Pore evolution mechanisms during directed energy deposition additive manufacturing. *Nat Commun*. 2024;15:1715.

doi: 10.1038/s41467-024-45913-9

34. Kuriya T, Koike R, Mori T, Kakinuma Y. Relationship between solidification time and porosity with directed energy deposition of inconel 718. *J Adv Mech Des Syst Manuf*. 2018;12:Jamdsm0104.

doi: 10.1299/jamdsm.2018jamdsm0104

35. Thanapol P, Lavangnananda K, Bouvry P, Pinel F, Leprévost F. Reducing Overfitting and Improving Generalization in Training Convolutional Neural Network (CNN) Under Limited Sample Sizes in Image Recognition. In: *2020 - 5th International Conference on Information Technology (InCIT)*; 2020. p. 300-305.

doi: 10.1109/incit50588.2020.9310787

36. Brennan MC, Keist JS, Palmer TA. Defects in metal additive manufacturing processes. *J Mater Eng Perform*. 2021;30:4808-4818.

doi: 10.1007/s11665-021-05919-6

37. Mukherjee T, Elmer JW, Wei HL, *et al.* Control of grain structure phases and defects in additive manufacturing of high-performance metallic components. *Prog Mater Sci*. 2023;138:101153.

doi: 10.1016/j.pmatsci.2023.101153

38. Zheng B, Haley JC, Yang N, *et al.* On the evolution of microstructure and defect control in 316L SS components fabricated via directed energy deposition. *Mater Sci Eng A*. 2019;764:138243.

doi: 10.1016/j.msea.2019.138243

39. Lu QY, Wong CH. Additive manufacturing process monitoring and control by non-destructive testing techniques: Challenges and in-process monitoring. *Virtual Phys Prototyp.* 2018;13:39-48.

doi: 10.1080/17452759.2017.1351201

40. He W, Shi W, Li J, Xie H. *In-situ* monitoring and deformation characterization by optical techniques; part I: Laser-aided direct metal deposition for additive manufacturing. *Opt Laser Eng*. 2019;122:74-88.

doi: 10.1016/j.optlaseng.2019.05.020

41. Zhang X, Shen W, Suresh V, *et al. In situ* monitoring of direct energy deposition via structured light system and its application in remanufacturing industry. *Int J Adv Manuf Technol*. 2021;116:959-974.

doi: 10.1007/s00170-021-07495-4

Appendices

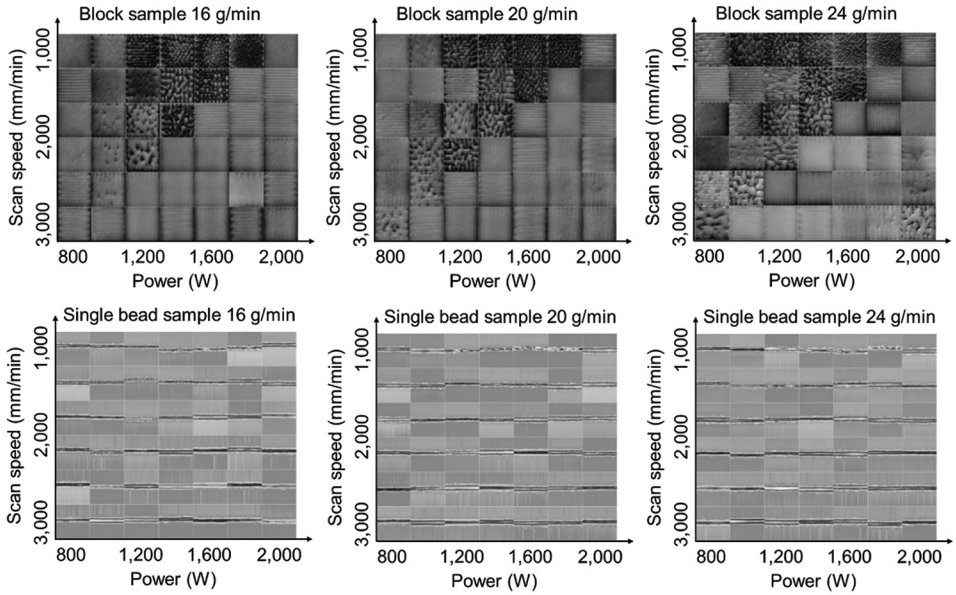

Figure A1. Surface profiles for block samples (top row) and bead samples (bottom row). Each figure represents a unique combination of print parameters, including variations in scanning speed, power, and feed rate.

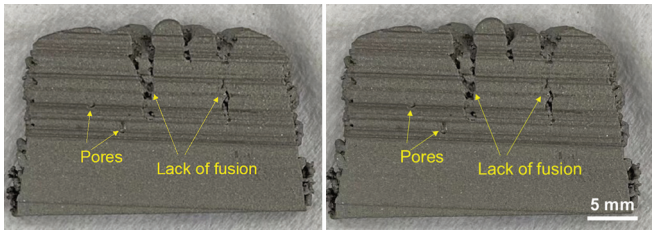

Figure A2. Cross-section of a printed block sample with defects inside the sample, which sacrifices the production of tensile specimens. Scale bar: 5 mm.

ACCSCIENCE PUBLISHING

Engineering Science in Additive Manufacturing

ORIGINAL RESEARCH ARTICLE

Dimensional accuracy and surface roughness of thin-wall geometries in laser powder bed fusion of 316L stainless steel

Tianyu Zhang and Lang Yuan*

Department of Mechanical Engineering, Molinaroli College of Engineering and Computing, University of South Carolina, Columbia, South Carolina, United States of America

Abstract

Thin-wall geometries produced by laser powder bed fusion combine high manufacturing efficiency, design flexibility, and cost-effectiveness for specialized applications. In such features, surface quality directly impacts dimensional accuracy and functional performance. This study investigates the effects of laser power, scan path, build orientation, and nominal gap distance on the top- and vertical-surface roughness, surface features, and dimensional error (DE) of 316L stainless steel thin walls. Optical microscopy was employed to characterize melt pool morphology and surface characteristics. Increasing laser power enlarges melt pools, promotes lateral migration, and induces dross formation on vertical surfaces, raising roughness and DE. Incorporating a contour scan with an inward offset reduces the scanned area, limits melt pool migration, and improves dimensional accuracy. Print orientation has a negligible influence on DE under the tested conditions, while small gaps may close entirely at high power due to large melt pools and migration. Compared to cubes fabricated with identical parameters, thin walls exhibit rougher top surfaces at high power, attributed to reduced track overlap, limited wetting from previous layers, and powder redistribution near vertical edges, whereas vertical-surface behavior remains similar. These findings provide practical guidelines for optimizing dimensional accuracy and surface quality in thin walls through coordinated control of process parameters and geometry.

Keywords: Additive manufacturing; Thin-wall structures; Surface roughness; Dimensional accuracy; Melt pool migration

***Corresponding author:**
Lang Yuan
(langyuan@cec.sc.edu)

Citation: Zhang T, Yuan L. Dimensional accuracy and surface roughness of thin-wall geometries in laser powder bed fusion of 316L stainless steel. *Eng Sci Add Manuf*. 2025;1(3):025340022. doi: 10.36922/ESAM025340022

Received: August 19, 2025

Revised: August 27, 2025

Accepted: August 28, 2025

Published online: September 10, 2025

1. Introduction

Laser powder bed fusion (LPBF) has emerged as one of the leading metal additive manufacturing processes, due to its geometric flexibility and ability to deliver high-performance components.[1-4] It is particularly advantageous for fabricating unique thin-wall structures commonly used in industrial applications, such as turbines and heat exchangers, to achieve optimal performance.[5-8] In such features, side-wall surface roughness and topography critically affect the dimensional accuracy, such as the intervening feature distances[9] and functional and structural performance.[10-12] For example, uneven surfaces increase the contact area between the fluid and the thin-wall structures, thereby influencing heat transfer efficiency in heat exchangers.[13-15]

Likewise, irregular channel morphologies modify fluid resistance and permeability, affecting performance in applications such as turbines and nozzles.[16,17]

Prior research has shown that surface features and roughness are strongly governed by fabrication parameters.[18-20] Feng *et al.*[21] investigated the evolution of surface features in overhang regions of 17-4 precipitation hardening stainless steel. They reported that the dominant downward surface features transitioned from powder adhesion to powder clusters, warped deformation, and dross formation as the overhang angle increased. A similar progression was observed by Zhang and Yuan,[22] where the domination feature shifted from bare melt tracks with partially melted particles to pronounced dross as energy density increased. In related parametric studies, Klingaa *et al.*[23,24] revealed that surface roughness and its variation decrease with the increasing orientation angle due to a reduction of sintered particles on the surfaces. Beyond orientation angles, Gockel *et al.*[25] investigated the effect of contour power and speed on vertical surface roughness in alloy 718 pillar samples, finding that higher scan speeds promote melt pool instability and balling, thereby elevating roughness. With a further understanding of contour–hatch interactions, Patel *et al.*[26] demonstrated that contour and hatch parameters have a comparable impact on side-skin quality in Ti-6Al-4V cylinders through attached particles, spatter, and balling.

To deepen the understanding of the factors influencing dimensional accuracy and surface roughness in thin-wall geometries, previous work has examined pulsed-laser operation, geometric design, alloy composition, and scan strategy. For example, Mumtaz and Hopkinson[27] investigated the use of pulsed lasers on Inconel 625 in LPBF. They revealed that a ramp-down pulsed laser improved the top surface quality but negatively impacted the vertical surfaces due to decreased viscosity and prolonged melting times. In contrast, a suppressed pulsed mode lowers energy input, reduces satellite formation, and improves vertical surfaces. Jamshidinia and Kovacevic[28] reported an inverse relationship between inter-wall gaps and roughness in electron-beam-melted thin plates, attributing higher roughness at small gaps to heat accumulation. Furthermore, surface roughness increased with the thickness of the powder layer between the walls. Examining three alloys, Wu *et al.*[9] demonstrated that thin-wall thickness is alloy-dependent, governed by thermophysical properties, material shrinkage, and inclination angles. Through *in situ* X-ray imaging of multilayer single-track melt pools, Bhatt *et al.*[29] observed that bi-directional multilayer scanning can lead to defects such as lapping and humping, which increase surface roughness.

Although the influence of processing parameters such as power and speed on vertical surface roughness in bulk geometries (e.g., cubes) has been thoroughly investigated, the relationship between surface roughness and dimensional accuracy in thin walls, representing a distinct class of additive manufacturing-preferred features, remains underexplored.[30] Key engineering aspects, including different scanning paths, orientations, and the coupled relationships among wall thickness, inter-wall gap, and dimensional error (DE), have yet to be systematically investigated. This study addresses these gaps by examining how LPBF process conditions affect vertical surface roughness and dimensional accuracy in thin walls and their intervening gaps. The underlying surface features and their formation mechanisms are analyzed to identify the root causes of surface roughness and their implications for dimensional accuracy. Furthermore, while cubic samples are often used for process parameters development, this work further compares melt pool morphology and surface quality between thin-wall and cubic geometries under identical laser parameters, providing insights into optimizing process parameters specifically for thin-wall structures.

2. Methodology

Thin-wall specimens were designed with nominal dimensions of 0.20 mm thickness, 3 mm height (height-to-thickness ratio of 15 to 1), and 10 mm length. Each build group consisted of three thin walls, producing two intervening gaps of equal nominal width. All thin walls were supported on a common base, as shown in Figure 1.

Gas-atomized 316L stainless steel powder (Carpenter Technology, Germany) was used as the feedstock. The chemical composition is presented in Table 1. The particle size distribution ranges from 15 to 45 μm, with an average particle size of 30 μm. Figure 2 shows the powder morphology, emphasizing the sphericity of the powder.

Based on previous studies,[31,32] an unstable cross-sectional ellipse-shaped melt pool transforms into a stable half-ellipse melt pool as the laser power increases from 260 W to 620 W, at a constant laser scanning speed of 1,466.6 mm/s in cube samples. Consequently, the top surface quality improved with increasing power due to the elimination of melt pool instability and discontinuity. To investigate the impact of the melt pool morphology on surface quality in thin walls, the same scan speed (1,466.6 mm/s) was used with three power settings: 260 W, 440 W, and 620 W. For each power, three groups of thin walls were fabricated under identical parameters within each group, shown in Figures 1 and 3. To evaluate the effect of gap distance on dimensional accuracy, three nominal

Table 1. The nominal chemical composition (wt.%) of stainless steel 316L

Element	Iron	Nickel	Chromium	Oxygen	Silicon	Sulfur	Phosphorus	Nitrogen	Carbon	Molybdenum	Manganese	Copper
Wt.%	Balance	12.7	17.7	0.03	0.62	0.01	0.01	0.10	0.02	2.36	0.65	0.02

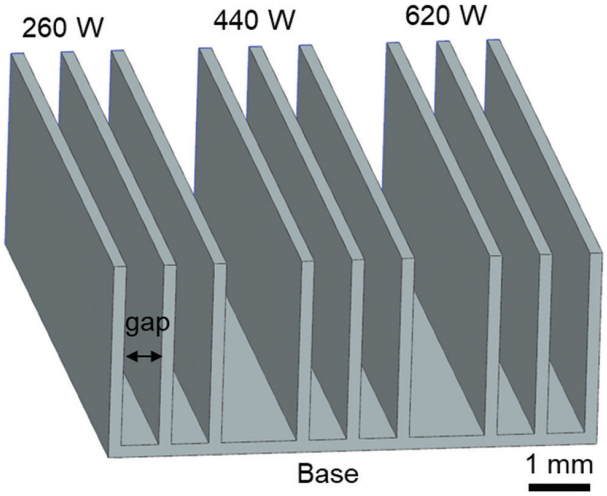

Figure 1. The thin-wall geometry design. Scale bar: 1 mm.

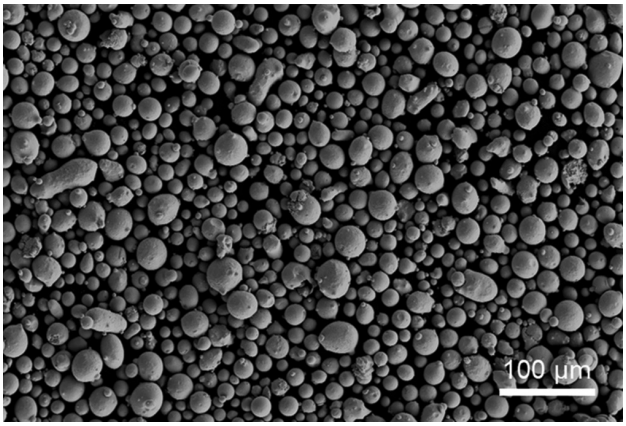

Figure 2. The powder morphology through scanning electron microscopy of 316L stainless steel. Scale bar: 100 µm; magnification: 1000×.

inter-wall gaps were designed, namely, 0.2 mm, 0.4 mm, and 0.6 mm (Figure 3).

As contour scans have been generally applied to control the surface roughness, two scan paths were employed, one with and one without contours. As illustrated in Figure 4A, in Scan Path 1, only hatch scans were utilized, where the hatch scans (red lines) extend to the geometry boundary. In Scan Path 2, the hatch scans offset inward by 50 µm, followed by a contour scan along the boundary using the same power and speed. In both scan paths, successive layers were rotated by 90°. Two orthogonal build orientations relative to the gas-flow/recoating

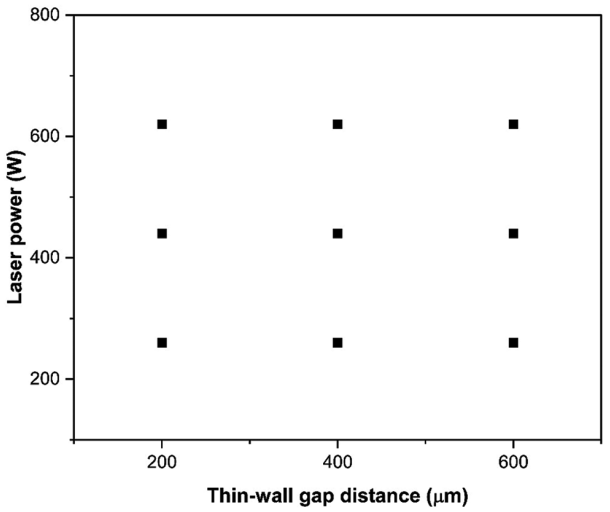

Figure 3. Experimental parametric design

direction were also tested: Parallel and perpendicular, as shown in Figure 4B.

Sample names followed the format P*_G*_S*_R, where P is power (W), G is gap distance (µm), S is scanning path, and R denotes perpendicular orientation to gas flow (e.g., P260_G200_S1_R indicates 260 W, Scan Path 1, 200 µm gap, and perpendicular orientation).

All builds were produced on an AconityMIDI LPBF system (United States) equipped with a single-mode fiber laser (maximum power 1,000 W). The laser spot diameter and hatch spacing were fixed at 100 µm, with a layer thickness of 30 µm. Laser scans were conducted with skywriting to minimize the impact of laser acceleration and deceleration.[33] During the printing, an argon atmosphere with oxygen levels below 100 ppm was maintained. Each condition was printed in duplicates to validate repeatability. All specimens were fabricated at ambient room temperature.

To assess the melt pool behavior on the thin-wall samples, top-down optical images were captured using the Keyence VHX 5000 digital optical microscope (Japan). An example is shown in Figure 5A. The samples were then sectioned perpendicular to the top layer track direction, followed by potting, polishing, and etching using a solution of 75 vol% hydrochloric acid and 25 vol% nitric acid for 15 s. Images were then acquired, offering a detailed depiction of the surface features of the thin-wall geometry,

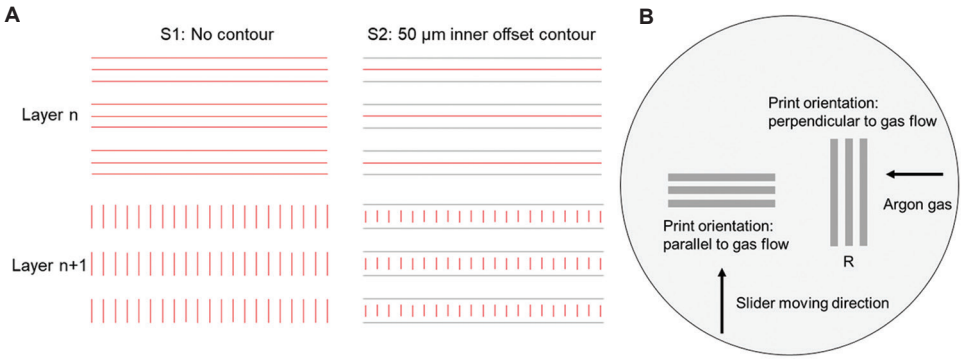

Figure 4. Illustration of printing setup: (A) different scan paths and (B) different print orientations

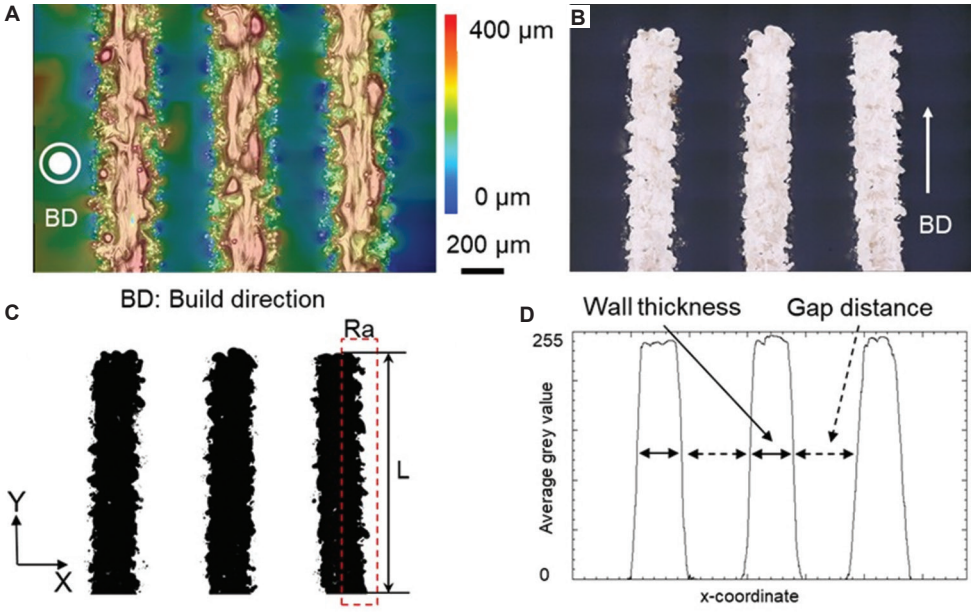

Figure 5. Characterization of thin-wall structures. (A) The topography of thin walls from the top-down view, (B) cross-sections, (C) the binarized image of (B), and (D) the continuous distribution map of average grey value along the x-axis based on (C). Scale bar: 200 μm; magnification: 500×.

as shown in Figure 5B. The images were then binarized to distinguish thin-wall and gap regions, as exemplified in Figure 5C. An average continuous grey value distribution along the x-axis was calculated and shown in Figure 5D. The average wall thickness or gap distance was measured from the average grey value 128 (half of the highest value 256). Multiple measurements were taken to account for measurement error with the standard deviation, as marked in Figure 5D. In addition to the dimensional measurements, surface roughness of vertical surfaces, quantified by Ra (arithmetic mean deviation of the roughness profile from the mean line), was calculated from the side-wall profile outlines, as expressed in Equation I:

$$Ra = \frac{1}{L}\int_0^L \left|x(y)\right| dy \quad \text{(I)}$$

where L means the nominal length of the outline, and x(y) denotes the local deviation of the surface from the mean profile position along the vertical (Y) direction. For example, to calculate the Ra of the vertical line highlighted in Figure 5C, the x-coordinate of the outline of the surface was obtained directly from the binarized cross-sectional image. Then, x(y) was calculated by subtracting the mean values of all x values from the local x-coordinate. For each process condition, the Ra values for six surface outlines were calculated, and the mean value and its standard deviation are reported. Note that the top-surface Ra was not quantified in this study due to the inherent strong stochastic variations caused by local melt pool instability under thin-wall conditions.

For comparison, 10 × 10 × 10 mm^3 cube samples were printed using the same laser parameters with a hatch

spacing of 100 μm and a hatch-contour offset of 50 μm (Scan Path 2) and characterized identically to thin walls.

3. Result and discussion

DE, defined by the difference between the measured and the nominal dimensions, is utilized to reflect the dimensional accuracy. For example, the thin-wall DE equals the measured wall thickness minus the constant design wall thickness, and the intervening gap DE is calculated by the measured gap distance minus the nominal gap distance (e.g., 200, 400, or 600 μm). In this study, DE analysis was limited to wall thickness and inter-wall gaps, as these directly govern functional accuracy. DE values associated with wall height, which is primarily dictated by top-surface variations and layer count, were not considered. Given the large height-to-thickness ratio (>15) in this study, fluctuations in wall height are negligible compared with errors in vertical wall thickness and gap dimensions. Figure 6 summarizes the DE of printed thin walls and the intervening gaps across all build conditions. The interpretation of the results is discussed in detail, regarding the effects of power, scanning path, sample orientation, and gap distance.

3.1. Role of laser power on surface roughness and dimensional accuracy

As shown in Figure 6, thin-wall DE generally increases with laser power, while gap DE decreases proportionally, reflecting the increase in thin-wall thickness. As the laser power increased, the cross-sectional melt pool morphology transformed from a small ellipse shape to a larger half-ellipse shape with a larger overlapping region of surrounding melt pools. To examine the details, Figure 7 depicts the melt pool morphology and surface features under G600_S2 conditions. Meanwhile, the melt pool areas (calculated by the pixel size in each figure and decided by the melt pool width and depth) and the vertical surface Ra are presented in Table 2. The average melt pool area increased significantly from 3,842 μm² to 9,662 μm² as the

Table 2. Melt pool area and surface roughness of vertical surface for G200_S2 thin walls

Thin walls	Melt pool area (μm²)	Ra (μm)
P260_G200_S2	3,842±1,452	13.94±0.79
P440_G200_S2	6,399±996	19.32±0.36
P620_G200_S2	9,662±2,481	21.35±4.43

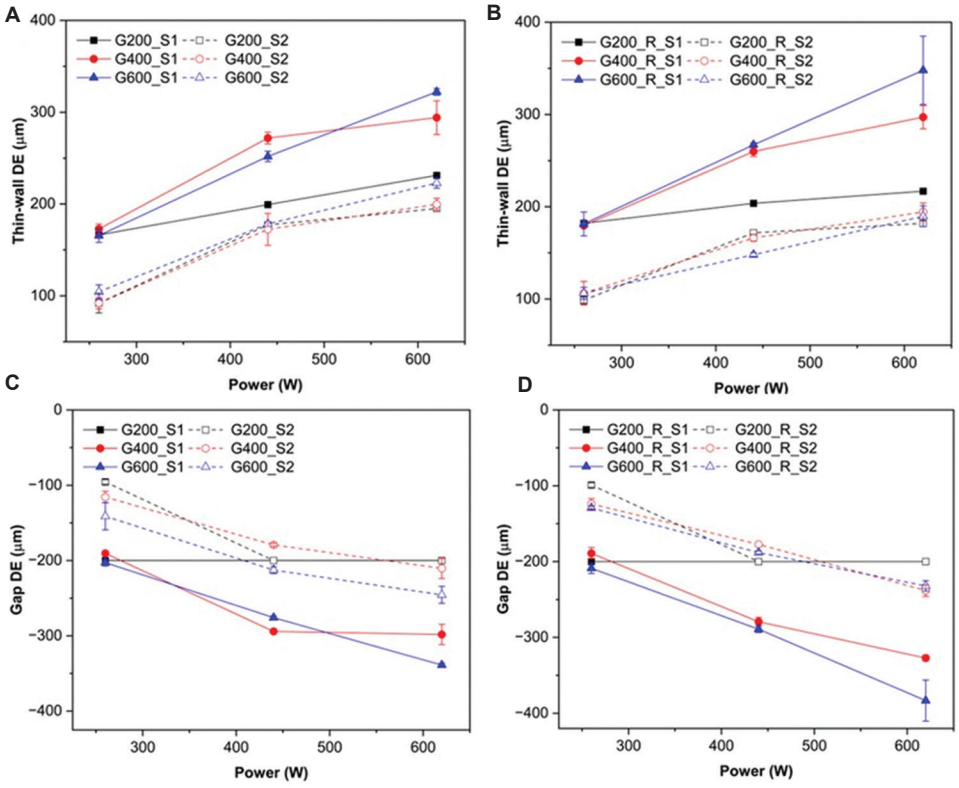

Figure 6. The DE as a function of the laser power. (A) Thin-wall DE for samples printed parallel to the gas flow, (B) thin-wall DE perpendicular to the gas flow, (C) DE of intervening gaps for samples printed parallel to the gas flow, and (D) DE of intervening gaps perpendicular to the gas flow.
Abbreviation: DE: Dimensional error.

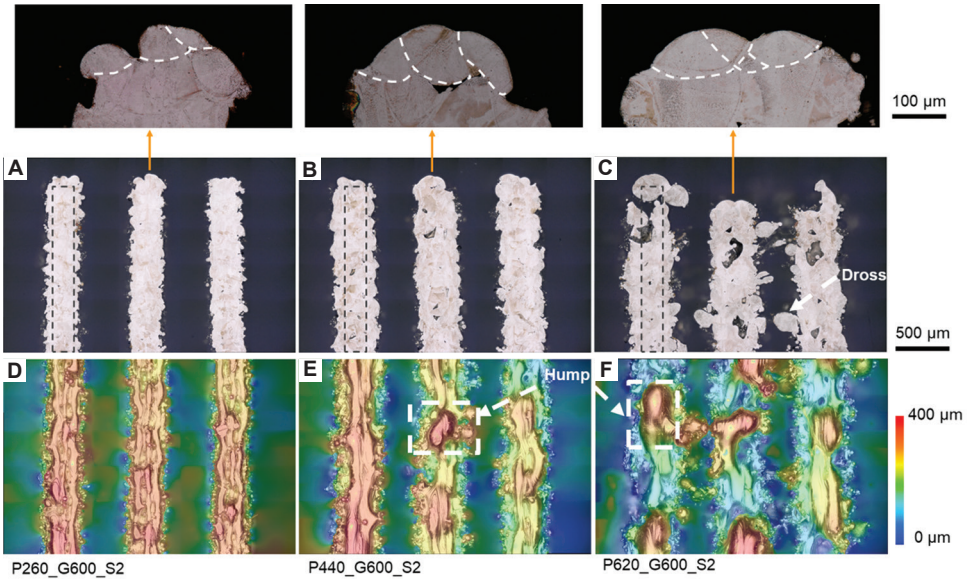

Figure 7. Thin-wall cross-sections (A-C) and topography for top surfaces (D-F) under group G600_S2 (the dashed line indicates the nominal geometry). (A and D) P260_G600_S2, (b and e) P440_G600_S2, (C and F) P620_G600_S2. Scale bar: 500 μm; magnification: 500×. The top row shows a zoomed-in view of the middle wall in each group. Scale bar: 100 μm; magnification: 1000×.

laser power increased from 260 W to 620 W. The increase in the melt pool size under higher laser power directly led to an increase in thin-wall thickness.

Higher power also alters vertical surface morphology. Enlarged melt pools promoted instability and spherical protrusion formation, increasing Ra from 13.94 μm to 21.35 μm. With low laser power at 260 W, a stable melt pool led to a better surface finish, where the melt tracks and partially attached particles dominated the side surface features (Figure 7A). As the power increases, the surface roughness worsens. Protrusions, as seen in Figure 7B and C, are typically referred to as the dross.[34,35] They dominate the side surface quality at 620 W conditions. The formation of dross is attributed to the asymmetric heat dissipation near the surface region. Since powder between walls impedes heat dissipation, it resulted in an asymmetric and large melt pool.[36] As the powder is absorbed by the melts and the physical support from the powder base diminishes, the enlarged melt pool migrates toward it, promoting the formation of dross.[37] As observed in Figure 7C, dross protruded beyond the intended thin-wall geometry, further supporting that the melt pool migration is responsible for its formation and the resultant rough surfaces. Consequently, average wall thickness rose from 304.3 μm to 422.9 μm (DE = 104.3 μm to 222.9 μm) between 260 W and 620 W.

3.2. Role of scan path

As shown in Figure 6A and B, thin-wall DEs manufactured without contour scanning (Scan Path 1, solid lines, ranging from 165.6 μm to 347.8 μm) consistently surpassed those produced with a 50 μm offset distance contour (Scan Path 2, dashed lines, ranging from 91.9 μm to 199.7 μm). Consequently, the gap DE without contour was constantly lower (solid lines in Figure 6C and D). As an example, with a fixed gap distance of 400 μm, the samples with Scan Path 1 (Figure 8A-C) have thicker walls than those under the Scan Path 2 (Figure 8D-F). The application of an inner offset, as shown in (Figure 4A) Scan Path 2 (S2), minimizes the scanning region and naturally compensates for the geometry expansion (melt pool extents out of the laser scanning paths). Larger overlaps with the inner hatches also restrict the melt pool migration, leading to less dross formation and better dimensional accuracy in the final products. In addition, the increase in thin-wall DE with rising laser power is evident in Figure 8. With and without contour scans, a more stable melt pool under low power conditions is preferred to minimize the expansion beyond the nominal geometry (Figure 8A and D). In contrast, higher power produces larger melt pools that not only increase wall thickness but also promote dross formation, thereby degrading surface quality (Figure 8C and D).

Such observation strongly indicates that the application of an inner offset can enhance printing precision in thin-wall geometries. Without or with a low offset distance, the melt pool naturally increases the thin-wall thickness. In contrast, an excessive offset distance may lead to a lack of fusion between contour and hatch scans, which could compromise the mechanical properties of the product.[22] The optimal contour offset is therefore strongly dependent

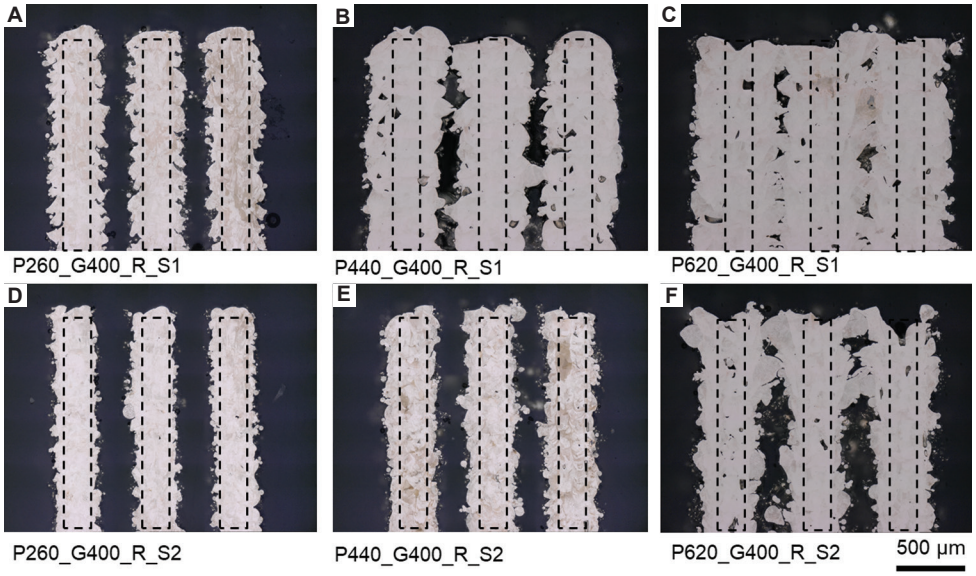

Figure 8. (A-F) Cross-section views of thin walls under different process conditions and scan paths. Scale bar: 500 µm; magnification: 500×.

on laser parameters. To balance vertical surface quality and fusion integrity, a relatively low energy density that is achieved through reduced power or increased scan speed should be used to suppress dross formation. Meanwhile, the offset distance should not exceed the combined melt pool widths of contour and hatch scans. For example, when using a low-power contour followed by low-power hatching, a smaller offset is recommended to avoid lack-of-fusion defects. In contrast, higher hatch energy density (e.g., high power) warrants both increased offset and contour power to mitigate dross formation from the hatch scans.

3.3. The impact of print orientation

Figure 6A and B show the thin-wall DEs printed in two orientations, both exhibiting a consistent increasing trend with laser power and a close proximity in the values of each data point across both orientations. A similar pattern is also observed in Figures 6C and D for gap DEs. The differences in thin-wall DEs between orientations are quantified in Figure 9A, which compares corresponding data points from Figure 6A and B. Across all gap sizes (black square = 200 µm, red dot = 400 µm, blue triangle = 600 µm) and both scan paths (solid and dashed lines), DE differences exhibited both negative and positive values and ranged from –33.2 µm to +33.2 µm. The maximal relative error was also < 9.5% of the overall thin-wall DE range (91.9–347.8 µm in Figure 6), including the measurement errors and process instabilities. This suggests that print orientation has only a limited influence on the dimensional accuracy of both thin walls and gaps.

To further validate the significance of print orientation statistically, a three-way analysis of variance was conducted on the DE data based on Scan Path 1 (data shown in Figure 6), with laser power (three levels), gap distance (three levels), and printing orientation (two levels) as factors. The results are summarized in Table 3. Both laser power (p<0.0001) and scan path (p=0.0053) were found to be statistically significant contributors to DE (the underlying mechanisms are discussed in Sections 3.1 and 3.3), while print orientation is not significant (p=0.5841). These findings quantitatively confirm the experimental observation that orientation effects are negligible in this study.

Both the magnitude and variability (error bars) of DEs increased with higher laser power for both thin walls and gaps, as shown in Figure 9A and B. This increase is likely due to greater melt pool instability at elevated power levels. Figure 10 presents cross-sectional views of thin walls fabricated with the two print orientations without contour scanning. Within each column of Figure 10, comparable dimensional accuracies and geometrical features are observed, with differences of < 4% between orientations, aligning with the trends in Figure 9. For example, at 260 W conditions, the surfaces are dominated by the melt track mitigations (Figure 10A and D). As the laser power increased, the wall gaps diminished, with voids randomly distributed between walls (Figure 10C and D). Although previous studies have reported that the slider recoating direction impacts the powder size distribution,[38,39] the results in this study suggest that both recoating direction and gas flow direction exert limited influence on the final geometric accuracy of thin walls and intervening gaps.

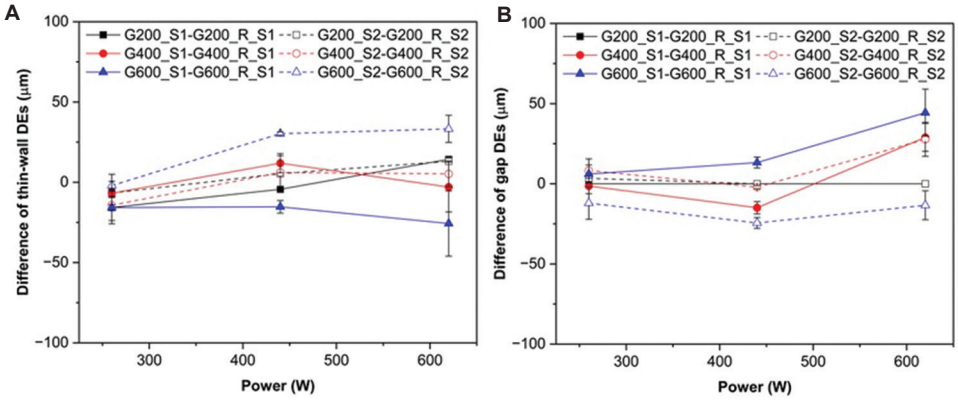

Figure 9. The difference in DEs between the two printing orientations. (A) Thin-wall thickness and (B) gap distance.
Abbreviation: DE: Dimensional error.

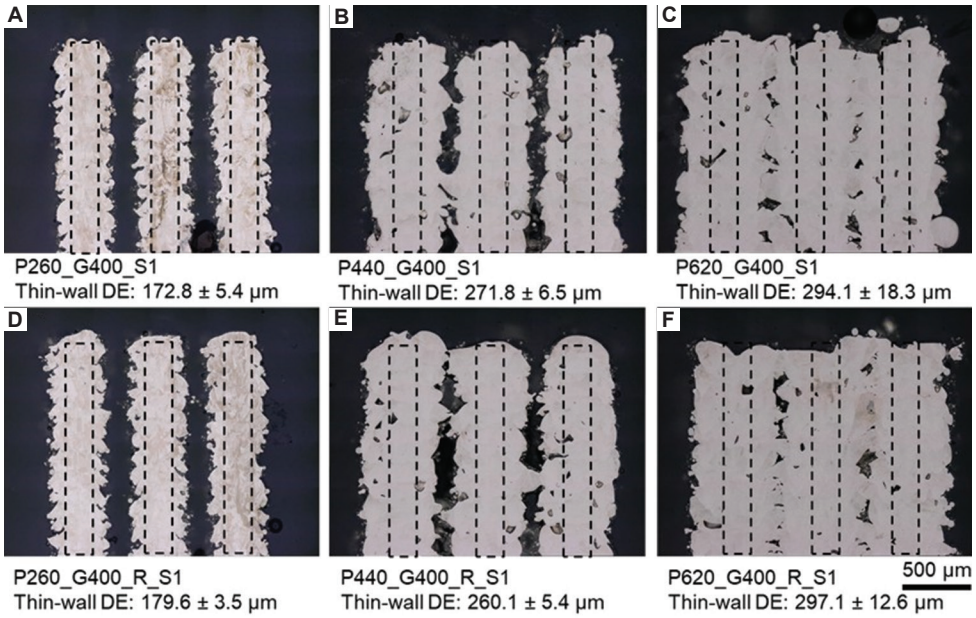

Figure 10. (A-D) Optical images of samples from cross-section view with print orientations parallel or perpendicular to the gas flow direction. Scale bar: 500 μm; magnification: 500×.
Abbreviation: DE: Dimensional error.

Table 3. Three-way analysis of variance for dimensional error

Source	Sum of squares	Degrees of freedom	Mean square	*F*	*p* (Prob > *F*)
Laser power	37,085.5	2	18,542.8	28.98	<0.0001
Gap distance	10,718.5	2	5,359.3	8.38	0.0053
Orientation	202.5	1	202.5	0.32	0.5841

3.4. The impact of gap distance

Three nominal gap distances (0.2 mm, 0.4 mm, and 0.6 mm) were examined to assess their influence on dimensional accuracy. Figure 11 shows the increase in melt pool migration as the gap distance widens under P440_R_S1 and P620_R_S1 conditions. At the smallest gap (0.2 mm in Figure 11A and D), adjacent walls coalesce at high laser power, restricting inward melt pool expansion. Under such conditions, the designed gap is eliminated entirely, representing a functional failure of the part. As the nominal gap increases, the constraint on melt pool

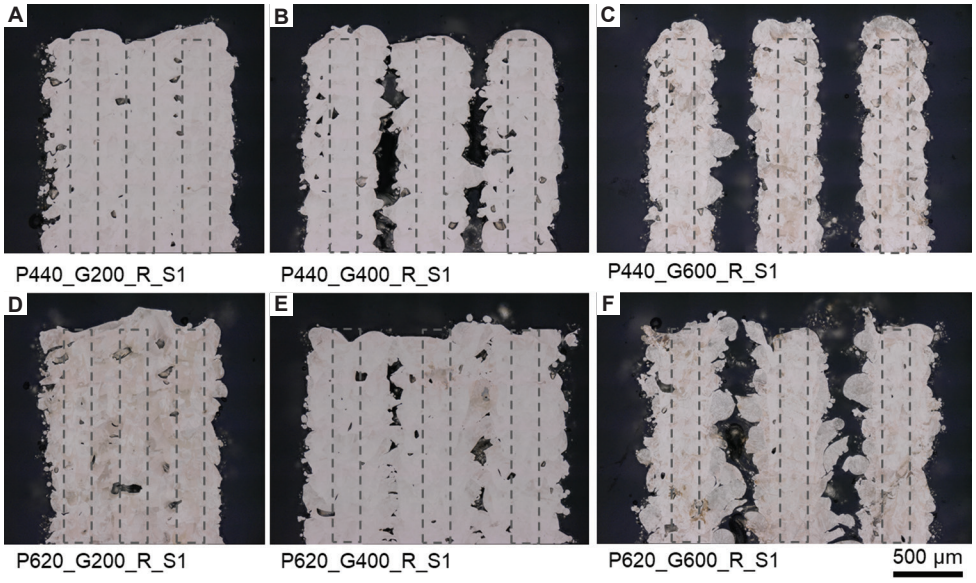

Figure 11. (A-F) Cross-sectional view under different nominal gap distances. Scale bar: 500 µm; magnification: 500×.

migration decreases, enabling more pronounced lateral flow and dross formation along the vertical surfaces. This increased thin-wall DE and slowed gap widening, resulting in smaller gap DE values (Figure 6C and D).

Given that the absolute values of DE at G200 were lower, but the gap was closed, Figure 12 presents the relative DEs for the gaps printed with two different orientations. At large gaps and high power, for example, P620_G600_R_S1 (Figure 11F), the actual gap was 216.7 µm, corresponding to an absolute DE of –383.3 µm (–64% relative DE). At smaller gaps, absolute DE decreased (–200 µm at G200), but relative DE reached –100% due to wall coalescence. This highlights that the final actual gap distance is determined by the extent of melt pool migration (especially at high power conditions) and the nominal gap distance, suggesting that a suitable design tolerance should be considered based on print conditions. To further provide general guidance, the final gap distance can be estimated as (Equation II):

$$D_g = D_N - D_{offset} - D_w \quad \text{(II)}$$

where the D_g denotes the final gap distance between thin walls, D_N is the nominal gap distance, D_{offset} is the contour offset distance (negative value as inward offset and positive value for outward offset) or the distances of the outermost hatch line from the nominal wall boundary if no contour is applied, and D_w is the melt pool width of the contour scan or outermost hatch track.

Under an ideal scenario, when the inward offset equals the melt pool width, $D_g = D_N$, resulting in minimal error. Note that, at high energy density (e.g., 620 W, 1,466.6 mm/s in this study), contour scans promote dross formation, which leads to large variations in surface roughness (exemplified in Figure 7C). To reduce the gap distance error and its variability, low energy density conditions with reduced laser power are recommended (e.g., 260W, 1,466.6 mm/s in Figure 7A). However, when hatch scans are conducted at high power conditions, low-energy contour scans may not fully overlap with the hatch tracks. In such cases, an increased inward offset distance would be applied to accommodate the extension of the hatch melt pool beyond the contour track.

While the present work was conducted at a fixed scan speed, hatch spacing, and layer thickness, the representative process parameters under different laser power illustrate three representative regimes of vertical-surface formation:[40] (i) Stable melt pools dominated by partially melted particles, (ii) Highly unstable melt pools where lateral migration produces dross, and (iii) Intermediate states between the two. Although the exact roughness values and wall thickness will vary under different process windows, the underlying mechanisms by which melt pool behaviors govern vertical surface quality and accuracy remain broadly valid. In this context, the guideline to reduce the DE, such as adopting an appropriate inward contour offset based on the melt pool behavior, is applicable to different process conditions.

The data in Figure 12A and B show minimal differences between orientations, reinforcing the earlier conclusion that print orientation plays a limited role. Moreover, the impact of the nominal wall distance on heat accumulation and melt pool temperature (expansion and migration) has been found to be limited due to the

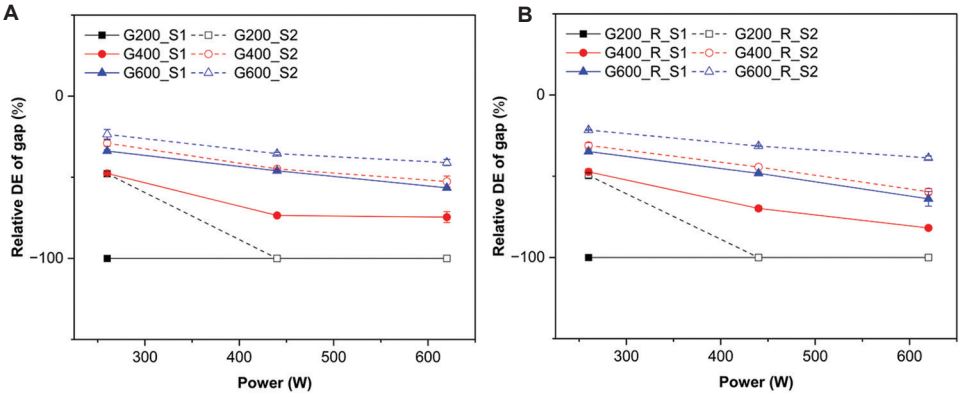

Figure 12. Relative DE of thin-wall structures: (A) gap printed parallel to the gas flow direction, and (B) gap printed perpendicularly to the gas flow direction
Abbreviation: DE: Dimensional error.

similarity of melt pool dimensions in different nominal gap distance conditions.

3.5. Surface characteristics in thin walls and cubes

In addition to vertical surfaces, the top-surface quality and dimensional accuracy are also important performance metrics, yet are rarely discussed. As seen in Figures 7, 8, 10, and 11, the 260 W condition produces insufficient energy input, resulting in disconnected melt tracks and valley formation that dominate the top surface. At higher laser powers, such as 440 W and 620 W, large humps, approximately 200 µm in height, form on the top surface and dominate the top surface feature, as marked in Figure 7E and F. These humps originate from melt pool migration from previous tracks, which disrupts uniform powder distribution in the subsequent layers, reduces melt pool stability for the later tracks, and degrades surface quality.[2,32]

In contrast to previous studies,[31,32] where higher laser power improved top-surface finish in cube samples, the present work observes opposite behavior for thin walls. To verify these differences, 10 × 10 × 10 mm^3 cube samples were fabricated using identical parameters. As shown in Figure 13, the larger melt pool and overlapping region in cube samples reduce the melt pool instability and smooth the top surface (Ra decreasing from 31.27 µm to 12.06 µm) with the laser power increases (260 W to 620 W). This improvement arises from enhanced wetting between melt pools and prior layers, aided by larger contact areas, lower viscosity, and longer solidification times that promote gravity-driven leveling and centrifugal Marangoni flow (under low sulfur and oxygen content in stainless steel[41]). In addition, repeated remelting from subsequent high-power scans further smooth the surface by eliminating the top surface

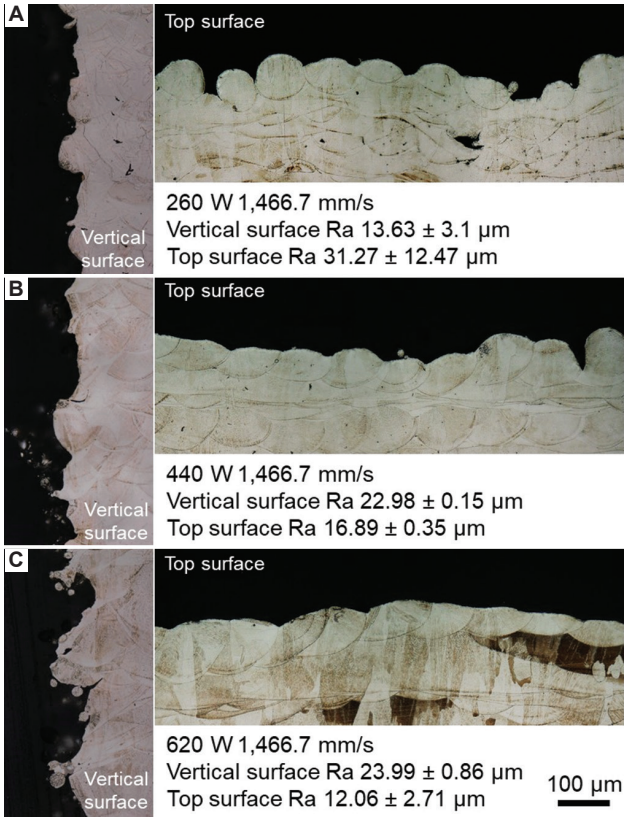

Figure 13. The cross-sectional views of the top and vertical surface regions of the cube samples. (A) 260W 1,466.7 mm/s, (B) 440 W 1,466.7 mm/s, (C) 620 W 1,466.7 mm/s. Scale bar: 100 µm; magnification: 1000×.

humps. However, these stabilizing and remelting effects are absent in thin-wall builds. The limited number of scan tracks amplifies track-to-track interactions and produces large variations in melt pool dimensions due to pronounced local geometry changes, which in turn alter solidification conditions. Melt pool migration, combined

with possible powder denudation at vertical edges, could also lead to uneven powder distribution near thin walls, further disrupting melt pool stability at the top surface and resulting in a poorer top surface finish, as shown in Figure 7C and F. Increasing wall thickness promotes melt pool stabilization as the melt progresses, explaining why cube samples exhibit improved top surfaces under higher power while thin walls do not.

For vertical surfaces, however, both cubes and thin walls exhibited similar trends: Ra increased with laser power due to dross formation, rising from 13.61 μm to 23.99 μm in cubes and from 13.94 μm to 21.35 μm in thin walls. This similarity suggests that cube samples can serve as a useful proxy for optimizing vertical-surface quality and dimensional accuracy in thin-wall manufacturing. Notably, surface quality and dimensional accuracy are more critical on vertical surfaces compared to top surfaces in thin-wall applications.

Overall, achieving better dimensional accuracy in thin-wall geometries and their intervening gaps requires careful integration of print conditions and design parameters. As sufficient energy for hatch scans must be maintained to achieve fully dense walls, an appropriate hatch-contour offset can minimize thin-wall DE. To achieve a desired intervening gap dimension, the melt pool expansion and migration need to be accommodated with the designed contour offset distance, particularly in high-power contour scans. This is especially important when rougher surface quality is acceptable or preferred for specific applications.

4. Conclusion

This study systematically examined the effects of laser power, scanning paths, print orientation, and nominal gap distance on surface quality and dimensional accuracy in thin-wall structures of 316L stainless steel in LPBF. Dominant surface characteristics and their formation mechanisms were identified for both top and vertical surfaces and direct comparisons were made with cube geometries fabricated under identical process conditions.

Higher power and larger scanned areas increased vertical surface roughness and DE due to melt pool migration and dross formation. Dross protrusions at wall edges provided direct evidence of lateral melt pool movement along vertical surfaces. In addition, applying a modest inward hatch offset with a contour scan reduced melt pool migration, suppressed dross formation, and improved dimensional accuracy. Offsets that are too small permit overbuilding, while excessive offsets risk lack-of-fusion defects; optimal values should reflect laser energy density and melt pool width.

Orientation relative to the gas-flow/recoating direction had a negligible influence on dimensional accuracy or surface quality under the tested conditions. The actual gap size was jointly determined by melt pool migration and the nominal design. Small gaps may close entirely under high-power conditions, while larger gaps remain open but are reduced by lateral melt flow. Appropriate design tolerances are essential, especially for high-energy scans.

In high-power conditions, cube samples exhibited smoother top surfaces than thin walls due to improved melt pool wetting, larger overlap, and repeated remelting. Thin walls lack these stabilizing effects due to denudation and powder redistribution near vertical edges, leading to reduced top-surface quality. Vertical surface roughness trends, however, were similar in both geometries, making cubes a suitable proxy for optimizing side-wall conditions.

These results clarify the interplay between processing parameters, geometry, and feature spacing in determining surface roughness and dimensional accuracy in thin-wall LPBF. They provide a framework for localized process control, enabling geometry-specific optimization of surface quality and dimensional accuracy to meet functional requirements in complex additive manufacturing components.

Acknowledgments

None.

Funding

The authors would like to acknowledge the support from the National Science Foundation under grant number 2029425, the U.S. Department of Commerce, the National Institute of Standards and Technology under grant number 70NANB23H030, and the U.S. Department of Energy, Savannah River National Laboratory under contract no. 89303321CEM000080.

Conflict of interest

Lang Yuan is an Editorial Board Member of this journal but was not in any way involved in the editorial and peer-review process conducted for this paper, directly or indirectly. Separately, the other author declared that he/she has no known competing financial interests or personal relationships that could have influenced the work reported in this paper.

Author contributions

Conceptualization: Lang Yuan
Formal analysis: Tianyu Zhang
Funding acquisition: Lang Yuan
Investigation: Tianyu Zhang
Methodology: All authors
Supervision: Lang Yuan
Writing–original draft: Tianyu Zhang
Writing–review & editing: All authors

Ethics approval and consent to participate

Not applicable.

Consent for publication

Not applicable.

Availability of data

All data analyzed have been presented in the paper.

References

1. Yakout M, Cadamuro A, Elbestawi MA, Veldhuis SC. The selection of process parameters in additive manufacturing for aerospace alloys. *Int J Adv Manuf Technol*. 2017; 92(5-8):2081-2098.

   doi: 10.1007/s00170-017-0280-7

2. Jing G, Wang Z. Defects, densification mechanism and mechanical properties of 300M steel deposited by high power selective laser melting. *Addit Manuf*. 2021;38:101831.

   doi: 10.1016/j.addma.2020.101831

3. Gu DD, Meiners W, Wissenbach K, Poprawe R. Laser additive manufacturing of metallic components: Materials, processes and mechanisms. *Int Mater Rev*. 2012;57(3):133-164.

   doi: 10.1179/1743280411Y.0000000014

4. DebRoy T, Wei HL, Zuback JS, *et al*. Additive manufacturing of metallic components - Process, structure and properties. *Prog Mater Sci*. 2018;92:112-224.

   doi: 10.1016/j.pmatsci.2017.10.001

5. Rastan H, Abdi A, Hamawandi B, Ignatowicz M, Meyer JP, Palm B. Heat transfer study of enhanced additively manufactured minichannel heat exchangers. *Int J Heat Mass Transf*. 2020;161:120271.

   doi: 10.1016/j.ijheatmasstransfer.2020.120271

6. Tian B, Chang W, Santi E, Li C, Zhang T, Yuan L. Two-Phase Milli/Microchannel Cooling for SiC Power Module Using Dielectric Fluid Coolant. In: *2021 IEEE Electric Ship Technologies Symposium, ESTS 2021*. 2021.

   doi: 10.1109/ESTS49166.2021.9512324

7. Chakraborty A, Tangestani R, Esmati K, Sabiston T, Yuan L, Martin É. Mitigating inherent micro-cracking in laser additively manufactured RENÉ 108 thin-wall components. *Thin Walled Struct*. 2023;184:110514.

   doi: 10.1016/J.TWS.2022.110514

8. Kaur I, Singh P. State-of-the-art in heat exchanger additive manufacturing. *Int J Heat Mass Transf*. 2021;178:121600.

   doi: 10.1016/J.IJHEATMASSTRANSFER.2021.121600

9. Wu Z, Narra SP, Rollett A. Exploring the fabrication limits of thin-wall structures in a laser powder bed fusion process. *Int J Adv Manuf Technol*. 2020;110(1-2):191-207.

   doi: 10.1007/s00170-020-05827-4

10. Mehrabi O, Seyedkashi SMH, Moradi M. Functionally graded additive manufacturing of thin-walled 316L stainless steel-inconel 625 by direct laser metal deposition process: Characterization and evaluation. *Metals (Basel)*. 2023;13(6):1108.

    doi: 10.3390/met13061108

11. Feng Z, Wang G, Hao Z, *et al*. Influence of scale effect on surface morphology in laser powder bed fusion technology. *Virtual Phys Prototyp*. 2024;19(1):e2336157.

    doi: 10.1080/17452759.2024.2336157

12. Poncelet O, Marteleur M, van der Rest C, *et al*. Critical assessment of the impact of process parameters on vertical roughness and hardness of thin walls of AlSi10Mg processed by laser powder bed fusion. *Addit Manuf*. 2021;38:101801.

    doi: 10.1016/J.ADDMA.2020.101801

13. Thompson SM, Aspin ZS, Shamsaei N, Elwany A, Bian L. Additive manufacturing of heat exchangers: A case study on a multi-layered Ti-6Al-4V oscillating heat pipe. *Addit Manuf*. 2015;8:163-174.

    doi: 10.1016/j.addma.2015.09.003

14. Zhang Z, Huang Y, Rani Kasinathan A, *et al*. 3-Dimensional heat transfer modeling for laser powder-bed fusion additive manufacturing with volumetric heat sources based on varied thermal conductivity and absorptivity. *Opt Laser Technol*. 2019;109:297-312.

    doi: 10.1016/j.optlastec.2018.08.012

15. Lee J, Hussain A, Ha J, *et al*. Mechanical properties of Ti-6Al-4V thin walls fabricated by laser powder bed fusion. *Addit Manuf*. 2024;94:104484.

    doi: 10.1016/J.ADDMA.2024.104484

16. Zhang J, Wang H. Magnetically driven internal finishing of AISI 316L stainless steel tubes generated by laser powder bed fusion. *J Manuf Process*. 2022;76:155-166.

    doi: 10.1016/j.jmapro.2022.02.009

17. Favero G, Berti G, Bonesso M, *et al*. Experimental and numerical analyses of fluid flow inside additively manufactured and smoothed cooling channels. *Int Commun*

Heat Mass Transfer. 2022;135:106128.

doi: 10.1016/J.ICHEATMASSTRANSFER.2022.106128

18. Cao L, Li J, Hu J, Liu H, Wu Y, Zhou Q. Optimization of surface roughness and dimensional accuracy in LPBF additive manufacturing. *Opt Laser Technol*. 2021;142:107246.

doi: 10.1016/j.optlastec.2021.107246

19. Wang D, Yang Y, Yi Z, Su X. Research on the fabricating quality optimization of the overhanging surface in SLM process. *Int J Adv Manuf Technol*. 2013;65(9-12):1471-1484.

doi: 10.1007/s00170-012-4271-4

20. Lu Z, Tan MJ, Zhang Y, An J, Chua CK. Impact of machine factors on the surface quality of parts fabricated via powder bed fusion. *Eng Sci Addit Manuf*. 2025;1(2):025240014.

doi: 10.36922/ESAM025240014

21. Feng S, Kamat AM, Sabooni S, Pei Y. Experimental and numerical investigation of the origin of surface roughness in laser powder bed fused overhang regions. *Virtual Phys Prototyp*. 2021;16(S1):S66-S84.

doi: 10.1080/17452759.2021.1896970

22. Zhang T, Yuan L. Interaction of contour and hatch parameters on vertical surface roughness in laser powder bed fusion. *J Mater Res Technol*. 2024;32:3390-3401.

doi: 10.1016/j.jmrt.2024.08.170

23. Klingaa CG, Dahmen T, Baier S, Mohanty S, Hattel JH. X-ray CT and image analysis methodology for local roughness characterization in cooling channels made by metal additive manufacturing. *Addit Manuf*. 2020;32:101032.

doi: 10.1016/j.addma.2019.101032

24. Klingaa CG, Dahmen T, Baier-Stegmaier S, Mohanty S, Hattel JH. Investigation of the roughness variation along the length of LPBF manufactured straight channels. *Nondestr Test Eval*. 2020;35(3):304-314.

doi: 10.1080/10589759.2020.1785445

25. Gockel J, Sheridan L, Koerper B, Whip B. The influence of additive manufacturing processing parameters on surface roughness and fatigue life. *Int J Fatigue*. 2019;124:380-388.

doi: 10.1016/j.ijfatigue.2019.03.025

26. Patel S, Rogalsky A, Vlasea M. Towards understanding side-skin surface characteristics in laser powder bed fusion. *J Mater Res*. 2020;35(15):2055-2064.

doi: 10.1557/jmr.2020.125

27. Mumtaz KA, Hopkinson N. Selective laser melting of thin wall parts using pulse shaping. *J Mater Process Technol*. 2010;210(2):279-287.

doi: 10.1016/j.jmatprotec.2009.09.011

28. Jamshidinia M, Kovacevic R. The influence of heat accumulation on the surface roughness in powder-bed additive manufacturing. *Surf Topogr*. 2015;3(1):014003.

doi: 10.1088/2051-672X/3/1/014003

29. Bhatt A, Huang Y, Leung CLA, *et al*. In situ characterisation of surface roughness and its amplification during multilayer single-track laser powder bed fusion additive manufacturing. *Addit Manuf*. 2023;77:103809.

doi: 10.1016/j.addma.2023.103809

30. Vu HM, Meiniger S, Ringel B, *et al*. Investigation on surface characteristics of wall structures out of stainless steel 316L manufactured by laser powder bed fusion. *Prog Addit Manuf*. 2024;9(6):2041-2060.

doi: 10.1007/S40964-023-00559-9/FIGURES/15

31. Zhang Z, Zhang T, Sun C, Karna S, Yuan L. Understanding melt pool behavior of 316L stainless steel in laser powder bed fusion additive manufacturing. *Micromachines (Basel)*. 2024;15(2):170.

doi: 10.3390/mi15020170

32. Zhang T, Yuan L. Melt pool characteristics on surface roughness and printability of 316L stainless steel in laser powder bed fusion. *Rapid Prototyp J*. 2024.

doi: 10.1108/RPJ-02-2024-0078

33. Tian Y, Tomus D, Rometsch P, Wu X. Influences of processing parameters on surface roughness of Hastelloy X produced by selective laser melting. *Addit Manuf*. 2017;13:103-112.

doi: 10.1016/j.addma.2016.10.010

34. Charles A, Bayat M, Elkaseer A, Thijs L, Hattel JH, Scholz S. Elucidation of dross formation in laser powder bed fusion at down-facing surfaces: Phenomenon-oriented multiphysics simulation and experimental validation. *Addit Manuf*. 2022;50:102551.

doi: 10.1016/j.addma.2021.102551

35. Charles A, Elkaseer A, Paggi U, Thijs L, Hagenmeyer V, Scholz S. Down-facing surfaces in laser powder bed fusion of Ti6Al4V: Effect of dross formation on dimensional accuracy and surface texture. *Addit Manuf*. 2021;46:102148.

doi: 10.1016/j.addma.2021.102148

36. Wrobel R, Del Guidice L, Scheel P, *et al*. Influence of wall thickness on microstructure and mechanical properties of thin-walled 316L stainless steel produced by laser powder bed fusion. *Mater Des*. 2024;238:112652.

doi: 10.1016/j.matdes.2024.112652

37. Zhang T, Yuan L. Understanding surface roughness on vertical surfaces of 316 L stainless steel in laser powder bed fusion additive manufacturing. *Powder Technol*. 2022;411:117957.

doi: 10.1016/j.powtec.2022.117957

38. Mussatto A, Groarke R, O'Neill A, Obeidi MA, Delaure Y, Brabazon D. Influences of powder morphology and spreading parameters on the powder bed topography uniformity in

powder bed fusion metal additive manufacturing. *Addit Manuf*. 2021;38:101807.

doi: 10.1016/j.addma.2020.101807

39. Averardi A, Cola C, Zeltmann SE, Gupta N. Effect of particle size distribution on the packing of powder beds: A critical discussion relevant to additive manufacturing. *Mater Today Commun*. 2020;24:100964.

doi: 10.1016/j.mtcomm.2020.100964

40. Snyder JC, Thole KA. Understanding laser powder bed fusion surface roughness. *J Manuf Sci Eng Trans ASME*. 2020;142(7):1071003.

doi: 10.1115/1.4046504/1074958

41. Leung CLA, Marussi S, Towrie M, Atwood RC, Withers PJ, Lee PD. The effect of powder oxidation on defect formation in laser additive manufacturing. *Acta Mater*. 2019;166:294-305.

doi: 10.1016/j.actamat.2018.12.027

ACCSCIENCE PUBLISHING

Engineering Science in Additive Manufacturing

ORIGINAL RESEARCH ARTICLE

Three-dimensional (3D) bioprinting of coral-polyp bio-skin using ultrashort and biofunctionalized peptide bioinks for transplantation on coral skeletons

Alexander U. Valle-Pérez[1,2], Manola Moretti[1,2], Panayiotis Bilalis[1,2], Sebastian Overmans[3], Kyle J. Lauersen[3], Christian Baumgartner[4], and Charlotte A. E. Hauser[1,2,4]*

[1]Laboratory for Nanomedicine, Division of Biological and Environmental Science and Engineering (BESE), King Abdullah University of Science and Technology, Thuwal, Mecca Province, Kingdom of Saudi Arabia

[2]Computational Bioscience Research Center (CBRC), King Abdullah University of Science and Technology, Thuwal, Mecca Province, Kingdom of Saudi Arabia

[3]Laboratory for Sustainable & Synthetic Biotechnology, Division of Biological and Environmental Sciences and Engineering (BESE), King Abdullah University of Science and Technology (KAUST), Thuwal, Mecca Province, Kingdom of Saudi Arabia

[4]Institute of Health Care Engineering with European Testing Center of Medical Devices, Graz University of Technology (TU Graz), Graz, Styria, Austria

***Corresponding author:**
Charlotte A.E. Hauser
(charlotte.hauser-funke@tugraz.at)

Citation: Valle-Pérez AU, Moretti M, Bilalis P, *et al.* Three-dimensional (3D) bioprinting of coral-polyp bio-skin using ultrashort and biofunctionalized peptide bioinks for transplantation on coral skeletons. *Eng Sci Add Manuf*. 2025;1(3):025270017. doi: 10.36922/ESAM025270017

Received: July 5, 2025

Revised: August 12, 2025

Accepted: August 19, 2025

Published online: September 18, 2025

Abstract

There is growing interest in applying 3D printing technologies to environmental restoration, particularly for fabricating bio-inspired artificial reefs and printing coral skeletons to attract fish and support coral growth and survival. More recently, tissue engineering and 3D bioprinting strategies have been employed to develop biomimetic biomaterials that more closely replicate the natural coral microenvironment, including the incorporation of coral symbionts, to aid restoration efforts. In this study, we investigate the use of diverse ultrashort peptide- and biofunctionalized peptide-based bioinks to support bail-out polyp re-settlement and subsequent micropropagation. Among the 13 bioinks examined, eight demonstrated polyp biocompatibility and stability under seawater conditions. We focused on two Scleractinia species, *Stylophora pistillata* and *Pocillopora verrucosa*, and optimized a culture strategy for microencapsulated bail-out polyps following re-settlement, comparing a single-entity versus clustered-entity approach. These advancements lay the groundwork for polyp transplantation using biomimetic biomaterials. The top-performing bioinks were selected based on bioink underwater stability, polyp biocompatibility, and suitability for 3D bioprinting of polyps onto coral skeletons. This led to the development of a coral-inspired, polyp-containing bio-skin graft designed to promote coral tissue regeneration. Here, we report the first results demonstrating the use of bioinks for coral polyp microencapsulation and 3D bioprinting with ultrashort peptide-based bioinks to support coral regeneration and transplantation on coral skeletons.

Keywords: 3D bioprinting; Artificial coral tissue; Ultrashort peptide bioinks; Biofunctionalized bioinks; Coral polyp microencapsulation; Coral polyp transplantation; Polyp bail-out

1. Introduction

Corals are crucial organisms within coral reefs, which are among the most biodiverse marine ecosystems, despite covering only about 1% of the ocean floor. The presence and health of corals are key indicators of ecosystem resilience or vulnerability. However, climate change and anthropogenic pressures, such as rising sea surface temperatures and the metabolic costs of growth, place corals at substantial risk. This vulnerability also endangers many associated species. During heat waves and ocean acidification events, corals often expel their symbiotic microalgae, causing coral bleaching. Therefore, there is an urgent need to strengthen coral resilience through both conventional restoration practices and the development of innovative biotechnological approaches.

Corals maintain a symbiotic relationship with zooxanthellae, symbiotic microalgae residing within their tissues, which are responsible for the coral's vivid pigmentation. Through photosynthesis and the metabolism of nitrates and phosphates, these algae provide essential nutrients to their coral hosts. However, corals are highly sensitive to environmental fluctuations, especially abrupt temperature increases. During a heat wave, when water temperatures rise and remain elevated for prolonged periods, this relationship is disrupted, leading to a reduction in the symbiotic microalgae population (coral bleaching). As a result, the coral loses its color, exposing its whitish calcium carbonate skeleton. At this stage, the coral becomes vulnerable to starvation and diseases. While recovery is possible if conditions improve, prolonged stress often leads to mortality. In addition, research has shown that a single coral colony can host multiple species of microalgae.[1,2]

The term "polyp bail-out" refers to the detachment of individual polyps from a coral as a response to environmental stress and as a form of asexual reproduction in certain species, such as reef-building (scleractinian) corals.[3,4] Recently, the bail-out has been used as a model system in coral biology, with single-detached polyps utilized in applications such as the development of polyp-on-chip microfluidic devices for polyp culture and development.[5-7] The bail-out process has been previously described in the literature.[8] One method of inducing bail-out is changing osmolarity to stress the coral, which results in the detachment of individual polyps from the underlying coral skeleton. After bail-out, polyps disperse, settle in new locations, and initiate skeletogenesis and calcification.[3] However, successful re-settlement remains challenging, as only a small proportion of polyps reattach, and many show no signs of settlement even 3 months after bail-out.[4] In addition, the viability of polyps post-bail-out varies depending on the coral species and experimental conditions.[5,8]

The amphiphilic self-assembling peptides used in this study are compounds with both hydrophobic and hydrophilic regions. These peptides assemble into fibers and subsequently into 3D fibrous supramolecular structures in the form of hydrogels via non-covalent interactions. When ionic solutions such as phosphate-buffered saline (PBS) are added to aqueous peptide solutions, fiber formation is accelerated, reducing gelation times to minutes or even seconds, depending on the specific peptide sequence and concentration. For example, peptide-based bioinks B1–B3, employed in the present study and previously reported in other research, gelate within 1–3 min when dissolved in water at a concentration of 10 mg/mL and subsequently mixed with 10× PBS.[9] Thus, gelation time is strongly dependent on peptide concentration. These properties emphasize amphiphilic peptides as ideal bioink materials for extrusion-based 3D bioprinting, allowing for instantaneous layer-by-layer printing of cell-laden constructs.

Furthermore, the attachment of bioactive cellular motifs to ultrashort peptide compounds yields biofunctionalized peptides with enhanced functionality, which can induce cellular responses such as cell adhesion, proliferation, and differentiation. However, these biofunctionalized peptides often exhibit reduced or inhibited self-assembling capabilities. To overcome this limitation, strictly defined ratios of biofunctionalized peptides can be mixed with ultrashort self-assembling peptides, thereby enabling nanofiber and hydrogel formation. This approach results in functional scaffold microenvironments suitable for cell culture and 3D bioprinting applications.

The technique of 3D bioprinting is expected to play a crucial role in future coral reef restoration efforts.[10] This technology has already been widely applied in biomanufacturing human cell-laden organs and tissues, such as skin and cartilage, as well as in the microencapsulation of microalgae-based structures.[11-14] More recently, the integration of 3D bioprinting, bioinks, and biomaterials has been explored for coral restoration.[15,16] Advancements include the 3D printing of microalgal structures using silk/hydroxypropyl methylcellulose ink mixtures, coral propagation through additive manufacturing, the development of bacteria-based materials for coral restoration, bioprinting symbionts to create coral-like skeletons, and the fabrication of microenvironments resembling natural corals, among other applications.[13,14,17-21] Furthermore, biomaterials have been engineered with antioxidants to mitigate coral bleaching and promote coral

cell adhesion.[22,23] Therefore, developing next-generation bioinks and biomaterials incorporating symbiotic microorganisms through biofabrication could significantly enhance ongoing coral restoration efforts. Future research may focus on employing 3D bioprinting and bioinks to accelerate coral tissue regeneration *in situ*.

In the current research, we combined ultrashort peptide-based bioinks, 3D bioprinting, and bail-out polyps to create a coral-inspired bio-skin biomaterial for coral tissue regeneration. Polyps were microencapsulated in 3D scaffolds using various biocompatible bioinks, and their potential for sustaining bail-out polyps and enabling micropropagation was assessed. Two species of bail-out polyps, *Stylophora pistillata* and *Pocillopora verrucosa*, were microencapsulated, and two culture methods were explored: individual units and clustered entities. Eight out of 13 investigated bioinks (Table 1) facilitated polyp re-settlement and supported micropropagation. Polyps cultured as clustered entities formed interconnections, retained their green and red fluorescence, and produced surrounding tissue, all indicative of micropropagation. The viscoelastic properties of the most effective bioinks were subsequently evaluated under seawater conditions to assess their suitability for field applications. After identifying the top-performing bioink in terms of underwater stability and polyp biocompatibility, we optimized a robotic-assisted extrusion-based 3D bioprinting system to create a structurally stable coral bio-skin that supported viable polyps for up to 10 days.

2. Materials and methods

2.1. Peptide synthesis

Thirteen individual ultrashort peptides and biofunctionalized peptide derivatives were synthesized to develop bioinks (Table 1). All synthesized peptides were N-terminally acetylated (Ac–peptide) and C-terminally amidated (peptide–NH_2) to prevent the influence of terminal charges (Ac–peptide–NH_2). The synthesized peptide sequences were as follows: Ac-Ile-Cha-Cha-Lys-NH_2 (IZZK), Ac-Ile-Ile-Cha-Lys-NH_2 (IIZK), Ac-Ile-Ile-Phe-Lys-NH_2 (IIFK), Ac-Phe-Phe-Ile-Lys-NH_2 (FFIK), Ac-Phe-Ile-Ile-Lys-NH_2 (FIIK), Ac-Leu-Ile-Val-Ala-Gly-Lys-NH_2 (LIVAGK), Ac-Ile-Val-Cha-Lys-NH_2 (IVZK), Ac-Ile-Val-Phe-Lys-NH_2 (IVFK), Ac-Ile-Ile-Cha-Lys-Gly-Gly-Gly-Arg-Gly-Asp-Ser-NH_2 (IIZKGGGRGDS), Ac-Ile-Ile-Cha-Lys-Gly-Gly-Gly-Phe-Hyp-Gly-Glu-Arg-NH_2 (IIZKGGGFOGER), Ac-Ile-Ile-Phe-Lys-Gly-Gly-Gly-Tyr-Ile-Gly-Ser-Arg-NH_2 (IIFKGGGYIGSR), Ac-Ile-Ile-Phe-Lys-Gly-Gly-Gly-Arg-Gly-Asp-Ser-NH_2 (IIFKGGGRGDS), and Ac-Ile-Cha-Cha-Glu-NH_2 (IZZE).

Peptides were synthesized using solid-phase peptide synthesis on a CS136X synthesizer (CSBIO, US). After synthesis, peptides were cleaved from the resin using a mixture of 95% trifluoroacetic acid, 2.5% triisopropylsilane, and 2.5% water at room temperature for 2 h. Precipitation was initiated by adding cold diethyl ether to the peptide solution, which was then kept overnight at 4°C. The precipitated peptides were collected by centrifugation and subsequently purified by reverse-phase high-performance

Table 1. Bioink scaffold formulations and stability under seawater conditions

Bioink	Peptide sequence 1	Peptide sequence 2	Mixing ratio	Total final concentration (mg/ml)	Assembled under seawater conditions?	Stability under seawater conditions (days)	Remarks after 30 days in seawater
B1	IIZK	NA	NA	10	Yes	>30	100% of samples remained stable
B2	IZZK	NA	NA		Yes	>30	100% of samples remained stable
B3	IIFK	NA	NA		Yes	>30	100% of samples remained stable
B4	FFIK	NA	NA		Yes	<14	100% of samples dissolved
B5	FIIK	NA	NA		Yes	>30	75% of samples remained stable; partial dissolution observed
B6	LIVAGK	NA	NA		Yes	<24	100% of samples dissolved
B7	IVZK	NA	NA		Yes	>30	75% of samples remained stable; partial dissolution observed
B8	IVFK	NA	NA		Yes	>30	75% of samples remained stable; partial dissolution observed
B9	IIZKGGGRGDS	IIZK	1:1		Yes	>30	75% of samples remained stable; partial dissolution observed
B10	IIZKGGGFOGER	IIZK	1:1		Yes	>30	50% of samples remained stable
B11	IIFKGGGYIGSR	IIFK	2:1		Yes	>30	75% of samples remained stable; partial dissolution observed
B12	IIFKGGGRGDS	IIFK	2:1		Yes	>30	25% of samples remained stable
B13	IZZE	NA	NA		No	0	100% of samples dissolved

liquid chromatography on a C-18 column (2–98% acetonitrile over 15 min) at a flow rate of 20 mL/min, achieving yields of over 60%. Peptides were stored in sealed Falcon containers at −80°C, and peptide aliquots were prepared for experiments. Chemical structures were verified through mass spectrometry.

2.2. Bioink scaffold formation

The ultrashort peptides exhibited self-assembling scaffold capabilities even in the presence of water. Peptide solutions were prepared by dissolving the selected ultrashort peptide powder in 900 µL of ultrapure cell culture-grade water. In contrast, biofunctionalized peptides lacked self-assembling capability and were therefore mixed with ultrashort peptide powder before dissolution. The mixed peptide powders were weighed and dissolved in 900 µL of ultrapure, cell culture-grade water, as described in Table 1. Hydrogel scaffold formation was accelerated by adding PBS at a 1:10 ratio (PBS to peptide solution).

2.3. Polyp bail-out

The coral species *S. pistillata* and *P. verrucosa* were obtained from the Al Fahal reef (22.305118 N; 38.964568 E). Small fragments (1 cm long) were collected and used for polyp extraction through the high-salinity seawater method. The fragments were placed in a container with 3 L of isosmotic seawater connected to a peristaltic pump. High-salinity seawater was then introduced into the container at a flow rate of 126 mL/h for 24 h. This high-salinity seawater was prepared by adding sodium chloride to 3 L of Red Sea water (40 PSU) until a total salinity of 74 PSU was reached. The resulting osmotic stress caused the detachment of individual polyps. Further details on the bail-out methodology can be found in the literature.[5,6]

2.4. Polyp microencapsulation and 3D bioprinting

Peptides and peptide mixtures were prepared at a concentration of 10 mg/mL (w/v) using a 1:10 ratio, as shown in Table 1. Each peptide solution was prepared by dissolving the weighted peptide powder in 900 µL of ultrapure cell culture-grade water. Hydrogel biomaterials were then generated by carefully placing either a single polyp or a cluster of five nearby polyps (not in direct contact) into a 96-well plate containing 135 µL of peptide solution. Immediately after adding the polyp(s), 15 µL of PBS was introduced into each well to initiate microencapsulation. Filtered seawater (FSW; using a 20 µm filter) was subsequently added until the biomaterials were completely submerged. The hydrogels were maintained on a magnetic stirrer with temperature control (IKA® RCT basic, IKA-Werke GmbH & Co. KG, Germany) at 27°C under aquarium lights (Radion XR15 G5 Blue, controlled by the Mobius app including the acclimation feature software, EcoTech Marine, US) with a 12 h light–dark cycle at 50% light intensity.

2.5. Polyp culture

The hydrogel biomaterials were cultured under semi-batch conditions, with FSW replaced every 2 days. A thermometer was used throughout the experiment to monitor and prevent overheating of the system.

2.6. Viscoelastic characterization

Hydrogels were prepared by mixing 135 µL of peptide solution with 15 µL of PBS inside a 9 mm internal-diameter glass ring. FSW was then added until the hydrogels were fully covered. After 12 h, the glass rings were removed, and the samples were monitored for 30 days. The viscoelastic properties of the peptide hydrogels – including stiffness, viscosity, and thixotropy – were analyzed using an Ares-G2 Rheometer (TA Instruments, US) equipped with an advanced Peltier system (Waters, TA Instruments, APS, US). Stiffness was measured using an 8 mm parallel plate with a 1.5 mm gap between the upper and lower plates. Three consecutive tests were performed:

- Time-sweep: 5 min at an angular frequency of 1 rad/s and a strain of 0.1%.
- Frequency-sweep: 0.1–100 rad/s at 0.1% strain.
- Amplitude-sweep: strain gradually increased from 0.01% to 100% at 1 rad/s.

Oscillation strain curve data were interpolated using the trace interpolation tool in Origin Pro (version 2022b, OriginLab Corporation, US). Thixotropic properties were measured at an angular frequency of 1 rad/s and a sampling rate of 1 point/s. An initial strain of 0.1% was applied for 5 min, after which the hydrogel was exposed to 11 oscillation cycles alternating between 100% (1 min) and 0.1% strain (10 min). The total test duration was 3,600 s per sample. Stability studies consisted of monitoring the samples relative to their initial state.

2.7. Phase-contrast microscopy

Polyp hydrogel biomaterials were analyzed using a Leica DMI3000 B inverted microscope equipped with a 6-position M25 objective turret (Leica Camera AG, Germany). Illumination was provided by a 12 V/100 W halogen lamp with a manual field diaphragm. The microscope was operated in phase-contrast mode. Images were processed and analyzed using ImageJ software (version 1.54p; imagej.net) to evaluate the micropropagated tissue.

2.8. Epifluorescence microscopy

Biomaterials were examined using the EVOS epifluorescence microscope (EVOS epifluorescence

microscope, Thermo Fisher Scientific, US). Images were captured using a 5-position automated objective turret with a focus mechanism capable of sub-micron resolution (0.150 μm). Epifluorescence microscopy was performed using the following excitation/emission filter sets: Green fluorescence (Ex: 470 nm, Em 525 nm) and chlorophyll (Ex: 585 nm, Em 624 nm). Phase-contrast mode was also employed. All filters were sourced from Thermo Fisher Scientific (US). Image analysis of the micropropagated tissue was performed using ImageJ software.

2.9. Spectrophotometry

Polyp biomaterials were analyzed using a PHERAstar FS microplate reader (PHERAstar FS Microplate Reader, BMG Labtech, Germany). The fluorescence intensity of each well was measured through bottom scanning using specific optical modules. Native polyp green fluorescence was assessed at 485 nm excitation and 520 nm emission, while symbiotic chlorophyll fluorescence was measured at 570 nm excitation and 680 nm emission. These wavelengths were selected based on previously reported values for the coral fluorescence.[24] The optimal focal height was determined automatically, and total fluorescence intensity was measured with 10 flashes per scan point. Data were analyzed using the MARS Data Analysis Software (MARS Data Analysis Software, BMG Labtech, Germany).

2.10. MINI-PAM II photosynthesis yield analyzer

The health of zooxanthellae (the symbiotic microalgae within corals) was examined using a MINI-PAM II instrument (Heinz Walz GmbH, Germany). The instrument utilizes a red light-emitting diode (655 nm) to measure photosynthetic yield. Variable chlorophyll fluorescence of photosystem II (PSII) was assessed using pulse amplitude modulation (PAM) fluorometry (Mini-PAM-II, Heinz Walz GmbH, Germany). To ensure that PSII was in an open state, samples were dark-adapted for 10 min following exposure to aquarium lights. The maximum photochemical efficiency (Fv/Fm) was then calculated using Equation I, where Fm and F_0 represent the maximal and minimal PSII fluorescence of dark-acclimated microencapsulated zooxanthellae, respectively. This method was adapted from previously reported procedures for PAM measurements.[25,26]

$$\left(\frac{F_v}{F_m}\right)=\left(\frac{F_m-F_0}{F_m}\right) \quad \text{(I)}$$

2.11. 3D bioprinting

Bioprinting experiments were conducted using a robotic 3D bioprinter (Dobot, China). The bioprinter comprised a five-degrees-of-freedom robotic arm, a custom-designed dual-coaxial nozzle, microfluidic pumps, and a stirring hot plate (IKA® RCT basic, XXX, IKA-Werke GmbH & Co. KG, Germany). The robotic arm was controlled via Repetier-Host, while printing files were designed in SolidWorks and converted to g-code using the Slic3r and Repetier software (version 1.4.18, Hot-World GmbH & Co. KG, Germany). The dual-coaxial nozzle was fabricated following a previously reported design,[11] with slight modifications for polyp-laden bioprinting. It consisted of two outlets and one inlet. The first nozzle comprised an 18G nozzle outlet (1,270 μm outer, 965 μm inner diameter) for the peptide solution and a 21G nozzle inlet (820 μm outer, 510 μm inner diameter) for the PBS solution. The 21G nozzle was connected to the 18G nozzle, where ionic-driven hydrogel crosslinking occurred. Together, they formed the first part of the dual-coaxial nozzle. The second part consisted of a single 18G nozzle (1,270 μm outer, 965 μm inner diameter).

After the bail-out, *S. pistillata* coral polyps formed spheroids between 200 and 600 μm in diameter, and the reported nozzle dimensions were found to be suitable for extrusion without compromising polyp viability (Figure S1). The nozzle configuration enabled smooth extrusion of bail-out polyps while minimizing clogging risks associated with polyp size. Polyps were successfully extruded without evidence of bursting or clogging.

Commercial microfluidic pumps were operated in automated pulse mode using a square-wave function.[27] The dual-coaxial nozzle was connected to the pumps through three 1,000 μm-diameter microfluidic tubes (Figure S1). Based on the reported viscosity[11] and polyp dimensions, optimized pumping flow rates were determined: 40–45 μL/min (peptide solution), 15–20 μL/min (5× PBS), and 30 μL/min (FSW with polyps). All 3D bioprinting experiments were performed at 27°C. Notably, the interaction between PBS and the peptide solution inside the nozzle resulted in hydrogel formation required for extrusion-based bioprinting.[11] Efficient extrusion of individual polyp units depended on maintaining the optimized flow rates established in the present study.

For cell extraction, a 1 ml syringe filled with FSW was used to gently flush cells through the tubing. Coral skeletons were treated with bleach overnight, washed three times with water, immersed in ethanol for 1 h, and washed again three times with FSW. The coral skeletons were then left in water overnight and subsequently stored at room temperature. Tweezers were sterilized using a Panasonic MLS-3781L autoclave (Japan) at 121°C for 15 min.

2.12. Statistical analysis

Statistical analyses and data visualization were performed using OriginPro 2022b software (OriginLab Corporation, US). Multiple comparisons of population means were

conducted using Tukey's test, with statistical significance set at $p<0.05$.

3. Results and discussion

3.1. Polyp microencapsulation and 3D bioprinting

An overview of the developed strategy and the coral anatomy is shown in Figure 1. The polyp bioink microencapsulation and 3D bioprinting strategy, based on ultrashort peptide-derived bioinks for coral regeneration and polyp culture, is shown in Figure 1A. These bioinks have been extensively used in cell culture and tissue engineering with human cells.[11,28] The primary advantages of formulating bioinks with synthetic peptide-based hydrogels include their bioinertness, biocompatibility, ability to self-assemble into 3D structures, low immunogenicity, minimal batch-to-batch variation compared to naturally derived bioinks, and inherent tendency to accelerate fiber formation in the presence of PBS.[29] In particular, ultrashort self-assembling peptides, recognized for their low immunogenicity, have been widely applied in medicine and, more recently, in environmental technologies such as underwater adhesives.[11,30] Therefore, employing self-assembling peptides composed of natural amino acids offers an interesting strategy for underwater environmental applications. Although recent research has highlighted the successful development of calcium carbonate-based coral-like skeletons and the 3D bioprinting of symbiont-laden bionic coral hydrogels,[13,19,31,32] there are, to date, no reports describing the development of a polyp–symbiont-laden 3D bioprinted biomimetic interphase. Here, we underline the emerging role of ultrashort peptide-based bioinks, in combination with biofunctionalized bioinks, for developing coral-like microenvironments that could serve as a groundwork for future coral tissue transplantation technologies.

A schematic representation of coral polyp anatomy (Figure 1B) and images of a native *S. pistillata* coral polyp (Figure 1C and D) are provided to illustrate the biological context. In these images, green fluorescence highlights the polyp tissue (Figure 1C), while red fluorescence identifies the symbiotic microalgae (Figure 1D).

We evaluated multiple peptide bioink scaffolds for structurally stability under seawater conditions. Bail-out polyps were then microencapsulated in hydrogel-based bioinks to develop polyp-inspired biomaterials. Comparative experiments were performed using two polyp species (*S. pistillata* and *P. verrucosa*), with both individual polyps and clustered configurations tested to enhance survival. The resulting biomaterials were monitored *in vitro* for 45 days, with morphology and

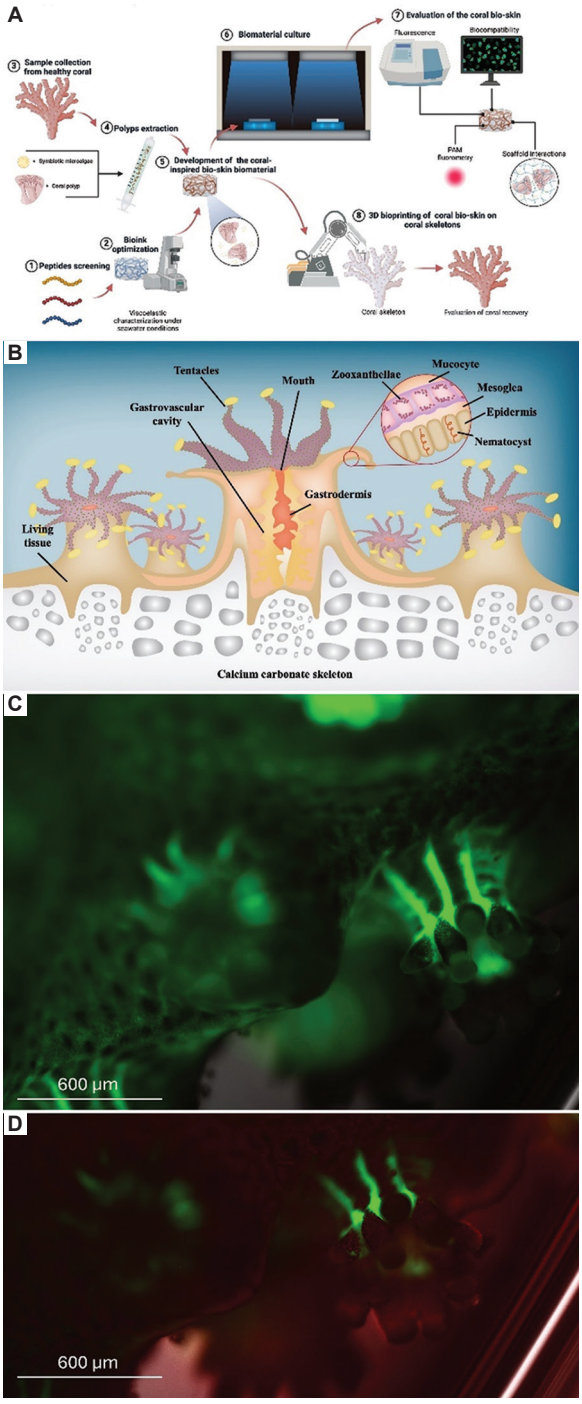

Figure 1. Development of a coral-inspired bio-skin biomaterial to support coral regeneration. (A) Schematic overview of the strategy for developing a coral bio-skin biomaterial to support coral tissue regeneration. (B) A designed illustration of the polyps. (C) Native *Stylophora pistillata* coral polyps, identified by their green autofluorescence, and (D) their symbiotic zooxanthellae, exhibiting a characteristic red fluorescence, are shown on top of their calcium carbonate skeleton. Scale bars: 600 µm; magnification: 10×. The Biorender software was used to prepare Figure 1A.
Abbreviation: PAM: Pulse amplitude modulation.

fluorescence (native green tissue and zooxanthellae) assessed.

Our results identified at least eight peptide-based bioinks as biocompatible with polyps. The best-performing bioinks were selected based on both biocompatibility and mechanical stability (viscoelasticity and degradation resistance) under seawater conditions, making them suitable for 3D bioprinting applications. Furthermore, we optimized a robotic-assisted 3D printer for polyp bioprinting, detailing the optimization process. The most effective combination of bioink and polyp species (Table 2) was then employed to 3D bioprint a unique coral bio-skin on top of coral skeletons, providing a potential strategy to support coral regeneration.

3.2. Bioinks' stability under seawater conditions

Thirteen peptide compounds were selected to create hydrogel-based scaffolds for polyp microencapsulation,

Table 2. Top-performing bioinks for polyp cultivation

Coral polyp specie	Top-performing bioinks	Bioink properties under seawater conditions	Polyp micropropagation	Polyp morphology	Polyp survival time
Stylophora pistillata	B2	Stiffer scaffold (10 kPa), biocompatible, pH 7.7	3.81 mm^2 with visible zooxanthellae spreading through the micropropagated surrounding tissue	Polyp conserves its morphology with signs of emitted green fluorescent protein (GFP) from its tentacles and high zooxanthellae density	Up to 24 days
	B5	Soft scaffold (1 kPa), biocompatible, pH 7.7	2.4 mm^2, visible zooxanthellae spreads through the micropropagated surrounding tissue	Polyp conserves its morphology with signs of emitted GFP from its tentacles and high zooxanthellae density	
	B8	Soft scaffold (1 kPa), collagen-mimetic, biocompatible, pH 7.9	4.16 mm^2, visible zooxanthellae spreads through the micropropagated surrounding tissue	Polyp conserves its morphology with signs of emitted GFP from its tentacles and high zooxanthellae density, signs of potential skeletongenesis underneath	
	B9	Soft scaffold (1 kPa), fibronectin-derived RGDS epitope promoting cell adhesion, biocompatible, pH 7.8	3.53 mm^2, visible zooxanthellae spreads through the micropropagated surrounding tissue	Polyp conserves its morphology with signs of emitted GFP from its tentacles and high zooxanthellae density, signs of potential skeletogenesis underneath	
Pocillopora verrucosa	B2	Stiff scaffold (10 kPa), biocompatible, pH 7.7	4.23 mm^2, visible zooxanthellae spreads through the micropropagated surrounding tissue	Polyp conserves its morphology, contracted tentacles, and high zooxanthellae density	Up to 12 days
	B3	Soft scaffold (1 kPa), biocompatible, pH 7.7	2.41 mm^2, visible zooxanthellae spreads through the micropropagated surrounding tissue	Polyp conserves its morphology, contracted tentacles exhibit GFP, and high zooxanthellae density	
	B4	Soft scaffold (1 kPa), biocompatible, low adhesion, pH 7.7	2.12 mm^2, visible zooxanthellae spreads through the micropropagated surrounding tissue	Polyp conserves its morphology, contracted tentacles, and high zooxanthellae density	
	B6	Soft scaffold (1 kPa), biocompatible, pH 7.6	3.17 mm^2, visible zooxanthellae spreads through the micropropagated surrounding tissue	Polyp conserves its morphology, contracted tentacles, and high zooxanthellae density	
	B8	Soft scaffold (1 kPa), collagen-mimetic, pH 7.9	3.77 mm^2, visible zooxanthellae spreads through the micropropagated surrounding tissue	Polyp conserves its morphology, contracted tentacles exhibit GFP, and high zooxanthellae density	
	B11	Soft scaffold (1 kPa); laminin-derived YIGSR epitope promoting cell adhesion, migration, and differentiation; biocompatible, pH 7.9	4.59 mm^2, visible zooxanthellae spreads through the micropropagated surrounding tissue	Polyp conserves its morphology, contracted tentacles, and high zooxanthellae density	

resulting in the development of bioinks with unique properties for 3D polyp culture (Table 1). Bioinks B1–B8 and B13 were composed of self-assembling peptides 1–8 and 13, respectively, while bioinks B9–B12 were prepared by mixing peptides 9–12 with peptide 1 or 3. Peptides 9–12 were synthesized by attaching biofunctional motifs to the ultrashort peptide compounds 1 and 3. On their own, peptides 9–12 lacked self-assembling capacity; however, when mixed with ultrashort peptides 1 or 3 at defined ratios, they formed bioinks B9–B12.

The bioactive motifs incorporated included RGDS (a fibronectin-derived epitope that mediates cell adhesion and binding), FOGER (a collagen-derived epitope), and YIGSR (a laminin-derived epitope that promotes cell adhesion, migration, and differentiation). Under seawater conditions, bioinks B1–B12 successfully formed hydrogels, whereas bioink B13 did not (Figure 2). Bioinks B1–B3 exhibited the highest stability, retaining their structural integrity without visible degradation or dissolution for over 30 days in seawater (Tables 1 and S1). In contrast, bioinks B4 and B6 formed hydrogels that dissolved in less than 14 days and 24 h, respectively.

The nine rationally designed tetrameric peptides studied (B1–B9, B13) are amphiphilic, comprising hydrophobic and hydrophilic domains.[11] Depending on their sequence, the C-terminus carried either a positively charged residue (B1–B9) or a negatively charged residue (B13). While charged amino acids and pH strongly influence peptide aggregation and assembly,[33] these tetramers assembled exclusively through amphiphilic-driven antiparallel stacking stabilized by van der Waals and hydrogen bonding interactions, consistent with Hauser *et al.*[9] Although previously studied under physiological conditions (pH 7.4) for human cell culture,[11] here they also demonstrated stable assembly under seawater conditions (Tables 1 and S1), to our knowledge for the first time. When FSW was combined with a small amount of PBS (1:10 ratio), the pH ranged between 7.65 and 7.9, depending on the bioink used (Figure S2). This range lies between physiological pH (7.35 to 7.45) and natural seawater (7.78 to 8.21).[34,35] However, even small pH shifts (0.5–1 units) have been reported to negatively affect marine species productivity and community composition.[36] It is important to note that PBS was added only to accelerate bioink formation for subsequent 3D bioprinting; seawater

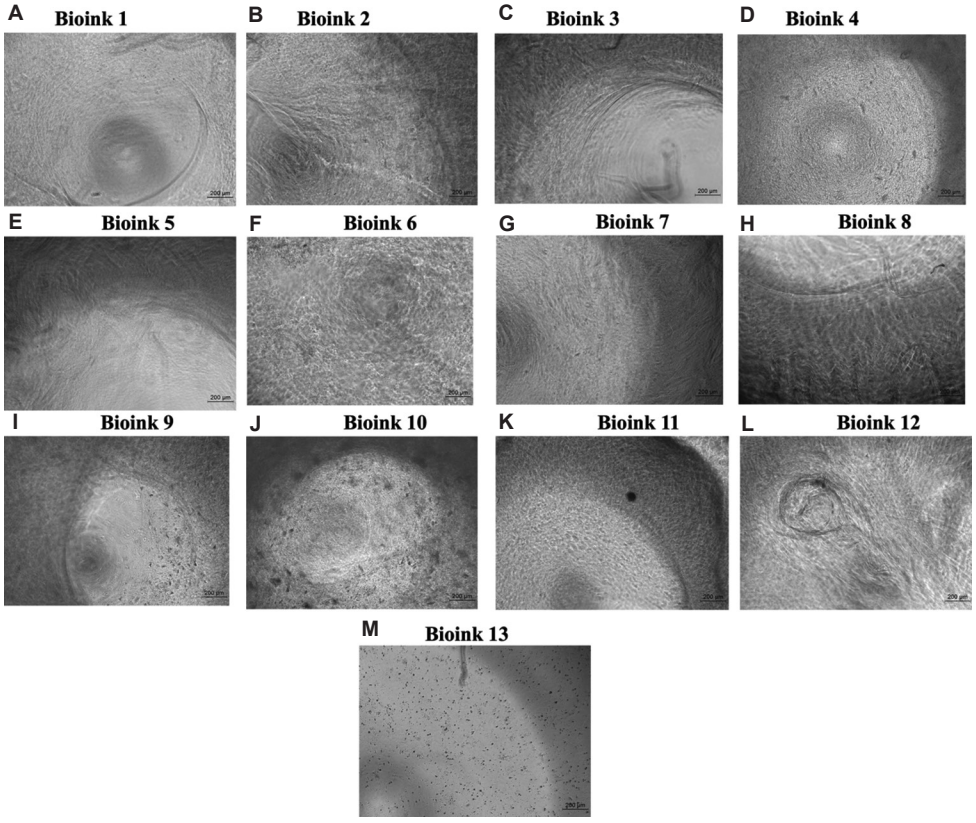

Figure 2. Bioinks under seawater conditions. Bioinks B1–B12 (A–L) contain hydrophilic amino acid (lysine) as the C-terminal residue, whereas bioink B13 (M) contains hydrophilic amino acid (glutamic acid) at the C-terminus. Scale bars: 200 μm; magnification: 20×.

alone can also induce self-assembly due to its natural salt content and the peptides' intrinsic properties. However, using seawater alone may reduce control over the gelation process and slightly alter pH, which could be a limitation for translation applications.

The remarkable stability of these bioinks arises primarily from the rational design of ultrashort self-assembling peptides, which contain a hydrophobic N-terminal tail and a polar C-terminal residue.[11,28,37,38] Even a single amino acid substitution can significantly alter molecular self-assembly and viscoelastic properties.[39] The presence of certain amino acids significantly enhances bioink stability and stiffness under seawater conditions at 27°C. In particular, the exceptional stability of bioink B2 is attributed to the cyclohexylalanine (Z) residue. Bioink B2 outperformed almost identical sequences differing by only one amino acid, as well as bioink B3, which differs from B2 at two positions. Although bioinks B2, B3, and related bioinks remained structurally stable under seawater conditions, they exhibited distinct viscoelastic properties, particularly in storage modulus. Structurally, the Z residue in B2 features a cyclohexane ring, in contrast to the aromatic benzene ring of phenylalanine in B3.[40] These results suggest that ultrashort peptides containing two adjacent cyclohexylalanine residues readily form robust bioinks suitable for potential seawater applications.

Cyclohexylalanine, a synthetic amino acid not naturally present in the human proteome, has demonstrated remarkable biocompatibility with various human cells and may also be compatible with other biological systems, such as coral polyps.[11] Therefore, bioinks incorporating these residues offer distinct advantages for underwater applications. By contrast, bioink B13, which contains an amphiphilic peptide with glutamic acid (a negatively charged residue) at the C-terminus, fails to assemble under seawater conditions (Table S1). In comparison, peptides with a positively charged lysine residue at the C-terminus successfully formed hydrogel-based bioinks under seawater conditions. Depending on the peptide sequence, some of these lysine-containing bioinks remained structurally stable without visible deformation for more than 30 days, while others dissolved within 2 weeks or even less than 24 h (Tables 1 and S1). Overall, most bioinks retained at least 75% of their structure for 30 days in seawater. This stability highlights their potential for field applications, where they could provide localized, durable scaffolds for targeted coral restoration. Accordingly, amphiphilic peptide sequences with positive C-terminal charges are considered promising candidates for seawater bioprinting applications.

3.3. Polyp microencapsulation and 3D bioprinting after bail-out

Polyps were encapsulated using two different strategies: as clustered entities and as individual units. Previous studies have reported the use of epifluorescence microscopy and spectrophotometry to monitor the health status of bail-out polyps.[6,7] Therefore, two complementary methods were employed in this study to assess polyp health after bail-out and subsequent microencapsulation. These methods included (i) quantitative monitoring of the polyp's natural green fluorescence and the chlorophyll red fluorescence of the symbiotic zooxanthellae, and (ii) qualitative assessment using phase-contrast and epifluorescence microscopies to evaluate polyp morphology (Figure 3). As controls, fluorescence was monitored in FSW (Figure 3A), cultured polyps suspended in seawater (Figure 3B), native coal fragments (Figure 3C), and scaffolds without polyps.

Natural *S. pistillata* coral fragment before (Figure 4A) and after polyp bail-out (Figure 4B) were imaged, along with their structural details (Figure 4C and D). After the bail-out, suspended polyps adopt a spherical shape and detach from the natural coral skeleton. Bail-out polyps from both *S. pistillata* and *P. verrucosa* were observed spinning continuously in seawater without re-settling (Figure 4E and F).

In contrast, microencapsulated polyps were immediately provided with a substrate for anchorage and reoriented their oral region toward the incident light source (Figure 5). By comparison, *S. pistillata* and *P. verrucosa* polyps cultured in FSW underwent cellular lysis and membrane rupture within 5 days (Figures S3 and S4). This degeneration was accompanied by a loss of green fluorescence and a marked increase in red fluorescence (Figure S5). Previous studies have highlighted that the success rate of polyp re-settlement after bail-out is typically low.[3,4] However, when microencapsulated within bioinks, polyps re-settled within 24 h. This enhanced re-settlement is attributed to their direct contact with bioink fibers, which serve as a suitable substrate for instantaneous polyp re-settlement (Figure 5). Comparable behavior has been observed in *Pocillopora damicornis* polyps cultured in a coral-on-a-chip microfluidic device, where microscopy was used to track native green fluorescent protein and chlorophyll autofluorescence (red) over 6 weeks.[6] The red fluorescence of bail-out polyps has been linked to algae chlorophyll, as seen in symbiotic zooxanthellae.[6,7]

3.4. Polyp biomaterial cultivation

Unlike other methods, such as suspending polyps in water, the use of self-assembling peptide-based bioinks for bail-

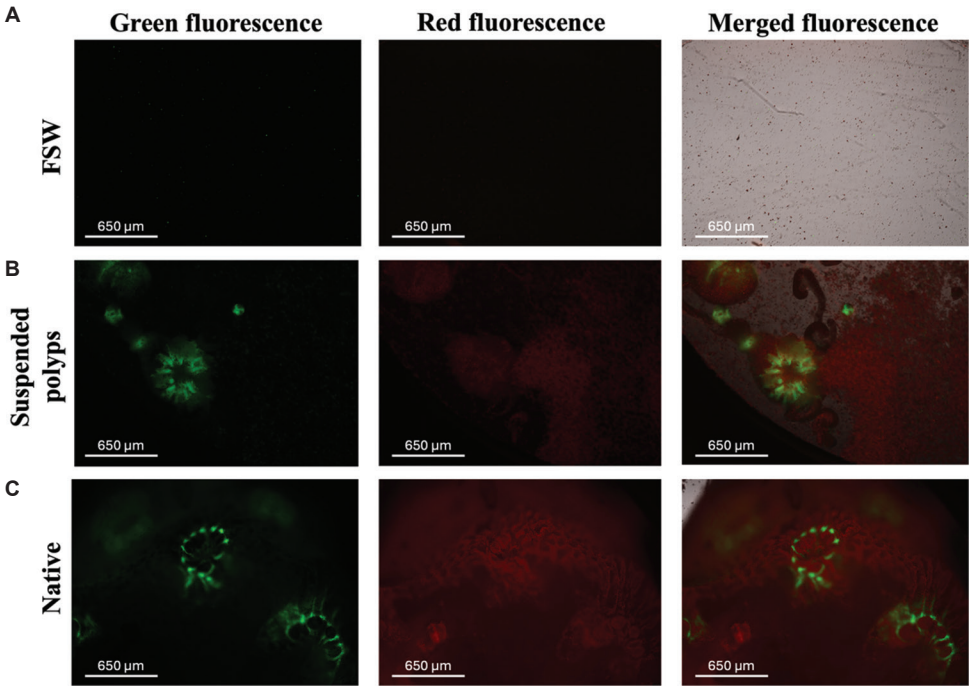

Figure 3. Experimental controls. (A) Filtered seawater (FSW); (B) suspended *Stylophora pistillata* polyps after polyp bail-out; and (C) native *S. pistillata* coral fragment. Scale bars: 650 µm; magnification: 10×.

out polyps promotes instantaneous interaction with the scaffold surface. This facilitates rapid reattachment and subsequent micropropagation. *S. pistillata* polyps cultured in FSW (Figure 5A) were compared to microencapsulated *S. pistillata* polyps (Figure 5B). The microencapsulated polyps maintained their morphology and displayed native green fluorescence (Figure 5C) for up to 24 days. In contrast, *P. verrucosa* polyps cultured in FSW (Figure 5D) were compared with their microencapsulated counterparts (Figure 5E). Suspended polyps exhibited lysis when cultured in FSW (Figures S3 and S4), whereas microencapsulated polyps preserved their spherical morphology and displayed characteristic native green fluorescence in their tentacles (Figure 5E and F).

Structurally, *S. pistillata* polyps retained their shape when cultured in bioinks (Figure 6). When microencapsulated (Figure 6A and B), tissue production was accelerated when at least two polyps were cultured in close proximity (Figure 6C and D). These findings demonstrate that microencapsulated *S. pistillata* polyps maintained their morphology and self-generated fluorescence for up to 24 days. The most effective bioinks for polyp cultivation were bioinks B2, B5, B8, and B9. These bioinks promoted the formation of surrounding tissue within *S. pistillata* polyps within 6 days (Figure 6E-H), indicating active polyp micropropagation. Bioinks B2, B5, and B8 were composed of ultrashort self-assembling peptides without additional biofunctionalities, whereas bioink B9 incorporated the fibronectin-derived RGDS adhesion motif covalently attached to the scaffold. Our results suggest that *S. pistillata* polyps adapted to both stiff and soft bioink scaffolds, though stiff bioinks provided a microenvironment more closely resembling the interface between the coral tissue coenosarc and the natural calcium carbonate skeleton. The biofunctional RGDS motif, known to mimic integrin recognition sites, plays a key role in mediating cell adhesion. Although this motif has primarily been studied in mammalian cells, our results indicate that RGDS also enhances polyp re-settlement. This finding highlights the potential of incorporating biofunctionalized motifs into biomimetic scaffolds to enhance bail-out polyp micropropagation. For instance, the integrin β subunit, which has been identified in several coral species, is involved not only in cell adhesion, fertilization, and symbiont uptake but also in cell–extracellular matrix interactions.[41-44] Therefore, combining RGDS with either soft or stiff scaffolds could significantly enhance integrin-mediated recognition of biomimetic scaffolds by bail-out polyps and accelerate tissue micropropagation. Further experiments aiming to recreate the coenosarc microenvironment of *S. pistillata* should consider stiff bioinks supplemented with RGDS motifs. The initial total area of an *S. pistillata* bail-out polyp was 0.11 mm^2, which increased significantly after 24 days of cultivation due to micropropagation (Table 2).

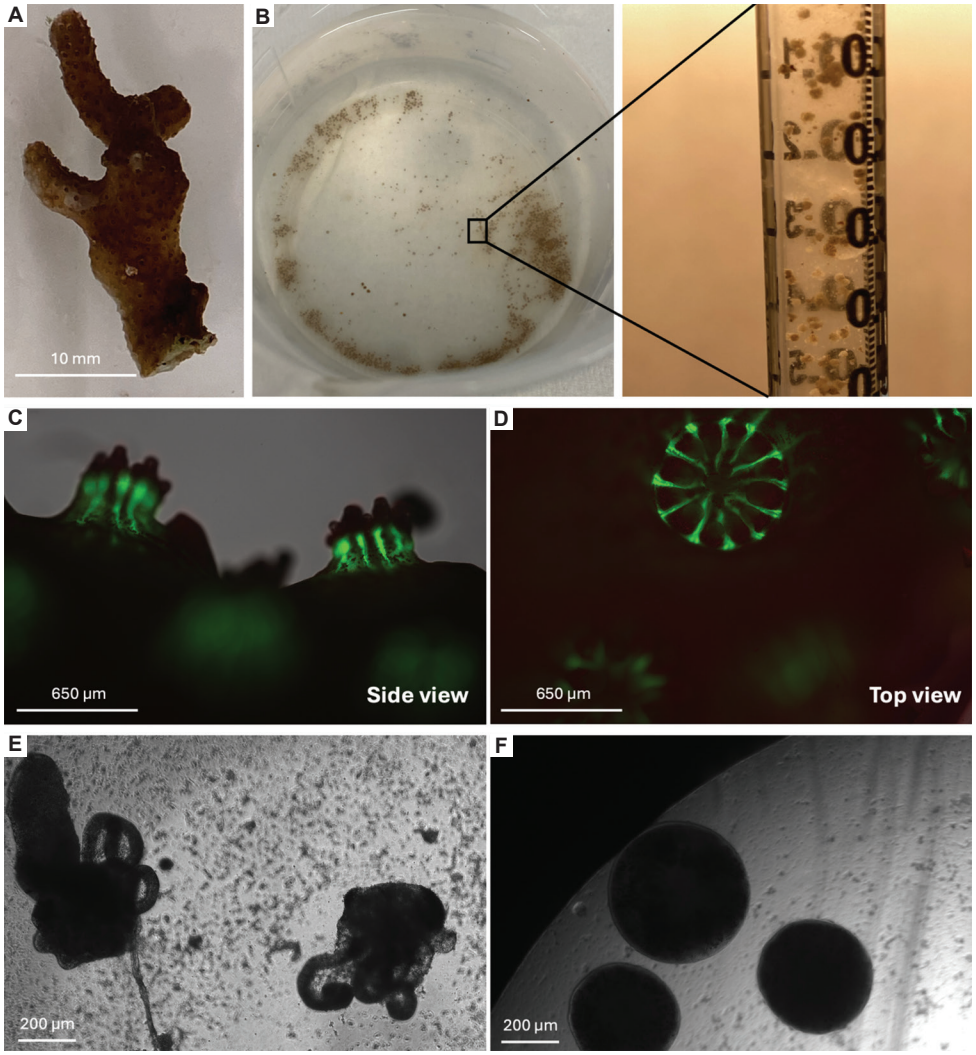

Figure 4. Extracted polyps. (A) Native *Stylophora pistillata* coral fragment. (B) Extracted polyps batch. *S. pistillata* polyps on the calcium carbonate skeleton: Side view (C) and top view (D). *S. pistillata* (E) and *Pocillopora verrucosa* polyps (F). Scale bars: (C & D) 650 µm, (E & F) 200 µm; magnification: 10× (C & D), 20× (E & F).

The top-performing bioinks for *P. verrucosa* polyps were B2, B3, B4, B6, B8, and B11 (Figure 7). Polyps were microencapsulated (Figure 7A), and after 3 days of culture, micropropagated tissue was observed (Figure 7B). Tissue production accelerated when at least two polyps were cultured in close proximity (Figure 7C), although the extent varied depending on the underlying peptide sequence of each bioink (Figure 7D-I). Based on these findings, microencapsulated *P. verrucosa* polyps maintained their morphology and displayed self-generated fluorescence for up to 12 days. Bioinks B2, B3, B4, B6, and B8 consisted of ultrashort self-assembling peptides without additional biofunctional motifs, whereas B11 incorporated the laminin-derived YIGSR cell adhesion motif. *P. verrucosa* polyps responded favorably to both stiff and soft scaffolds. It aligns with reports that the natural coral skeleton microstructure of this coral contains radially arranged calices with a gradient of compressive properties.[45] As a result, the coral exhibits both high strength and localized deformation due to its natural calcium carbonate architecture. This is congruent with our results that bail-out polyps from this coral species exhibited affinity for both soft and stiff bioinks.

The YIGSR motif, previously applied in mammalian organoid culture, also promoted polyp re-settlement in *P. verrucosa*.[46] Our findings indicate that the use of a moderately stiff bioink in combination with the YIGSR motif facilitated attachment, successful re-settlement, and subsequent micropropagation. Further studies aiming to create a biomimetic microenvironment that closely resembles the coenosarc tissue of *P. verrucosa* should

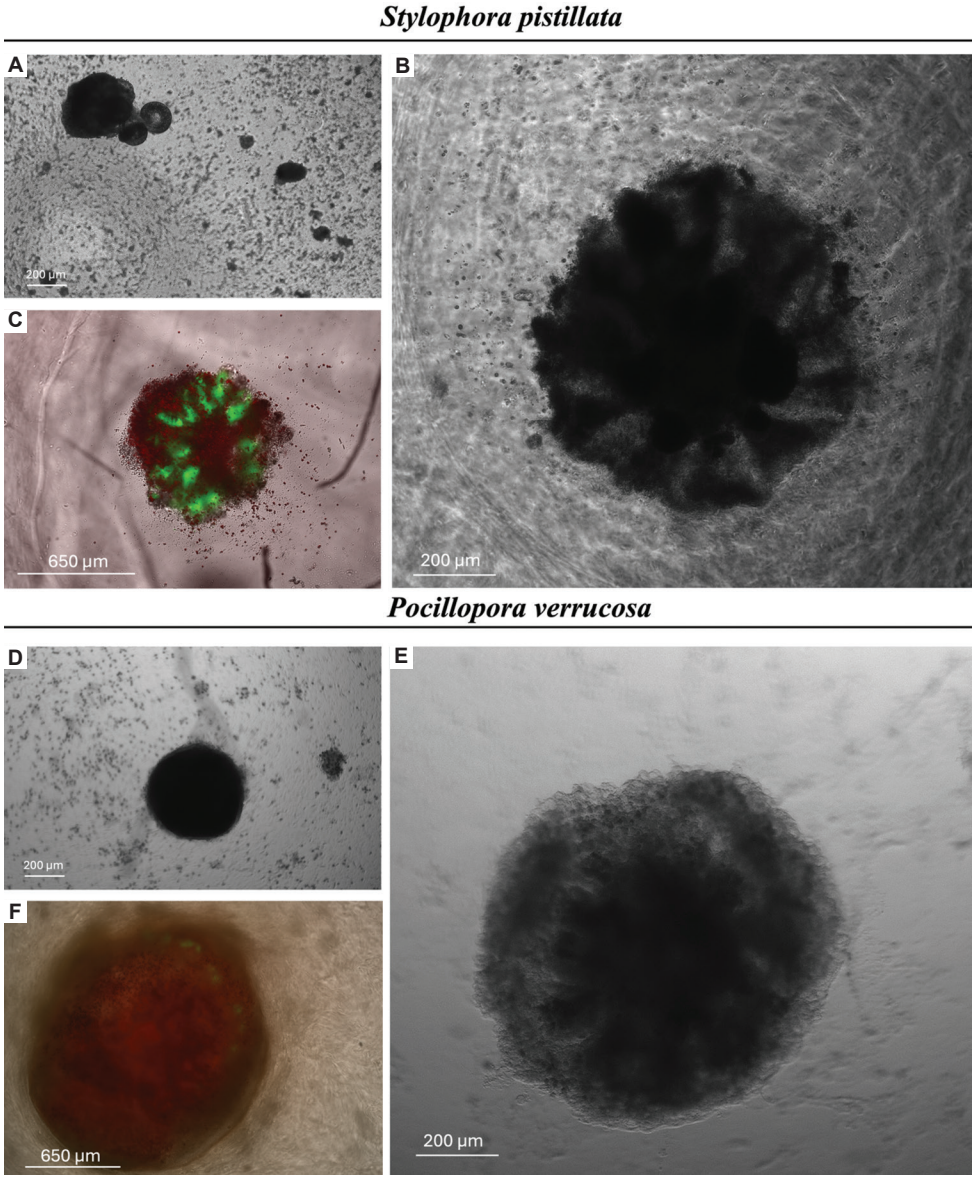

Figure 5. Microencapsulated *Stylophora pistillata* and *Pocillopora verrucosa* polyps. (A) Suspended *S. pistillata* polyp in seawater. Scale bars: 200 µm; magnification: 20×. (B) Phase-contrast imaging of a microencapsulated *S. pistillata* polyp in bioink B2 after 24 h. Scale bars: 200 µm; magnification: 20×. (C) Epifluorescence imaging of microencapsulated coral tissue (green) and zooxanthellae (red). Scale bars: 650 µm; magnification: 10×. (D) Suspended *P. verrucosa* polyp in seawater. Scale bars: 200 µm; magnification: 20×. (E) Phase-contrast imaging of a microencapsulated *P. verrucosa* polyp in bioink B3 after 24 h. Scale bars: 650 µm; magnification: 10×. (F) Epifluorescence imaging of the microencapsulated coral tissue (green) and zooxanthellae (red). Scale bars: 200 µm; magnification: 20×.

consider scaffolds with a stiffness gradient combined with YIGSR binding motifs. The initial area of a *P. verrucosa* bail-out polyp was 0.18 mm^2, which increased significantly after 12 days of cultivation due to micropropagation (Table 2).

For both polyp species, accelerated micropropagation (Figures 6C and 7C) and inter-polyp interactions (Figures 6D and 7D) were observed when bail-out polyps were cultivated within 0.5 mm of each other inside bioink scaffolds. Conversely, polyps cultured in FSW underwent lysis within 24 h (Figures S3-S5). These findings highlight the potential of biofunctionalized bioinks for supporting polyp cultivation.

Fluorescence data supported these findings (Figure 8). In *S. pistillata*, green fluorescence decreased gradually, reaching baseline levels by day 45 (Figure 8A). In contrast, *P. verrucosa* polyps exhibited a steep decrease in green fluorescence after 5 days (Figure 8E). These results indicate

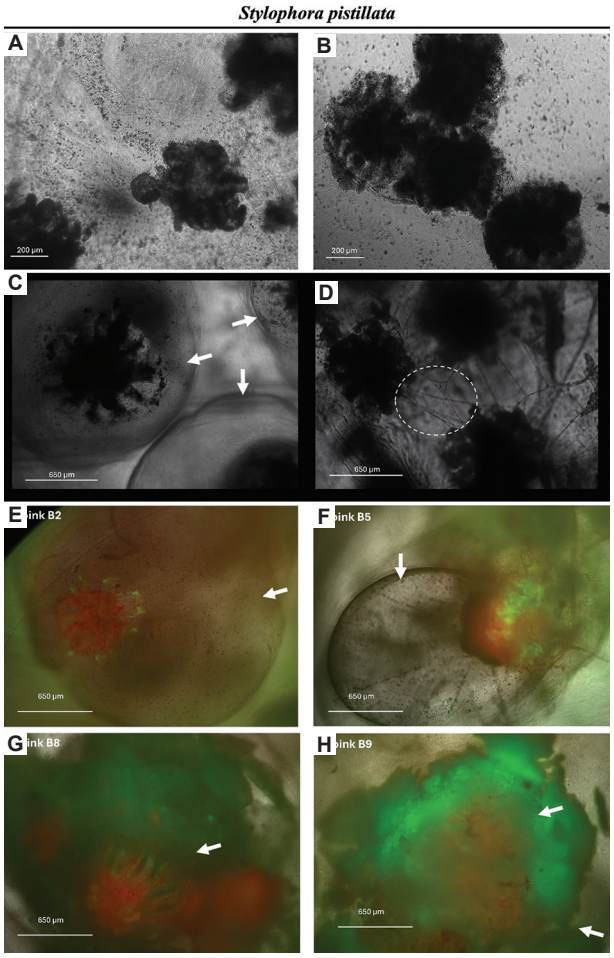

Figure 6. Culture of *Stylophora pistillata* polyps in cluster form. (A) Day 0; (B) after 24 h; (C) surrounding halo formation on day 6; (D) inter-polyp interactions after 6 days. *S. pistillata* polyps in the best-performing bioinks after 24 days: (E) B2, (F) B5, (G) B8, (H) B9. White arrows indicate surrounding halo micropropagation (C, E–H), and the dashed circle denotes inter-polyp connections (D). Scale bars: (A & B) 200 µm, (C–H) 650 µm; magnification: 20× (A & B), 10× (C–H).

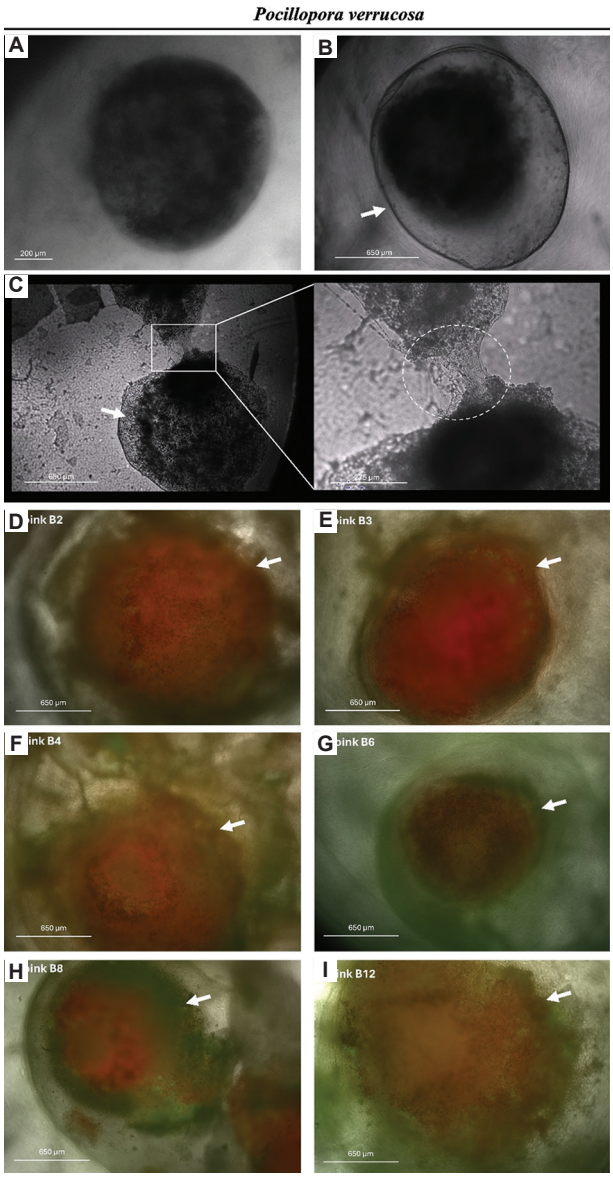

Figure 7. Culture of *Pocillopora verrucosa* polyps in cluster form. (A) Day 0; (B) surrounding halo formation after 6 days; (C) inter-polyp interactions after 6 days; *P. verrucosa* polyps in the best-performing bioinks after 12 days: (D) B2, (E) B3, (F) B4, (G) B6, (H) B8, (I) B11. White arrows indicate surrounding halo micropropagation (B, D-I), and the dashed circle denotes inter-polyp connections (C). Scale bars: (A) 200 µm, (B-I) 650 µm, inset in (C) 275 µm; magnification: (A) 20×, (B-I) 10×, inset in (C) 20×.

that while bioinks can function as biomimetic scaffolds resembling coral coenosarc tissue and sustain bail-out polyps outside of their natural coral skeleton for several days, the current cultivation conditions and scaffold architecture require further refinement to achieve longer-term viability (e.g., polyp cultivation in flow chambers or with integrated calcium carbonate layers).

After encapsulation, both polyp species showed low and unstable red fluorescence, which increased significantly after 5 days. This increase was attributed to chlorophyll autofluorescence from the symbiotic zooxanthellae (Figure 8C and G). Red fluorescence was higher in *P. verrucosa* than in *S. pistillata*. In clustered polyps, red fluorescence decreased after 15 days in *S. pistillata* and after 20 days in *P. verrucosa*, with similar trends observed in single polyps. After this period, red fluorescence increased again, accompanied by a further decrease in green fluorescence.

Of the 13 bioinks tested, eight supported polyp morphology and the formation of surrounding halos. The appearance of surrounding halos, previously documented in bail-out polyps cultured within microfluidic devices,

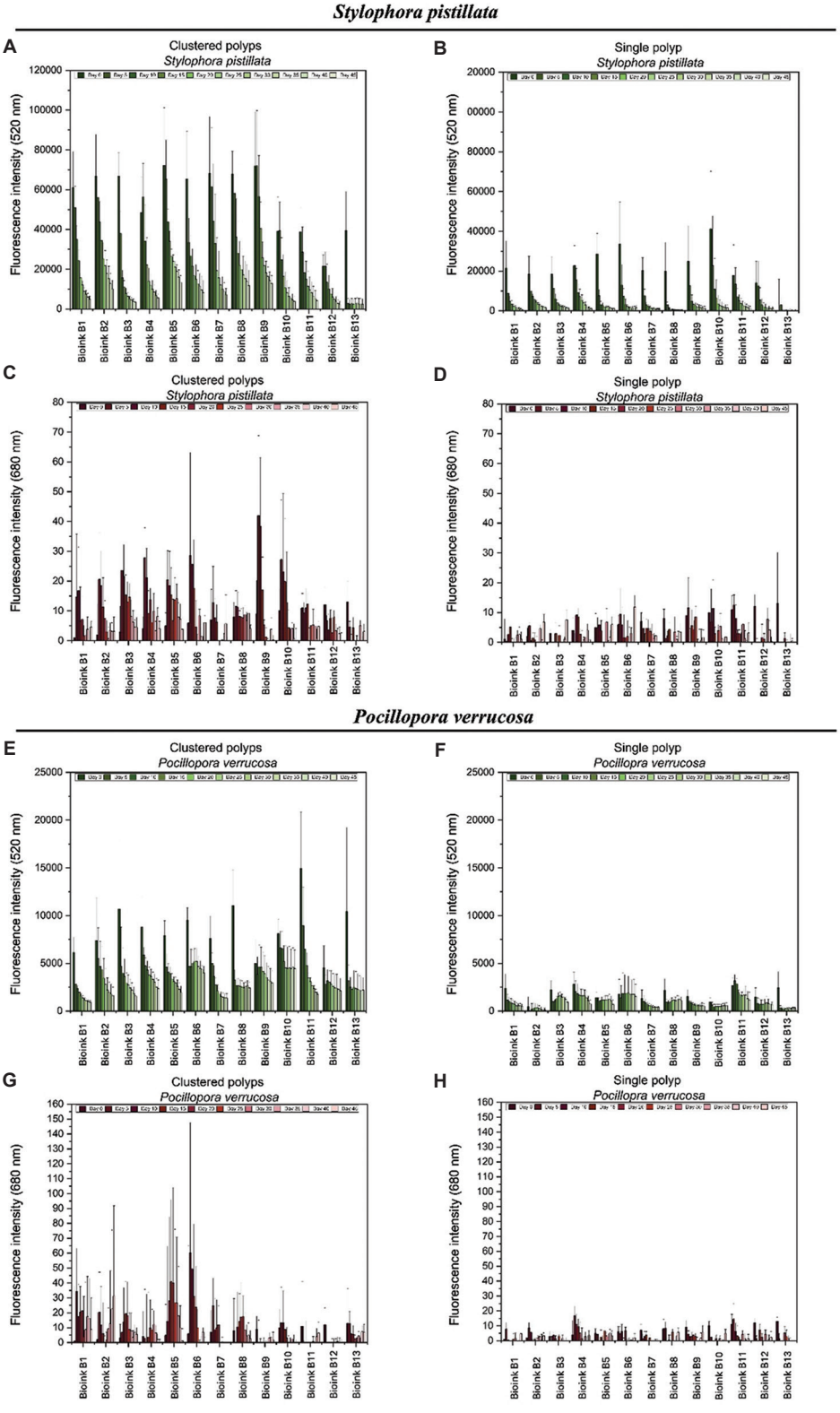

Figure 8. Green and red fluorescence intensity in *Stylophora pistillata* and *Pocillopora verrucosa* polyps. (A–D) S. pistillata polyps cultured in clusters (A, C) and as single units (B, D). (E–H) P. verrucosa polyps cultured in clusters (E, G) and as single units (F, H). Each experiment was performed with replicates of $n = 6$.

is considered an indicator of successful re-settlement and subsequent micropropagation.[6] This occurs because bioinks differ in softness or stiffness and generate fibers of varying thickness, which influence cell adhesion, differentiation, cytocompatibility, and nutrient diffusion within the bioink scaffolds. These parameters collectively create distinct microenvironments for cell growth and proliferation.[11,47-49]

It is suggested that following polyp bail-out, some symbiotic microalgae shut down photosynthesis due to the initial high stress of being outside their natural symbiotic environment within the coral dermis. After 5 days of adjustment, some symbionts from their membrane-bound symbiosomes were released during bail-out and remained present during encapsulation. A similar pattern was observed in bail-out polyps cultured in a microfluidic chip, where symbiont chlorophyll increased post-bail-out.[6] A similar trend was also observed in suspended polyps, where red fluorescence increased while green fluorescence decreased (Figure S5). This change may be attributed to microalgal breakdown under nutrient deprivation. Other studies suggest that corals may even feed on their photosynthetic symbionts under starvation conditions.[50,51]

These observations indicate a potential disruption of symbiosis when bail-out polyps are transplanted into bioinks, leading to species-specific fluorescence dynamics. Furthermore, there appears to be an optimal timeframe during which both polyps and zooxanthellae are in ideal conditions for transfer of this biomaterial under semi-batch conditions to continuous systems (e.g., microfluidic devices or aquaria) that provide enhanced nutrient inflow. A summary of the top-performing bioinks and their compatibility with bail-out polyps in terms of micropropagation, morphology, and survival is presented in Table 2.

3.5. Bioinks' viscoelastic properties under seawater conditions

Based on the preceding results, we selected *S. pistillata* polyps for 3D bioprinting experiments to create a coral-inspired bio-skin biomaterial. For potential *in situ* applications, we evaluated the viscoelastic properties (Figure 9) of the best-performing bioinks for *S. pistillata* polyps, selected according to seawater stability (Table 1) and polyp biocompatibility (Table 2).

Initially, we assessed the ability of each bioink to store energy before deformation, measured by storage and loss modulus. Bioink B2 exhibited a significantly higher storage modulus compared to the other bioinks ($p<0.001$) (Figure S6), indicating superior structural stability under seawater conditions. These findings align with earlier results in the present study, where bioinks containing adjacent cyclohexylalanine (Z) residues demonstrated enhanced stability (Tables 1 and S1). Next, we assessed scaffold network strength by measuring responses to increasing angular frequency. All bioinks displayed low frequency dependence, suggesting the formation of well-organized 3D scaffold networks due to their self-assembling capabilities. Among them, B2 exhibited the strongest network integrity. We also evaluated oscillation strain behavior. All bioinks underwent a transition from solid-like to liquid-like states at different oscillation strains. Bioinks B3, B5, and B9 tolerated higher oscillation stress but exhibited lower structural stability under static conditions. Overall, bioinks B1 and B2 demonstrated the greatest mechanical structural stability under seawater conditions, although both were still capable of transitioning into a liquid state under oscillatory forces. Statistical significance was determined using the Tukey test and is reported in Figure S6.

Our results further indicate that polyps transplanted from their natural coral skeleton to hydrogel-based scaffolds – serving as artificial, biomimetic coral skin – do not immediately die. Instead, the polyps adapt to the scaffold, maintain their morphology, and continue to emit green and red fluorescence for several days. This suggests that their survival could be prolonged under improved conditions, such as open systems with continuous nutrient supply, or by supplementing FSW with additional nutrients.

Transferring these biomaterials to open system conditions is feasible because the bioinks exhibit diverse mechanical and viscoelastic properties depending on their peptide sequence, resulting in distinct stability profiles under seawater (Figure 9 and Table S1). Accordingly, *S. pistillata* and *P. verrucosa* polyps can be maintained in microcapsules for at least 10 days and subsequently transferred to continuous culturing systems. During this period, the polyps retain their shape and fluorescence, though eventual disruption of their symbiotic relationship occurs. Further investigation of the viscoelastic properties of these biomaterials is required to optimize their performance under seawater conditions.

3.6. Development of a coral-inspired bio-skin biomaterial

We achieved the first-of-its-kind 3D bioprinting of coral polyps to create a coral-inspired bio-skin biomaterial (Figure 10). The overall strategy is presented in Figure 10A. The robotic-assisted 3D bioprinting system was optimized specifically for polyp-laden bioprinting (Figure 10B and C). Optimization parameters included pumping speed, robotic arm movement, PBS concentration, gelation speed, nozzle tip dimensions, and nozzle tubing dimensions, all

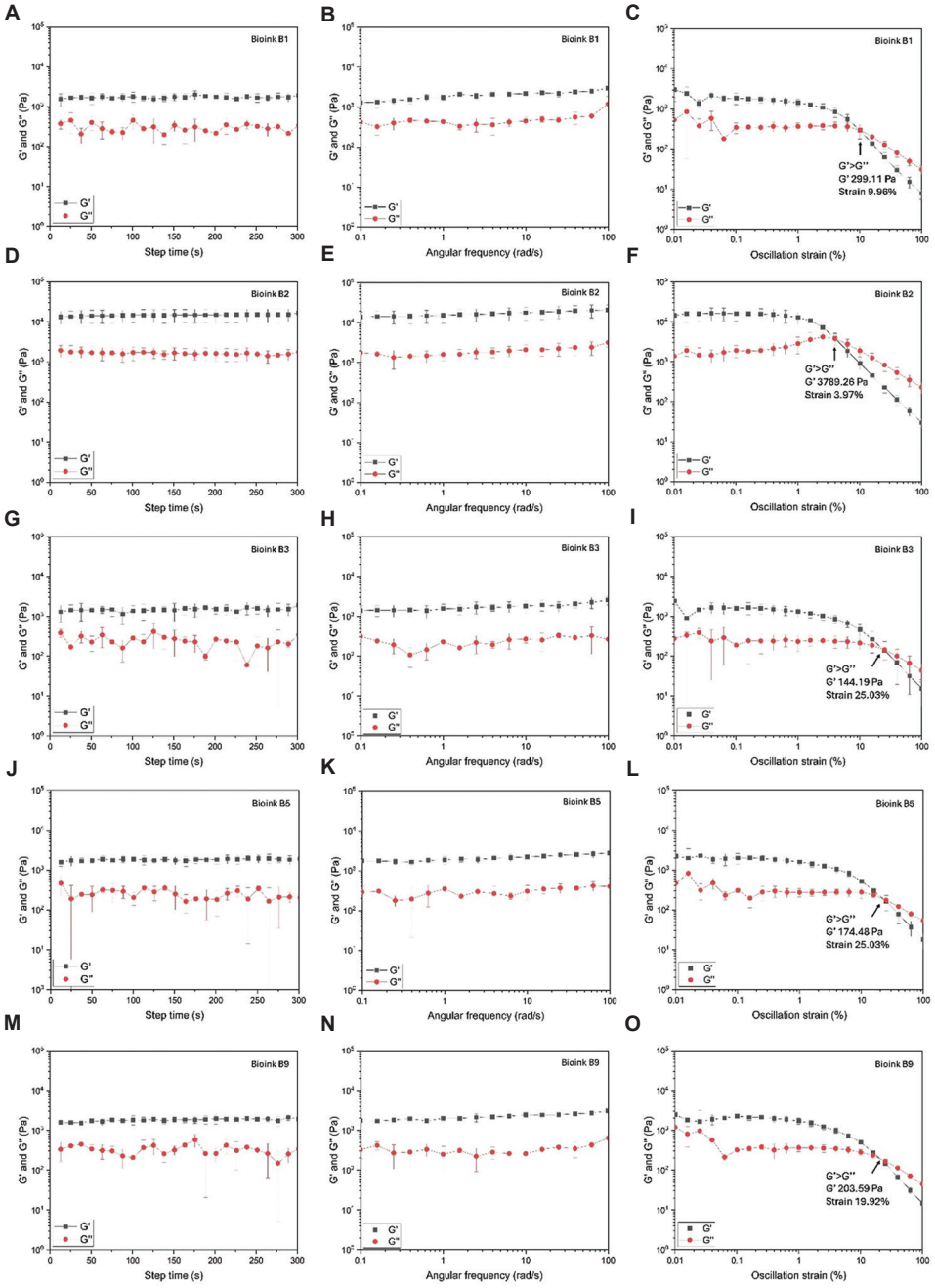

Figure 9. Rheological characterization of top-performing bioinks after 30 days of seawater submersion. Viscoelastic properties were evaluated through step time (A, D, G, J, M), angular frequency (B, E, H, K, N), and oscillation strain (C, F, I, L, O). The turnover points were as follows: B1, 299.11 Pa at 9.96% strain (C); B2, 3789.26 Pa at 3.97% strain; B3, 144.19 Pa at 25.03% strain; B5, 174.48 Pa at 25.03% strain; and B9, 203.59 Pa at 19.92% strain. Experiments were conducted at 27°C with $n = 6$ replicates.

adjusted according to the morphological properties of bail-out *S. pistillata* polyps (Figure S1) and the viscoelastic properties of the selected bioink. In this study, we used the Ac-Ile-Cha-Cha-Lys-NH_2 (IZZK) peptide because of its biocompatibility with polyps, high printability, and stability under seawater conditions. This enabled the successful bioprinting of a polyp-laden coral bio-skin biomaterial directly onto coral skeletons (Figure 10C and D). Under the optimized conditions, the 3D bioprinter was able to deposit polyps without inducing lysis. Although microencapsulated, the polyps retained tentacle movement (Video S1). Thixotropic analysis further revealed that the

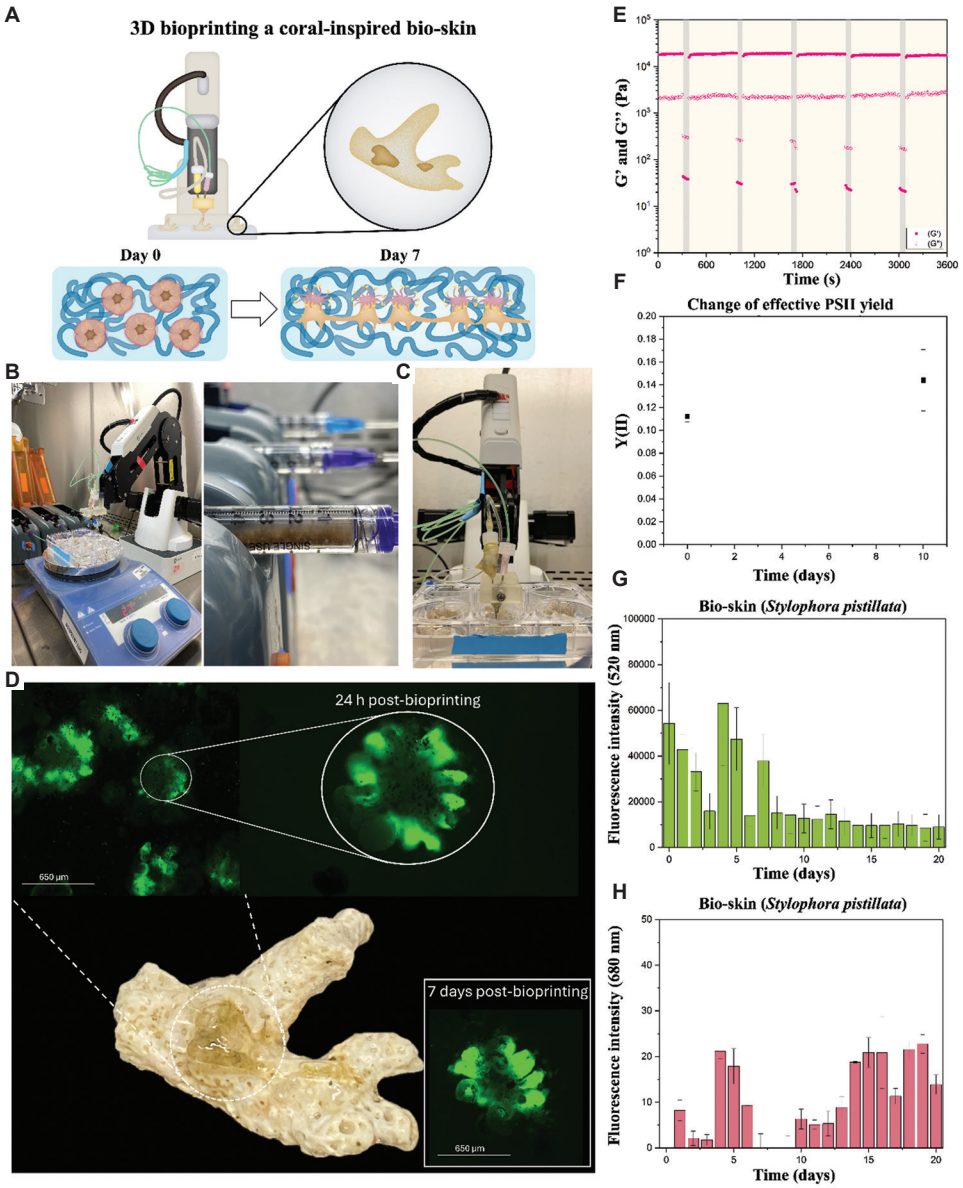

Figure 10. 3D bioprinting of coral-inspired bio-skin on calcium carbonate coral skeletons. (A) A schematical design illustrating the 3D bioprinting of the coral bioskin. (B) 3D bioprinter setup for polyp bioprinting. (D) Bioprinting of coral skin onto coral skeletons. (D) 3D-bioprinted coral-inspired bio-skin containing *Stylophora pistillata* polyps after 24 h and 7 days post-bioprinting. Scale bars: 650 µm, magnification: 10×. (E) Self-healing properties of the polyp bio-skin biomaterial. (F) Effective photosystem II (PSII) yield (Y[II]) of immobilized polyps during a 10-day cultivation period, measured using MINI-PAM-II Photosynthesis Yield Analyzer. (G) Polyp-associated green fluorescence. (H) Zooxanthellae red fluorescence.

combination of polyps and bioink formed a self-healing biomaterial, supporting its potential application *in situ* for regenerating coral substrates (Figure 10E).

In addition, PAM results confirmed that the symbiotic zooxanthellae remained metabolically active and stable after 10 days (Figure 10F). The successful presence of 3D-bioprinted polyps within the coral-inspired bio-skin biomaterial was corroborated by epifluorescence microscopy, further supporting our findings that microencapsulated polyps retain tentacle movement after bioprinting (Video S2). These results were consistent with fluorescence intensity measurements associated with coral tissue and symbionts (Figure 10G and H). Tentacle movement within hydrogel scaffolds can be attributed to the remarkable properties of ultrashort self-assembling peptides, which form nanofibrous 3D scaffolds. These scaffolds not only allow nutrient diffusion through their mesh-like architecture but can also reorganize their

fiber network due to the innate thixotropic nature of the hydrogel scaffolds. However, further research is required to elucidate the effect of bioink thickness on the performance of 3D-bioprinted coral-polyp bio-skins.

Fluorescence analysis revealed a notable decrease in green fluorescence, suggesting that cultivation conditions could be further optimized. Consistent with earlier results, red fluorescence associated with zooxanthellae decreased, likely due to nutrient starvation, and subsequently increased when green fluorescence (Figure 10G) stabilized at low constant levels (Figure 10H).

These findings suggest that the extrusion-based 3D bioprinting process imposes greater stress on polyps compared to manual microencapsulation, reinforcing the need to optimize culture conditions to enhance long-term viability. Nevertheless, this study highlights the potential of 3D bioprinting for generating polyp-laden biomaterials. Under the tested conditions, the 3D-bioprinted biomaterial supported viable polyps for approximately 7 days, sustained solely with FSW as the nutrient source.

Future research should investigate the cultivation of 3D-bioprinted polyp biomaterials under diverse environmental conditions, such as temperature, salinity, and nutrient enrichment, to improve polyp survival after transplantation. Recent progress in this field includes the development of bionic corals fabricated with GelMA-based 3D bioprinting platforms that mimic coral skeletons and incorporate symbionts.[13,14] Other studies have explored calcium carbonate-based materials and bioinks to support coral restoration,[32,52] while antioxidant-enriched biomaterials (e.g., biodegradable composites with curcumin, zein, and polyvinylpyrrolidone) have been formulated to mitigate thermal stress on corals.[22] Advancements in 3D printing and bioprinting technologies have enabled the fabrication of cutting-edge coral-inspired structures and biomaterials for coral restoration. For instance, GelMA-based hydrogels have been employed to replicate living coral tissue and skeletons with micron-scale resolution.[13] Sustainable calcium carbonate-based materials have also been used to print coral-like structures, and bioprinted coral microenvironments have successfully mimicked coral–algal symbiosis.[13,14,19,32,52] Hydrogel-based systems have additionally been engineered to promote the growth of synthetic algal–bacterial consortia.

Coral tissue thickness (covering the coral skeleton) ranges from 100 μm to 0.5 cm, depending on the species. Extrusion-based bioprinting technology can replicate these 3D structures by integrating appropriate biological components with scaffold materials. In this study, we present ultrashort and biofunctionalized peptide-based scaffolds designed specifically for underwater applications, contributing to the development of coral-inspired bio-skin biomaterials. These biomaterials represent a promising platform for coral tissue transplantation and a significant advancement toward *in situ* coral regeneration.

4. Conclusion

We developed a novel method, termed polyp microencapsulation and 3D bioprinting (or abbreviated as PM3D), for bail-out polyp transplantation. Our results revealed that successful polyp micropropagation occurs when multiple polyps are microencapsulated within bioink scaffolds. We identified eight peptide-based bioinks suitable for both polyp micropropagation and 3D bioprinting and analyzed their viscoelastic properties under seawater conditions. Some of the supporting peptide bioinks incorporated bioactive motifs such as RGDS and YIGSR, which are commonly used to mimic the mammalian cellular microenvironment. Interestingly, these bioactive motifs also positively influenced polyp propagation.

The identified peptide bioinks did not harm bail-out polyps and remained stable under seawater conditions. They were able to rapidly form fibers, enabling settlement between bail-out polyps and hydrogel substrates, thus serving as external scaffolds to support polyp growth outside their natural tissue. We also observed changes in red fluorescence following bail-out and subsequent microencapsulation, indicating disruption of the symbiotic relationship between the polyp and zooxanthellae, likely due to nutrient scarcity. Importantly, bioprinted polyps microencapsulated in ultrashort peptide bioinks still exhibited tentacle movement (Videos S1 and S2), depending on scaffold stiffness, thickness, and crosslinker concentration. These parameters can be further optimized to improve polyp viability post-printing. Future research aimed at the long-term cultivation of artificial polyp–bio-skin biomaterials should consider integrating flow-through microfluidic devices to better mimic field-like conditions, incorporating biomimetic coral cues, optimizing biomaterial compositions, and cultivating these biomaterials in nutrient-enriched media.

To advance coral tissue regeneration technologies, we selected the top-performing bioink to 3D bioprint a coral-inspired bio-skin biomaterial onto calcium carbonate coral skeletons. These findings pave the way for coral tissue engineering by harnessing polyp-directed bioinks derived from ultrashort self-assembling and biofunctionalized peptides, which can serve as support scaffolds for future coral tissue transplantation strategies.

Acknowledgments

We thank the Core Labs for providing the high-end research facilities that enabled this work. We would like to thank

Kowther Kahin and Zainab Khan for their contributions to the development of the 3D bioprinting system and dual-coaxial nozzle, as well as to all past and present members of the Bioprinting Team for their contributions to the development of the robotic-assisted 3D bioprinter. We also thank Montserrat del Socorro Valle Perez for the design of some illustrations.

Funding

This research was funded by King Abdullah University of Science and Technology (KAUST) to Charlotte A. E. Hauser. Additional funding was provided by Graz University of Technology (TU Graz) to Christian Baumgartner, and by research start-up funds awarded to Charlotte A. E. Hauser.

Conflict of interest

Charlotte A. E. Hauser is an Editorial Board Member of this journal, but was not in any way involved in the editorial and peer-review process conducted for this paper, directly or indirectly. Separately, other authors declared that they have no known competing financial interests or personal relationships that could have influenced the work reported in this paper.

Author contributions

Conceptualization: Alexander U. Valle-Pérez, Charlotte A.E. Hauser

Formal analysis: Alexander U. Valle-Pérez, Charlotte A. E. Hauser, Manola Moretti, Panayiotis Bilalis

Funding acquisition: Charlotte A. E. Hauser, Christian Baumgartner

Investigation: Alexander U. Valle-Pérez, Sebastian Overmans

Methodology: Alexander U. Valle-Pérez, Panayiotis Bilalis, Sebastian Overmans, Kyle J. Lauersen

Supervision: Charlotte A. E. Hauser

Visualization: Alexander U. Valle-Pérez

Writing–original draft: Alexander U. Valle-Pérez

Writing–review & editing: Alexander U. Valle-Pérez, Charlotte A. E. Hauser, Christian Baumgartner

Ethics approval and consent to participate

Not applicable.

Consent for publication

Not applicable.

Availability of data

Any additional information required to reanalyze the data reported in this paper is available from the corresponding author on reasonable request.

References

1. Mieog JC, Van Oppen MJH, Berkelmans R, Stam WT, Olsen JL. Quantification of algal endosymbionts (*Symbiodinium*) in coral tissue using real-time PCR. *Mol Ecol Resour*. 2009;9(1):74-82.

   doi: 10.1111/j.1755-0998.2008.02222.x

2. Silverstein RN, Correa AMS, Baker AC. Specificity is rarely absolute in coral-algal symbiosis: Implications for coral response to climate change. *Proc R Soc B.* 2012;279(1738):2609-2618.

   doi: 10.1098/rspb.2012.0055

3. Sammarco P. Polyp Bail-Out: An escape response to environmental stress and a new means of reproduction in corals. *Mar Ecol Prog Ser.* 1982;10:57-65.

   doi: 10.3354/meps010057

4. Serrano E, Coma R, Inostroza K, Serrano O. Polyp bail-out by the coral *Astroides calycularis* (*Scleractinia, Dendrophylliidae*). *Mar Biodiv*. 2018;48(3):1661-1665.

   doi: 10.1007/s12526-017-0647-x

5. Cardoso PM, Alsaggaf AA, Villela HM, Peixoto RS. Inducing polyp bail-out in coral colonies to obtain individualized micropropagates for laboratory experimental use. *J Vis Exp.* 2022;(182):63840.

   doi: 10.3791/63840

6. Shapiro OH, Kramarsky-Winter E, Gavish AR, Stocker R, Vardi A. A coral-on-a-chip microfluidic platform enabling live-imaging microscopy of reef-building corals. *Nat Commun.* 2016;7(1):10860.

   doi: 10.1038/ncomms10860

7. Pang AP, Luo Y, He C, Lu Z, Lu X. A polyp-on-chip for coral long-term culture. *Sci Rep.* 2020;10(1):6964.

   doi: 10.1038/s41598-020-63829-4

8. Chuang PS, Ishikawa K, Mitarai S. Morphological and genetic recovery of coral polyps after bail-out. Front Mar Sci. 2021;8:609287.

   doi: 10.3389/fmars.2021.609287

9. Hauser CAE, Deng R, Mishra A, *et al*. Natural tri- to hexapeptides self-assemble in water to amyloid β-type fiber aggregates by unexpected α-helical intermediate structures. *Proc Natl Acad Sci USA*. 2011;108(4):1361-1366.

   doi: 10.1073/pnas.1014796108

10. Roger LM, Lewinski NA, Putnam HM, Roxbury D, Tresguerres M, Wangpraseurt D. Nanobiotech engineering for future coral reefs. *One Earth.* 2023;6(7):778-789.

    doi: 10.1016/j.oneear.2023.05.008

11. Susapto HH, Alhattab D, Abdelrahman S, *et al.* Ultrashort peptide bioinks support automated printing of large-scale

constructs assuring long-term survival of printed tissue constructs. *Nano Lett*. 2021;21(7):2719-2729.

doi: 10.1021/acs.nanolett.0c04426

12. Tóth GS, Backman O, Siivola T, *et al.* Employing photocurable biopolymers to engineer photosynthetic 3D-printed living materials for production of chemicals. *Green Chem*. 2024;26(7):4032-4042.

doi: 10.1039/D3GC04264B

13. Wangpraseurt D, You S, Azam F, *et al*. Bionic 3D printed corals. *Nat Commun*. 2020;11(1):1748.

doi: 10.1038/s41467-020-15486-4

14. Wangpraseurt D, Sun Y, You S, *et al*. Bioprinted living coral microenvironments mimicking coral-algal symbiosis. *Adv Funct Mater*. 2022;32(35):2202273.

doi: 10.1002/adfm.202202273

15. Roger L, Lewinski N, Putnam H, *et al.* Nanotechnology for coral reef conservation, restoration and rehabilitation. *Nat Nanotechnol*. 2023;18(8):831-833.

doi: 10.1038/s41565-023-01402-6

16. de León EHP, Valle-Pérez AU, Khan ZN, Hauser CAE. Intelligent and smart biomaterials for sustainable 3D printing applications. *Curr Opin Biomed Eng*. 2023;26:100450.

doi: 10.1016/j.cobme.2023.100450

17. Zhao S, Guo C, Kumarasena A, Omenetto FG, Kaplan DL. 3D printing of functional microalgal silk structures for environmental applications. *ACS Biomater Sci Eng.* 2019;5(9):4808-4816.

doi: 10.1021/acsbiomaterials.9b00554

18. Krujatz F, Lode A, Brüggemeier S, *et al*. Green bioprinting: Viability and growth analysis of microalgae immobilized in 3D-plotted hydrogels versus suspension cultures. *Eng Life Sci*. 2015;15(7):678-688.

doi: 10.1002/elsc.201400131

19. Wangpraseurt D, You S, Sun Y, Chen S. Biomimetic 3D living materials powered by microorganisms. *Trends Biotechnol*. 2022;40(7):843-857.

doi: 10.1016/j.tibtech.2022.01.003

20. Valenzuela Matus I, Góis J, Vaz-Pires P, Lino Alves J. Coral propagation in substrates obtained through additive manufacturing: Influence of mortar formulations on seawater parameters. *ACS Sustain Chem Eng.* 2024;12(37):13721-13740.

doi: 10.1021/acssuschemeng.4c01276

21. Levy N, Kundu S, Freckelton M, *et al.* Microbial living materials promote coral larval settlement. PNAS Nexus. 2025;4(9):pgaf268.

doi: 10.1093/pnasnexus/pgaf268

22. Contardi M, Fadda M, Isa V, *et al*. Biodegradable Zein-based biocomposite films for underwater delivery of curcumin reduce thermal stress effects in corals. *ACS Appl Mater Interfaces*. 2023;15(28):33916-33931.

doi: 10.1021/acsami.3c01166

23. Luo C, Li M, Yuan R, Yang Y, Lu Z, Ge L. Biocompatible self-healing coating based on schiff base for promoting adhesion of coral cells. *ACS Appl Bio Mater*. 2020;3(3):1481-1495.

doi: 10.1021/acsabm.9b01113

24. Roger LM, Adarkwa Darko Y, Bernas T, *et al.* Evaluation of fluorescence-based viability stains in cells dissociated from scleractinian coral *Pocillopora damicornis*. *Sci Rep.* 2022;12(1):15297.

doi: 10.1038/s41598-022-19586-7

25. Baker NR. Chlorophyll fluorescence: A probe of photosynthesis *in vivo*. *Annu Rev Plant Biol.* 2008;59(1):89-113.

doi: 10.1146/annurev.arplant.59.032607.092759

26. Overmans S, Ignacz G, Beke AK, *et al*. Continuous extraction and concentration of secreted metabolites from engineered microbes using membrane technology. *Green Chem.* 2022;24(14):5479-5489.

doi: 10.1039/D2GC00938B

27. Khan Z, Kahin K, Hauser C. Time-dependent pulsing of microfluidic pumps to enhance 3D bioprinting of peptide bioinks. In: Gray BL, Becker H, editors. *Microfluidics, BioMEMS, and Medical Microsystems XIX*. Washington, DC: SPIE; 2021. p. 5.

doi: 10.1117/12.2578830

28. Rauf S, Susapto HH, Kahin K, *et al*. Self-assembling tetrameric peptides allow in situ 3D bioprinting under physiological conditions. *J Mater Chem B.* 2021;9(4): 1069-1081.

doi: 10.1039/D0TB02424D

29. Unal AZ, West JL. Synthetic ECM: Bioactive synthetic hydrogels for 3D tissue engineering. *Bioconjugate Chem.* 2020;31(10):2253-2271.

doi: 10.1021/acs.bioconjchem.0c00270

30. Bilalis P, Alrashoudi AA, Susapto HH, *et al*. Dipeptide-based photoreactive instant glue for environmental and biomedical applications. *ACS Appl Mater Interfaces*. 2023;15(40): 46710-46720.

doi: 10.1021/acsami.3c10726

31. Jia Y, Abdelrahman S, Hauser CAE. Developing a sustainable resin for 3D printing in coral restoration. *MSAM*. 2024;3(2):3125.

doi: 10.36922/msam.3125

32. Albalawi HI, Khan ZN, Valle-Pérez AU, *et al.* Sustainable

and eco-friendly coral restoration through 3D printing and fabrication. *ACS Sustain Chem Eng*. 2021;9(37): 12634-12645.

doi: 10.1021/acssuschemeng.1c04148

33. Do TD, LaPointe NE, Economou NJ, *et al.* Effects of pH and charge state on peptide assembly: The YVIFL model system. *J Phys Chem B*. 2013;117(37):10759-10768.

doi: 10.1021/jp406066d

34. Hopkins E, Sanvictores T, Sharma S. *Physiology, Acid Base Balance*. Treasure Island, FL: StatPearls Publishing; 2024.

35. Abdelmongy A, El-Moselhy K. Seasonal variations of the physical and chemical properties of seawater at the Northern Red Sea, Egypt. *Open J Ocean Coastal Sci*. 2015;2(1):1-17.

doi: 10.15764/OCS.2015.01001

36. Rasul NMA, Stewart ICF, editors. *Oceanographic and Biological Aspects of the Red Sea.* Berlin: Springer International Publishing; 2019.

doi: 10.1007/978-3-319-99417-8

37. Hauser CAE, Zhang S. Designer self-assembling peptide nanofiber biological materials. *Chem Soc Rev*. 2010;39(8):2780.

doi: 10.1039/b921448h

38. Zhao X, Pan F, Xu H, *et al*. Molecular self-assembly and applications of designer peptide amphiphiles. *Chem Soc Rev*. 2010;39(9):3480.

doi: 10.1039/b915923c

39. Chan KH, Lee WH, Ni M, Loo Y, Hauser CAE. C-terminal residue of ultrashort peptides impacts on molecular self-assembly, hydrogelation, and interaction with small-molecule drugs. *Sci Rep.* 2018;8(1):17127.

doi: 10.1038/s41598-018-35431-2

40. Haerianardakani S, Kreutzer AG, Salveson PJ, Samdin TD, Guaglianone GE, Nowick JS. Phenylalanine mutation to cyclohexylalanine facilitates triangular trimer formation by β-hairpins derived from Aβ. *J Am Chem Soc*. 2020;142(49):20708-20716.

doi: 10.1021/jacs.0c09281

41. Brower DL, Brower SM, Hayward DC, Ball EE. Molecular evolution of integrins: Genes encoding integrin β subunits from a coral and a sponge. *Proc Natl Acad Sci USA*. 1997;94(17):9182-9187.

doi: 10.1073/pnas.94.17.9182

42. Iguchi A, Márquez LM, Knack B, *et al.* Apparent involvement of a β1 type integrin in coral fertilization. *Mar Biotechnol*. 2007;9(6):760-765.

doi: 10.1007/s10126-007-9026-0

43. Jones VAS, Dorr M, Siemers I, *et al*. Symbiont-specific uptake is mediated by integrins in cnidarian larvae. bioRxiv. 2025.

doi: 10.1101/2025.01.21.633834

44. Levy S, Elek A, Grau-Bové X, *et al*. A stony coral cell atlas illuminates the molecular and cellular basis of coral symbiosis, calcification, and immunity. *Cell*. 2021; 184(11):2973-2987.e18.

doi: 10.1016/j.cell.2021.04.005

45. Mao X, Nie Y, Huang Y, Ji H, Li X. A radial distribution of calices in coral skeleton of *Pocillopora verrucosa* (Ellis and Solander, 1786) against ocean currents. *Mar Biol.* 2021;168(12):171.

doi: 10.1007/s00227-021-03982-0

46. Xu J, Pérez-Pedroza R, Moretti M, *et al*. 3D bioprinting of colon organoids in ultrashort self-assembling and decorated peptide matrices. *IJB*. 2024;0(0):3033.

doi: 10.36922/ijb.3033

47. Su T, Liu Y, He H, *et al*. Strong bioinspired polymer hydrogel with tunable stiffness and toughness for mimicking the extracellular matrix. *ACS Macro Lett*. 2016;5(11):1217-1221.

doi: 10.1021/acsmacrolett.6b00702

48. Trappmann B, Chen CS. How cells sense extracellular matrix stiffness: A material's perspective. *Curr Opin Biotechnol*. 2013;24(5):948-953.

doi: 10.1016/j.copbio.2013.03.020

49. Wen JH, Vincent LG, Fuhrmann A, *et al*. Interplay of matrix stiffness and protein tethering in stem cell differentiation. *Nat Mater*. 2014;13(10):979-987.

doi: 10.1038/nmat4051

50. Wiedenmann J, D'Angelo C, Mardones ML, *et al*. Reef-building corals farm and feed on their photosynthetic symbionts. *Nature*. 2023;620(7976):1018-1024.

doi: 10.1038/s41586-023-06442-5

51. Weis VM. Corals have algal friends for dinner. *Nature*. 2023;620(7976):951-952.

doi: 10.1038/d41586-023-02593-7

52. Avila-Ramírez A, Valle-Pérez AU, Susapto HH, *et al*. Ecologically friendly biofunctional ink for reconstruction of rigid living systems under wet conditions. *Int J Bioprint*. 2021;7(4):398.

doi: 10.18063/ijb.v7i4.398

ACCSCIENCE PUBLISHING

Engineering Science in Additive Manufacturing

ORIGINAL RESEARCH ARTICLE

Effect of build distribution and particle properties on the physical characteristics of laser powder bed fusion of *in situ* alloyed nitinol

Declan Bourke[1,2,3,4]*, Medad C.C. Monu[2,3,4], Paul Healy[1], Alexander Sloane[5], Inam Ul Ahad[2,3,4], and Dermot Brabazon[2,3,4]

[1]Department of Product Development, Fort Wayne Metals Ireland, County Mayo, Connacht, Ireland

[2]I-Form, the SFI Research Centre for Advanced Manufacturing, Dublin City University, Dublin, Ireland

[3]School of Mechanical and Manufacturing Engineering, Faculty of Engineering and Computing, Dublin City University, Dublin, Ireland

[4]DCU Institute for Advanced Processing Technology, Dublin City University, Dublin, Ireland

[5]School of Chemical, Materials and Biological Engineering, Faculty of Engineering, University of Sheffield, Yorkshire, United Kingdom

Abstract

The impact of powder flow characteristics on *in situ* nickel (Ni)-titanium (Ti) alloy formation within the laser powder bed fusion (LPBF) process is poorly understood. In this study, flow segregation patterns of Ni-Ti powder blends within the LPBF build chamber were examined and were found to be influenced by the substrate surface, build layout distribution, and particle size distribution. These segregation patterns significantly impacted relative density (RD) and elasto-caloric properties of *in situ* alloyed nitinol components, with regions of lower RD correlated with lower Ni content and higher phase transformation enthalpies than regions with higher Ni content. It was found that powder segregation rates between Ti and Ni particles were higher for rougher substrates, which also contained higher amounts of unmelted powder than smoother substrates. Furthermore, the position of the unmelted powder relative to the deposition arm sweep impacted powder segregation patterns throughout the build chamber. Powder segregation patterns in the LPBF deposition bed were also affected by differences in material density between Ni and Ti and interparticle cohesive forces. The insights gained from this work provide a route to achieving improved microstructural and chemical homogeneity of *in situ* alloyed nitinol, with tailored thermo-mechanical performance.

Keywords: Nitinol; Additive manufacturing; Laser powder bed fusion; *In situ* alloying

***Corresponding author:**
Declan Bourke
(declan.bourke7@mail.dcu.ie)

Citation: Bourke D, Monu MCC, Healy P, Sloane A, Ahad IU, Brabazon D. Effect of build distribution and particle properties on the physical characteristics of laser powder bed fusion of *in situ* alloyed nitinol. *Eng Sci Add Manuf.* 2025;1(3):025340020. doi: 10.36922/ESAM025340020

Received: August 5, 2025

Revised: August 22, 2025

Accepted: August 28, 2025

Published online: September 18, 2025

1. Introduction

Nitinol is a family of shape memory alloys predominantly composed of nickel (Ni) and titanium (Ti), with properties such as shape memory, super-elasticity, and good fatigue strength and corrosion resistance. It is suited to a wide range of biomedical and industrial applications.[1] However, due to its poor machinability, the range of geometries

that are achievable from conventional manufacturing methods is typically limited to wire, tube, or sheet form.[2] Additive manufacturing offers many advantages over conventional processing, including increased flexibility of design geometry, microstructure, and thermomechanical properties.[3,4] Among the available additive manufacturing technologies, laser powder bed fusion (LPBF) offers high levels of geometrical flexibility, dimensional resolution,[5] microstructural flexibility,[6] chemical purity,[7] and controllable levels of surface roughness.[8] The powder can be pre-alloyed or can be generated by blending powders of the constituent elements and alloying *in situ* during the LPBF process.[9] Challenges with using pre-alloyed powder include time and expense in producing new blends.[10,11] *In situ* alloying offers the opportunity to accelerate the pace of research into complex binary, ternary, and quaternary nitinol alloy systems.[12]

However, *in situ* alloying within additive manufacturing poses numerous challenges compared to pre-alloyed powder. Research to date into *in situ* alloying of nitinol has been limited due to challenges with chemical inhomogeneity,[13] brittle precipitates,[14] and high impurities.[15] Chemical homogeneity can be affected by differences in density and mixing of the elements in the liquid state—leading to higher levels of variation in thermal and mass distribution within the melt pool than pre-alloyed powders[16]—the size of the powder particles relative to the melt pool size,[17] and solute trapping.[18] Chemical homogeneity is also affected by differences in thermal diffusivity and particle size between elemental powders,[10] powder morphology,[19] and unevenness of powder deposition.[20] Furthermore, higher non-uniform thermal distribution in the melt pool leads to a larger surface tension gradient, creating increased Marangoni flow relative to pre-alloyed powders.[21] The exothermic reaction of the mixing enthalpy of Ni and Ti varies with the atomic ratio of the constituent elements[22] and affects underlying thermodynamic conditions, lowering the required input energy.[23] In addition, the highly localized nature of the Ni-Ti exothermic reactions within the rapid cooling environment of LPBF is thought to influence solidification rate and contribute to precipitation of a greater volume of hard, brittle intermetallic phases and higher rates of cracking compared to pre-alloyed material.[16,24]

More than 130 parameters are known to influence the LPBF process,[25] and these can be divided into four broad categories: Laser, scan pattern, temperature profile, and powder parameters.[26] Most studies on *in situ* alloying of nitinol have focused on the impact of factors affecting volume energy density (laser power, scan speed, hatch spacing, and layer thickness) or scan strategies, on microstructural characteristics and thermo-mechanical properties. Stoll *et al.*[15] using equi-atomic elementally blended Ni and Ti, measured significantly higher rates of Ni evaporation compared to pre-alloyed nitinol powder, as well as high levels of cracking and chemical inhomogeneity.[15] Shoji Aota *et al.*[18] found that one of the most important LPBF process parameters for the promotion of increased chemical homogeneity during *in situ* alloying is increased residence time of the laser beam in the molten pool, through the use of slower scan speeds or larger spot size, provided that energy density is kept below the keyholing threshold.[18] Zhao *et al.*,[27] using equi-atomic elementally blended Ni-Ti, recommended scan speeds of <400 mm/s within a laser power range of 100 W–200 W, to maximize chemical homogeneity and relative density (RD).[27] Chmielewska *et al.*[28] achieved success in improving homogeneity and reducing cracking with *in situ* alloying of nitinol using a relatively low volume energy density of 33 J/mm^3, achieved through the use of low laser power (25 W) and moderate scan speed (1000 mm/s), and by employing a remelt scan strategy to reduce thermal gradients and improve melt homogeneity.[28]

None of the previous studies into *in situ* alloying in LPBF examined the impact of powder characteristics such as particle size distribution (PSD) and powder spread ability on nitinol component properties. Recent experimental and discrete element method simulation studies of powder spreading in LPBF systems found that a ratio of layer height to d_{90} <1 led to significantly poorer spread ability than a ratio of layer height to d_{90} > 2.[29,30] Xu & Nan[31] found that spread ability and rate of powder segregation are controlled by not just powder flowability, layer height, and particle size, but also by the shear action of the blade on the powder heap and substrate surface roughness.[31] In particular, flowability is influenced by the granular bond number, which is the ratio of interparticle forces to gravity.[32] For metallic particles within the size range used for LPBF, interparticle forces are dominated by van der Waals forces, and the granular bond number is relatively large.[33] Therefore, it is reasonable to expect powders of blended elements with significant differences in density and cohesiveness, such as Ni and Ti, to be more affected by variations in powder deposition and particle segregation than pre-alloyed powders. It is also reasonable to expect that substrate roughness will impact deposition and segregation patterns in such a blend. Segregation patterns are expected to impact localized chemical concentration ratios, thereby affecting component properties, including phase transformation characteristics.[34] This work aims to study the impact of variations of substrate surface, build layout distribution, and PSD on the resulting homogeneity and properties of components produced from *in situ*

alloyed elementally blended powders within the LPBF process.

2. Data and methods

2.1. Materials

One batch of inert gas atomized spherical Ni powder from AEM, China, with a PSD d_{10}-d_{50}-d_{90} range of 22–33–48 µm, referred to hereafter as Ni(i), was mixed with plasma atomized Ti powder from AP&C, Canada, with a PSD d_{10}-d_{50}-d_{90} range of 21–32–48 µm, referred to hereafter as Ti(i). These were mixed in an acoustic resonance mixer supplied by Resodyn (United States), model LabRam I, at an atomic ratio of Ni = 52%at. and Ti = 48%at., to generate a blend hereafter referred to as $Ni_{(i)}$+$Ti_{(i)}$. A second batch of gas atomized spherical Ni powder from AEM, with a PSD d_{10}-d_{50}-d_{90} range of 33–47–65 µm, referred to hereafter as $Ni_{(ii)}$, was mixed with a second plasma atomized Ti powder from AP&C, with PSD d_{10}-d_{50}-d_{90} range 35–48–64, referred to hereafter as $Ti_{(ii)}$, in the same manner as above, to generate a blend hereinafter referred to as $Ni_{(ii)}$+$Ti_{(ii)}$. PSD was measured on a Malvern Mastersizer 3000 (Malvern Panalytical, United Kingdom) dynamic light scattering unit.

2.2. Cuboidal LPBF sample fabrication

To study the impact of specimen layout and powder bed substrate on powder deposition and segregation, powder batch $Ni_{(i)}$+$Ti_{(i)}$ was used to three-dimensionally print various specimens of size 7 × 7 × 7 mm^3 in an AconityMINI LPBF system with a 200 W fiber laser of 1068 nm wavelength, in three different layouts, A, B and C per Figure 1, each with different proportions of melted versus unmelted substrate. Layout A consisted of six columns of specimens printed in the lower half of the build plate (colored orange), and one central column with specimens printed along the entire sweep of the deposit arm (colored green), with largely unmelted substrate in the upper half of the coater arm sweep. Layout B consisted of six columns of specimens printed in the upper half of the build plate (colored blue) and one central column with specimens printed along the entire sweep of the coater arm (colored green), with largely unmelted powder in the lower half of the coater arm sweep. Layout C consisted of seven columns with specimens printed along most of the coater arm sweep (colored green).

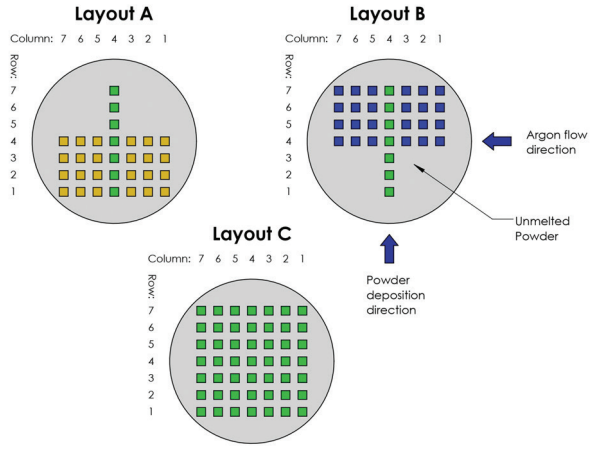

Figure 1. Schematic of build layouts A, B, and C

Process settings used for all specimens were laser power 200 W, scan speed 800 mm/s, hatch spacing 150 µm, layer thickness 60 µm, and spot size 111 µm. The laser scan direction was rotated by 70° after completion of each layer. The re-coater arm deposition speed over the LPBF powder bed was fixed for all trials at 50 mm/s.

2.3. Powder fluidity assessment

To study the impact of PSD on powder deposition and segregation, powder batch $Ni_{(ii)}$+$Ti_{(ii)}$ PSD d_{50} = 44 µm, was used to three-dimensionally print specimens of the same size (7 × 7 × 7 mm^3) using the same settings as described above, in accordance with Layout A (Figure 1) for comparison with powder batch $Ni_{(i)}$+$Ti_{(i)}$ PSD d_{50} = 32 µm. Properties relating to flow energy and bulk density were measured for each batch of powder before and after blending with a Freeman Technology (United Kingdom) Model FT4 Powder Rheometer®.[35] Each measurement on the FT4 device was performed on virgin powder conditioned immediately before testing to remove any variability that may have been introduced while loading the powder by passing a rotating blade at low energy through the powder column, minimizing any precompaction or excess air effects. The flow energy properties measured were basic flow energy (BFE), which is the energy required to establish a particular flow pattern in a conditioned, precise volume of powder, under compression, and specific energy (SE), which is a measure of how powder will flow in an unconfined or low stress environment for a conditioned, precise volume of powder. The conditioned bulk density, the density of a 25 mL powder volume conditioned on the FT4 in the manner described above, was also measured before weighing.

Powder dynamic flow and particle cohesiveness were measured using a GranuDrum powder fluidity measurement instrument from GranuTools™ (Belgium) for the Ni, Ti, and blended Ni-Ti powders from batch $Ni_{(ii)}$+$Ti_{(ii)}$.[36] This automated powder flowability device uses a horizontal cylinder with transparent side walls, which contains a powder volume and rotates around its axis at incremental angular velocities. A high-frequency

optical camera (Granutools, Belgium) was used to capture images of the edge of the powder profile for each angular velocity. The dynamic angle of repose was computed from the average edge profile position. This is a measure of flowability that depends on both contact friction forces and interparticle cohesive forces, and decreases with improved flowability.[37] Fluctuations in the edge profile were monitored to calculate the cohesive index (CI), a measure of inter-particle cohesion and flowability influenced by a combination of Van der Waals, capillary, and electrostatic interactions. Based on N = 50 images, the standard deviation (σ_x) of the fluctuation height of the interface was calculated using Equation I[37]:

$$\sigma_x = \sqrt{\frac{\Sigma_{i=1}^{\mathbb{N}y(x)} \left(\bar{y}(x) - y_i(x)\right)^2}{\mathbb{N}_y(x)}} \quad \text{(I)}$$

where $\bar{y}(x)$ is the mean coordinate height for the slope of the angle of repose at position x, and y_i (x) is the measured coordinate height at position x. CI was then calculated by averaging σ_x over the visible length of the interface. The drum rotation speed was mapped to the equivalent recoater deposition arm speeds by calculating the tangential velocity and multiplying the rotational speed (radians/second) by the drum radius (r = 42 mm).[38] By this calculation, the recoater arm speed employed in the LPBF trials, 50 mm/s, corresponded to a rotating drum speed of 11.4 rpm. Drum rotating speeds tested ranged from 2 rpm to 60 rpm.

2.4. Specimen characterization

RD measurements were performed on all specimens using Archimedes' principle in accordance with ASTM B962-17, using a Sartorius (Germany) weighing scale with measurement accuracy ± 0.1 mg and acetone, against a theoretical maximum density of 6.55 g/cm^3.

Differential scanning calorimetry (DSC) testing on selected specimens was performed in accordance with ASTM F2004-17 on a TA Instruments (United States) Discovery DSC2500 device, subjected to a temperature range of −150°C–+150°C in a nitrogen atmosphere at heating and cooling rates of 10°C/min.

Sample preparation for optical, energy-dispersive X-ray spectroscopy (EDX), and X-ray diffraction (XRD) analysis was performed by grinding cold resin mounts with silicon carbide papers of 80, 300, 600, 800, and 1,200 grit, and polishing with diamond suspension of 9, 3, and 1 µm at a rotary speed of 200–250 rpm. For optical analysis, 10 mL of nitric acid, 4 mL of hydrofluoric acid, and 40 mL of deionized water were utilized as an etchant after polishing. EDX measurements were performed on a Zeiss (Germany) EVO LS-15 scanning electron microscope (SEM) and analyzed with Oxford Instruments® Aztec software (version 6.2). Ni content was measured by the map spectrum over an area 1.8 × 2.2 mm^2 (magnification 150×) near the center of vertical sections of selected specimens. Statistical analysis of RD, DSC, and XRD data was performed using Microsoft Excel (version 2506) and Minitab (version 22.1).

Micro-computed tomography (CT) for porosity measurement was performed using a GE Phoenix V|tome|x (Waygate Technologies, Germany) device on a central section measuring 2 × 2 × 2 mm^3 of six selected specimens representing low, nominal, and high RD. Measurement resolution was 10 µm, and 600 images were taken per scan.

XRD measurements were performed on an Anton Paar (Austria) XRDynamic 500 for phase identification between 2Θ 35° and 80°, using a copper K-alpha X-ray source with a wavelength of 1.5406 Å. Specimens were sectioned parallel to the build direction (vertical plane), and ground and polished, such as the SEM-EDX specimens. Relevant NiTi crystal structures from the Crystallography Open Database[39] were used for indexing the XRD spectra. Quantitative spectral analysis of phases and their volume fractions was achieved by Rietveld refinement using the FullProf software (version April 2024),[40] integrated into the Match! software (version 4.1).[41] From this data, the percentage phase composition was calculated.

3. Results

3.1. Powder characterization

Scanning electron microscopy micrographs for each of the powder batches are presented in Figure 2, demonstrating good sphericity for all powders, both before and after mixing. PSD results for the powder batches are presented in Figure 3, confirming closely matched powder PSDs for Ni and Ti in each batch. The d_{10}-d_{50}-d_{90} for Ni and Ti for $Ni_{(i)}$+$Ti_{(i)}$ and $Ni_{(ii)}$+$Ti_{(ii)}$ measured 21–32–49 µm and 33–47–65 µm, respectively.

Powder flow fluidity and bulk density (FT4) as well as dynamic flow and cohesive measurements (Granudrum) are presented in Figures 4 and 5, respectively. BFE, measured using the FT4, for batch $Ni_{(i)}$+$Ti_{(i)}$ was 656 mJ compared to 595 mJ for batch $Ni_{(ii)}$+$Ti_{(ii)}$. Similarly, SE was higher for batch $Ni_{(i)}$+$Ti_{(i)}$ at 3.28 mJ/g compared to 2.58 mJ/g for $Ni_{(ii)}$+$Ti_{(ii)}$. Within each batch, the FT4 basic flow energy for the Ni powder, which averaged 972 mJ across both batches, was significantly higher than for the Ti powder, which averaged 398 mJ across both batches. The conditioned bulk density of batch $Ni_{(i)}$+$Ti_{(i)}$ at 3.75 g/mL was marginally lower than for batch $Ni_{(ii)}$+$Ti_{(ii)}$ at 3.88 g/mL.

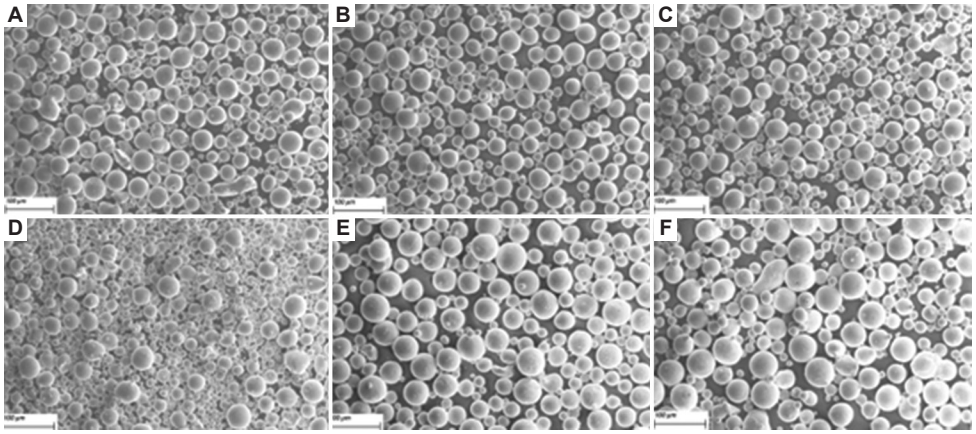

Figure 2. Scanning electron microscopy micrographs of the powders. (A) $Ni_{(i)}$, (B) $Ti_{(i)}$, (C) $Ni_{(i)}$+$Ti_{(i)}$, (D) $Ni_{(ii)}$, (E) $Ti_{(ii)}$, and (F) $Ni_{(ii)}$+$Ti_{(ii)}$. Scale bar: 100 μm; magnification: 500×.
Abbreviations: Ni: Nickel; Ti: Titanium.

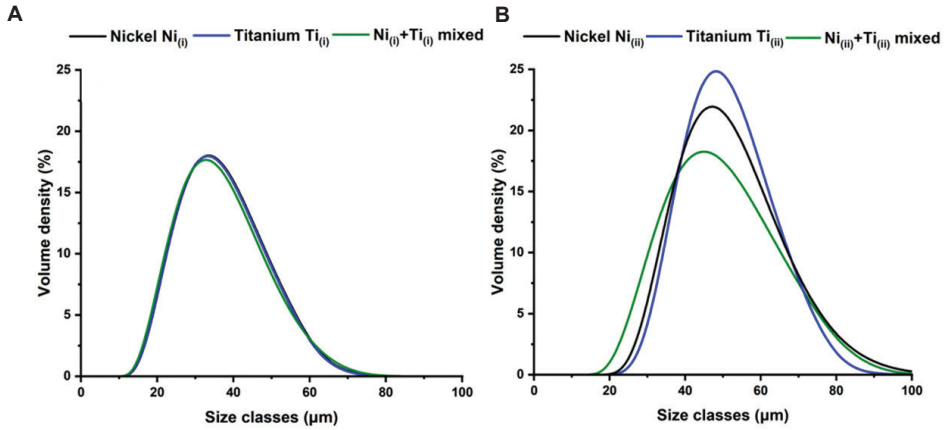

Figure 3. Particle size distributions of the powders used in this study. *In situ* elementally blended (A) $Ni_{(i)}$+$Ti_{(i)}$ and (B) $Ni_{(ii)}$+$Ti_{(ii)}$.

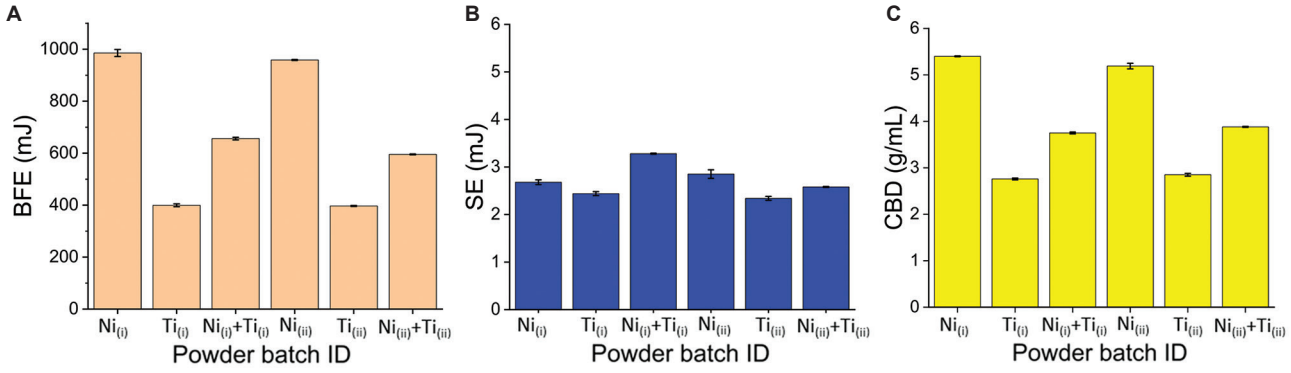

Figure 4. Powder FT4 fluidity characterization results. (A) Basic flow energy (BFE), (B) specific energy (SE), and (C) conditioned bulk density (CBD).
Abbreviations: Ni: Nickel; Ti: Titanium.

The BFE and SE measurements for the Ni powders were significantly lower than those of their corresponding Ti powders of the same nominal size range.

The dynamic angle of repose on the Granudrum device was similar for both the Ni and Ti powders across the full range of speeds tested (Figure 5B). The measured

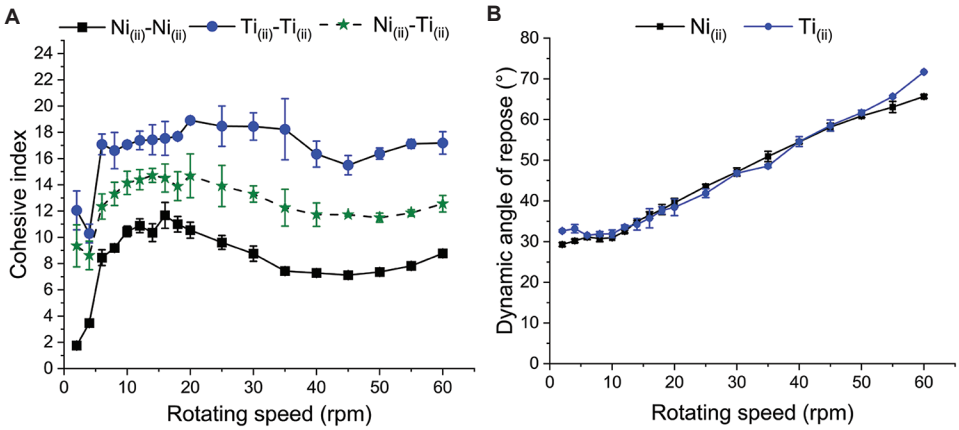

Figure 5. Powder granudrum dynamic flow results for $Ni_{(ii)}$-$Ni_{(ii)}$, $Ti_{(ii)}$-$Ti_{(ii)}$, and $Ni_{(ii)}$+$Ti_{(ii)}$. (A) Cohesive index and (B) dynamic angle of repose.
Abbreviations: Ni: Nickel; Ti: Titanium.

CI as a function of rotating speed, for Ni-Ni, Ti-Ti, and Ni-Ti particle interactions, is presented in Figure 5A. At all rotating drum speeds, the CI for Ti-Ti interactions was significantly higher than that of the Ni-Ni interactions. At a rotating drum speed of 11.4 rpm, which corresponds most closely to the deposition arm speed of 50 mm/s as discussed earlier, the CI for the Ti-Ti powder particle interaction was 1.62 times higher than the Ni-Ni powder particle interaction, indicating significantly higher interparticle cohesive forces for the Ti than for the Ni powder. The CI recorded for the blended Ni-Ti batch was close to the average of the Ni-Ni and Ti-Ti measurements.

3.2. RD

Average RD was measured, and standard deviation was calculated for each of the four trials (Figure 6), for each column (Figure S1), and for each row (Figures 7 and S2).

Average RD for the three trials with batch $Ni_{(i)}$+$Ti_{(i)}$ (PSD d_{50} = 32 μm) did not vary significantly from each other, measuring 98.6%, and ranging from 97.7% to 99.4% across the three runs (Figure 6). Standard deviation of RD for each of these three trials was 0.39% for Layout A, 0.44% for Layout B, and 0.26% for Layout C.

Average RD for the trial from batch $Ni_{(ii)}$+$Ti_{(ii)}$, (PSD d_{50} = 44 μm), was significantly different from batch $Ni_{(i)}$+$Ti_{(i)}$, and measured 97.1%, ranging from 96.2% to 98.5%. The standard deviation for this trial was the highest of all the trials at 0.59%.

An analysis of RD trends by column position (Figure S1) revealed no correlation with RD. Standard deviation across the seven columns for each trial averaged 0.41% for batch $Ni_{(i)}$+$Ti_{(i)}$ Layout A, 0.44% for batch $Ni_{(i)}$+$Ti_{(i)}$ Layout B, 0.27% for batch $Ni_{(i)}$+$Ti_{(i)}$ Layout C, and 0.62% for batch $Ni_{(ii)}$+$Ti_{(ii)}$ Layout A

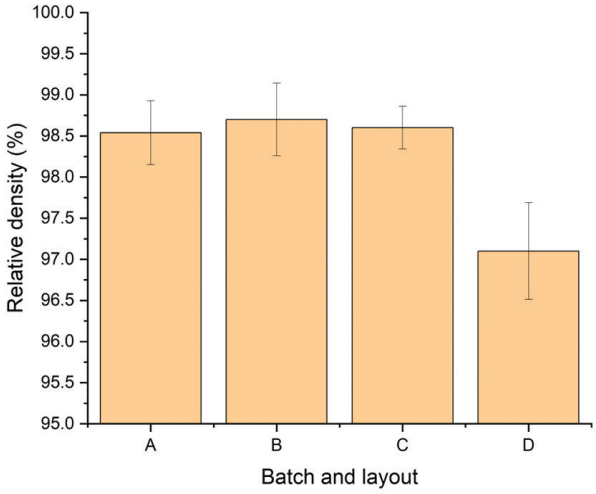

Figure 6. Average relative density for each run. (A) batch $Ni_{(i)}$+$Ti_{(i)}$ layout A, (B) batch $Ni_{(i)}$+$Ti_{(i)}$ layout B, (C) batch $Ni_{(i)}$+$Ti_{(i)}$ layout C, and (D) batch $Ni_{(ii)}$+$Ti_{(ii)}$ layout A.
Abbreviations: Ni: Nickel; Ti: Titanium.

An analysis of RD trends by row position (Figures 7 and S2) revealed a consistent correlation between RD and row position within each layout. With reference to Figure 1, this indicates that the build position concerning powder deposition distance has significantly impacted RD. Standard deviation by row for each trial averaged 0.19% for batch $Ni_{(i)}$+$Ti_{(i)}$ Layout A, 0.29% for batch $Ni_{(i)}$+$Ti_{(i)}$ Layout B, 0.15% for batch $Ni_{(i)}$+$Ti_{(i)}$ Layout C, and 0.22% for batch $Ni_{(ii)}$+$Ti_{(ii)}$ Layout A.

RD variation was observed to be influenced by the powder bed substrate, showing distinct RD patterns: Regions where the deposition arm had travelled over

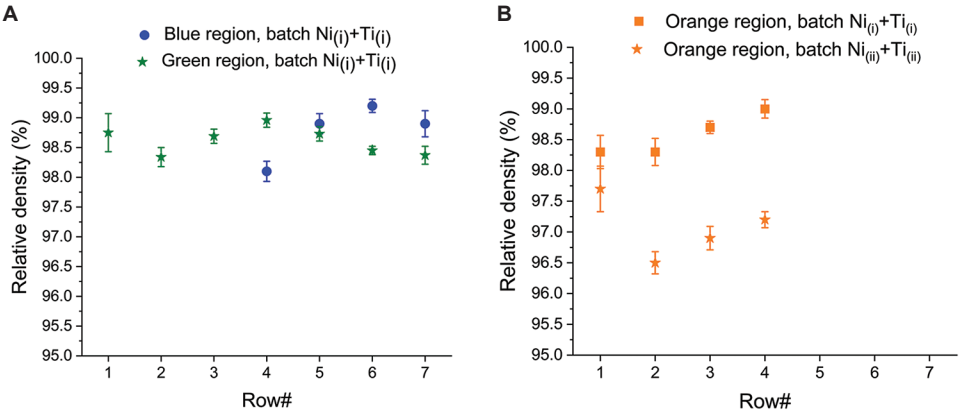

Figure 7. Relative density by row. (A) blue and green regions, batch $Ni_{(i)}$+$Ti_{(i),}$ layouts B. (B) Orange regions, batches $Ni_{(i)}$+$Ti_{(i)}$ and $Ni_{(ii)}$+$Ti_{(ii)}$, layout A. Abbreviations: Ni: Nickel; Ti: Titanium.

predominantly printed specimens (orange and green regions, Figure 1) differed from those where it traveled over mostly unmelted powder before reaching the specimens (blue region, Figure 1). Figure 7A compares the RD pattern of the blue and green regions for batch $Ni_{(i)}$+$Ti_{(i)}$ and demonstrated that by the time the powder is deposited at Row 4, a significant difference has emerged in the RD of the two regions, with Row 4 of the green region having an average RD of 99.0% (σ = 0.11%) and Row 4 of the blue region having an average RD of 98.2% (σ = 0.36%). Furthermore, RD for the green and blue regions exhibited opposite trends between Rows 4 and 7: in the green region, RD at Row 6 decreased to 98.4% (σ = 0.10%), whereas in the blue region, RD at Row 6 increased to 99.2% (σ = 0.11%).

RD variation was also observed to be influenced by average particle size. Figure 7B reveals a significant difference in the RD distributions of the orange region for batch $Ni_{(i)}$+$Ti_{(i)}$ compared to the orange region for batch $Ni_{(ii)}$+$Ti_{(ii)}$. Specifically, RD in Row 1 was lower for $Ni_{(ii)}$+$Ti_{(ii)}$ than for $Ni_{(i)}$+$Ti_{(i)}$. $Ni_{(ii)}$+$Ti_{(ii)}$ also exhibited a significantly wider range of RD variation than $Ni_{(i)}$+$Ti_{(i).}$ This is most notable between Row 1 and Row 2, where RD is unchanged at 98.2% (σ = 0.33% and σ = 0.20% for Row 1 and 2, respectively), whereas RD for $Ni_{(ii)}$+$Ti_{(ii)}$ decreased from 97.5% (σ = 0.37%) to 96.5% (σ = 0.18%). Both batches showed an increasing trend in RD between Rows 2 and 4, with RD = 99.0% (σ = 0.13%) at Row 4 for batch $Ni_{(i)}$+$Ti_{(i)}$, and RD = 97.2% (σ = 0.13%) at Row 4 for batch $Ni_{(ii)}$+$Ti_{(ii)}$.

3.3. Chemistry

Ni composition measurements, based on EDX map spectra as described above, on 50 selected specimens divided equally between both powder batches, averaged 49.4%at., varying from 47.7%at. to 51.6%at. A regression analysis of RD against Ni content for these specimens is presented in Figure 8,

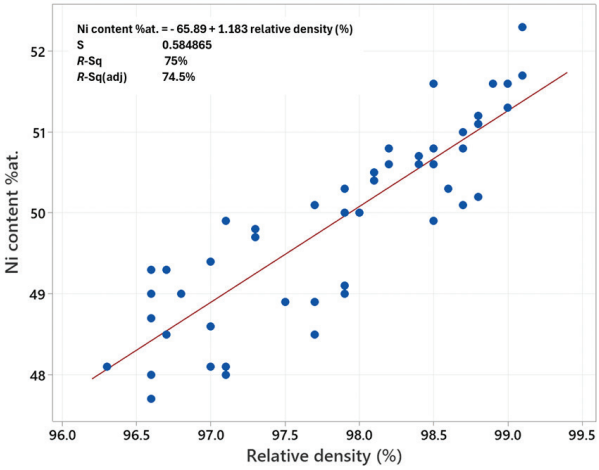

Figure 8. Correlation between nickel content and relative density for *in situ* alloyed specimens, combining batches $Ni_{(i)}$+$Ti_{(i)}$ and $Ni_{(ii)}$+$Ti_{(ii)}$ Abbreviations: Ni: Nickel; *R*-sq: *R*-squared; Ti: Titanium.

demonstrating a strong positive correlation with a Pearson coefficient of $R = 0.87$ and an R^2 coefficient of 74.5%.

3.4. Micro-CT analysis

Density based on porosity measurements from micro-CT scans for the six selected specimens ranged from 99.31% to 99.97%. As stated earlier, these specimens represented the lowest, highest, and nominal RD, as measured by the Archimedes method. Figure S3 shows the micro-CT density results plotted as a function of Archimedes' RD and demonstrates no correlation between the two attributes. This indicates that the variation in RD across the specimens is primarily driven by Ni content and not porosity.

3.5. Phase transformation

Phase transformation temperatures, hysteresis values, ranges, and enthalpies are summarized in Table 1 and

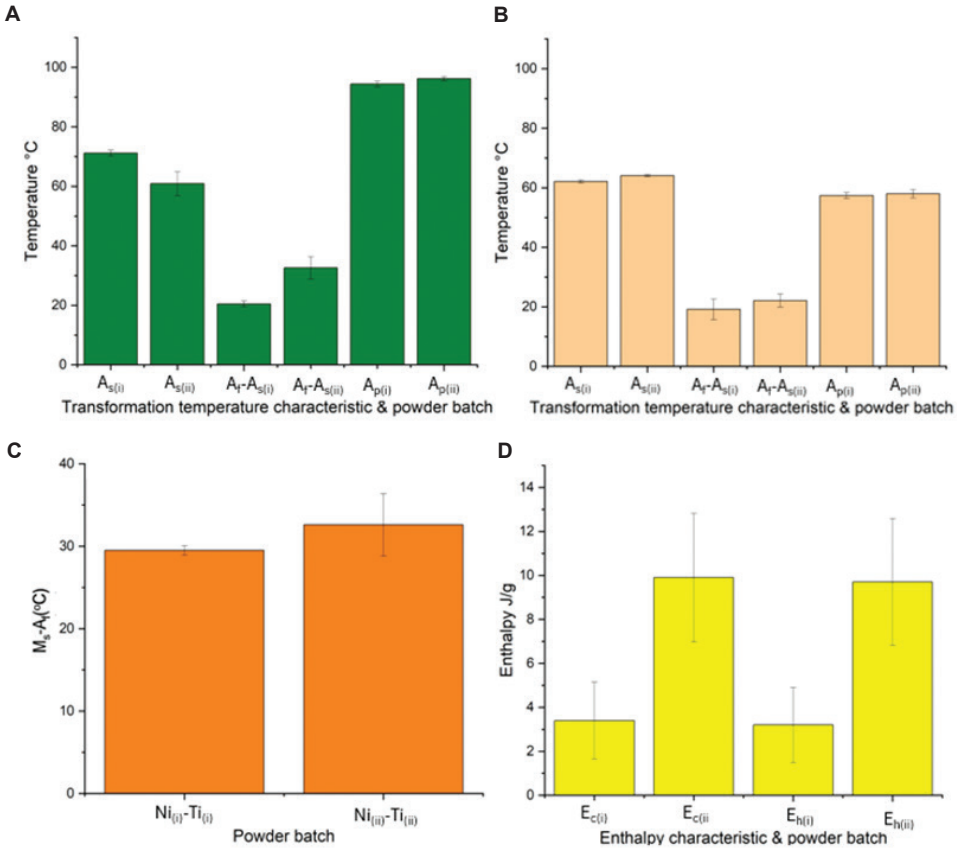

Figure 9. Phase transformation characteristics for powder batches $Ni_{(i)}+Ti_{(i)}$ and $Ni_{(ii)}+Ti_{(ii)}$. (A) Heating cycle transformation temperatures and ranges, (B) cooling cycle transformation temperatures and ranges, (C) hysteresis values, and (D) enthalpies.
Abbreviations: A_f: Austenitic finish temperature; A_p: Austenitic peak temperature; A_s: Austenitic start temperature; E_c: Cooling cycle (exothermic) phase transformation enthalpy; E_h: Heating cycle (endothermic) phase transformation enthalpy; M_f: Martensitic finish temperature; M_p: Martensitic peak temperature; M_s: Martensitic start temperature; Ni: Nickel; Ti: Titanium.

Table 1. Differential scanning calorimetry data for the elementally mixed powders for the low and high particle size distributions

Temperature	Batch	M_s	M_s–M_f	M_p	A_s	A_f–A_s	A_p	A_f–M_s	E_c (J/g)	E_h (J/g)
Average (°C)	$Ni_{(i)}+Ti_{(i)}$	62.1	19.2	57.4	71.2	20.5	84.4	29.5	3.4	3.2
	$Ni_{(ii)}+Ti_{(ii)}$	64.1	22.1	58.0	60.9	32.6	86.2	32.6	9.9	9.7
Minimum (°C)	$Ni_{(i)}+Ti_{(i)}$	60.2	13.5	53.8	68.7	18.4	82.0	28.3	1.4	1.3
	$Ni_{(ii)}+Ti_{(ii)}$	63.3	18.2	54.0	54.2	24.3	84.7	24.3	5.1	5.0
Maximum (°C)	$Ni_{(i)}+Ti_{(i)}$	63.5	28.5	58.7	73.4	22.5	85.9	30.8	8.7	8.4
	$Ni_{(ii)}+Ti_{(ii)}$	64.9	25.9	60.4	70.0	38.8	87.6	38.8	15.5	14.9

Abbreviations: A_f: Austenitic finish temperature; A_p: Austenitic peak temperature; A_s: Austenitic start temperature; E_c: Cooling cycle (exothermic) phase transformation enthalpy; E_h: Heating cycle (endothermic) phase transformation enthalpy; M_f: Martensitic finish temperature; M_p: Martensitic peak temperature; M_s: Martensitic start temperature; Ni: Nickel; Ti: Titanium.

illustrated in Figure 9. Martensitic start, martensitic peak, martensitic finish, austenitic start, austenitic peak, and austenitic finish temperatures are represented by M_s, M_p, M_f, A_s, A_p, and A_f, respectively. Cooling cycle (exothermic) and heating cycle (endothermic) phase transformation enthalpies are represented by E_c and E_h, respectively. M_s and M_p did not vary significantly, with M_s measuring an average of 62.1°C with a min-max range of 60.2°C–63.5°C for $Ni_{(i)}+Ti_{(i)}$, and an average of 64.1°C with a min-max range of 63.3°C–64.9°C for $Ni_{(ii)}+Ti_{(ii)}$ The widths of the martensitic transformation curves (M_s–M_f) were 19.2°C for $Ni_{(i)}+Ti_{(i)}$ and 22.1°C for $Ni_{(ii)}+Tii_{(i)}$. The widths of the austenitic transformation curves (A_s–Af) were 20.5°C for $Ni_{(i)}+Ti_{(i)}$ and 32.6°C for $Ni_{(ii)}+Tii_{(i)}$. There was a significant

difference in average A_s and standard deviation between the two batches, with average A_s = 71.2°C (σ = 0.98) for $Ni_{(i)}$+$Ti_{(i)}$ and 60.9°C (σ = 4.02) for $Ni_{(ii)}$+$Ti_{(ii)}$. A_p did not vary significantly across all specimens for both batches, from a minimum temperature of 82.0°C to a maximum temperature of 87.6°C.

Figure 10 shows the DSC transformation curves for selected specimens, representative of the median enthalpy for each batch. All specimens exhibited direct phase transformations on heating (M–A) and cooling (A–M) cycles, with no evidence of secondary R-phase. As shown in Table 1, average cooling and heating enthalpy values for batch $Ni_{(i)}$+$Ti_{(i)}$ were 3.4 J/g and 3.2 J/g, respectively, considerably lower than the corresponding values for batch $Ni_{(ii)}$+$Ti_{(ii)}$ at 9.9 J/g and 9.7 J/g. There was considerable variation in phase transformation enthalpy within each batch, with cooling enthalpy for $Ni_{(i)}$+$Ti_{(i)}$ ranging from a minimum of 1.4 J/g to a maximum of 8.7 J/g. For batch $Ni_{(ii)}$+$Ti_{(ii)}$, cooling enthalpy varied from a minimum of 5.1 J/g to a maximum of 15.5 J/g. In general, transition enthalpy changes were 1%–5% higher in the cooling cycle than in the heating cycle. The enthalpy values were influenced by specimen position and were strongly negatively correlated with RD. The regression plot in Figure 11 has an R^2 coefficient of 88%.

3.6. XRD phase analysis

Analysis of XRD results using Rietveld refinement across 13 specimens, selected for high, low, and nominal phase transformation enthalpy across both batches, indicated that at room temperature, more than 95% of the area fraction in all specimens consisted of a mixture of two phases, austenite B2 and martensite B19'. Figure 12 shows representative XRD plots for low, nominal, and high enthalpy. The area fraction of B19' varied from 9% to 63% and was positively correlated with phase transformation enthalpy, as shown in Figure 13.

3.7. Microstructure

A multi-modal grain structure was observed in all specimens, as demonstrated in Figure 14. This consisted of near-equiatomic (Ni = 48%at. to 52%at.) coarse columnar grains, approximately 50 µm–150 µm in size, interspersed with clusters of Ni-poor (Ni = 45%at. to 48%at.) equi-axed grains <2 µm in size and Ni-poor dendritic grains up to 5 µm in length. Regions of unmelted or partially melted Ti (Ni < 10%at.) and coarse Ti_2Ni precipitates (Ni = 33.3%) up to 30 µm in size were also present.

4. Discussion

4.1. RD

The positive correlation between Ni content and RD (Figure 8) and the absence of any correlation between density measured by micro-CT porosity and RD, as measured by Archimedes (Figure S3), indicate that the patterns in RD in Figure 7 are primarily attributable to chemistry variation. Chemistry variation may be due to one or both of two factors: Variation in particle size throughout the powder bed, which impacts chemical homogeneity, and melt pool size and temperature, causing variations in the rate of Ni evaporation,[42] or segregation of the Ni and Ti particles during deposition on the powder bed. The repeating trends in RD for each row in all four trials (Figure S2), in the direction of powder deposition, and the absence of any corresponding trend by column (Figure S1), indicate that RD variation is attributable to powder deposition patterns as a function of distance from the start position of the spreader arm.

Regarding Figure 7, the segregation patterns by row number, as defined in Figure 1, follow consistent non-linear patterns. For powders melted in Rows 1–4 (green and orange regions), there was a decrease in RD followed by an increase between Rows 2 and 4, and a decrease between Rows 4 and

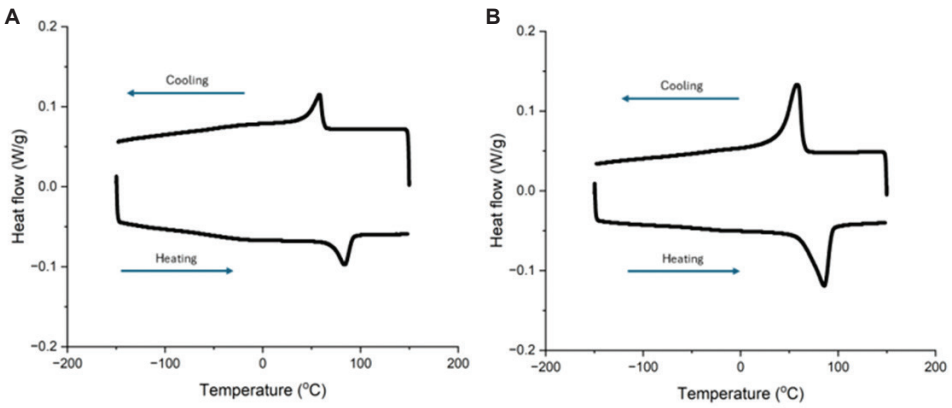

Figure 10. Differential scanning calorimetry curve for selected median specimens. *In situ* batch (A) $Ni_{(i)}$+$Ti_{(i)}$, and (B) $Ni_{(ii)}$+$Ti_{(ii)}$. Abbreviations: Ni: Nickel; Ti: Titanium.

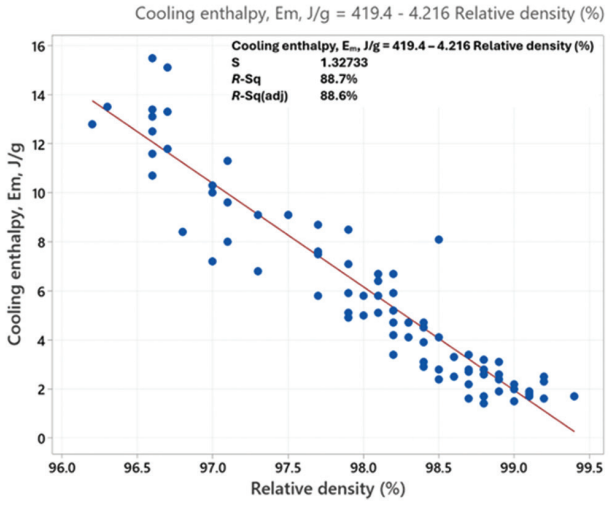

Figure 11. Phase transformation cooling enthalpy versus relative density, combining batches $Ni_{(i)}$+$Ti_{(i)}$ and $Ni_{(ii)}$+$Ti_{(ii)}$.
Abbreviations: Ni: Nickel; *R*-sq: *R*-squared; Ti: Titanium.

7. For unmelted powders in Rows 1–3 (blue region), there was an increase in RD from Rows 4 to 6, followed by a slight decrease between Rows 6 and 7. This indicates that the substrate over which the powder travels (melted versus unmelted regions) impacts deposition patterns.

The effect of the substrate on powder deposition patterns can also be assessed by comparing the standard deviation in RD across the layouts. Batch $Ni_{(i)}$+$Ti_{(i)}$ Layout C had the lowest standard deviation of the four trials, indicating that the rate of segregation between Ti and Ni over powder bed regions with the highest fraction of melted powder and smoothest substrate is lower than for regions containing higher fractions of unmelted powder. This may be attributable to lower friction resistance against the movement of the powder arm over smoother areas with higher fractions of melted powder.

Powder flow in LPBF is controlled by competing factors, including a cohesive effect due to interparticle forces and a geometric effect due to spreader arm clearance with the powder particles.[32] It is known that for particles below 100 µm in size, the ratio of interparticle forces to gravity, known as the Granular Bond number, B_0, is negatively correlated with flowability,[43] and can be expressed as Equation II[33]:

$$B_0 = \frac{F_C}{Fw} \quad \text{(II)}$$

where F_C is the inter-particle cohesive force and F_W is the gravimetric force. F_C is directly proportional to the CI for each bulk powder interaction.[36] Furthermore, because the PSDs of the batches of Ti and Ni powders are closely matched for each blend (Figure 3), F_W is directly proportional to the density of each material. The ratio between the bond numbers B_{oTi} and B_{oNi} for the Ti-Ti and Ni-Ni powder interactions, respectively, can therefore be expressed as Equation III:

$$\frac{B_0 T_i}{B_{oN_i}} = \frac{CI_{T_i} \cdot \rho_{N_i}}{CI_{N_i} \cdot \rho_{T_i}} \quad \text{(III)}$$

The dynamic flow results from the GranuDrum trials (Figure 5A) demonstrated that the ratio of the interparticle cohesive forces, CI_{Ti}: CI_{Ni}, at rotating speed corresponding to the deposition speed in the trials (11 rpm/50 fpm) is 1.63. The gravimetric force ratio ρ_{Ni}: ρ_{Ti} = 8.89: 4.51 = 1.97.[44,45] Multiplying the CI_{Ti}: CI_{Ni} by the gravimetric force ratio ρ_{Ni}:ρ_{Ti} gives 3.2, meaning the Bond number of the Ti-Ti powder interaction is 3.2 times higher than that of the Ni-Ni powder interaction, and the two materials are likely to spread at different rates and segregate within the powder bed. The dynamic flow CI results for the Ni-Ti blend indicate that the Ni-Ti interparticle cohesion is an average of the Ni-Ni and Ti-Ti interparticle cohesion.

Powder deposition patterns are also influenced by the PSD range, with smaller particles being deposited closer to the start position of the deposition arm sweep than larger particles, as demonstrated by Mussatto *et al.*[20]

The higher variation in RD and lower overall average RD of $Ni_{(ii)}$+$Ti_{(ii)}$ compared to $Ni_{(i)}$+$Ti_{(i)}$ (Figure 6) can be partly explained by the larger particle size in the former, leading to larger melt pools and longer homogenization times, increasing Ni evaporation[9] and chemical inhomogeneity.[10,46] Another reason for the higher variation in RD within the batch with the larger particle size is the effect of the ratio between layer thickness and d_{90} particle size on flowability.[47] Ahmed *et al.*[30] found that flowability improved as this ratio increased, with optimum flowability occurring at a ratio of 2.5 or greater.[30] The ratio between layer thickness (t = 60 µm) and d_{90} particle size is 0.92 for $Ni_{(ii)}$+$Ti_{(ii)}$ and 1.22 for $Ni_{(i)}$+$Ti_{(i)}$, indicating reduced flowability for the former, which is most likely linked to an increased rate of particle segregation. Another factor that is likely contributing to increased variation in RD $Ni_{(ii)}$+$Ti_{(ii)}$ compared to $Ni_{(i)}$+$Ti_{(i)}$, based on earlier observations of higher powder segregation over substrates of higher roughness, is that the larger powder particles are creating a rougher substrate than the smaller particles.

The higher FT4 BFE and SE for $Ni_{(i)}$+$Ti_{(i)}$ relative to $Ni_{(ii)}$+$Ti_{(ii)}$ (Figure 4A and B) are likely attributable to the wider PSD span and higher fraction of fine powder of the former.[48] Despite the higher flow energy, the lower overall segregation rate within $Ni_{(i)}$+$Ti_{(i)}$ indicates that FT4 bulk

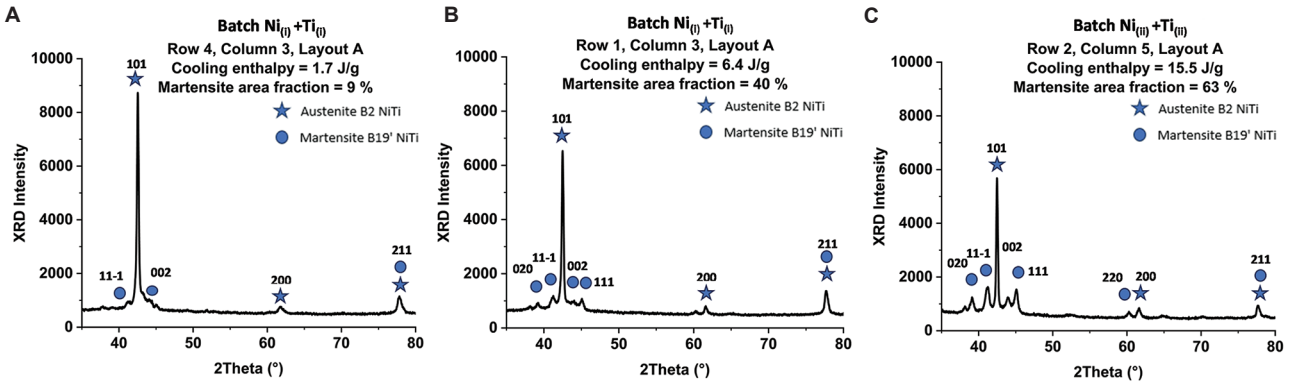

Figure 12. X-ray diffraction plots of selected specimens. (A) Low cooling enthalpy and low martensite area fraction, (B) nominal cooling enthalpy and nominal martensite area fraction, and (C) high cooling enthalpy and high martensite area fraction.
Abbreviations: Ni: Nickel; Ti: Titanium; XRD: X-ray diffraction.

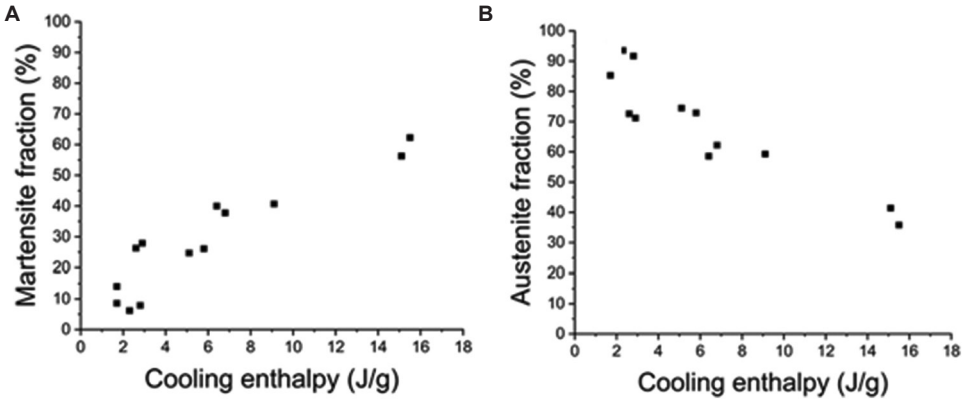

Figure 13. Phase transformation. (A) Cooling enthalpy versus martensite and (B) cooling enthalpy versus austenite area fractions of selected specimens calculated by Rietveld analysis of X-ray diffraction data.

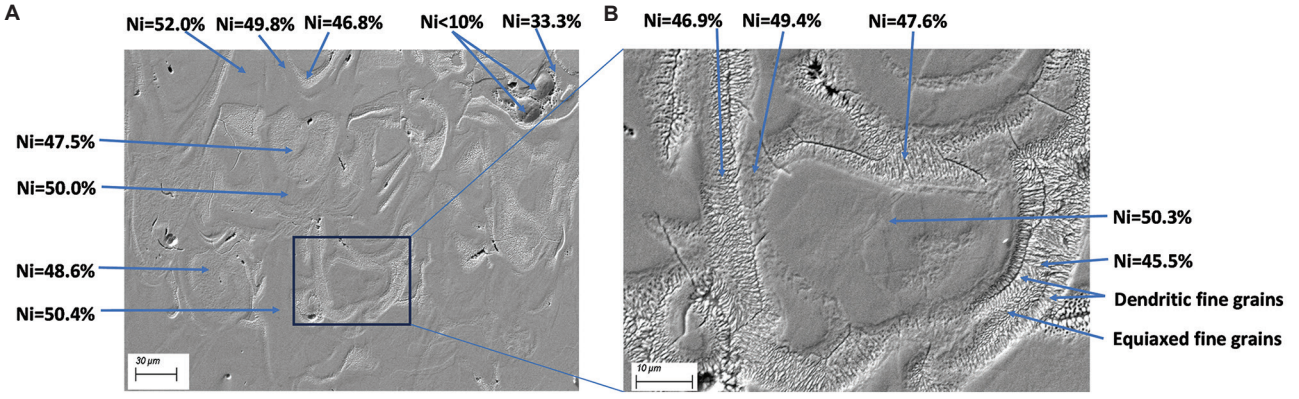

Figure 14. Representative vertical cross-section and energy-dispersive X-ray spectroscopy map spectra results for the vertical cross-section of an *in situ* alloyed specimen. Batch $Ni_{(i)}$+$Ti_{(i)}$ at (A) low magnification (Scale bar: 30 µm; magnification: 1000×) and (B) a higher magnification (Scale bar: 10 µm; magnification: 4000×) of the identified region in (A).
Abbreviations: Ni: Nickel; Ti: Titanium.

flow energy characteristics, as measured, within the ranges tested, have a lesser influence on powder flow segregation than the other factors discussed above. In summary, the segregation patterns of the Ni and Ti powders in the LPBF powder bed are primarily affected by differences in material density, interparticle cohesive forces, the substrate over which the powder travels during deposition, and the PSD.

4.2. Phase transformation behavior

The variation in phase transformation enthalpy as a function of RD/Ni content (Figure 11) is a remarkable feature of the results. Phase transformation enthalpy ΔH_{NET} is made up of chemical, $\Delta H_{CH,}$ elastic, ΔH_{EL}, and surface friction, ΔH_{FR}, components, in accordance with Equation IV.[49]

$$\Delta H_{NET} = \Delta H_{CH} + \Delta H_{EL} + \Delta H_{FR} \quad \text{(IV)}$$

The chemical driving force, ΔH_{CH}, generates reversible transformation energy and depends on the volume fraction of reversible NiTi.[50] XRD analysis (Figure 12) indicated the presence of both B19' martensite phase and B2 austenite phase at room temperature, with varying relative area fractions. The positive correlation between the calculated area fraction of B19' and phase transformation enthalpy in Figure 13 indicates that the B19' area fraction is providing the chemical driving force for phase transformation behavior. The negative correlation between the B2 area fraction and phase transformation enthalpy indicates that the driving force of the B2 microstructure may be more significantly inhibited by localized chemical inhomogeneity than that of the B19' microstructure. Furthermore, the high phase transformation temperatures are consistent with a dominantly martensite microstructure,[34] indicating the absence of any significant driving force from the B2 fraction.

The elastic strain energy component, ΔH_{EL}, of the phase transformation enthalpy is necessary to accommodate transformational shape and volume changes. Increased Ni content increases density, which causes decreased elastic strain energy.[49,51] The strong negative correlation between enthalpy and RD (Figure 11) and the strong positive correlation between Ni content and RD discussed above (Figure 8) indicate that variation in Ni content is likely to significantly cause the observed variation in enthalpy within each trial. Furthermore, these correlations indicate that the lower average Ni content of batch $Ni_{(ii)}+Ti_{(ii)}$ relative to $Ni_{(i)}+Ti_{(i)}$ is likely to be a significant reason for the former's higher average enthalpy.

The frictional energy component, ΔH_{FR}, of the phase transformation enthalpy, represents energy dissipated to overcome frictional barriers during heating or cooling, and is a measure of the hysteresis, which can be measured from the DSC transformation temperature data as A_f–M_s.[50] The difference in hysteresis between the two batches is relatively small (Table 1 and Figure 9C), with a value of 29.5°C for $Ni_{(i)}+Ti_{(i)}$ and a value of 32.6°C for $Ni_{(ii)}+Ti_{(ii)}$, indicating that frictional losses may be marginally greater for $Ni_{(ii)}+Ti_{(ii)}$.

In summary, the recorded variation in phase transformation enthalpy can be primarily attributed to the chemical driving force from NiTi existing as B19' at room temperature, and variations in elastic strain energy negatively correlated with RD and Ni content. While the austenite phase transformation has to occur when the martensitic phase transformation occurs, the martensitic phase transformation is regarded as more important for contributing to the enthalpy response than the austenitic phase transformation (Figure 13). The variation in frictional driving force, measured by thermal hysteresis variation, is not significant.

Another noteworthy difference in the DSC curves of the two powder batches is the width of the heating transformation enthalpy curve A_f–A_s (Table 1). The average A_f–A_s was 20.5°C for $Ni_{(i)}+Ti_{(i)}$ and 32.6°C for $Ni_{(ii)}+Ti_{(ii)}$. This indicates the likelihood of higher chemical inhomogeneity in $Ni_{(ii)}+Ti_{(ii)}$ relative to $Ni_{(i)}+Ti_{(i)}$,[52,53] and is consistent with the higher variation in Ni content and RD that were measured in $Ni_{(ii)}+Ti_{(ii)}$ relative to $Ni_{(i)}+Ti_{(i)}$ (Figures 6 and 7B).

The low variation in martensitic start temperature across all tested specimens indicates low average overall Ni content. It is well known that at Ni contents below 50%at., martensitic start temperatures vary negligibly.[34,54] Average Ni content across the specimens, as measured by EDX mapping, was 49.4%. Although regions of coarse columnar with Ni content as high as 51.6%at. were identified (Figure 14), it appears that such regions do not contribute to phase transformation, and are likely to be composed of high proportions of Ni-rich precipitates. This is supported by the relatively low average phase transformation enthalpies (3.4 J/g for batch $Ni_{(i)}+Ti_{(i)}$ and 9.9 J/g for $Ni_{(ii)}+Ti_{(ii)}$). Phase transformation enthalpies for LPBF nitinol from pre-alloyed powder have been reported by Kordizadeh *et al.*[55] as 16–20 J/g[55] and by Khanlari *et al.*[56] as 13.8–15.7 J/g.[56] Analysis of the composition, size, and distribution of precipitates, as well as their effect on phase change and enthalpies, is beyond the scope of this work and is a recommended area for future research.

4.3. Microstructure

The multi-modal grain patterns throughout the microstructure (Figure 14) are evidence of a wide variation in the driving forces for grain nucleation and growth. Increased chemical inhomogeneity promotes increased constitutional supercooling and increases the complexity of phase transformation paths.[57] Higher non-uniform thermal distribution in the melt pool leads to a larger surface tension gradient, creating the conditions for increased Marangoni flow relative to pre-alloyed powders.[21] Furthermore, the highly localized nature of the Ni-Ti exothermic reactions

within the rapid cooling environment is expected to cause increased variation in thermal gradients.[16] The combined effect of these driving forces results in a greater grain size and morphology variety.

In summary, this study has established new insights into powder segregation during *in situ* alloying within the LPBF process and has found a direct link between powder segregation during deposition and nitinol phase transformation properties. The insights gained from this work into the effect of particle size and build distribution on properties will assist future studies in achieving improved microstructural and chemical homogeneity of *in situ* alloyed nitinol with tailored thermo-mechanical performance.

5. Conclusion

Powder segregation patterns of Ni and Ti powders in the LPBF process had a significant impact on RD and elasto-caloric properties of *in situ* alloyed nitinol, with regions of lower RD correlated with lower Ni content and higher phase transformation enthalpies compared to regions with higher Ni content. Powder segregation patterns between Ti and Ni particles varied more for an elementally blended batch with a d_{10}-d_{50}-d_{90} PSD of 33–47–65 μm than 21–32–48 μm.

The location and relative area fractions of unmelted and melted powder, as determined by the build layout, significantly impacted powder segregation patterns. It was found that powder segregation rates between Ti and Ni particles were higher for rougher substrates containing higher amounts of unmelted powder than smoother substrates containing higher amounts of melted and solidified powder. Furthermore, the position of the unmelted powder relative to the deposition arm sweep impacted powder segregation patterns throughout the build plate.

In addition to PSD and build layout, powder segregation patterns in the LPBF deposition bed were also affected by differences in material density between Ni and Ti and interparticle cohesive forces. The findings of this work concerning powder segregation within the LPBF process have significant implications for *in situ* alloying of nitinol and other alloys and can assist future studies in improving microstructural and chemical homogeneity and tailoring thermo-mechanical performance.

Acknowledgments

XRD testing was conducted at the Bernal Institute, University of Limerick, Limerick, Ireland. Micro-CT scanning was performed at the South-Eastern Applied Materials Research Centre, Waterford Institute of Technology, Waterford, Ireland. Optical microscopy and PSD measurements were conducted at the Nano Research Facility in Dublin City University.

Funding

This publication has emanated from research supported by a research grant from the Science Foundation Ireland (SFI) under grant number 16/RC/3872 and is co-funded by I-Form industry partner Fort Wayne Metals Ireland.

Conflict of interest

The authors declare that they have no competing interests.

Author contributions

Conceptualization: Declan Bourke, Dermot Brabazon
Formal analysis: Declan Bourke, Medad Monu, Inam Ul Ahad, Dermot Brabazon
Investigation: Declan Bourke, Medad Monu, Alexander Sloane, Inam Ul Ahad, Dermot Brabazon
Methodology: Declan Bourke, Medad Monu, Paul Healy, Alexander Sloane, Dermot Brabazon
Writing–original draft: Declan Bourke
Writing–review & editing: Inam Ul Ahad, Dermot Brabazon

Ethics approval and consent to participate

Not applicable.

Consent for publication

Not applicable.

Availability of data

Requests to access the datasets should be directed to the corresponding author.

References

1. Khoo ZX, Liu Y, An J, Chua CK, Shen YF, Kuo CN. A review of selective laser melted NiTi shape memory alloy. *Materials*. 2018;11(4):519.

   doi: 10.3390/ma11040519

2. Sharma N, Jangra KK, Raj T. Fabrication of NiTi alloy: A review. *Proc Inst Mech Eng Part J Mater Des Appl.* 2018;232(3):250-269.

   doi: 10.1177/1464420715622494

3. Farber E, Zhu JN, Popovich A, Popovich V. A review of NiTi shape memory alloy as a smart material produced by additive manufacturing. *Mater Today Proc.* 2020;30:761-767.

   doi: 10.1016/j.matpr.2020.01.563

4. Zhan J, Wu J, Ma R, Li K, Lin J, Murr LE. Tuning the functional properties by laser powder bed fusion with

partitioned repetitive laser scanning: Toward editable 4D printing of NiTi alloys. *J Manuf Process.* 2023;101:1468-1481.

doi: 10.1016/j.jmapro.2023.07.009

5. Duda T, Raghavan LV. 3D metal printing technology. *IFAC Pap.* 2016;49(29):103-110.

doi: 10.1016/j.ifacol.2016.11.111

6. Bormann T, Müller B, Schinhammer M, Kessler A, Thalmann P, De Wild M. Microstructure of selective laser melted nickel-titanium. *Mater Charact.* 2014;94:189-202.

doi: 10.1016/j.matchar.2014.05.017

7. Chekotu JC, Groarke R, O'Toole K, Brabazon D. Advances in selective laser melting of nitinol shape memory alloy part production. *Materials (Basel).* 2019;12(5):809.

doi: 10.3390/ma12050809

8. Alagha AN, Hussain S, Zaki W. Additive manufacturing of shape memory alloys: A review with emphasis on powder bed systems. *Mater Des.* 2021;204:109654.

doi: 10.1016/j.matdes.2021.109654

9. Elahinia M, Shayesteh Moghaddam N, Taheri Andani M, Amerinatanzi A, Bimber BA, Hamilton RF. Fabrication of NiTi through additive manufacturing: A review. *Prog Mater Sci.* 2016;83:630-663.

doi: 10.1016/j.pmatsci.2016.08.001

10. Bourke D, Selvam KT, Obeidi MA, Ul Ahad I, Brabazon D. Effect of powder and process parameters on *in-situ* alloying of nitinol during laser powder bed fusion. *J Mater Res Technol.* 2024;30:7988-7997.

doi: 10.1016/j.jmrt.2024.05.178

11. Wang S, Shi Y, Fan K, Wang Q, Li Y, Teng X. Microstructure and elastocaloric effect of NiTi shape memory alloy *in-situ* synthesized by laser directed energy deposition additive manufacturing. *Mater Charact.* 2024;210:113831.

doi: 10.1016/j.matchar.2024.113831

12. Ewald S, Kies F, Hermsen S, Voshage M, Haase C, Schleifenbaum JH. Rapid alloy development of extremely high-alloyed metals using powder blends in laser powder bed fusion. *Materials(Basel).* 2019;12(10):1706.

doi: 10.3390/ma12101706

13. Wang C, Tan XP, Du Z, *et al.* Additive manufacturing of NiTi shape memory alloys using pre-mixed powders. *J Mater Process Technol.* 2019;271:152-161.

doi: 10.1016/j.jmatprotec.2019.03.025.

14. Zhang B, Chen J, Coddet C. Microstructure and transformation behavior of *in-situ* shape memory alloys by selective laser melting Ti-Ni mixed powder. *J Mater Sci Technol.* 2013;29(9):863-867.

doi: 10.1016/j.jmst.2013.05.006

15. Stoll P, Spierings A, Wegener K. SLM processing of elementally blended NiTi shape memory alloy. *Procedia CIRP.* 2020;95:121-126.

doi: 10.1016/j.procir.2020.02.250

16. Mosallanejad MH, Niroumand B, Aversa A, Saboori A. *In-situ* alloying in laser-based additive manufacturing processes: A critical review. *J Alloys Compd.* 2021;872:159567.

doi: 10.1016/j.jallcom.2021.159567

17. Li H, Brodie EG, Hutchinson C. Predicting the chemical homogeneity in laser powder bed fusion (LPBF) of mixed powders after remelting. *Addit Manuf.* 2023;65:103447.

doi: 10.1016/j.addma.2023.103447

18. Shoji Aota L, Bajaj P, Zschommler Sandim HR, Aimé Jägle E. Laser powder-bed fusion as an alloy development tool: Parameter selection for *in-situ* alloying using elemental powders. *Materials.* 2020;13(18):3922.

doi: 10.3390/ma13183922

19. Knieps MS, Reynolds WJ, Dejaune J, Clare AT, Evirgen A. *In-situ* alloying in powder bed fusion: The role of powder morphology. *Mater Sci Eng A.* 2021;807:140849.

doi: 10.1016/j.msea.2021.140849

20. Mussatto A, Groarke R, O'Neill A, Obeidi MA, Delaure Y, Brabazon D. Influences of powder morphology and spreading parameters on the powder bed topography uniformity in powder bed fusion metal additive manufacturing. *Addit Manuf.* 2021;38:101807.

doi: 10.1016/j.addma.2020.101807

21. Zhao C, Fezzaa K, Cunningham RW, *et al.* Real-time monitoring of laser powder bed fusion process using high-speed X-ray imaging and diffraction. *Sci Rep.* 2017;7:3602.

doi: 10.1038/s41598-017-03761-2

22. Thiedemann U, Rösner-Kuhn M, Drewes K, Kuppermann G, Frohberg MG. Temperature dependence of the mixing enthalpy of liquid Ti-Ni and Fe-Ti-Ni alloys. *J Non Cryst Solids.* 1999;250-253:329-335.

doi: 10.1016/S0022-3093(99)00258-6

23. Chen Y, Zhang X, Parvez MM, Liou F. A review on metallic alloys fabrication using elemental powder blends by laser powder directed energy deposition process. *Materials (Basel).* 2020;13(16):3562.

doi: 10.3390/ma13163562

24. Chmielewska A, Wysocki B, Buhagiar JP, *et al. In situ* alloying of NiTi: Influence of laser powder bed fusion (LBPF) scanning strategy on chemical composition. *Mater Today Commun.* 2022;30:103007.

doi: 10.1016/j.mtcomm.2021.103007

25. Yadroitsev I. *Selective Laser Melting: Direct Manufacturing of 3D-Objects by Selective Laser Melting of Metal Powders.*

Germany: LAP Lambert Academic Publishing; 2009.

26. Aboulkhair NT, Everitt NM, Ashcroft I, Tuck C. Reducing porosity in AlSi10Mg parts processed by selective laser melting. *Addit Manuf.* 2014;1-4:77-86.

    doi: 10.1016/j.addma.2014.08.001

27. Zhao C, Liang H, Luo S, Yang J, Wang Z. The effect of energy input on reaction, phase transition and shape memory effect of NiTi alloy by selective laser melting. *J Alloys Compd.* 2020;817:153288.

    doi: 10.1016/j.jallcom.2019.153288

28. Chmielewska A, Wysocki BA, Gadalińska E, *et al.* Laser powder bed fusion (LPBF) of NiTi alloy using elemental powders: The influence of remelting on printability and microstructure. *Rapid Prototy J.* 2022;28:1845-1868.

    doi: 10.1108/RPJ-08-2021-0216

29. Nan W, Pasha M, Bonakdar T, *et al.* Jamming during particle spreading in additive manufacturing. *Powder Technol.* 2018;338:253-262.

    doi: 10.1016/j.powtec.2018.07.030

30. Ahmed M, Pasha M, Nan W, Ghadiri M. A simple method for assessing powder spreadability for additive manufacturing. *Powder Technol.* 2020;367:671-679.

    doi: 10.1016/j.powtec.2020.04.033

31. Xu R, Nan W. Analysis of the metrics and mechanism of powder spreadability in powder-based additive manufacturing. *Addit Manuf.* 2023;71:103596.

    doi: 10.1016/j.addma.2023.103596

32. He Y, Hassanpour A, Bayly AE. Combined effect of particle size and surface cohesiveness on powder spreadability for additive manufacturing. *Powder Technol.* 2021;392:191-203.

    doi: 10.1016/j.powtec.2021.06.046

33. Giraud M, Gatumel C, Vaudez S, *et al.* Investigation of a granular Bond number based rheological model for polydispersed particulate systems. *Chem Eng Sci.* 2020;228:115971.

    doi: 10.1016/j.ces.2020.115971

34. Frenzel J, George EP, Dlouhý A, Somsen C, Wagner WF, Eggeler G. Influence of Ni on martensitic phase transformations in NiTi shape memory alloys. *Acta Mater.* 2010;58(9):3444-3458.

    doi: 10.1016/j.actamat.2010.02.019

35. Groarke R, Vijayaraghavan RK, Powell D, Rennie A, Brabazon D. Powder characterization-methods, standards, and state of the art. In: Yadroitsev I, Yadroitsava I, Du Plessis A, MacDonald E, editors. *Fundamentals of Laser Powder Bed Fusion of Metals. In Additive Manufacturing Materials and Technologies*. Netherlands: Elsevier; 2021. p. 491-527.

    doi: 10.1016/B978-0-12-824090-8.00006-8

36. Tondare VN, Whiting JG, Pintar AL, Moylan S, Neveu A, Francqui F. An interlaboratory study for assessing repeatability and reproducibility of the data generated by rotating drum powder rheometers (part 1: Granudrum). *Powder Technol.* 2024;441:119810.

    doi: 10.1016/j.powtec.2024.119810

37. Neveu A, Francqui F, Lumay G. Measuring powder flow properties in a rotating drum. *Measurement*. 2022;200:111548.

    doi: 10.1016/j.measurement.2022.111548

38. ISO. *ISO/ASTM TR 52952:2023*. ISO. Available from: https://www.iso.org/standard/83717.html [Last accessed on 2025 Apr 03].

39. *Crystallography Open Database*. Available from: https://www.crystallography.net/cod/index.php [Last accessed on 2024 Feb 06].

40. Rodriguez-Carvajal J. Introduction to the program FULLPROF: Refinement of crystal and magnetic structures from powder and single crystal data, Laboratoire Léon Brillouin (CEA-CNRS). France: CEA/Saclay; 2001. [Online]. Available: https://www.researchgate.net/publication/267375610

41. *Match! - Phase Analysis using Powder Diffraction*. Available from: https://www.crystalimpact.de/match [Last accessed on 2024 Nov 04].

42. Wang J, Zhu R, Liu Y, Zhang L. Understanding melt pool characteristics in laser powder bed fusion: An overview of single- and multi-track melt pools for process optimization. *Adv Powder Mater.* 2023;2(4):100137.

    doi: 10.1016/j.apmate.2023.100137

43. Capozzi LC, Sivo A, Bassini E. Powder spreading and spreadability in the additive manufacturing of metallic materials: A critical review. *J Mater Process Technol.* 2022;308:117706.

    doi: 10.1016/j.jmatprotec.2022.117706

44. *ASM Material Data Sheet*. Available from: https://asm.matweb.com/search/specificmaterial.asp?bassnum=ntime35a [Last accessed on 2025 Apr 11].

45. *Nickel, Cobalt, and their Alloys (asm Specialty Handbook) [PDF] [12ncqllkk93o]*. Available from: https://vdoc.pub/documents/nickel/cobalt/and/their/alloys/asm/specialty/handbook/12ncqllkk93o [Last accessed on 2025 Apr 11].

46. Yadroitsev I, Krakhmalev P, Yadroitsava I. Titanium alloys manufactured by *in situ* alloying during laser powder bed fusion. *JOM*. 2017;69(12):2725-2730.

    doi: 10.1007/s11837-017-2600-7

47. Spierings A, Levy G. *Comparison of Density of Stainless Steel 316 L Parts Produced with Selective Laser Melting using Different Powder Grades*; 2009. Available from: https://www.semanticscholar.org/paper/comparison/

of/density/of/stainless/steel/316/l/with/spierings/levy/e5a132bae55615a773d2468c4692c28865abf313 [Last accessed on 2025 Feb 26].

48. Snow Z, Martukanitz R, Joshi S. On the development of powder spreadability metrics and feedstock requirements for powder bed fusion additive manufacturing. *Addit Manuf.* 2019;28:78-86.

doi: 10.1016/j.addma.2019.04.017

49. Ortín J, Planes A. Thermodynamic analysis of thermal measurements in thermoelastic martensitic transformations. *Acta Metall.* 1988;36(8):1873-1889.

doi: 10.1016/0001-6160(88)90291-X

50. Humbeeck JV, Stalmans R, Chandrasekaran M, Delaey L. *On the Stability of Shape Memory Alloys*. Netherlands: Elsevier; 1990. p. 96-105.

doi: 10.1016/B978-0-7506-1009-4.50012-3

51. Khalil-Allafi J, Amin-Ahmadi B. The effect of chemical composition on enthalpy and entropy changes of martensitic transformations in binary NiTi shape memory alloys. *J Alloys Compd.* 2009;487(1):363-366.

doi: 10.1016/j.jallcom.2009.07.135

52. Sam J, Franco B, Ma J, Karaman I, Elwany A, Mabe JH. Tensile actuation response of additively manufactured nickel-titanium shape memory alloys. *Scr Mater.* 2018;146:164-168.

doi: 10.1016/j.scriptamat.2017.11.013

53. Zhang Q, Hao S, Liu Y, *et al.* The microstructure of a selective laser melting (SLM)-fabricated NiTi shape memory alloy with superior tensile property and shape memory recoverability. *Appl Mater Today*. 2020;19:100547.

doi: 10.1016/j.apmt.2019.100547

54. Wang X, Yu J, Liu J, *et al.* Effect of process parameters on the phase transformation behavior and tensile properties of NiTi shape memory alloys fabricated by selective laser melting. *Addit Manuf.* 2020;36:101545.

doi: 10.1016/j.addma.2020.101545

55. Kordizadeh F, Mohajerani S, Safaei K, *et al.* Investigating the elastocaloric effect of the NiTi fabricated by laser powder bed fusion: Effect of the building orientation. *Materialia*. 2023;30:101817.

doi: 10.1016/j.mtla.2023.101817

56. Khanlari K, Shi Q, Li K, Hu K, Cao P, Liu X. Effects of printing volumetric energy densities and post-processing treatments on the microstructural properties, phase transformation temperatures and hardness of near-equiatomic NiTinol parts fabricated by a laser powder bed fusion technique. *Intermetallics*. 2021;131:107088.

doi: 10.1016/j.intermet.2021.107088

57. Collins C, Brice DA, Samimi P, Ghamarian I, Fraser HL. Microstructural control of additively manufactured metallic materials. *Annu Rev Mater Res.* 2016;46:63-91.

doi: 10.1146/annurev-matsci-070115-031816

ACCSCIENCE PUBLISHING

OUR JOURNALS

Materials Science in Additive Manufacturing (MSAM) aims to bridge the cutting-edge research between additive manufacturing and the entire spectrum of materials science. The journal covers all applied and fundamentals of processing, synthesis, structure, composition, properties and performance of materials designed or manipulated for additive manufacturing. The journal covers a wide scope of innovative techniques, processes, methods, and applications. Topics of particular interest include, but are not limited to:

- Theory and modelling
- Artificial intelligence
- Polymers
- Metals and alloys
- Ceramics
- Composites
- Magnetic materials
- Smart materials
- Nano-materials
- Materials for electronics
- Characterization techniques

International Journal of AI for Materials and Design is an international, peer-reviewed open-access journal that aims to bridge the cutting-edge research between AI and materials, AI and design. In recent years, the tremendous progress in AI is leading a radical shift of AI research from a mainly academic endeavor to a much broader field with increasing industrial and governmental investments. The maturation of AI technology brings about a step change in the scientific research of various domains, especially in the world of materials and design. Machine learning (ML) algorithms enable researchers to analyze extensive datasets on material properties and accurately predict their behavior in different conditions. This subsequently impact the industry to leverage on big data and advanced analytics to build scientific strategies, scale operational performance of processes and drive innovation.

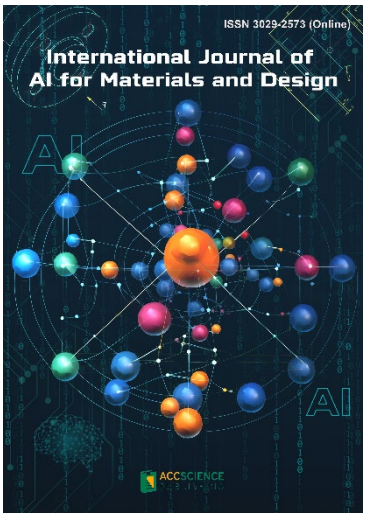

International Journal of AI for Materials and Design covers the following topics: AI or machine learning for material discovery, AI for process optimization, AI and data-driven approaches for product or systems design, application of AI in advanced manufacturing processes such as additive manufacturing, IoT, sensors, robotics, cloud-based manufacturing, intelligent manufacturing for various applications, autonomous experiments, material intelligence, energy intelligence, and AI-linked decarbonization technologies.

Start a new journal

Write to us via email if you are interested to start a new journal with AccScience Publishing. Please attach your CV, professional profile page and a brief pitch proposal in your email. We shall inform you of our decision whether we are interested to collaborate in starting a new journal.

Contact: info@accscience.com

https://accscience.com/journal/ESAM

Contact
www.accscience.com
9 Raffles Place, Republic Plaza 1 #06-00 Singapore 048619
Email: editorial@accscience.com
Phone: +65 8182 1586